

**Modelling advanced reforming of bio-compounds  
for hydrogen production**

Jennifer Sarah Reeve

Submitted in accordance with the requirements for the degree of  
Doctor of Philosophy

The University of Leeds  
School of Chemical and Process Engineering

August 2020

The candidate confirms that the work submitted is her own, except where work which has formed part of jointly-authored publications has been included. The contribution of the candidate and the other authors to this work has been explicitly indicated below. The candidate confirms that appropriate credit has been given within the thesis where reference has been made to the work of others.

Chapter 3 within this thesis is based on the work that has formed one jointly-authored paper:

J. Spragg, T. Mahmud, V. Dupont. Hydrogen production from bio-oil: A thermodynamic analysis of sorption-enhanced chemical looping steam reforming. *International Journal of Hydrogen Energy*. 2018; .Volume 43, Issue 49: 22032-22045. <https://doi.org/10.1016/j.ijhydene.2018.10.068>.

In this paper, the modelling, results processing and paper writing are directly attributable to the candidate. The candidate's supervisors, Dr Valerie Dupont and Dr Tariq Mahmud, gave comments and edits on the paper.

This copy has been supplied on the understanding that it is copyright material and that no quotation from the thesis may be published without proper acknowledgement.

The right of Jennifer Spragg to be identified as Author of this work has been asserted by her in accordance with the Copyright, Designs and Patents Act 1988.

© 2020 The University of Leeds and Jennifer Spragg

## Acknowledgements

I am grateful to my supervisors Dr Valerie Dupont and Dr Tariq Mahmud, for all that they've taught me, and for their invaluable support and guidance throughout this work.

I would also like to thank the members of my research group, for their advice over the years, including Robert Bloom, Erik Resendiz Mora, Oliver Grasham, Zaheer Syed Abbas, and Robert White.

Many thanks also go to all my colleagues in the CDT in Bioenergy, particularly those in my cohort: Ella, Natalie, Charlotte, Iram, Daisy, Nicola, Ric, Sam, David, Weiyi, Chris, Christian, and Julius. I'm very glad to have shared this journey with them. I would also like to thank my other colleagues, past and present, who made me the engineer I am today.

I am also grateful to the staff of the CDT in Bioenergy, James McKay and Emily Bryan-Kinns, for all their practical support. I would also like to thank the technical staff at the University of Leeds, especially Ed Woodhouse, Karine Thorne, Scott Prichard, and Adrian Cunliffe.

Special thanks to my family – to my parents Sue and Chris, and to Andy and Jo for their kindness, encouragement, advice, and for their belief in me. Also to Chris Reeve, my superman, who has been a constant, calm support through the PhD and much more besides.

This thesis is dedicated to Jean Cockshutt, with gratitude for the world she created for us, and to her great-grandson Ellis Dalton, with hope for the future and the world that he'll inherit.

## Abstract

In the efforts to decarbonise the energy system, there has been a great deal of interest in the potential of hydrogen ( $H_2$ ) as a versatile, low carbon energy vector. To support rising demand for hydrogen in existing and new applications, it will be necessary to find cost-effective routes for hydrogen production at scale. Recent research has identified new methods to optimise the steam reforming process as a means to achieve this. These include chemical looping, in which a metal oxide provides an unmixed source of oxygen directly into the reforming reactor, to enable autothermal reactor operation. Other work has considered sorption enhancement, in which solid  $CO_2$  sorbents provide in situ  $CO_2$  capture, enhancing product purity and improving process yields.

Another branch of research considers the use of bioenergy feedstocks to reduce carbon intensity. One promising route is the fast pyrolysis of bioenergy feedstocks to produce bio-oils, followed by steam reforming. This route could combine the benefits of a flexible bio-based supply chain with those of the steam reforming process, including its thermal efficiency and cost-effectiveness.

This thesis brings together these two branches of process development, to consider the feasibility and benefits of using bio-oil in advanced reforming processes, to produce hydrogen with low, or negative, carbon emissions.

A thermodynamic evaluation is first presented, to determine the thermodynamic feasibility of different bio-oil reforming technologies, including conventional steam reforming (C-SR), sorption-enhanced steam reforming (SE-SR), chemical looping steam reforming (CLSR) and sorption-enhanced chemical looping steam reforming (SE-CLSR). When these benefits of chemical looping and sorption enhancement are combined, the resulting SE-CLSR process is autothermal, with reduced risk of carbon deposition, reduced  $H_2$  purification requirements, and the potential for readily separated  $CO_2$ .

A techno-economic evaluation is carried out on the viability of SE-CLSR and C-SR and with  $CO_2$  capture (C-SR-CCS), using heat and material balances derived from process models in Aspen Plus. C-SR-CCS and SE-CLSR produce hydrogen in a similar price range, of 3.8 to 4.6 \$  $kg_{H_2}^{-1}$ . Both processes have similar operating costs, but SE-CLSR has a lower capital cost, leading to a marginally lower hydrogen cost. SE-CLSR has certain other advantages, such as the elimination of fossil-based energy, and therefore increased potential for net negative emissions. Cost of carbon avoided, based on direct process



emissions, including negative emissions, is estimated to be in the range of 95 to 105 \$ t<sub>CO2</sub><sup>-1</sup>, similar to bioenergy with CCS (BECCS) in other industries.

The analysis identified that a key process stage is simultaneous reduction-calcination, during which the reactor bed undergoes several important functions required to complete the SE-CLSR cycle. These include sorbent regeneration, reduction of the oxygen transfer material, and bed cooling. In Chapter 7, a dynamic packed bed reactor model is created in gPROMS Modelbuilder™ 4.1.0. This confirms that simultaneous reduction-calcination in a nickel-based system is feasible in principle. However, certain design and operating strategies will be required to manage the many complex and interacting factors in the system, including CO<sub>2</sub> equilibrium pressure, CO<sub>2</sub> product purity, and the relative speeds of reduction and calcination fronts.

Future models of the entire SE-CLSR process will also require the derivation of bio-oil steam reforming kinetics. Chapter 7 details an experimental study on acetic acid, a major constituent of bio-oil that is commonly used as a model compound. A kinetic model is proposed, using a simplified reaction scheme comprised of acetic acid steam reforming, acetic acid decomposition to CO, and the water gas shift reaction. This model is subsequently used to compare steam methane reforming to bio-oil steam reforming in a low-pressure industrial-scale reactor bed. This identifies that the relatively slow kinetics of acetic acid steam reforming are another important aspect for consideration.

Taken together, the above analyses provide a high-level assessment of the advanced reforming of bio-oils. In principle, SE-CLSR could offer certain technical and economic advantages compared to conventional steam reforming, and could offer a competitive route to hydrogen production with negative emissions. However, this is contingent upon several priority areas identified for process development.

## Table of Contents

<b>Acknowledgements</b> .....	<b>ii</b>
<b>Abstract</b> .....	<b>iii</b>
<b>Table of Contents</b> .....	<b>v</b>
<b>List of Tables</b> .....	<b>ix</b>
<b>List of Figures</b> .....	<b>xii</b>
<b>List of Abbreviations</b> .....	<b>xviii</b>
<b>Chapter 1 – Introduction</b> .....	<b>1</b>
1.1 Research background .....	1
1.1.1 Climate change and decarbonisation.....	1
1.1.2 The role of low carbon hydrogen .....	3
1.1.3 Methods of decarbonising hydrogen production .....	4
1.1.4 Project scope .....	6
1.1.5 Research aims and objectives.....	7
<b>Chapter 2 – Literature review</b> .....	<b>10</b>
2.1 Hydrogen production processes.....	10
2.1.1 Introduction to hydrogen production processes .....	10
2.1.2 Electrolysis.....	11
2.1.3 Steam reforming .....	12
2.1.4 Partial oxidation .....	16
2.1.5 Autothermal reforming .....	18
2.1.6 Gasification .....	19
2.2 Bioenergy as a source of hydrogen .....	20
2.2.1 Routes from bioenergy to hydrogen.....	20
2.2.2 Bio-oils from pyrolysis .....	22
2.2.3 Steam reforming of bio-oils .....	23
2.3 Emissions from hydrogen production .....	24
2.3.1 The role of bioenergy .....	24
2.3.2 The role of CO <sub>2</sub> capture .....	25
2.3.3 Impact assessment of hydrogen production methods .....	25
2.4 CO <sub>2</sub> capture.....	27
2.4.1 CO <sub>2</sub> capture technologies .....	27
2.4.2 CO <sub>2</sub> capture from SMR .....	31
2.5 Advanced reforming technologies .....	37
2.5.1 Sorption enhancement.....	37

2.5.2	Chemical looping steam reforming .....	39
2.5.3	Oxygen transfer materials.....	40
2.6	Process modelling of steam reforming processes.....	43
2.6.1	Modelling conventional steam reforming .....	43
2.6.2	Modelling advanced steam reforming .....	43
<b>Chapter 3 – Methodology .....</b>		<b>46</b>
3.1	Introduction.....	46
3.2	Process modelling .....	46
3.2.1	Aspen Plus flowsheets.....	46
3.2.2	Thermodynamic equilibrium.....	49
3.2.3	Feedstock .....	49
3.3	Economic analysis.....	51
3.3.1	Design basis .....	51
3.3.2	Process performance indicators .....	53
3.3.3	Capital cost methodology.....	54
3.3.4	Operating cost methodology .....	57
3.3.5	Levelised cost of hydrogen .....	58
3.3.6	Carbon emissions and cost of CO <sub>2</sub> avoided .....	58
3.4	Dynamic reactor modelling.....	60
3.4.1	Modelling packed bed reactors .....	60
3.4.2	Governing equations.....	61
3.4.3	Mathematical modelling methodology.....	65
3.5	Experimental methods and materials for kinetic study.....	66
3.5.1	Bio-oil model compound .....	66
3.5.2	Packed bed reactor configuration .....	67
3.5.3	Packed bed reactor operation.....	69
3.5.4	Catalyst.....	70
3.5.5	Process outputs and material balance.....	71
3.6	Determination of reaction kinetics .....	72
3.6.1	Mass transfer limitations .....	73
3.6.2	Parameter fitting.....	75
<b>Chapter 4 – Thermodynamic analysis of advanced reforming of bio-oil .....</b>		<b>78</b>
4.1	Introduction.....	78
4.2	Methodology.....	80
4.2.1	Process description.....	80

4.2.2	Energy balance .....	83
4.2.3	Feedstocks.....	87
4.3	Results and discussion.....	88
4.3.1	Process comparison and effect of temperature .....	88
4.3.2	Feedstock comparison in the SE-CLSR process.....	90
4.3.3	Carbon deposition.....	91
4.3.4	Optimisation and autothermal operation in SE-CLSR.....	93
4.3.5	Heat recuperation .....	95
4.3.6	The effect of pressure on SE-CLSR .....	96
4.4	Conclusion.....	98
<b>Chapter 5 – Techno-economic analysis of advanced reforming of bio-oil .....</b>		<b>100</b>
5.1	Introduction.....	100
5.2	Methodology.....	103
5.2.1	Bio-oil feedstock.....	103
5.2.2	Desulphurisation .....	103
5.2.3	Steam reforming process description .....	104
5.2.4	SE-CLSR process description .....	108
5.2.5	Process modelling approach.....	112
5.2.6	Economic assumptions .....	124
5.3	Technical assessment.....	127
5.3.1	Heat and material balances .....	127
5.3.2	C-SR performance without CO <sub>2</sub> capture.....	132
5.3.3	C-SR performance with CO <sub>2</sub> capture.....	135
5.3.4	SE-CLSR performance with CO <sub>2</sub> capture .....	137
5.4	Economic assessment .....	140
5.4.1	Selection of a design basis .....	140
5.4.2	Economic comparison of processes .....	142
5.4.3	Sensitivity analysis.....	146
5.4.4	Impacts of desulphurisation and catalyst performance.....	147
5.5	Conclusion.....	150
<b>Chapter 6 – Reactor modelling of reduction-calcination .....</b>		<b>153</b>
6.1	Introduction.....	153
6.2	Methodology.....	157
6.2.1	Modelling methodology for reduction of NiO.....	157
6.2.2	Modelling methodology for mixed sorbent/catalyst bed .....	162

6.2.3	Modelling methodology for reduction-calcination.....	165
6.3	Results and discussion.....	170
6.3.1	Model validation.....	170
6.3.2	Reduction-calcination with different feed gases.....	171
6.3.3	Sensitivity analysis.....	176
6.3.4	Impacts on reactor design, operation and cost.....	180
6.4	Conclusion.....	182
<b>Chapter 7 – Kinetic study on acetic acid steam reforming.....</b>		<b>184</b>
7.1	Introduction.....	184
7.2	Methodology.....	192
7.2.1	Experimental methodology .....	192
7.2.2	Kinetic model .....	193
7.2.3	Modelling of lab-scale reactor .....	193
7.2.4	Mass transfer limitations .....	195
7.2.5	Industrial scale reactor modelling .....	196
7.3	Results and discussion.....	197
7.3.1	Confirming absence of mass transfer limitations .....	197
7.3.2	Experimental measurements of reactant conversion.....	198
7.3.3	Carbon deposition.....	200
7.3.4	Parameter fitting.....	201
7.3.5	Kinetic model validation .....	206
7.3.6	Reactor modelling .....	209
7.4	Conclusion.....	213
<b>Chapter 8 – Conclusions and future work.....</b>		<b>215</b>
8.1	Introduction.....	215
8.2	Recommendations for future work .....	217
<b>References.....</b>		<b>219</b>
<b>Appendix A – Plant capacity.....</b>		<b>249</b>
<b>Appendix B – Reactor design .....</b>		<b>250</b>
<b>Appendix C – Kinetic parameters.....</b>		<b>253</b>
C.1	Kinetic parameters for model of reduction .....	253
C.2	Kinetic parameters for model of SE-SMR .....	254
C.3	Kinetic parameters for model of reduction-calcination .....	255
<b>Appendix D – Code for model of reduction-calcination.....</b>		<b>257</b>

## List of Tables

Table 2.1 – Summary of hydrogen production processes.....	10
Table 2.2 – Bio-hydrogen yields from gasification and reforming [101] .....	21
Table 2.3 –Overview of commercially available CO <sub>2</sub> absorption processes [136].....	29
Table 2.4 - Options for CO <sub>2</sub> separation from syngas.....	33
Table 2.5 –Pre- and post-combustion capture options .....	36
Table 3.1 – Unit operation blocks in Aspen Plus software .....	47
Table 3.2 – Manipulator blocks in Aspen Plus software .....	48
Table 3.3 - PEFB bio-oil model mixture composition [225].....	51
Table 3.4 – Hydrogen specifications [21,231] .....	52
Table 3.5 – CO <sub>2</sub> purity specifications [233] .....	53
Table 3.6 – Equations for bare module cost of equipment [243].....	55
Table 3.7 – Methodology for cost of manufacture [243].....	57
Table 3.8 – Classification of packed bed reactor models [253].....	61
Table 3.9 – Mass and energy balances for 1D heterogeneous PBR [254] .....	63
Table 3.10 – Mass and energy balances for 1D adiabatic axially dispersed pseudo-homogeneous packed bed reactor [212].....	63
Table 4.1 - Main reactions in sorption-enhanced and chemical looping reforming of an organic compound $C_nH_mO_k$ .....	82
Table 4.2 –Stoichiometry for SE-CLSR of methane, bio-oil model compounds, and PEFB bio-oil surrogate mixture (Reaction 11) ..	87
Table 4.3 - Parameters for autothermal operation in SE-CLSR of bio-oil, acetic acid and furfural at 1.013 bar, 450°C, with CaO/C = 1. ....	95
Table 4.4 - Parameters for autothermal operation in SE-CLSR of bio-oil at various pressures, with CaO/C = 1. ....	98
Table 5.1 – Syngas conditions for absorption-based CO <sub>2</sub> capture .....	113
Table 5.2 – Utilities consumption for desulphurisation [311].....	114
Table 5.3 - Pressure drop assumptions for heat exchangers [330] ....	114
Table 5.4 - Efficiencies for the modelling of turbomachines [242].....	115
Table 5.5 – Manipulator blocks in Aspen Plus models of C-SR with and without CO <sub>2</sub> capture .....	119
Table 5.6 – Manipulator blocks in Aspen Plus model of SE-CLSR .....	120
Table 5.7 – Process variables for bio-oil C-SR with and without CO <sub>2</sub> capture.....	122
Table 5.8 – Process variables for SE-CLSR of bio-oil .....	123

Table 5.9 – Single point cost data for bare module cost.....	125
Table 5.10 – Assumptions for calculation of operating cost.....	126
Table 5.11 – Example heat and material balance for C-SR without CO <sub>2</sub> capture.....	127
Table 5.12 – Example heat and material balance for C-SR with CO <sub>2</sub> capture.....	129
Table 5.13 – Example heat and material balance for SE-CLSR.....	131
Table 5.14 – Design basis for economic comparisons .....	142
Table 5.15 – Comparison of total emissions and negative emissions	145
Table 5.16 – Cost of CO <sub>2</sub> avoided in BECCS processes .....	146
Table 5.17 – Sulphur levels at reformer inlet conditions in C-SR .....	148
Table 5.18 – Impact of desulphurisation on C-SR without CO <sub>2</sub> capture .....	149
Table 6.1 – Reactions in reduction-calcination stage [206,207,257]...	153
Table 6.2 – Properties of PSA off-gas from SE-CLSR, from Chapter 5	155
Table 6.3 – Material and energy balances for model of NiO reduction	157
Table 6.4 – Properties applied in model of lab-scale NiO reduction [348] .....	159
Table 6.5 – Reaction scheme and rate equations for model of NiO reduction [348].....	160
Table 6.6 – Mass and energy balances for model of mixed sorbent/catalyst bed.....	162
Table 6.7 – Reaction scheme and rate equations for model of SE-SMR [212] .....	163
Table 6.8 – Properties in model of lab-scale mixed bed reactor [212]	165
Table 6.9 – Mass and energy balances for model of reduction-calcination .....	166
Table 6.10 – Reaction scheme and rate equations for model of reduction-calcination [159,348,356].....	167
Table 6.11 – Properties for model of reduction-calcination.....	169
Table 6.12 – Basis of design for reduction-calcination.....	180
Table 6.13 – Effect of L/D ratio and gas mass flux on key time steps in reduction-calcination at 918°C, 1.2 bar .....	181
Table 7.1 – Review of bio-compound kinetic studies in literature .....	187
Table 7.2 - Summary of reactions in steam reforming of acetic acid [119,180] .....	190
Table 7.3 – Experimental conditions used for kinetic study.....	193
Table 7.4 – Mass and energy balances for lab-scale reactor model of acetic acid steam reforming .....	194

<b>Table 7.5 – Parameters for lab-scale reactor model of acetic acid steam reforming .....</b>	<b>194</b>
<b>Table 7.6 – Mass and energy balances for full-scale reactor model...</b>	<b>196</b>
<b>Table 7.7 – Parameters for industrial scale reactor model .....</b>	<b>197</b>
<b>Table 7.8 – Determination of internal and external mass transfer limitations.....</b>	<b>198</b>
<b>Table 7.9 – Reaction schemes in proposed kinetic models .....</b>	<b>201</b>
<b>Table 7.10 – Rate equations for Models 1A and 1B.....</b>	<b>202</b>
<b>Table 7.11 – Rate equations for Models 2A and 2B.....</b>	<b>203</b>
<b>Table 7.12 – Kinetic parameters estimated by gPROMS parameter fitting.....</b>	<b>204</b>
<b>Table 7.13 – Accuracy of predicted vs measured outlet concentrations .....</b>	<b>208</b>
<b>Table 7.14 – Comparison of reactor size for steam reforming of acetic acid and methane at 95% conversion.....</b>	<b>213</b>



## List of Figures

Figure 1.1 – Territorial CO <sub>2</sub> emissions 1751 – 2017 .....	2
Figure 1.2 – Schematic of chemical looping processes a) chemical looping combustion b) chemical looping steam reforming .....	5
Figure 1.3 – Schematic of advanced reforming of bio-compounds.....	6
Figure 1.4 – Flow diagram of research aims and objectives .....	9
Figure 2.1 – SMR process with CO <sub>2</sub> wash system and methanator [66] .....	14
Figure 2.2 – SMR process with pressure swing adsorber [66].....	15
Figure 2.3 – Block diagram for partial oxidation.....	17
Figure 2.4 – Example process flow diagram for ATR [91].....	19
Figure 2.5 – Routes from biomass to hydrogen [14]. .....	21
Figure 2.6 – Environmental impacts of SMR with and without CCS [55] .....	25
Figure 2.7 – Global warming potential of hydrogen production [52] ....	26
Figure 2.8 – Carbon dioxide capture technologies [135] .....	27
Figure 2.9 – Process flow sheet for CO <sub>2</sub> capture with MEA.....	28
Figure 2.10 – Schematic of PSA for separation of CO <sub>2</sub> from syngas [94] .....	30
Figure 2.11 – Schematic of membrane separation of flue gas [140].....	30
Figure 2.12 –CO <sub>2</sub> capture locations in the steam reforming process [16] .....	32
Figure 2.13 – Process flow diagram of Air Liquide CRYOCAP™ [146].	34
Figure 2.14 – Process block flow diagram of Port Arthur SMR CO <sub>2</sub> capture.....	34
Figure 2.15 – Proposed configuration for pre-combustion CO <sub>2</sub> capture in H21 Leeds City Gate Project.....	36
Figure 2.16 – Reactor configurations for chemical looping reforming.	40
Figure 3.1 Example Aspen Plus flowsheet.....	48
Figure 3.2 Plug flow reactor schematic .....	60
Figure 3.3 Annular differential ring continuity equations,.....	61
Figure 3.4 Modelling methodology hierarchy for reduction-calcination .....	65
Figure 3.5 – Reactor set-up for acetic acid steam reforming experiments.....	67
Figure 3.6 – Vaporisation test, showing the comparison between a 10-basket configuration and 2-basket configuration. ....	68

Figure 3.7 – Mass transfer and reaction steps for a spherical catalyst particle [252].....	73
Figure 3.8 – Procedure for parameter estimation in gPROMS. ....	76
Figure 4.1 - Schematic description of SE-CLSR, showing key energy terms and temperature assumptions.....	83
Figure 4.2 – Aspen Plus flowsheet for advanced reforming energy balances. ....	85
Figure 4.3 - The effect of reduction/reforming temperature (T1) for PEFB bio-oil surrogate mixture in C-SR, CLSR, SE-SR and SE-CLSR with S/C ratio of 2 at 1.013 bar. For SE-SR and SE-CLSR, CaO/C = 1 and NiO/C = 1. (a) mass yield, moisture-free basis, (b) H <sub>2</sub> purity, (c) net process energy balance.....	89
Figure 4.4 - The effect of reduction/reforming temperature (T1) on the main energy terms in advanced reforming of PEFB bio-oil surrogate mixture with S/C = 2 at 1.013 bar (a) CLSR, with NiO/C = 1 and CaO/C = 0, (b) SE-CLSR, with NiO/C = 1 and CaO/C = 1.....	89
Figure 4.5 - The effect of reduction/reforming temperature (T1) in SE-CLSR of acetic acid, bio-oil and furfural at 1.013 bar with S/C = 2, NiO/C = 1, CaO/C = 1 (a) mass yield, moisture-free basis, (b) yield in % of stoichiometric potential from the SE-CLSR global reaction, (c) net process energy balance.....	90
Figure 4.6 - Equilibrium carbon product in advanced reforming of PEFB bio-oil surrogate mixture with S/C = 1 at 1.013 bar (a) SE-SR, with NiO/C = 0, (b) CLSR, with CaO/C = 0, (c) SE-CLSR, with CaO/C = 1. ....	92
Figure 4.7 - Effect of CaO/C ratio in SE-CLSR of bio-oil at 1.013 bar, 450°C with NiO/C = 1. (a) mass yield, moisture-free basis, (b) net process energy balance.....	93
Figure 4.8 - Effect of NiO/C ratio in SE-CLSR of bio-oil at 1.013 bar, 450°C, with CaO/C = 1. (a) mass yield, moisture-free basis, (b) net energy balance, (c) hydrogen purity.....	94
Figure 4.9 - Effect of heat recuperation in SE-CLSR of bio-oil at 1.013 bar, with S/C = 1, CaO/C = 1, NiO/C = 1.....	96
Figure 4.10 - Effect of pressure in SE-CLSR of bio-oil, with S/C = 2, NiO/C = 1, CaO/C = 1 (a) mass yield, moisture-free basis, (b) H <sub>2</sub> purity, (c) methane production, (d) net process energy balance..	97
Figure 5.1 – Levelised cost projections for hydrogen production.....	102
Figure 5.2 – Process flow diagram for bio-oil C-SR without CO <sub>2</sub> capture. ....	104
Figure 5.3 – Process flow diagram of bio-oil C-SR with CO <sub>2</sub> capture. ....	107
Figure 5.4 – Simplified process flow diagram of bio-oil SE-CLSR.....	109
Figure 5.5 – Example SE-CLSR operating conditions on CO <sub>2</sub> equilibrium partial-pressure diagram. ....	109

Figure 5.6 – Switching valves in SE-CLSR process .....	112
Figure 5.7 – Aspen Plus flowsheet for bio-oil C-SR without CO <sub>2</sub> capture .....	116
Figure 5.8 – Aspen Plus flowsheet for bio-oil C-SR with CO <sub>2</sub> capture .....	117
Figure 5.9 – Aspen Plus flowsheet for bio-oil SE-CLSR .....	118
Figure 5.10 – Effect of reformer temperature and S/C ratio on (a) H <sub>2</sub> yield and (b) thermal efficiency in the C-SR of PEFB bio-oil.....	133
Figure 5.11 – Effect of reformer temperature and S/C ratio on (a) total specific CO <sub>2</sub> emissions and (b) biogenic emissions in the C-SR of PEFB bio-oil. Reformer pressure = 30 bar. ....	134
Figure 5.12 – Effect of reformer temperature and pressure on thermal efficiency of C-SR, with and without steam export (S/C = 5).....	135
Figure 5.13 – Effect of reformer temperature and S/C ratio on thermal efficiency in C-SR with CO <sub>2</sub> capture. Reformer pressure = 30 bar. ....	135
Figure 5.14 – Effect of reformer temperature and S/C ratio on (a) total specific CO <sub>2</sub> emissions, (b) CO <sub>2</sub> capture efficiency and (c) biogenic emissions in C-SR with CO <sub>2</sub> capture. ....	136
Figure 5.15 – Breakdown of (a) energy inputs and (b) energy outputs to C-SR without CO <sub>2</sub> capture. ....	137
Figure 5.16 – Breakdown of (a) energy inputs and (b) energy outputs to C-SR with CO <sub>2</sub> capture. S/C = 5 at 900°C, with reformer pressure of 30 bar. ....	137
Figure 5.17 – Thermal efficiency and yield of SE-CLSR, showing the effect of (a) temperature, (b) S/C ratio and (c) pressure. ....	138
Figure 5.18 – Effect of reformer temperature and S/C ratio on (a) total specific CO <sub>2</sub> emissions and (b) biogenic emissions in the SE-CLSR of PEFB bio-oil. Reformer pressure = 20 bar. ....	139
Figure 5.19 – Breakdown of (a) energy inputs and (b) energy output to SE-CLSR at 20 bar, 850°C, S/C = 2. ....	139
Figure 5.20 – Effect of S/C ratio and capacity on levelised cost of hydrogen in C-SR at 30 bar and 900°C (a) without steam export (b) with steam export. H <sub>2</sub> production capacity = 10,000 Nm <sup>3</sup> h <sup>-1</sup> .....	141
Figure 5.21 – Effect of S/C ratio on the levelized cost of hydrogen from SE-CLSR at 20 bar, with T <sub>1</sub> = 850°C. ....	141
Figure 5.22 – Cost analysis of base case C-SR and SE-CLSR processes with steam export (a) fixed capital costs (b) cost of manufacture, and (c) LCOH.....	143
Figure 5.23 – Breakdown of bare module costs and direct manufacturing costs in a 10,000 Nm <sup>3</sup> h <sup>-1</sup> process for (a) C-SR-CCS and (b) SE-CLSR.....	144

Figure 5.24 – Cost of carbon avoided in C-SR-CCS and SE-CLSR, compared to bio-oil C-SR base case (a) total direct CO <sub>2</sub> emissions and (b) including negative emissions.....	145
Figure 5.25 – Cost of carbon avoided (direct emissions) compared to methane C-SR, including negative emissions .....	146
Figure 5.26 – Effect of feedstock costs on LCOH, showing influence of (a) bio-oil price and (b) natural gas price .....	147
Figure 5.27 – Sensitivity analysis on capital costs.....	147
Figure 5.28 – Effect of catalyst lifetime, cost and hydrodesulphurisation on levelised cost of hydrogen from C-SR, 10,000 Nm <sup>3</sup> h <sup>-1</sup> .....	150
Figure 6.1 – Illustration of reduction-calcination stage .....	153
Figure 6.2 – Equilibrium pressure of CaO/CaCO <sub>3</sub> system, showing strategies for calcination .....	154
Figure 6.3 – Maximum CaO conversion as a function of cycle number .....	168
Figure 6.4 – Product gas composition in reduction of NiO at 800°C, 1 bar with 10% CH <sub>4</sub> in Ar as reducing gas.....	170
Figure 6.5 – Effect of pressure on product gas composition (dry, N <sub>2</sub> -free basis) at the outlet of SE-SMR reactor. (a) 3 bar (b) 5 bar (c) 7 bar and (d) 9 bar.....	171
Figure 6.6 – Modelling results from reduction-calcination with 15 mol% off-gas in H <sub>2</sub> O a) CaO carbonation conversion, (b) temperature at axial distance z. ....	172
Figure 6.7 – Modelling results for reduction-calcination with 10 mol% off-gas in H <sub>2</sub> O (a) CaO and NiO conversion at axial distance z, (b) outlet gas composition and (c) temperature at axial distance z. ....	173
Figure 6.8 – Rates of reaction at 120s for reduction-calcination with 10 mol% off-gas in H <sub>2</sub> O as reducing gas. (a) calcination and reduction, (b) other reactions.....	174
Figure 6.9 – Model results for reduction-calcination with 10 mol% H <sub>2</sub> in H <sub>2</sub> O, showing carbonation conversion and conversion of NiO. .	175
Figure 6.10 – Rates of reaction at 120s, 10 mol% H <sub>2</sub> in H <sub>2</sub> O.....	175
Figure 6.11 – Outlet gas composition, dry basis in reduction-calcination with 10 mol% H <sub>2</sub> in H <sub>2</sub> O as reducing gas.....	176
Figure 6.12 – Effect of gas mass flux in reduction-calcination, showing NiO and CaO conversion at bed outlet (z = 7.8m). (a) 0.1 kg m <sup>-2</sup> s <sup>-1</sup> (b) 0.3 kg m <sup>-2</sup> s <sup>-1</sup> . ....	177
Figure 6.13 – Effect of initial temperature in reduction-calcination, showing NiO and CaO conversion at bed outlet (z = 7.8m). (a) 918°C (b) 950°C .....	177
Figure 6.14 – Effect of temperature on rates of reaction at t = 120 s. (a) 918°C (b) 950°C .....	178

Figure 6.15 – Effect of pressure in reduction-calcination in 10 mol% off-gas in H <sub>2</sub> O. (a) NiO conversion at z = 4m (b) CaO conversion at bed outlet at z = 4m.....	178
Figure 6.16 – Modelling results with higher sorbent capacity ( $X_{\text{carb,max}} = 0.17$ ). (a) conversion of CaO and NiO at the bed outlet and (b) product gas compositions.....	179
Figure 6.17 – Ca and NiO conversion profiles at the bed outlet, for different reactor L/D ratios.....	181
Figure 7.1 – Langmuir-Hinshelwood and Eley-Rideal reaction mechanisms, adapted from [362].....	185
Figure 7.2 – Reaction mechanism for acetic acid steam reforming proposed by Hoang et al. [178] .....	192
Figure 7.3 – Experimental results used for calculation of mass transfer limitations (650°C, with S/C = 3, $y_{\text{N}_2} = 0.6$ ).....	197
Figure 7.4 – Conversion vs pseudo contact time for different temperatures at S/C = 3, $p_{\text{AcOH}} = 5.89$ , $p_{\text{H}_2\text{O},0} = 34.64$ kPa. (a) AcOH and (b) H <sub>2</sub> O .....	199
Figure 7.5 – Conversion vs pseudo contact time for different partial pressures of AcOH at 650°C, $p_{\text{H}_2\text{O},0} = 34.64$ kPa. (a) AcOH and (b) H <sub>2</sub> O .....	199
Figure 7.6 – Conversion vs pseudo contact time ( $W/F_{\text{AcOH},0}$ ) for different partial pressures of H <sub>2</sub> O at 650°C, $p_{\text{AcOH},0} = 5.89$ kPa. (a) AcOH and (b) H <sub>2</sub> O .....	199
Figure 7.7 – Carbon content in used catalyst vs conversion to C-gases. ....	200
Figure 7.8 – Conversion to solid carbon vs conversion to C-gases... ..	200
Figure 7.9 – Parity plots for Model 1A (a) AcOH conversion, (b) H <sub>2</sub> O conversion.....	205
Figure 7.10 – Parity plots for Model 1B (a) AcOH conversion, (b) H <sub>2</sub> O conversion.....	205
Figure 7.11 – Parity plots for Model 2B (a) AcOH conversion, (b) H <sub>2</sub> O conversion and (c) CH <sub>4</sub> in outlet gas .....	206
Figure 7.12 – Parity plots for outlet compositions from Model 1A (a) H <sub>2</sub> vol%, (b) CO <sub>2</sub> vol% and (c) CO vol%. .....	207
Figure 7.13 – Effect of temperature on (a) H <sub>2</sub> O conversion, (b) H <sub>2</sub> , CO and CO <sub>2</sub> content at equilibrium. Inlet conditions are 1 bar, S/C = 3. ....	208
Figure 7.14 – Effect of pressure on (a) H <sub>2</sub> O conversion, (b) H <sub>2</sub> , CO and CO <sub>2</sub> content at equilibrium. ....	209
Figure 7.15 – Effect of S/C ratio on (a) H <sub>2</sub> O conversion, (b) H <sub>2</sub> , CO and CO <sub>2</sub> content at equilibrium. ....	209

Figure 7.16 – Reactant conversion vs axial distance for different values of mass flux in acetic acid steam reforming at 1.2 bar, 700°C with S/C = 3, effectiveness factor 0.3 (a) AcOH conversion (b) H <sub>2</sub> O conversion.....	210
Figure 7.17 – Model results from steam reforming of acetic acid at 1.2 bar, 700°C with S/C = 3, $G_z = 0.1 \text{ kg m}^{-2} \text{ s}^{-1}$ (a) rates of reaction, (b) gas composition .....	210
Figure 7.18 – Reactant conversion profiles for different S/C ratios in AcOH steam reforming at 1.2 bar, 700°C. (a) AcOH conversion (b) H <sub>2</sub> O conversion.....	211
Figure 7.19 – Reactant conversion vs axial distance for SR of methane and acetic acid at 1.2 bar, 700°C, mass flux $0.09 \text{ kg m}^{-2} \text{ s}^{-1}$ . 100% excess of H <sub>2</sub> O (S/C = 2 for AcOH, S/C = 4 for CH <sub>4</sub> ). (a) fuel conversion, (b) H <sub>2</sub> O conversion. ....	212
Figure 7.20 – Reaction rates at entrance to reactor tube for SR of methane at 1.2 bar, 700°C, mass flux $0.09 \text{ kg m}^{-2} \text{ s}^{-1}$ , S/C = 4.....	212

## List of Abbreviations

<b>Abbreviation</b>	<b>Definition</b>
AAD	Absolute average deviation
AcOH	Acetic acid
ATR	Autothermal reforming
BECCS	Bioenergy with carbon capture and storage
BDF	Backward differentiation formulae
BEV	Battery electric vehicle
BFDM	Backward finite difference method
CaO/C ratio	Calcium oxide-to-carbon ratio (molar)
CCA	Cost of carbon avoided
CCS	Carbon dioxide capture and storage
CEPCI	Chemical engineering plant cost index
CLC	Chemical looping combustion
CLSR	Chemical looping steam reforming
C-SR	Conventional steam reforming
C-SR-CCS	Conventional steam reforming with CO <sub>2</sub> capture
DAE	Differential algebraic equations
DASOLV	Differential algebraic solver
FCEV	Fuel cell electric vehicle
GDP	Gross domestic product
GHG	Greenhouse gas(es)
HDS	Hydrodesulphurisation
HTS	High temperature shift
HP	High pressure
IEA	International Energy Agency
IFBR	Interconnected fluidized bed reactor
IGCC	Integrated gasification combined cycle
IPCC	Intergovernmental Panel on Climate Change

LCOH	Levelised cost of hydrogen
LHV	Lower heating value
LP	Low pressure
LTS	Low temperature shift
MDEA	Methyl diethanolamine
MEA	Monoethanolamine
NETL	US National Energy Technology Laboratory
m.f.	Moisture-free
NiO/C ratio	Nickel oxide-to-carbon ratio (molar)
OECD	Organisation for Economic Co-operation and Development
OTM	Oxygen transfer material
PBR	Packed bed reactor
PEFB	Palm empty fruit bunch
PEM	Proton exchange membrane
POX	Partial oxidation
PSA	Pressure swing adsorption
RDS	Rate-determining step
SE-CLSR	Sorption-enhanced chemical looping steam reforming
SE-SR	Sorption-enhanced steam reforming
SMR	Steam methane reforming
SR	Steam reforming
S/C ratio	Steam-to-carbon ratio (molar)
TSA	Temperature swing adsorption
VSA	Vacuum swing adsorption
WGS	Water gas shift
WHSV	Weight hourly space velocity



Symbol	Definition	Units
$A$	Cross-sectional area of reactor	$m^2$
$a$	Catalyst activity	-
$a_v$	Interfacial area per volume of catalyst bed	$m^2 m^{-3}$
$B_1, B_2$	Factors in bare module cost equation	-
$C$	Total gas phase concentration	$mol m^{-3}$
$C_1, C_2$	Factors in pressure factor equation	-
$C_{Ab}$	Bulk concentration of species A	$mol m^{-3}$
$C_{As}$	Surface concentration of species A	$mol m^{-3}$
$C_{BM}$	Bare module cost	\$
$C_C$	Concentration of carbon on catalyst	$kg_C kg_{cat}^{-1}$
$C_i$	Gas phase concentration of species i	$mol m^{-3}$
$C_{mod}$	Bare module cost of unit in cost scaling formula	\$
$C_{mod,0}$	Reference cost of bare module with size $S_{mod,0}$	\$
$C_{Ni}, C_{NiO}$	Concentration of Ni/NiO in catalyst	$kg_{Ni} kg_{cat}^{-1}$
$C_{OL}$	Cost of operating labour	$\$ yr^{-1}$
$C_{RM}$	Cost of raw materials	$\$ yr^{-1}$
$C_{TM}$	Total module cost	\$
$C_{UT}$	Cost of utilities	$\$ yr^{-1}$
$C_{WP}$	Weisz-Prater parameter	-
$C_{WT}$	Cost of waste treatment	$\$ yr^{-1}$
$C_p$	Heat capacity at constant pressure	$J kg^{-1} K^{-1}$
$C_{purc}^o$	Purchased cost at base case conditions	\$
$CCA$	Cost of carbon avoided	$\$ kg_{CO_2}^{-1}$
$CEPCI_Y$	Chemical engineering plant cost index in year Y	-
$COM$	Cost of manufacture	$\$ yr^{-1}$
$COM_d$	Cost of manufacture without depreciation	$\$ yr^{-1}$
$D$	Diameter of vessel	m
$d_p$	Particle diameter	m
$D_{A,B}$	Molecular diffusivity of species A in B	$m^2 s^{-1}$
$D_{c,i}$	Micropore diffusivity of species i	$m^2 s^{-1}$
$D_e$	Effective diffusivity	$m^2 s^{-1}$
$D_m$	Average molecular diffusivity	$m^2 s^{-1}$
$D_r$	Radial dispersion coefficient	$m^2 s^{-1}$
$D_z$	Axial dispersion coefficient	$m^2 s^{-1}$
$E_A$	Activation energy	$J mol^{-1}$
$E_{H_2}$	Emission factor for hydrogen	$kg_{CO_2} kg_{H_2}^{-1}$
$E_{el}$	Emissions factor for electricity	$kg_{CO_2} kW^{-1}$
$E_{th}$	Emissions factor for thermal energy	$kg_{CO_2} kW^{-1}$

$f$	Scaling exponent in cost scaling formula	-
$F_A$	Molar flow component A	mol s <sup>-1</sup>
$F_{BM}$	Bare module factor in bare module cost equation	-
$F_M$	Material factor in bare module cost equation	-
$F_P$	Pressure factor in bare module cost equation	-
$F_T$	Superheat factor in bare module cost equation	-
$FCI$	Fixed capital investment	\$
$G_z$	Gas mass flux	kg m <sup>-2</sup> s <sup>-1</sup>
$G$	Gibbs function	J
$g_a$	Rate of generation due to interphase addition	mol s <sup>-1</sup>
$g_c$	Rate of generation due to reaction	mol s <sup>-1</sup>
$\bar{g}_i$	Molar Gibbs function of component i	J mol <sup>-1</sup>
$H$	Enthalpy	J
$H_t$	Hydrogen generation in year t	kg <sub>H2</sub>
$h_s$	Specific enthalpy of steam	kJ kg <sup>-1</sup>
$h_{liq,sat}$	Specific enthalpy of saturated water	kJ kg <sup>-1</sup>
$h_w$	Gas/wall film heat transfer coefficient	J s m <sup>-1</sup> K <sup>-1</sup>
$I$	Installation factor in cost scaling formula	-
$J$	Molar flux due to diffusion	mol m <sup>-2</sup> s <sup>-1</sup>
$K_{eq,j}$	Equilibrium constant in reaction j	-
$K_i$	Absorption constant component i	-
$k$	Sorbent deactivation constant	-
$k_c$	Mass transfer coefficient	m s <sup>-1</sup>
$k_g$	Gas convective physical mass-transfer coefficient	m <sup>3</sup> m <sup>-2</sup> s <sup>-1</sup>
$k_j$	Kinetic rate constant reaction j	-
$L$	Bed length	m
$LCOH$	Levelised cost of hydrogen	\$ kg <sub>H2</sub> <sup>-1</sup>
$M_i$	Molar mass component i	kg kmol <sup>-1</sup>
$M_{av}$	Average molecular mass	kg kmol <sup>-1</sup>
$M_i$	Molecular mass component i	kg kmol <sup>-1</sup>
$M_t$	Operating and maintenance costs in	
$m_i$	Mass of component i	kg
$\dot{m}_i$	Mass flowrate of component i	kg s <sup>-1</sup>
$N$	Total number of measurements in parameter estimation	-
$N_j$	Molar flux due to flow and diffusion	mol m <sup>-2</sup> s <sup>-1</sup>
$NE$	Total number of experiments	-
$NV_i$	Number of variables measured in the <i>i</i> th experiment	-

$NM_{ij}$	Number of measurements of $i$ th variable in $j$ th experiment	-
$n_i$	Number of moles of component $i$	mol
$\dot{n}_i$	Molar flow rate of component $i$	mol s <sup>-1</sup>
$P$	Total pressure	Pa
$P_{el}^+$	Electrical power import	kJ s <sup>-1</sup>
$P_{el}^-$	Electrical power export	kJ s <sup>-1</sup>
$P_{vessel}$	Operating pressure of vessel	barg
$p_i$	Partial pressure of component $i$	p
$P_{in}$	Inlet pressure of the feed	Pa
$Pe$	Peclet number	-
$Pr$	Prandtl number	-
$\dot{Q}^+, \dot{Q}^-$	Heat import/export	kJ s <sup>-1</sup>
$\dot{Q}_A$	Heat rate in fuel/product A	kJ s <sup>-1</sup>
$q_a$	Heat addition or removal	J m <sup>-3</sup> s <sup>-1</sup>
$q_r$	Heat liberated or abstracted by reaction	J m <sup>-3</sup> s <sup>-1</sup>
$R$	Ideal gas constant	J mol <sup>-1</sup> K <sup>-1</sup>
$R_j$	Rate of reaction $j$	mol s <sup>-1</sup>
$r$	Radial distance	m
$r_D$	Discount rate	-
$r_{red}$	Rate of reduction reaction	mol kg <sup>-1</sup> s <sup>-1</sup>
$Re$	Reynolds number for a packed bed	-
$Re_p$	Particle Reynolds number	-
$S$	Entropy	J K <sup>-1</sup>
$S_i$	Selectivity component $i$	-
$S_{mod}$	Size of module in cost scaling formula	-
$S_{mod,0}$	Reference size of module in cost scaling formula	-
$Sc$	Schmidt number	-
$Sh$	Sherwood number	-
$S/C$	Molar steam-to-carbon ratio	-
$t$	Time	s
$T$	Gas temperature	K
$T_s$	Solid temperature	K
$T_w$	Wall temperature	K
$t$	Time	s
$t_{vessel}$	Vessel wall thickness	m
$TCI$	Total capital investment	\$
$u$	Superficial velocity	m s <sup>-1</sup>
$V$	Volume	m <sup>3</sup>

$W$	Mass of catalyst	kg
$X_{carb}$	Carbonation conversion of sorbent	-
$X_i$	Conversion of reactant $i$	-
$X_r$	Residual sorbent capacity for infinite cycles	-
$x_c$	Measured mass fraction of carbon	-
$Y_{biogenic}$	Percentage allocation of biogenic emissions	%
$Y_{fossil}$	Percentage allocation of fossil-based emissions	%
$Y_i$	Yield of component $i$	%
$y_i$	Molar fraction of component $i$	-
$z$	Axial position	m
$Z_{ijk}$	$k$ th predicted value of variable $j$ in experiment $i$	-
$\tilde{Z}_{ijk}$	$k$ th measured variable of variable $j$ in experiment $i$	-

Greek letter	Definition	Units
$\alpha_i$	Number of carbon atoms in a carbon species	-
$\beta_{i,j}$	Stoichiometric coefficient species $i$ in reaction $j$	-
$\Delta H$	Enthalpy change	J
$(-\Delta H_{ads})_i$	Heat of adsorption of component $i$	J mol <sup>-1</sup>
$-\Delta H_{rxn}$	Heat of reaction	J mol <sup>-1</sup>
$\varepsilon$	Voidage	-
$\eta$	Effectiveness factor	-
$\eta_{th,process}$	Process thermal efficiency	%
$\lambda$	Thermal diffusivity	W m <sup>-1</sup> K <sup>-1</sup>
$\mu_g$	Average gas viscosity	kg m <sup>-1</sup> s <sup>-1</sup>
$\rho$	Mass density	kg m <sup>-3</sup>
$\sigma_c$	Constriction factor	-
$\sigma_{ijk}^2$	Variance of $k$ th measurement of variable $j$ in experiment $i$	-
$\tau$	Tortuosity	-
$\Phi$	Objective function in parameter estimation	-
$\phi_n$	Thiele modulus for a reaction with order $n$	-
$v_i$	Special atomic diffusion volume	-
$v_{cat}$	Fraction of catalyst in catalyst/sorbent bed	-
$v_{sorb}$	Fraction of sorbent in catalyst/sorbent bed	-

# Chapter 1 – Introduction

## 1.1 Research background

### 1.1.1 Climate change and decarbonisation

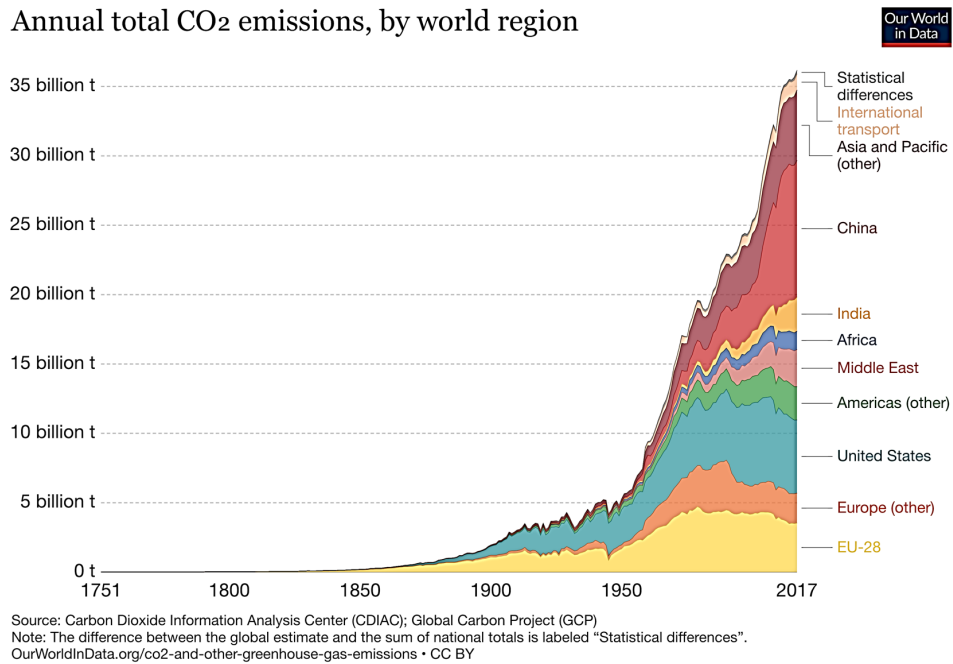
An increasing body of evidence is demonstrating the effects of human activity on climate systems. Possible consequences of climate change include extreme temperatures, sea-level rise, flooding, increased rainfall and intensified droughts. It is difficult to predict the exact timing, type or extent of such consequences, but it is now widely accepted that anthropogenic climate change is a genuine and serious phenomenon [1,2].

In December 2015, at the global climate conference COP21, 195 countries agreed to the first ever universal and legally binding climate deal, known as the Paris Agreement [3]. This agreement included the objective of [4]:

*“holding the increase in the global average temperature to well below 2°C above pre-industrial levels and to pursue efforts to limit the temperature increase to 1.5°C above pre-industrial levels”*

The International Panel on Climate Change (IPCC) has highlighted that this is an ambitious goal. At current rates of warming, 1.5°C is likely to be reached between 2030 and 2052, unless there is wide-scale and rapid transition [5]. Much of the climate change mitigation effort focuses on reducing greenhouse gas (GHG) emissions, as a large part of anthropogenic climate change is attributed to the increased atmospheric concentration of GHGs [6]. **Figure 7.1** shows the rise in global carbon dioxide emissions since the 1750s.

## Annual total CO<sub>2</sub> emissions, by world region



**Figure 1.1 – Territorial CO<sub>2</sub> emissions 1751 – 2017**  
 [7, with data from 8]

Since the beginning of the Industrial Revolution, the world has become increasingly industrialised, alongside rapid population growth. Within the last 50 years, the population has more than doubled, from around 3.5 billion in 1968 to over 7.5 billion in 2018 [9]. Both of these factors have contributed to an increase in energy demand. In 2018, around 80% of this primary energy demand came from fossil fuels [10].

The link between CO<sub>2</sub> emissions, population, the economy, and energy demand can be described by the Kaya identity [11]:

$$CO_2 = \frac{CO_2}{E} \times \frac{E}{GDP} \times \frac{GDP}{Pop} \times Pop \quad \text{Eq. 1.1}$$

where  $CO_2$  represents CO<sub>2</sub> emissions,  $E$  is energy consumption,  $GDP$  is gross domestic product and  $Pop$  is population. If emissions are to be controlled without compromising economic or population growth (the third and fourth terms in the equation), the first and second terms will have to be controlled. This requires a reduction in the carbon intensity of energy use, or a reduction in the link between energy use and the economy.

In 2014, energy-related emissions remained stable despite a 3% growth in the global economy. This was seen as an important milestone which could indicate that economic development had begun to decouple from energy-related emissions [12]. However, this trend was not sustained: in 2018, every 1% gain in global economic output was linked to a 0.5% increase in CO<sub>2</sub> emissions [10].

By 2035, global GDP is projected to double and energy consumption to increase by 34%. Nearly all of the increase in energy consumption is attributed to emerging economies, while energy demand within the OECD is expected to see little growth [13]. This trend is likely to be matched with a large growth in CO<sub>2</sub> emissions unless there is a concerted effort to reduce the carbon intensity of energy use. Urgent action is therefore needed to develop low carbon energy technologies.

### **1.1.2 The role of low carbon hydrogen**

One technology that has potential to decrease emissions across a range of sectors is the production of low carbon hydrogen. Hydrogen is used as a feedstock in a range of industries, including petrochemicals, fertilizer, electronics, food and metallurgical processing [14]. Global annual production is around 0.1 Gton, of which around 98% is produced from fossil fuels [15]. One of the foremost methods of production, steam methane reforming (SMR), contributes around 3% to global industrial emissions [16].

As well as being a significant feedstock, hydrogen is expected to play an increasingly important role in future energy systems, as a versatile energy carrier which delivers low carbon energy in a range of applications [15,17,18]. Parallels have been drawn to electricity, as both are energy carriers which contain no carbon and produce little or no emissions at point-of-use. However, hydrogen has one major advantage: the potential for long-term storage [17,19].

For example, hydrogen is envisaged as an alternative fuel for road transport which offers similar driving performance and refuelling times as conventional oil-based fuels [12]. The combustion of hydrogen produces only water and a small amount of NO<sub>x</sub> and thus, through the use of hydrogen in transport, local air pollution can be reduced. At the same time, if the hydrogen is produced from low carbon sources, significant carbon savings could be achieved when compared to conventional vehicle fuels [20]. As a result, hydrogen in transport can address environmental challenges at both a local and global scale.

However, with the current carbon-intensive methods of hydrogen production, the savings on well-to-wheel emissions of a fuel cell electric vehicle (FCEV) are minimal when compared to a battery electric vehicle (BEV) or plug-in hybrid [19]. Similar emissions challenges are faced in the heating sector, where hydrogen has been proposed as an alternative to natural gas [21]. Thus, if hydrogen is to have a future role as a sustainable energy carrier, it is essential to develop low carbon production methods.

### 1.1.3 Methods of decarbonising hydrogen production

One means of reducing the GHG emissions associated with hydrogen production, as well as reducing dependence on fossil fuels, is to use a feedstock derived from bioenergy. Bioenergy is a flexible type of renewable energy which can be converted into a range of different products, electricity, or liquid biofuels for transport. Bioenergy may play a significant role in meeting the energy demand in many sectors. For example, in the UK, it is predicted that bioenergy could meet around 10% of energy needs by 2050 [22]. Within the European Union, the Industrial Initiative on Bioenergy is working towards a 14% share of bioenergy in the energy mix by 2020 [23].

There are multiple methods to convert the organic compounds within biomass to hydrogen, via biological or thermochemical routes [14]. These are examined in **Section 2.2**. One promising method uses pyrolysis to convert solid biomass into bio-oil, which is subsequently used in a steam reforming process.

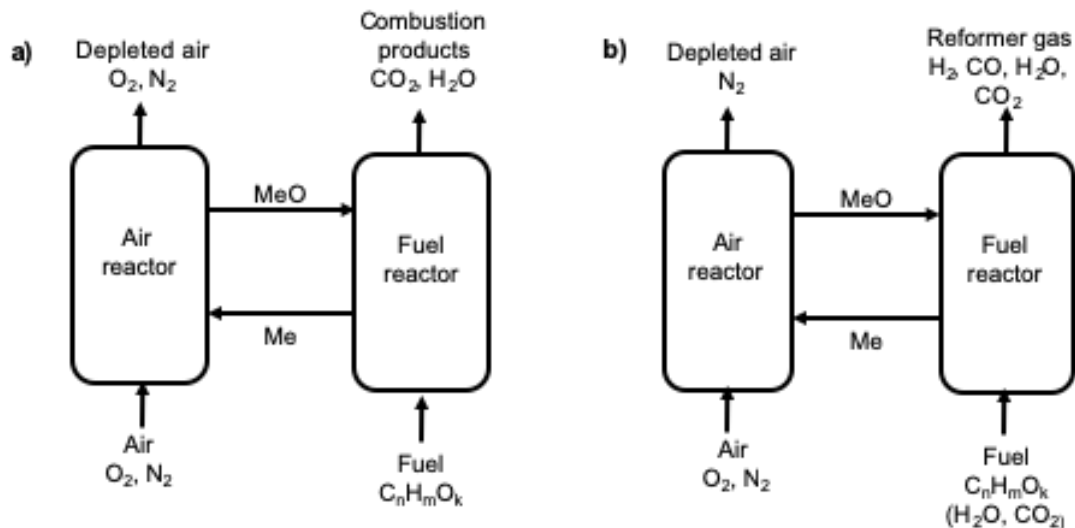
Another method to reduce the carbon intensity of hydrogen production is through the use of CO<sub>2</sub> capture and storage technology (CCS), in which CO<sub>2</sub> is separated or 'captured' from flue gases and transported to permanent geological storage. CCS has been identified as a major technology to mitigate carbon emissions from both industry and the power sector. Large-scale deployment is expected in the coming decades, although this will require significant investment and ongoing research and development efforts [12].

In the IEA analysis on hydrogen production until 2050, steam reforming with CCS is projected to play an increasingly important role if we are to meet the rising levels of hydrogen demand without endangering global climate change goals [19]. These IEA projections show no new steam methane reforming (SMR) capacity without CCS after 2030. It predicts that SMR-CCS will be cost-effective after this point, assuming a carbon price of 90 \$ t<sub>CO2</sub><sup>-1</sup> and carbon capture rates of 80%. The IEA analysis highlights the global importance of CCS within hydrogen production, and the need to establish cost-effective technologies for achieving this within decades. The role of carbon capture in hydrogen production is explored further in **Chapter 2**.

In a further development, it has been suggested that the combination of bioenergy with CCS technology (BECCS) could capitalise on the emissions reduction potential of both technologies in order to effectively offer negative overall emissions. Given the current trajectory of rising emissions, negative emission technologies such as this could form an important part of a long-term emissions abatement strategy in pursuit of the 2°C goal [24,25].



Another promising technology in hydrogen production is chemical looping. In chemical looping, an oxygen transfer material (OTM), typically a metal oxide, provides the oxygen required for fuel conversion. The OTM is then regenerated by oxidation, creating a loop in which the OTM is alternately reduced by the fuel and then oxidised [26]. The process can be employed in combustion or reforming processes, illustrated in **Figure 1.2**.



**Figure 1.2 – Schematic of chemical looping processes a) chemical looping combustion b) chemical looping steam reforming (adapted from [27])**

A major advantage of chemical-looping steam reforming (CLSR) is that it can be designed to be autothermal. The heat required for reforming can be provided by the exothermic oxidation reaction, rather than by external firing [28]. Another advantage is that the use of an OTM allows for the physical separation of air and fuel, thereby producing ready-separated gas streams and minimising the need for costly and energy-intensive gas separation [29].

A number of studies have examined the use of CLSR to produce syngas or hydrogen from methane. Earlier studies such as those by Fathi et al. [30] and Rydén et al. [29] demonstrated the feasibility of the process. More recent studies have examined the performance of a range of oxygen transfer materials, in order to produce materials with high activity as well as the stability which would give them sufficient lifetime for large-scale industrial processes [31–34]. The concept has been further developed by the use of novel fuels from bioenergy sources, including glycerol [35,36], waste lubricating oil [37], pyrolysis oils [38] and bioethanol [39].

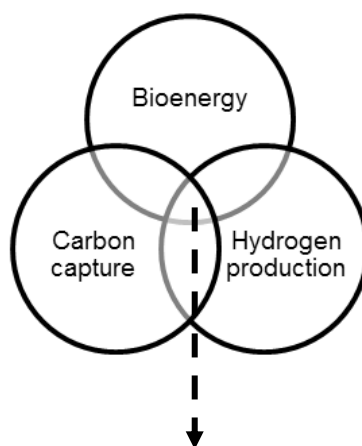
Steam reforming processes may also be enhanced by the use of sorption enhancement, in which a selective adsorbent is placed in the reactor for in situ CO<sub>2</sub> capture. By Le Chatelier's principle, the removal of one of the products

increases the conversion and the rate of the forward reaction. This results in high hydrogen purity and yield. In addition, the required operating temperature is decreased, thereby improving catalyst stability [40,41].

Sorption enhancement can be combined with CLSR to take advantage of the benefits of both techniques. The thermodynamic limitations on CLSR are reduced by the inclusion of sorption enhancement, while the cycling nature of the process allows the regeneration of the CO<sub>2</sub> sorbent [42]. The development of chemical looping and sorption-enhanced reforming systems is explored in further detail in **Chapter 2**.

#### 1.1.4 Project scope

This project focuses on the advanced reforming of bio-oil and bio-compounds, an area at the intersection of three areas of renewable energy technology: bioenergy, CO<sub>2</sub> capture and hydrogen production (**Figure 1.3**).



Advanced reforming of bio-compounds for the production of hydrogen

**Figure 1.3 – Schematic of advanced reforming of bio-compounds**

Finding ways to produce hydrogen from sustainable bioenergy sources, in combination with CO<sub>2</sub> capture technology, may serve multiple purposes. It could help reduce fossil fuel dependence and GHG emissions in the process industries. It may enable the provision of low carbon, renewable hydrogen to meet the rising demand from a growing population and potential new hydrogen applications. It may also be an important contributor to global climate goals, potentially acting as a means to achieve negative emissions.

Several studies have demonstrated the feasibility of various advanced reforming processes on a lab-scale, including steam reforming of bio-oils and

CLSR technology. Existing research on these technologies is reviewed in further detail in **Chapter 2**.

Further research and development is still required if these advanced reforming processes are to be scaled up for industrial use. An important stage will include process modelling. The development of process simulations allows qualitative analysis of key process parameters and sensitivities. This can provide useful insights on technical and economic aspects of process design, in order to support technology development. It is within this context that the following research is carried out on modelling the advanced reforming of bio-compounds for the production of hydrogen.

### **1.1.5 Research aims and objectives**

The project focusses on the production of hydrogen from bio-oil and bio-compounds. It aims to examine the feasibility and benefits of combining bio-oil feedstock with advanced reforming process designs. This aim was approached via the following objectives:

**Objective 1:** To carry out a thermodynamic analysis on hydrogen production from bio-oil and bio-oil model compounds. Examine various process types, including conventional steam reforming (C-SR), sorption-enhanced steam reforming (SE-SR), chemical looping steam reforming (CLSR) and sorption-enhanced chemical looping steam reforming (SE-CLSR).

**Objective 2:** To develop process simulations of C-SR, C-SR-CCS and SE-CLSR that represent hydrogen production at industrial scale.

**Objective 3:** To use the process simulations to examine the effects of process capacity, design and operation on performance indicators such as efficiency, emissions, cost of hydrogen, and cost of CO<sub>2</sub> avoided. Carry out comparative evaluations of:

- a) the conventional steam reforming process (i.e. a base case)
- b) steam reforming with CO<sub>2</sub> capture
- c) SE-CLSR with CO<sub>2</sub> capture

**Objective 4:** To develop a detailed model of a packed bed reactor containing OTM and sorbent, validated against literature data.

**Objective 5:** To use the packed bed reactor model to examine the reduction-calcination stage of SE-CLSR, in order to better understand the potential for CO<sub>2</sub> capture. Investigate the impacts of reactor design and operation on

process performance, particularly CO<sub>2</sub> purity, and identify opportunities for improvement.

**Objective 6:** To develop kinetic data for the steam reforming of acetic acid, a commonly used model compound for bio-oil. Carry out experimental work in a laboratory scale reactor at the University of Leeds, and use the experimental data to fit kinetic parameters.

**Objective 7:** Use the new kinetic data in the validated gPROMS model in order to assess the effects of bio-oil reaction kinetics on reactor design.

**Figure 1.4** illustrates how these objectives are inter-linked, and how they lead to the overall objectives of assessing feasibility and environmental impact.

These aims and objectives are discussed further in the chapters that follow.

**Chapter 2** provides a more detailed literature review, followed by an overview of methodology in **Chapter 3**. Thermodynamic feasibility is evaluated in

**Chapter 4**, and techno-economic aspects are explored in **Chapter 5**. **Chapter 6** provides a detailed model and evaluation of the reduction-calcination step.

**Chapter 7** describes the kinetic study. The thesis is concluded with **Chapter 8**, which summarises the research and provides suggestions for future work.

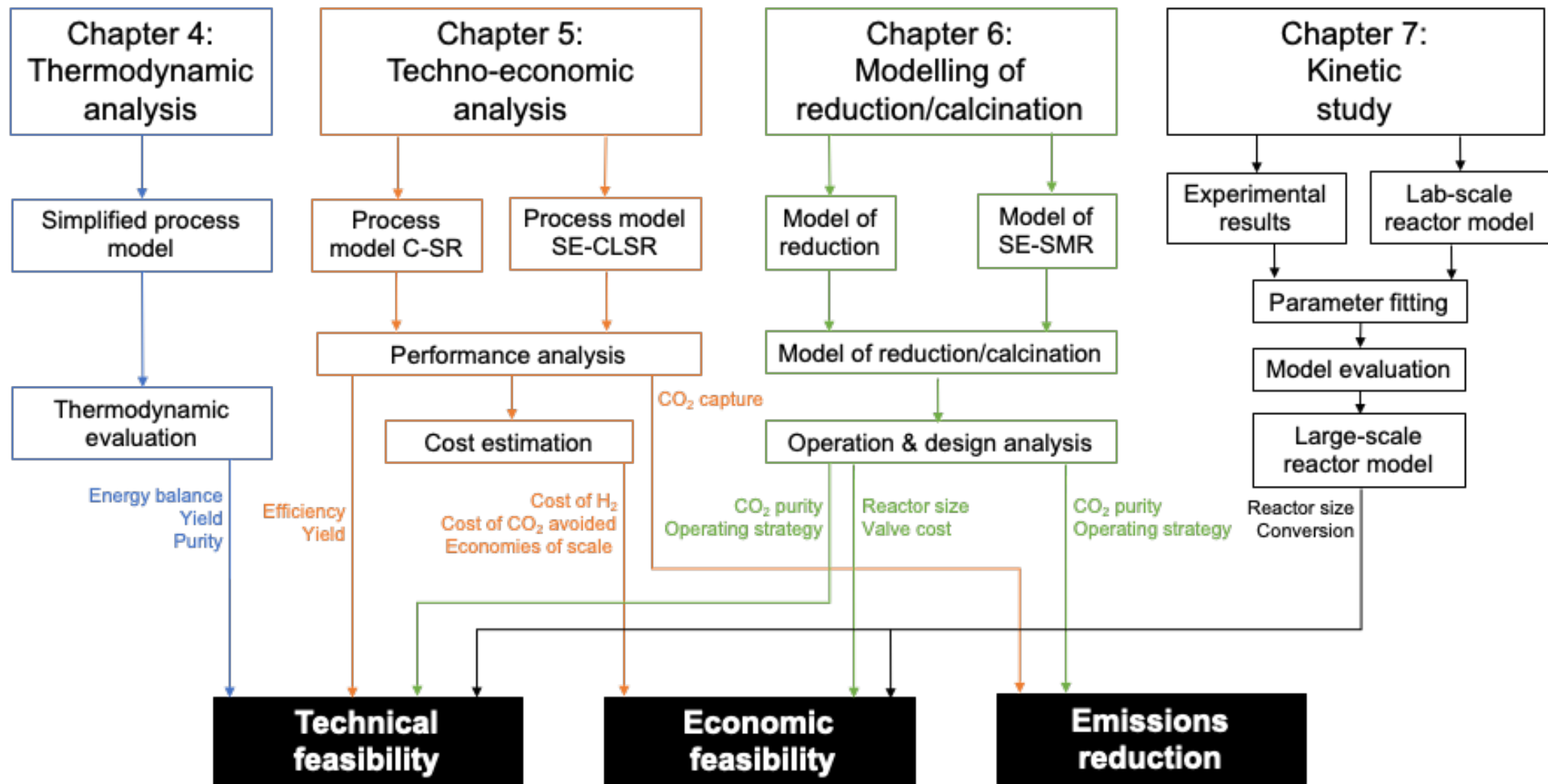


Figure 1.4 – Flow diagram of research aims and objectives

## Chapter 2 – Literature review

### 2.1 Hydrogen production processes

#### 2.1.1 Introduction to hydrogen production processes

The methods of hydrogen production may be categorised into three types: electrochemical, thermochemical and photochemical. The processes, raw materials and energy source for each method are summarised in **Table 2.1**.

**Table 2.1 – Summary of hydrogen production processes  
(adapted from [43])**

Category	Process	Raw Materials	Source of Energy
<b>Electrochemical</b>	Electrolysis	Water	Electricity from renewable or non-renewable sources
<b>Thermochemical</b>	Reforming	Natural gas	Natural gas/syngas combustion
		Hydrocarbons + Water	Concentrating solar thermal
	Gasification	Coal	Combustion of coal/biomass/ carbonaceous materials/syngas
		Carbonaceous materials	Concentrating solar thermal
		Biomass + Water	Natural gas combustion
Decomposition		Concentrating solar thermal	
Thermolysis		Concentrating solar thermal	
Thermochemical cycles		Concentrating solar thermal	
<b>Photochemical</b>	Photosynthesis	Water	Solar radiation, artificial light
		Microbial (e.g. algae)	Solar radiation
		+ Water	

A key consideration when selecting the process type is the size and type of application. Currently around 90% of hydrogen production is 'captive',

meaning the hydrogen is used in large-scale industrial applications such as oil refining, ammonia production or methanol production, where the hydrogen production process is highly integrated with the process of the industrial user. The remainder is produced for the merchant hydrogen market or the hydrogen energy (non-conventional) market. The merchant hydrogen market provides hydrogen to other industrial users and is largely supplied by the hydrogen by-product from processes such as methanol or ethylene production, while the energy market provides hydrogen for more novel uses such as transport fuel or other portable applications [44].

The merchant and energy markets may be supplied by centralized production facilities, or a distributed system of smaller scale processes. Decentralized facilities can offer more flexibility, but tend to lead to higher hydrogen costs, as they do not benefit from large economies of scale [15].

A further important aspect is the intended application, which may determine the required hydrogen purity. For example, Proton Exchange Membrane Fuel Cells (PEMFCs) require high purity H<sub>2</sub>, Solid Oxide Fuel Cells (SOFCs) are best used with H<sub>2</sub>-rich syngas [45]. The Fischer-Tropsch process uses a syngas with a preferred H<sub>2</sub>/CO ratio around 2 [46].

The following sections include a more detailed review of the major process types, primarily focussing on thermochemical routes, as these are the most prevalent methods used for large-scale production at present.

### **2.1.2 Electrolysis**

Electrolysis is an electrochemical route that uses electricity to split water molecules into H<sub>2</sub> and O<sub>2</sub>. The technology is relatively mature, having first been discovered in the 19<sup>th</sup> century. The two main technologies— alkaline and proton-exchange membrane (PEM) electrolyzers – are available in sizes ranging from laboratory scale to 2 MW or higher [47,48].

If the electricity is produced from low carbon sources, electrolysis is a low carbon source of hydrogen. Thus electrolysis is a particularly promising technology where there is a large amount of renewable electricity available. This strength may be further reinforced if electrolysis can be integrated into smart electricity systems in order to manage the intermittency of wind and solar power [18,49,50]. Renewable electrolysis may also work well as a part of an integrated system to serve the needs of a small community. For example, Hacetoglu et al. [51] proposed a system comprised of a single

wind turbine, an electrolyser, fuel cell and 8550 kg of hydrogen storage, that could serve a community of 50 homes in Canada.

However, electrolysis systems are less suitable for large-scale hydrogen production. The specific energy consumption of electrolysers ranges from 2.5 to 7.5 kWh Nm<sup>-3</sup> [52]. The price of electricity, combined with the efficiency limitations on current technology, mean that electrolysis is often not cost-competitive compared to other large-scale processes [53,54]. However, in the last decade, the cost of H<sub>2</sub> from electrolysis has reduced from 10-15 \$ kg<sub>H<sub>2</sub></sub><sup>-1</sup> to 4-6 \$ kg<sub>H<sub>2</sub></sub><sup>-1</sup>, and some analysis suggests it will fall by a further 60% by 2030 [47].

Despite these cost reductions, a technical limitation on production capacity remains. In a scenario where all transport needs are met by hydrogen from in 2050, the quantity of electricity used in hydrogen production by electrolysis would be nearly double the quantity consumed by all other sectors [15]. Such evidence suggests that electrolysis alone is unlikely to meet the large-scale needs of a hydrogen economy, and alternative low carbon technologies are required for large-scale production.

### 2.1.3 Steam reforming

Steam reforming (SR) is the major process used for large-scale production of hydrogen. Natural gas is the most common feedstock, responsible for around 75% of total global H<sub>2</sub> production [55], followed by the light fractions of petroleum up to and including naphtha [56]. Research on other feedstocks, including bioenergy, is ongoing (**Section 2.2**).

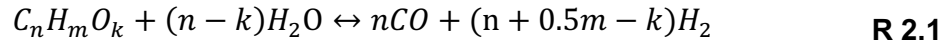
Supported nickel catalyst for steam reforming was first patented in 1912. The process was further developed by the first tubular reformer in 1930, and another breakthrough came in 1962 when ICI used high-pressure tubular reformers for the first time [57]. The technology has continued to develop to the present day. As a result, steam reforming has the highest energy efficiency of any of the hydrogen production alternatives, with efficiencies of over 80% being achieved in large systems, and consequently the lowest hydrogen selling price [58]. Smaller systems have been shown to achieve efficiencies of 65-75% [15].

The following sub-sections detail the basic chemistry of steam reforming, and an overview of the process design.



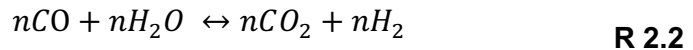
### 2.1.3.1 Steam reforming chemistry

The steam reforming process consists of two main stages. In the first stage, the fuel reacts with steam at high temperature and pressure, generally 800-1000°C and 20-35 bar [59]. The equation for the steam reforming reaction is as follows [60]:



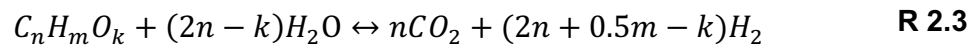
While low pressures are favourable from a thermodynamic standpoint, industrial steam reformers are typically operated at higher pressures to enable higher production flows and improved economies of scale [45].

The reformer is followed by a second stage, in which hydrogen yield is increased by the water gas shift (WGS) reaction:



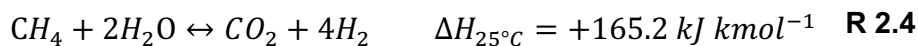
This is carried out at a lower temperature, in the region of 200-400°C [59].

When the two stages of steam reforming and the water gas shift reaction are combined, the global reaction is:



By this stoichiometry, the maximum theoretical yield of hydrogen is  $(2n+0.5m-k)$  per mol of  $C_nH_mO_k$  feedstock. This highlights one advantage of the steam reforming process: by converting hydrogen from both steam and fuel, the yield is relatively high [60]. However, it is also notable in the overall balance (R 2.3) that, for each mole of carbon in the feedstock, one mole of  $CO_2$  is released. If steam reforming is to be used in a low carbon energy system, it will be necessary to manage these emissions (**Section 2.3**).

Another challenge is that the process requires large amounts of heat to be applied. The first step is highly endothermic, while the second is slightly exothermic. Thus, the overall process is endothermic [61]. For example, the overall balance and enthalpy change for SMR is as follows:

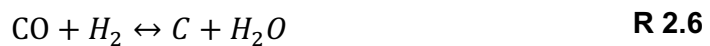


This heat is typically provided by the combustion of methane, further increasing the carbon emissions associated with the process.

An important parameter in steam reforming is the molar steam-to-carbon ratio, or S/C ratio. Increasing S/C ratio has a number of effects on the process. The increased availability of  $H_2O$  increases conversion and

hydrogen production. The production of CO at the exit of the reformer is reduced, as the production of CO<sub>2</sub> is favoured over the production of CO. This reduction in CO has effects in the WGS reactors by reducing the extent of the exothermic reaction [62]. This ratio is therefore an important parameter to examine during process evaluation.

Carbon deposition on the catalyst occurs by the Boudouard, Beggs and methane cracking reactions [63]:



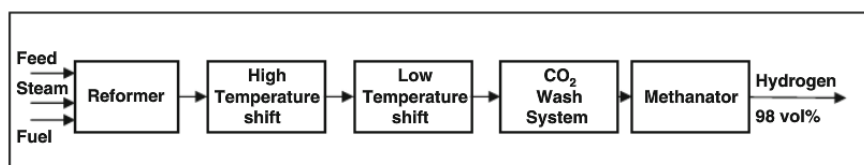
This carbon deposition is one of the major challenges in SR design and operation, as deposits cause catalyst deactivation and operational problems such as reformer tube blockages [64,65]. Novel bioenergy feedstocks can lead to increased carbon deposition, explored in **Section 2.2.3**.

### 2.1.3.2 Steam reforming process design

There are two main process designs used in industry [66]. The first, illustrated in **Figure 2.1**, features five main stages:

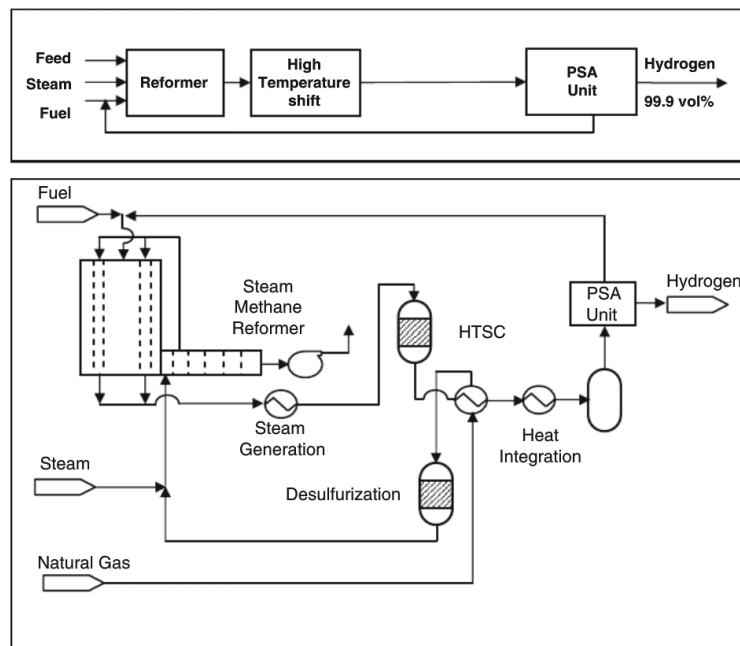
1. Feed pre-treatment in the desulfurisation unit, to remove catalyst poisons
2. Steam reforming to produce syngas (R 2.1)
3. Two water gas shift reactors (R 2.2), at high and then low temperature
4. A CO<sub>2</sub> absorption unit, using hot potassium carbonate or amine solution
5. A methanator, in which the remaining CO and CO<sub>2</sub> are converted into water.

In order to achieve maximum product purity, the water gas shift reaction is often completed in two stages – a high temperature shift (HTS) and low temperature shift (LTS) [67,68]. The extra cost incurred by introducing a second shift stage must be balanced with the benefit of higher hydrogen purity. The investment in an LTS stage is typically considered worthwhile where H<sub>2</sub> production rate is higher than 40,000 Nm<sup>3</sup> h<sup>-1</sup> [69].



**Figure 2.1 – SMR process with CO<sub>2</sub> wash system and methanator [66]**

The second alternative, illustrated in **Figure 2.2**, is a more recent design which is more commonly used in industry [70]. It uses different CO<sub>2</sub> removal technology and produces higher purity hydrogen. The use of pressure swing adsorption (PSA) for purification allows for omission of the LTS stage [66,69]. It is highly reliable, with availabilities over 99%, and offers flexible operation. It can also be fully automated even in more challenging operating conditions such as fluctuating flow, pressure and temperature [71].



**Figure 2.2 – SMR process with pressure swing adsorber [66]**

A commonly used design for industrial reformers is the multi-tubular reactor, in which the catalyst bed sits within tubes around 10 to 15 m long and 100 to 125 mm in diameter. Heat is provided indirectly via the tube walls, which are heated from outside by the combustion of fuel gas in a furnace chamber [72]. A typical steam methane reforming (SMR) plant with a production rate of 200,000 Nm<sup>3</sup> h<sup>-1</sup> will contain around 400 to 500 reformer tubes. Due to the high temperatures, the required number of tubes is determined by heat transfer and mechanical considerations, rather than catalyst activity, and so there is often an excess of catalyst [73].

While nickel has lower catalytic activity for SMR than some noble metals, and a greater tendency for deactivation, it is relatively inexpensive and so is a common choice for industrial reforming of methane [73]. As well as affordability, other key requirements for the catalyst include optimal heat and mass transfer, low pressure drop and high strength. It should also have the ability to withstand the extreme operating conditions, coke deposition and

the stress of any transient operating conditions which it may encounter over 50,000 h of continuous operation. Typically, the catalyst is around 12 to 20 wt% NiO supported on a refractory material such as Al<sub>2</sub>O<sub>3</sub>, MgO or SiO. It often contains promoters to improve performance, such as potassium or calcium alkali ions which suppress carbon deposition [56].

#### **2.1.4 Partial oxidation**

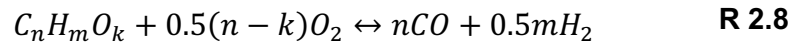
Hydrogen may also be produced by the partial oxidation (POX) of hydrocarbons. POX has gained interest as a less energy-intensive alternative to steam reforming [74]. The net energy balance in the reactor is mildly exothermic, giving the potential for autothermal operation over 1000°C, the elimination of an external heat supply, and a reduction in carbon emissions. In addition, the high reaction rates can lead to compact reactors which have high space-time yields [75]. An additional advantage is that it can use a wide range of feedstocks ranging from light hydrocarbons to heavy residual oil and petroleum coke, although it tends to be non-catalytic POX which uses heavier hydrocarbons while catalytic POX typically uses methane [56]. In addition, POX systems can be fast to start up and to respond to changes, making them flexible over varying loads [76].

The reduced energy requirement comes at the expense of a number of disadvantages. As there is no steam, the H<sub>2</sub> yield tends to be lower than for the SR process [45]. The exothermic reaction can lead to excessive coke formation and hot spots, which can make the temperature hard to control [77]. The process is often carried out using pure oxygen, which requires an expensive air separation plant. Where high levels of carbon deposition are encountered, large amounts of steam can be required for regeneration [74].

A number of potential feedstocks for POX have been investigated, including methane [78], methanol [79], ethanol [76], glycerol [80] and dimethyl ether, or DME [81]. Some literature has also examined the use of bioenergy feedstocks such as bio-ethanol [82,83] or bio-oils [84,85]. However, POX is still in the pre-commercialization stage of development, with no commercial scale reactors yet in operation [86]

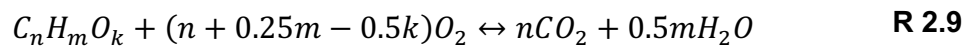
### 2.1.4.1 Partial oxidation chemistry

The partial oxidation reaction is shown below [60]:



The reaction is slightly exothermic. For example, for methane the enthalpy of reaction at standard conditions is  $-36 \text{ kJ mol}^{-1}$  [74].

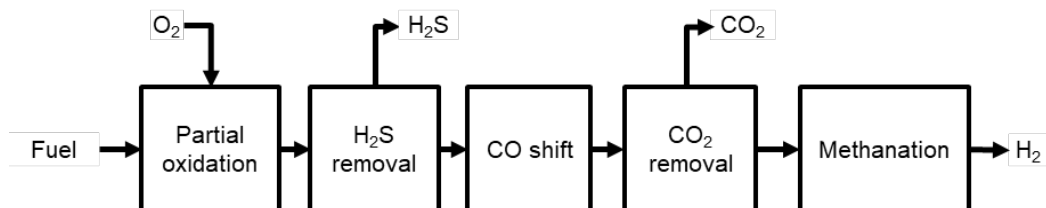
POX can occur non-catalytically, at high temperatures in the region of 1100-1500°C, or catalytically, at 600-900°C [56]. In non-catalytic POX, a number of side-reactions also occur, including such as cracking, incomplete carbon combustion and coke gasification [56]. In addition, local excesses of oxygen can lead to a small amount of complete combustion [45]:



Similar to steam reforming, POX can be combined with the water gas shift reaction (R 2.2) to increase hydrogen purity. With both reactions together, the theoretical  $H_2$  yield is  $(n+0.5m)$  moles per mole of  $C_nH_mO_k$  feedstock [60]. As a result of the lower  $H_2/CO$  ratio when compared to steam reforming, POX technology is preferred for applications which require a lower  $H_2$  content in the syngas [54].

### 2.1.4.2 Partial oxidation process design

**Figure 2.3** shows a block diagram of a POX process, containing the partial oxidation unit followed by a number of downstream stages to separate out impurities and improve hydrogen yield.



**Figure 2.3 – Block diagram for partial oxidation (adapted from [64])**

As the technology is not yet commercialised, there is no single catalyst which has been widely established for industrial use. A number of catalyst types have been proposed, including nickel, copper and noble metals, but further work is required to determine the optimal POX catalysts for different feedstocks [87].

### 2.1.5 Autothermal reforming

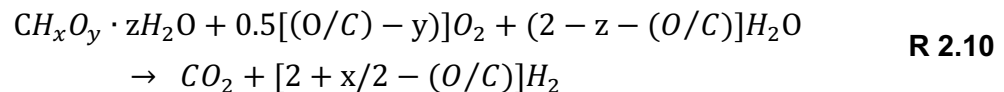
In autothermal reforming (ATR), the exothermic partial oxidation reaction is combined with the endothermic steam reforming reaction, to create a reforming process that does not require an external heat source [88].

The ATR process has been used in industry for a number of decades, particularly during the 1950s and 1960s for the production of syngas as feedstock for methanol and ammonia production [89]. When producing syngas for the Fischer-Tropsch process, oxygen-blown ATR has better economies of scale than a tubular reformer. Thus ATR is often the preferred choice for this application [46,57].

The elimination of an external heat supply results in a simpler and more scalable process which could be suitable for small-scale distributed hydrogen production [90], or on-board reformers for H<sub>2</sub> delivery to fuel cells in transport [45]. Other advantages of the process include high-purity H<sub>2</sub>, high efficiency, short start-up times and high flow ranges. In addition, it is fuel-flexible due to the sulphur tolerance, whilst the catalyst regeneration step allows coke to burn off. However, it has not been as widely used as SMR, largely because of the increased explosion risk [45].

#### 2.1.5.1 Autothermal reforming chemistry

ATR of an oxygenated hydrocarbon is described by [90]:



The oxygen-to-carbon (O/C) molar ratio is a significant factor which defines the required S/C molar ratio, and the maximum theoretical H<sub>2</sub> yield. It also determines the net adiabatic heat of reaction. This is a particularly important consideration for the ATR process, as the process becomes autothermal when the net adiabatic heat of reaction is zero [88]:

$$\Delta H_{rxn} = \sum_i \beta_{i(x)} H_i(T) = 0 \quad \mathbf{Eq.\ 2.1}$$

To account for heat transfer losses, the O/C ratio used in operation should be higher than the theoretical stoichiometric ratio. This ensures that the reactor is autothermal, while also raising the gas temperature so that product composition and coke formation are controlled [88]. The process is reasonably flexible in terms of the composition of product gas. By altering

the S/C or O/C ratios in the feed, it is possible to adjust the H<sub>2</sub>/CO ratio in the product gas [64].

### 2.1.5.2 Autothermal reforming process design

Main sections of the ATR process include a feed pre-heating section, reactor, heat recovery, and gas separation. Where the sulphur content needs to be controlled, there may also be a desulphurisation unit [91]. An example process scheme is illustrated in **Figure 2.4**. The process may also include an adiabatic pre-reformer upstream of the ATR reactor, which reduces the amount of oxygen required per unit of produced gas [46].

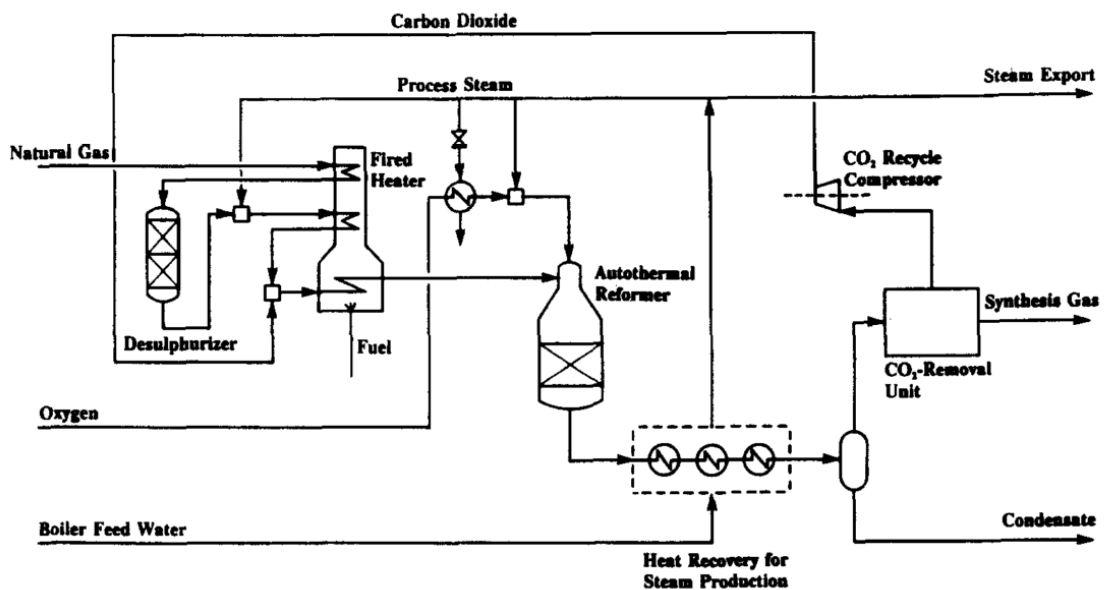


Figure 2.4 – Example process flow diagram for ATR [91]

The ATR reactor is comprised of a ceramic-lined tube and a fixed catalyst bed. Preheated feed streams enter from the top into the combustion zone, where partial oxidation takes place at around 1900°C. Beneath the combustion zone is the catalytic zone, in which Ni-based catalysts promote steam reforming and equilibration at 950 – 1150°C [54,64]. Due to the requirement for pure oxygen, the oxygen plant is a significant expense which can contribute 30-40% of the total investment cost [57].

### 2.1.6 Gasification

Gasification is a process in which a solid or liquid carbonaceous fuel reacts with air, oxygen, and/or steam at elevated temperature. The fuel undergoes a combination of reactions including partial oxidation, pyrolysis and steam

gasification to produce a gas containing CO, H<sub>2</sub>, CO<sub>2</sub>, CH<sub>4</sub> and N<sub>2</sub> [92]. This syngas, or producer gas, can be used to produce power (for example, in an Integrated Gasification Combined Cycle, or IGCC), or may be processed using WGS and purification steps to produce a pure H<sub>2</sub> product [19,93]. The gasifier operates at high temperatures, around 1500°C, and pressures ranging from 20 -100 bar, depending on the application [94]. There are various gasifier types available, with entrained-flow reactors being the most commonly used for commercial gasifiers [92,94].

Coal gasification is a well-established technology, being the third-largest contributor to annual hydrogen production [94]. The IEA's roadmap for hydrogen proposes the continued use of coal gasification in the medium term, but with the addition of CCS to mitigate associated carbon emissions [19]. One advantage of gasification is its ability to process solid fuels and so, more recently, there has been interest in gasification as a route to convert biomass to electricity or hydrogen [44,95–97]. However, biomass gasification is still not well established commercially, due to a number of scale-up challenges, including tar formation [92]. When combined with CCS, biomass gasification is a potential route to hydrogen with negative emissions [98].

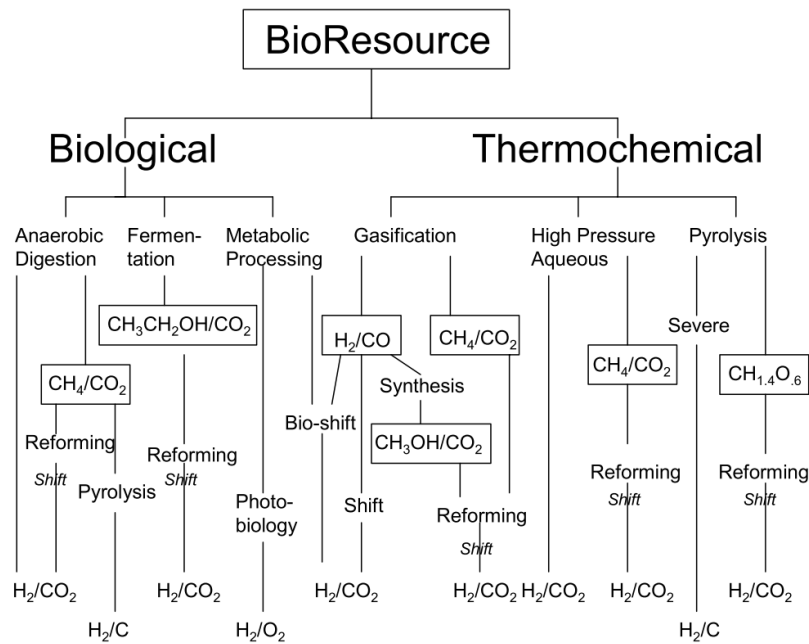
## **2.2 Bioenergy as a source of hydrogen**

### **2.2.1 Routes from bioenergy to hydrogen**

There is significant interest in the use of bioenergy as a versatile source of low carbon energy that could also reduce dependence on fossil fuels. It is a complex source of energy with a range of environmental, social, technical and economic challenges that span across its lifecycle. These include possible impacts on food security and availability, indirect land use change, and unsustainable biomass harvesting methods [24,99]. Thus it is important that any bioenergy feedstock is sourced according to appropriate sustainability criteria, as well as technical criteria.

There are multiple routes from biomass feedstock to hydrogen, via biological or thermochemical routes, shown in **Figure 2.5**.





**Figure 2.5 – Routes from biomass to hydrogen [14]. Boxes signify storable intermediates.**

A technical challenge when using biomass for hydrogen production is that the hydrogen content is typically low compared to that in fossil fuels. As a result, the theoretical hydrogen yield is limited [14]. In order to achieve maximum hydrogen yields and improve competitiveness, process optimisation is an important research focus.

While gasification followed by a shift reaction is the simplest pathway, pyrolysis followed by bio-oil reforming can offer more flexibility in the supply chain. Following pyrolysis, the biomass is transformed into an energy-dense liquid that can be easily transported. Thus, it may be possible to have a network of smaller pyrolysis plants which provide bio-oil to a centralised reforming plant [68,90,100], combining a flexible bio-based supply chain with an efficient and cost-effective centralised plant.

In addition, the pyrolysis and reforming route can offer relatively high hydrogen and energy yields, compared to the gasification route. **Table 2.3** shows the comparison between these two thermochemical routes.

**Table 2.2 – Bio-hydrogen yields from gasification and reforming [101]**

Process route	Yield of $H_2$ (wt% biomass)	Energy content (HHV) in $H_2$ /energy content of biomass (%)
Pyrolysis + catalytic reforming	12.6	91
Gasification + shift conversion	11.5	83

The following sections focus on the pyrolysis and reforming route, specifically the production and properties of bio-oil and research into bio-oil steam reforming. In addition to pyrolysis oils, reforming can also be carried out using other bioenergy feedstocks. For instance, waste cooking oil [102], sunflower oil [103] and other vegetable oils [104]. There is also some interest in the use of the crude glycerol by-product from biodiesel production, an area which has been reviewed by Dou et al. [105] and Silva et al. [106]. A key advantage of these feedstocks is that they can be sourced from waste materials from food or fuel producers. In addition, establishing a wider range of potential feedstocks will offer greater flexibility in future production of hydrogen from bioenergy, and may reduce feedstock constraints. While these alternative feedstocks are not the focus of this project, some aspects of the findings may be transferable to different types of oxygenated bio-compounds.

## **2.2.2 Bio-oils from pyrolysis**

Pyrolysis is a thermochemical method for the conversion of carbonaceous materials into a range of products. When biomass is thermally decomposed at around 375 to 530°C in the absence of oxygen, the lignocellulose is decomposed in several different reactions including dehydration, depolymerisation and C-C bond cleavage. This produces a solid char product, a combustible gas and a liquid known as pyrolysis oil, or bio-oil. The proportions of each product can be changed by the manipulation of process parameters such as heating rate or temperature [107,108].

The resulting bio-oil is a complex mix of compounds that can be categorised into three major groups [109]:

- i) Small carbonyl compounds including acetic acid, acetone, acetaldehyde, acetone, hydroxyketones, hydroxyaldehydes and carboxylic acids
- ii) Sugar-derived compounds including levoglucosan, furfural, anhydrosugars, and furan/pyran ring-containing compounds
- iii) Lignin-derived compounds, which are mostly phenols and guiacols but also include oligomers with molecular weights ranging from 900 to 2500.

Bio-oil tends to have relatively poor chemical and physical properties which make it unsuitable for use in most applications unless it undergoes further upgrading. It is thermodynamically unstable, viscous, and has a heating value less than half that of a conventional hydrocarbon fuel [110]. It is highly oxygenated, with an oxygen content around 35-40%, resulting in lower energy density and immiscibility with conventional fuels [111].

Despite the challenging properties of bio-oil, pyrolysis is a potentially useful method for transforming a range of different voluminous solid biomass feedstocks into a dense liquid which is easier to transport and handle [110]. With improved upgrading techniques, pyrolysis may therefore help to unlock the potential for bioenergy across the process industries, including hydrogen production [14].

Where a high liquid yield is required, fast pyrolysis is used. Key features of fast pyrolysis include a reaction temperature controlled around 500°C, and rapid cooling of pyrolysis vapours. The feed is finely ground to enable very high heating and heat transfer rates. In these conditions, the bio-oil yield can reach 80% of the mass of the dry feed [109,112]. Fast pyrolysis is in the early stages of commercialisation, having developed since the 1980s [90].

Rogers and Brammer [113] estimated that the cost of bio-oil production from energy crops in the UK is similar to the cost of mineral oils. Depending on plant capacity, it is estimated that the break-even price for bio-oil production from short rotation coppice willow ranges from 11 to 22 \$ GJ<sup>-1</sup>. Particularly influential factors were the price of electricity and biomass, and the potential to create value from the char by-product. The cost of bio-oil could have a significant impact on the resulting hydrogen cost, explored in **Chapter 5**.

### 2.2.3 Steam reforming of bio-oils

Research has considered the steam reforming of either whole bio-oil, or its fractions. The compounds within group (iii), the lignin-derived fraction of bio-oil, can typically yield more hydrogen than the aqueous fraction, consisting of groups (i) and (ii) [114]. The stoichiometry of the steam reforming reaction (R 2.3) determines that the theoretical yield of hydrogen is  $(2+0.5m/n-k/n)$  moles per mole of carbon. For the sugar-derived products, the term  $k/n$  is close to 1, while for aromatic phenolics the term is typically well below 1, resulting in a higher yield [101]. However, experiments on bio-oil reforming have found that the lignin fraction tends to decompose thermally, leading to carbon deposition on the upper layer of catalyst [111].

Some research on steam reforming of bio-oil focuses on steam reforming the aqueous, or volatile, fraction, which is less prone to carbon deposition [115–118]. Research has also been conducted on different reactor configurations and feeding configurations as a means to reduce carbon deposition. For instance, the feed can be sprayed onto the catalyst or encapsulated in water droplets to prevent thermal decomposition.

Alternatively, the process can use pre-reformers or fluidized bed reactors for improved control of carbon deposition [119].

According to Wu and Liu [120], the rate of carbon deposition is determined by two competing reactions: carbon formation and carbon elimination. At lower temperatures, the rate of carbon formation dominates, while elimination is dominant at higher temperatures. Carbon deposition can be reduced to some extent by using high temperatures and high S/C ratios [121–124]. Other strategies include fuel blending, regeneration with steam, or burn-off [85].

Carbon deposition may also be controlled by catalyst design. In the case of chemical looping processes (**Section 2.5.1**) the catalyst must also serve as an oxygen transfer material (OTM). Steam reforming catalysts and OTMs are discussed in more detail in **Section 2.5.3**. gives more detail on whole process analysis of bio-oil reforming is discussed in **Section 2.6**.

Due to the complex composition of bio-oils, many experimental and thermodynamic studies have used individual components as model compounds. Acetic acid has been used in several of these studies as it is one the most abundant compounds in bio-oils [119,125–128].

## 2.3 Emissions from hydrogen production

### 2.3.1 The role of bioenergy

As discussed in **Chapter 1**, an important justification for bioenergy use in hydrogen production is the potential for reduced carbon emissions. It is therefore important to understand the environmental impacts of the proposed production route.

By the nature of the chemical process, the reforming of bio-oil will inevitably release some CO<sub>2</sub>. However, the carbon contained within the bio-oil is biogenic, rather than fossil fuel-based, and so it is assumed that the bio-oil reforming has lower emissions than an equivalent fossil fuel process [44,119]. In practice, other life cycle aspects, such as the cultivation and processing of the bioenergy feedstock, must also be considered.

Heracleous et al. [129] carried out a Well-to-Wheel analysis, demonstrating that the use of bio-oil can reduce the global warming impact of hydrogen use in vehicles. Hydrogen from natural gas resulted in 180 g CO<sub>2,eq</sub> km<sup>-1</sup>, while hydrogen from waste wood bio-oil resulted in 90 g CO<sub>2,eq</sub> km<sup>-1</sup>. This study also noted the influence of the bio-oil production methods: GHG emissions

were increased 20% when using cultivated biomass feedstock rather than waste wood. This is due to the release of N<sub>2</sub>O, a powerful greenhouse gas, during crop growth and fertiliser production. Other influential factors were the use of methanol for bi-oil stabilisation, and electricity demand, both of which could have their impact reduced by using renewable energy sources.

### 2.3.2 The role of CO<sub>2</sub> capture

An alternative route to reduce emissions, and the one that is currently receiving the most focus for short-term implementation, is the use of CO<sub>2</sub> capture and storage (CCS) to capture and permanently sequester the CO<sub>2</sub> emissions from steam reforming [19,21,47,130].

Dufour et al. [55] carried out a life cycle assessment (LCA) on a number of hydrogen production processes, including SMR with and without CCS. While the addition of CCS reduces GHG emissions, it causes a slightly higher overall impact when considering all of the environmental factors as a whole (**Figure 2.6**). This is because the carbon capture process requires a large amount of electricity. With the electricity supply assumed in 2009, this would lead to high impact in the winter smog, acidification and heavy metals categories, although the authors did note the potential for improvement as the electricity system trends towards cleaner energy sources. This highlights the importance of using clean energy sources for an energy-intensive CO<sub>2</sub> capture process, as well as energy-efficient process design. CO<sub>2</sub> capture processes are discussed in further detail in **Section 2.4**.

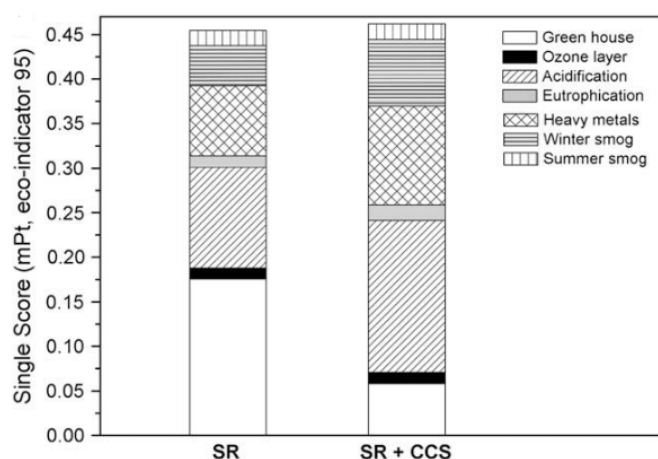
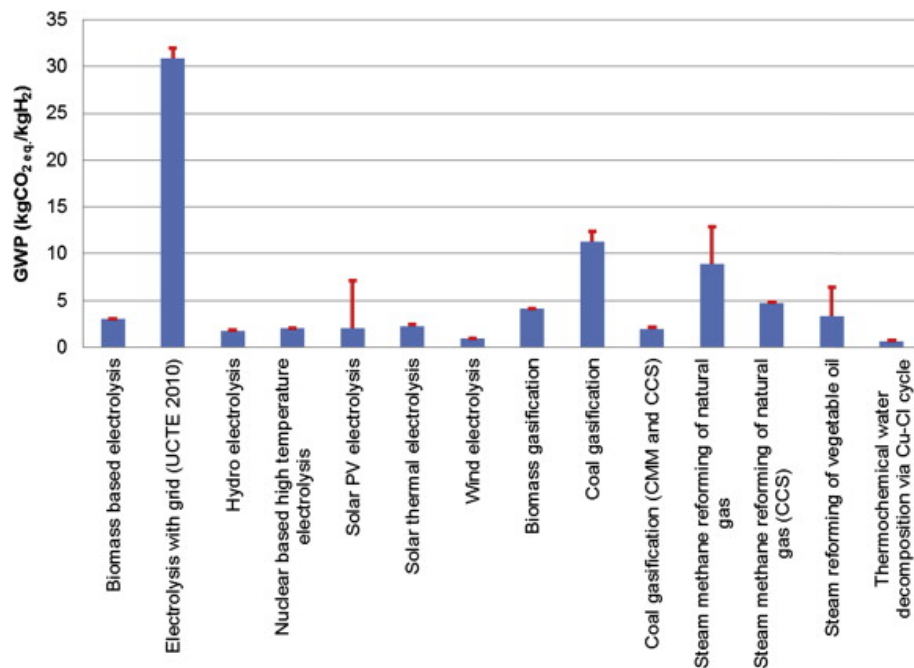


Figure 2.6 – Environmental impacts of SMR with and without CCS [55]

### 2.3.3 Impact assessment of hydrogen production methods

There have been a number of attempts to quantify the environmental impact of hydrogen production through Life Cycle Assessment (LCA). A review of

the subject is given in Bhandari et al. [52]. **Figure 2.7** shows a summary of the Global Warming Potential (GWP) of a range of hydrogen production technologies. It shows that electrolysis using grid electricity has the highest emissions. However, if the electricity is sourced from renewable sources, the impact is reduced to the extent that electrolysis has the lowest GWP. The emissions of thermochemical methods, such as gasification of reforming, are reduced by the use of biomass or addition of CCS.



**Figure 2.7 – Global warming potential of hydrogen production [52]**

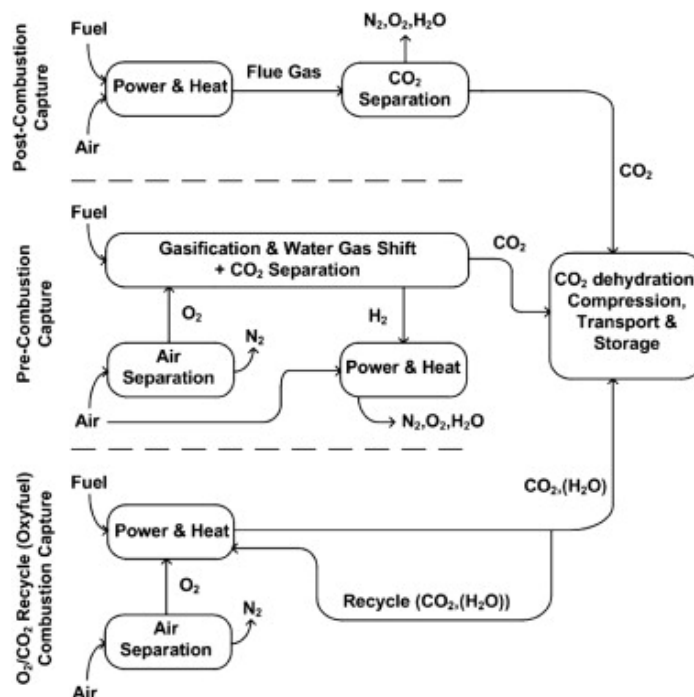
While renewable-based electrolysis is commonly found to have a very low environmental impact [131–133], the scale and cost limitations discussed in **Section 2.1.2** illustrate that other low carbon production methods will be required alongside renewable electrolysis.

Fossil fuel steam reforming has a relatively high carbon footprint, but also has a high energy efficiency [132,133]. Thus, if steam reforming could be combined with methods to mitigate emissions, such as low carbon feedstocks and CCS, it could be a promising solution for efficient production of hydrogen in large volumes, with low or potentially negative carbon emissions. To date, there is no LCA for hydrogen production from bio-oil steam reforming with CCS. The process modelling in this thesis provides a first assessment of direct CO<sub>2</sub> emissions from the process, with the potential to be used as an input for future LCA.

## 2.4 CO<sub>2</sub> capture

### 2.4.1 CO<sub>2</sub> capture technologies

CO<sub>2</sub> capture processes are often described by three categories: post-combustion, pre-combustion and oxy-fuel combustion. In post-combustion CCS, CO<sub>2</sub> is captured from the flue gases of a combustion process. In pre-combustion CCS, the fuel is gasified or reformed and CO<sub>2</sub> is captured from the syngas, before the remainder is combusted. In oxy-fuel combustion, combustion takes place in pure oxygen so that the need for flue gas purification is minimised [134]. The concepts are illustrated in **Figure 2.8**.

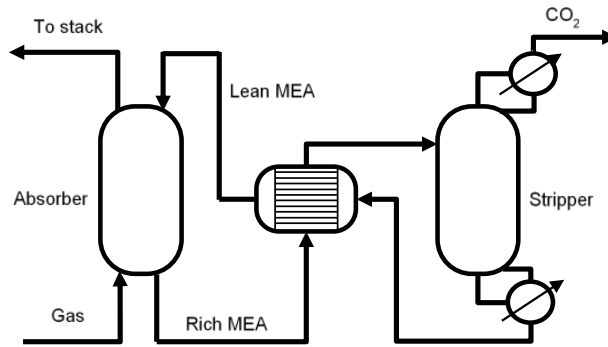


**Figure 2.8 – Carbon dioxide capture technologies** [135]

The capture of CO<sub>2</sub> from a steam reforming process is a type of pre-combustion capture, in which fuels are converted to H<sub>2</sub> and CO<sub>2</sub>, the CO<sub>2</sub> is captured and the produced hydrogen is utilised on-site, or transported for use elsewhere

The separation of CO<sub>2</sub> from a gas stream can be achieved in a number of different ways. The four key techniques are absorption, adsorption, membrane separation and cryogenic distillation [136].

The absorption technique uses a physical or chemical liquid solvent to capture CO<sub>2</sub>. **Figure 2.9** shows a simplified process flow sheet, using the common solvent MEA as an example.



**Figure 2.9 – Process flow sheet for CO<sub>2</sub> capture with MEA (adapted from [137])**

The gas is contacted with MEA by flowing counter-currently through the absorber column. The CO<sub>2</sub> is a weak base while the MEA is a weak acid, and so the fluids react to produce a water-soluble salt. The rich MEA is then pre-heated by cross-exchange with the warm lean MEA stream, before entering the stripper. Here, the reaction is reversed and CO<sub>2</sub> is liberated. The CO<sub>2</sub> stream exits from the top of the stripper, while the regenerated MEA is recycled to the absorber via the heat exchanger [137].

MEA has been used for a number of years for natural gas sweetening in industry. The technological maturity, high efficiency and relatively low cost of the MEA process makes it an appealing CO<sub>2</sub> separation option in many applications [134]. However, it does carry certain disadvantages, such as the high energy requirements and solvent corrosion issues [16]. Its use in novel process streams can pose challenges, such as in flue gases from combustion processes, where gas volumes are high with relatively low CO<sub>2</sub> concentrations. The combination of low solvent flow rates and high superficial gas velocities can lead to high gas phase pressure drop, flooding of the packing materials, and liquid channelling [138].

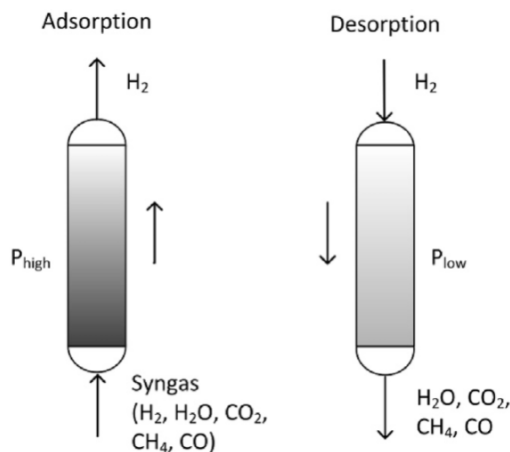
A range of physical and chemical solvents, which use the same principle of absorption and regeneration, are commercially available for CO<sub>2</sub> capture. The main solvent types are detailed in **Table 2.3**. Generally, chemical solvents are better suited to low CO<sub>2</sub> partial pressures, as their absorption capacity is limited by saturation. Physical solvents are preferred for high CO<sub>2</sub> partial pressures, as their absorption capacity increases linearly with CO<sub>2</sub> partial pressure according to Henry's Law [94].



**Table 2.3 –Overview of commercially available CO<sub>2</sub> absorption processes [136]**

<b>Absorption process</b>	<b>Solvent<sup>a</sup></b>	<b>Process conditions<sup>b</sup></b>
<i>Physical solvent</i>		
Rectisol	Methanol	-60 to -30°C, > 20 bar
Selexol	Dimethyl esters of polyethylene glycol (DMPEG)	0-40°C, 20-30 bar
<i>Chemical solvent</i>		
<i>Organic (amine-based)</i>		
MEA	2.5 N 2-aminoethanol and chemical inhibitors in water	40-60°C, ambient-intermediate pressures
MDEA	2 N Bis(2-hydroxyethyl)methylamine in water	Wide range
<i>Inorganic</i>		
Benfield and Catacarb	Potassium carbonate and (Lurgi or Catacarb) catalysts in water	70-120°C, 22-70 bar
<i>Mixed solvents</i>		
Sulfinol-D and Sulfinol-X	Mixture of Diisopropanolamine (DIPA) or MDEA, tetrahydrothiophene (DIPAM) and diethylamine or piperazine in water	>5 bar
ADIP	Mixture of 2-4 N DIPA and 2 N MDEA in water	35-40°C, >1 bar
ADIP-X	Mixture of MDEA and piperazine in water	35-45°C, 2-27 bar
<sup>a</sup> N signifies molar amount of alkaline sites per litre of solution		
<sup>b</sup> Common process conditions when the CO <sub>2</sub> is captured		

In adsorption processes, the CO<sub>2</sub> is adsorbed onto a solid such as activated carbon, zeolites or calcium oxides. The adsorbed CO<sub>2</sub> is then recovered and the sorbent regenerated by a pressure swing or temperature swing [134]. The principle of pressure swing adsorption (PSA) is illustrated in **Figure 2.10**. Temperature swing adsorption (TSA) uses a similar principle, except it uses variations in temperature instead of pressure.



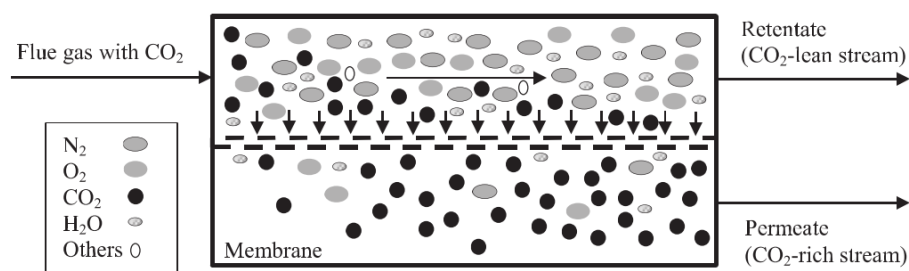
**Figure 2.10 – Schematic of PSA for separation of CO<sub>2</sub> from syngas [94]**

Temperature swing adsorption (TSA) is limited by heat transfer and requires long cycle times, in the order of hours. The ability for rapid cycling means pressure swing adsorption (PSA) is generally the preferred option for CO<sub>2</sub> separation [139]. PSA has a number of attractive features such as reliability and flexible operation, and is already widely used for purification at SMR plants [71].

A variation on PSA is vacuum swing adsorption (VSA), which use negative pressures for sorbent regeneration. The sorption half of the swing cycle can occur at lower pressures and the need for compression is minimised. This is a particularly important consideration for post-combustion flue gases, which are at low pressures, in large volumes and contain significant quantities of nitrogen [139]. However, in steam reforming, the syngas is at elevated pressure, enabling pressure swing with minimal extra compression [94].

While adsorption systems use less energy than a comparable absorption process, they require electricity rather than thermal energy, potentially reducing opportunities for energy savings through heat integration. In addition, achieving high CO<sub>2</sub> purity can require strong vacuums which demand complex multistage vacuum systems [139].

Membrane separation uses semi-permeable barriers, which act as a filter to selectively separate components out of the gas stream (**Figure 2.11**).



**Figure 2.11 – Schematic of membrane separation of flue gas [140]**

Advantages of membrane separation including a low energy requirement, simplicity, modularity, and absence of waste streams [141]. As a result, membranes have been commercially implemented in some natural gas sweetening systems [140]. However, several limitations prevent their use for CO<sub>2</sub> capture. It is challenging to achieve the required levels of separation in a single stage, leading to a requirement for multiple stages or recycling [141,142]. Membranes are therefore not yet economical for cases where there is low feed concentration or requirement for a high purity product. In addition, the gas must be at high pressure to provide a driving force across the membrane. Finally, new membrane designs are required as the separation of CO<sub>2</sub> from N<sub>2</sub> or H<sub>2</sub> requires different characteristics to those membranes which are already commercially available for the separation of CO<sub>2</sub> from natural gas [140].

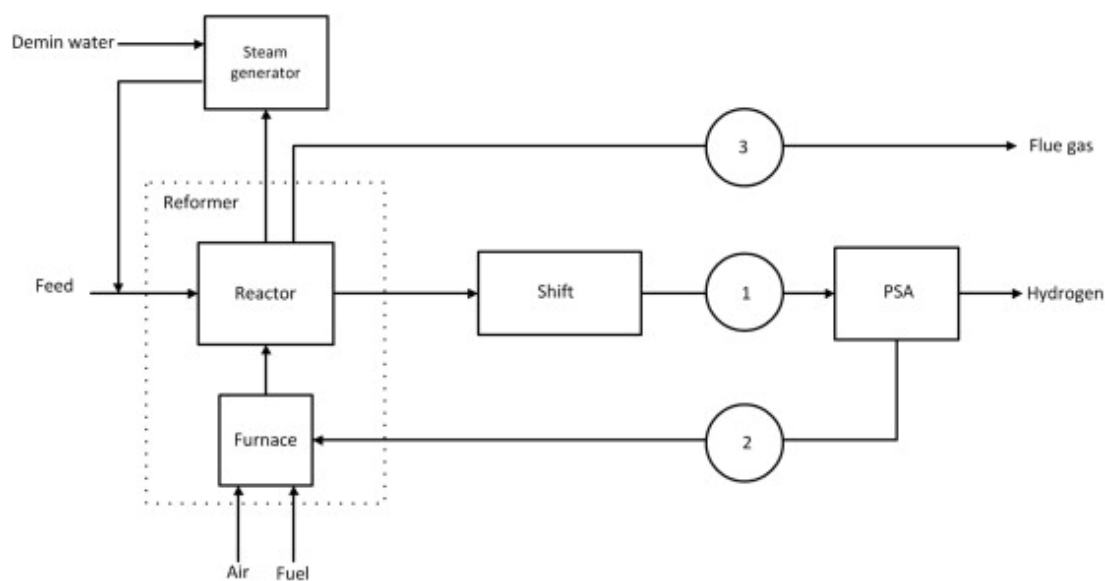
Cryogenic distillation works by liquefaction of the CO<sub>2</sub> using low temperature and high pressure. A major advantage of the cryogenic process is that it creates liquefied CO<sub>2</sub> ready for transport. In addition, CO<sub>2</sub> recovery rates and purity are very high [143]. However, it offers limited flexibility, as small changes to feed composition can alter the boiling point and affect product purity. The systems can be unreliable if the pre-treatment system fails and contaminants freeze. The energy requirement is among the highest of the CO<sub>2</sub> capture options, due to the significant cooling requirement [136,142].

#### **2.4.2 CO<sub>2</sub> capture from SMR**

There are several features of the steam reforming process which make it an attractive candidate for CO<sub>2</sub> capture. The facilities are large, stationary emitters of CO<sub>2</sub>, enabling relatively simple capture on a large scale. In addition, the CO<sub>2</sub> is pressurised and at high concentration, and therefore can be captured efficiently. The proximity to waste heat streams offers opportunities for heat integration. It has been estimated that carbon capture at SMR plants costs in the range of 30 to 96 \$ t<sub>CO2</sub><sup>-1</sup>. By comparison, post-combustion capture at natural gas-fired power plants is estimated to be between 52 and 108 \$ t<sub>CO2</sub><sup>-1</sup> [136]. The addition of CO<sub>2</sub> capture facilities onto SMR increases the cost of hydrogen by 25-30% [20].

A key consideration is the location of the CO<sub>2</sub> capture facility, as there are a number of CO<sub>2</sub>-containing streams with an SMR plant. Soltani et al. [16] examined CO<sub>2</sub> capture from an externally fired SMR process, in particular

the potential for CO<sub>2</sub> capture from different locations within the process. The locations are shown in **Figure 2.12**.



**Figure 2.12 –CO<sub>2</sub> capture locations in the steam reforming process [16]**

The authors evaluated the different CO<sub>2</sub> capture locations against criteria that determine suitability for carbon capture: CO<sub>2</sub> partial pressure, molar concentration and mass flow ratio (the mass flow of CO<sub>2</sub> in the stream as a percentage of the total CO<sub>2</sub> emitted). Without weighting to signify the relative importance of each criteria, location 1 was the highest-ranked location across the range of S/C ratios, due to the high CO<sub>2</sub> concentration and high partial pressure. Location 3 is the least preferable option, due to low CO<sub>2</sub> concentration and partial pressure.

However, it was noted that capture of the CO<sub>2</sub> from the flue gas stream (location 3) may be preferable in circumstances where maximum CO<sub>2</sub> capture is being targeted, as this stream contains CO<sub>2</sub> from the furnace as well as the reformer. Oxygen enrichment of the furnace feed may improve location 3 with respect to CO<sub>2</sub> concentration and partial pressure. However, the provision of oxygen enrichment is costly, and further techno-economic evaluation would be required to understand the implications.

As well as carbon capture location, another key consideration is the technology type. Studies on CO<sub>2</sub> capture from syngas have included a range of the four key capture technologies described above. Performance data, according to Voldsund et al. [94], are summarised in **Table 2.4**.

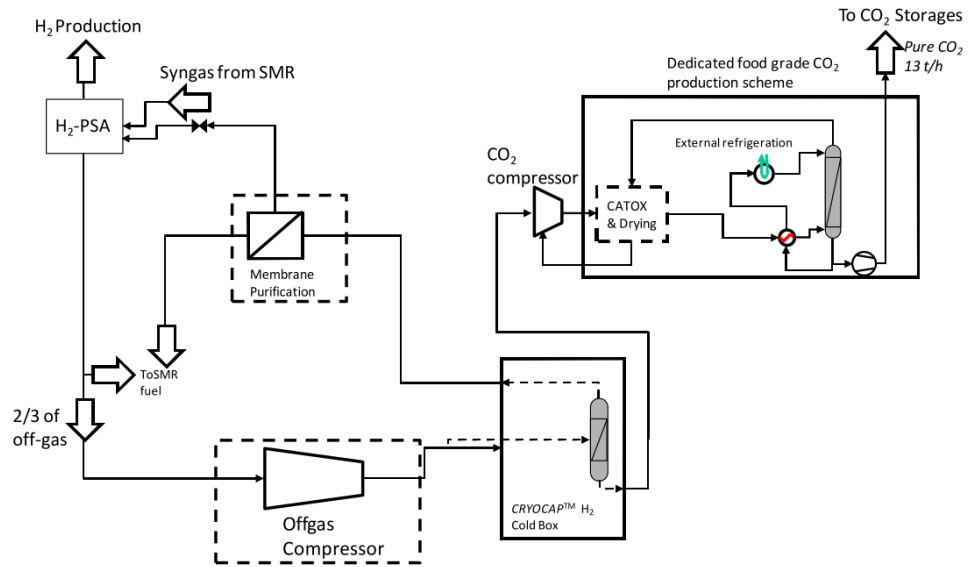
**Table 2.4 - Options for CO<sub>2</sub> separation from syngas  
(adapted from [94])**

	Adsorption		Absorption		Membrane (Pd)	Low temp. CO <sub>2</sub> capture
	H <sub>2</sub> PSA	CO <sub>2</sub> VSA	MDEA	Physical		
<b>H<sub>2</sub> purity, mol%</b>	98-99.9999+	Low (<91)	Low (58 <sup>a</sup> )	Low (83-86)	99-99.995	Low (81-83)
<b>H<sub>2</sub> recovery, %</b>	70-95	High	High	High	n/a	High
<b>CO<sub>2</sub> purity, mol%</b>	Low (39-57)	>97	99.9	95-99.7	Low	99.97-99.9
<b>CO<sub>2</sub> recovery, %</b>	High	>90	95	90-97	High	85-90
<b>Syngas type</b>	SMR	SMR	Air-blown ATR	Gasified coal	SMR	Gasified coal

<sup>a</sup> This value is for air-blown ATR for power generation. The hydrogen contains 40% nitrogen.

One early example of technology for CO<sub>2</sub> capture from SMR is Fluor's CO<sub>2</sub>LDSep™ process. The process is designed to capture CO<sub>2</sub> from PSA off-gases, using liquefaction. It can capture between 50 and 90% of the CO<sub>2</sub> in the stream, although the quoted figure for PSA off-gas is 63.1%. If a reboiled stripper is included, the process can give food-grade CO<sub>2</sub> [144].

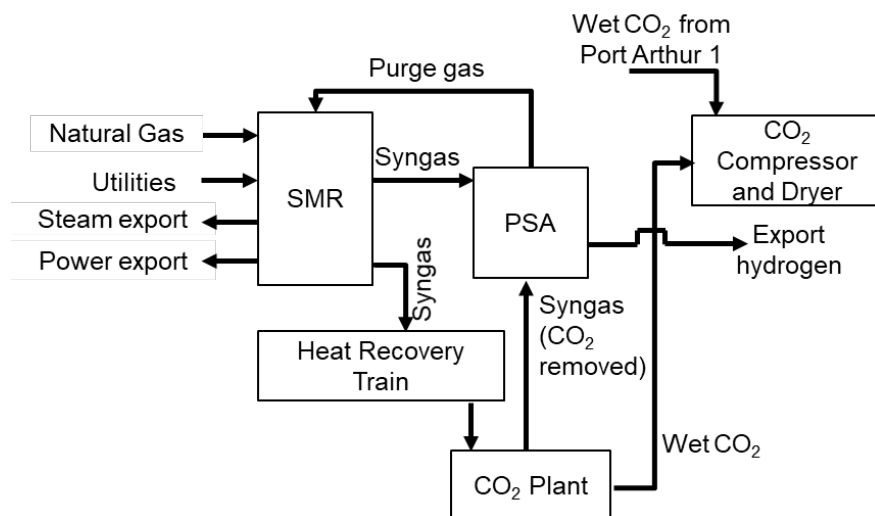
More recently, SMR-CCS has been achieved in large-scale applications. One such technology is Air Liquide's CRYOCAP™ process. The first commercial CRYOCAP™ process began operation at Port-Jérôme in France in 2015 [145]. Air Liquide estimates the price of CO<sub>2</sub> capture using CRYOCAP™ technology is around 40 \$ t<sub>CO2</sub><sup>-1</sup>, up to 40% less expensive than an equivalent process with activated MDEA [146]. The process uses cryogenic separation of PSA off-gas, followed by multi-stage membrane separation. The membranes increase CO<sub>2</sub> recovery, and recover H<sub>2</sub>, which is recycled to PSA. The residue from the membrane is added to the burner fuel gas. To attain food grade CO<sub>2</sub>, the process can include an additional CO<sub>2</sub> purification unit. A schematic is shown in **Figure 2.13**.



**Figure 2.13 – Process flow diagram of Air Liquide CRYOCAP™ [146]**

As the membrane recovers H<sub>2</sub> from the PSA off-gas, hydrogen production is increased by approximately 10 to 20%. Hydrogen and CO<sub>2</sub> recoveries from the syngas are 98% and 97% respectively. However, the overall CO<sub>2</sub> capture efficiency is limited. The process only captures the CO<sub>2</sub> from the syngas and not from combustion products, so around two-thirds of the total CO<sub>2</sub> from the plant is captured [146].

CO<sub>2</sub> capture has also been achieved from two SMRs at the Valero refinery in Port Arthur, Texas, in a demonstration project that ran from January 2013 to September 2016 [147]. **Figure 2.14** shows the Port Arthur CO<sub>2</sub> plant within the overall process scheme. The CO<sub>2</sub> capture plant is comprised of two VSA trains with a common compressor and dryer [148]. Two SMRs in close proximity enabled the use of a common CO<sub>2</sub> drying and compression system, thereby improving the economies of scale [149].



**Figure 2.14 – Process block flow diagram of Port Arthur SMR CO<sub>2</sub> capture [adapted from 148]**

The placement of the CO<sub>2</sub> capture plant on the syngas stream, upstream of PSA, is equivalent to location 1 in **Figure 2.13**. It takes advantage of the high CO<sub>2</sub> concentration and partial pressure within this stream. The process is designed to capture over 90% of the CO<sub>2</sub> in the syngas stream, and to concentrate it to 97% purity. The wet CO<sub>2</sub> is dried and compressed, before it is delivered to a pipeline for Enhanced Oil Recovery (EOR). It was estimated to capture around one million metric tons of CO<sub>2</sub> per year [150]. As with the CRYOCAP™ process, the CO<sub>2</sub> capture capability at Port Arthur is limited to a syngas stream and so does not allow for total capture of the CO<sub>2</sub>, for example from the flue gases of the furnace.

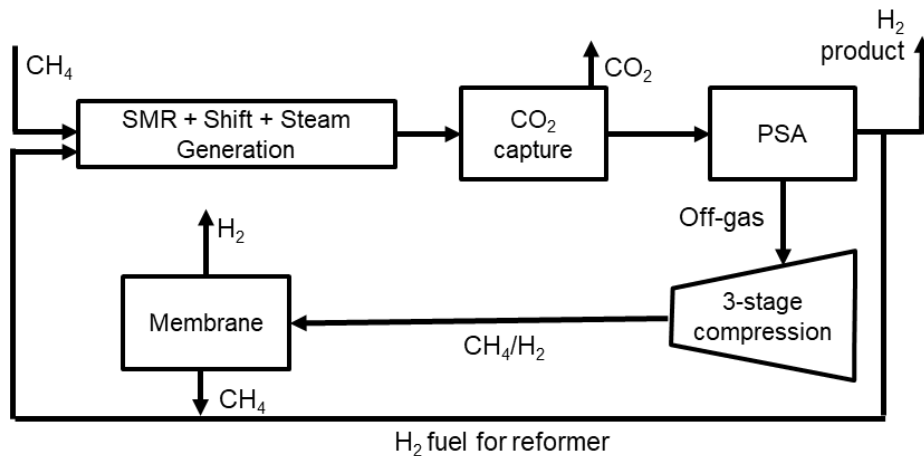
The Quest Project in Alberta, Canada was designed to capture up to 1 million tonnes per year of CO<sub>2</sub> from three SMR units at a bitumen upgrading facility. The process utilises Shell's Cansolv technology, an activated amine scrubbing process, which was retrofitted onto the facility. It produces CO<sub>2</sub> which is 99.2% pure [151]. In July 2020, the project announced that a total of 5 million tonnes of CO<sub>2</sub> have been captured, with an operating cost 35% lower than the original forecast in 2015 [152].

The Tomakomai project in Japan captures CO<sub>2</sub> from the hydrogen production unit at a refinery. CO<sub>2</sub> is captured from the PSA off-gases using an activated amine process. It utilises a two-stage absorption system with a low pressure flash, which reduces the energy consumption to 1.5 GJ t<sub>CO2</sub>. The resulting CO<sub>2</sub> is at least 99% pure [151,153]. Injection began in 2016, and ran until 2019, injecting a total of over 300,000 tonnes of CO<sub>2</sub> [154].

The H21 Leeds City Gate project examined the potential for conversion of the natural gas network in Leeds to a hydrogen network. The proposed project would use low carbon hydrogen generated by a SMR facility with CCS in the North East of England, with the CO<sub>2</sub> transported via pipeline to geological storage beneath the North Sea. The project's 2016 report [21] evaluates two configurations for carbon capture:

1. Post-combustion capture – in which a scrubbing column removes 90% of the CO<sub>2</sub> from the furnace flue gases (location 3 in **Figure 2.12**)
2. Pre-combustion capture – in which carbon capture is installed in the syngas stream (location 1 in **Figure 2.12**), capturing 98% of the CO<sub>2</sub>.

In the proposed pre-combustion configuration, a proportion of the H<sub>2</sub> is recycled to be used as fuel for the furnace, instead of methane. The PSA off-gases are separated using a membrane, so that methane is recycled to the reformer while any H<sub>2</sub> remaining in the off-gas is added to the furnace fuel. The concept is illustrated in **Figure 2.15**.



**Figure 2.15 – Proposed configuration for pre-combustion CO<sub>2</sub> capture in H21 Leeds City Gate Project (adapted from [21])**

The furnace fuel is comprised of a slip stream of hydrogen product, as well as the hydrogen within the PSA off-gas. As a result, the carbon within methane has been captured before combustion, so that furnace flue gases do not contain CO<sub>2</sub>. Thus this option takes advantage of the high pressure and CO<sub>2</sub> concentration in the syngas stream, while also enabling nearly total CO<sub>2</sub> capture from the process. Of the two options, pre-combustion capture gives the lowest estimated emissions (**Table 2.5**). While the pre-combustion case had a lower energy conversion efficiency, this was outweighed by the higher CO<sub>2</sub> capture efficiency.

**Table 2.5 –Pre- and post-combustion capture options (data from [21])**

Case	Post-combustion (90% H <sub>2</sub> recovery)	Pre-combustion (90% H <sub>2</sub> recovery)
Overall energy conversion efficiency	0.76	0.72
CO <sub>2</sub> emission from fuel supply (fraction)	0.18	0.19
CO <sub>2</sub> emission due to incomplete capture	0.13	0.03
CO <sub>2</sub> capture fraction	0.90	0.98
Total CO <sub>2</sub> emitted as fraction in net feed	0.31	0.22
Emissions g kWh <sup>-1</sup>	57.2	39.8

In summary, CO<sub>2</sub> capture in SMR has already achieved technological maturity, with a number of large-scale plants demonstrated or in development. However, at the early stage of deployment appears there is no



single configuration or technology choice which has taken precedence in SMR-CCS. Instead, technology selection depends on project-specific factors. There are two key considerations when designing CCS capability into an SMR process: the process configuration (or location of CO<sub>2</sub> capture), and the technology which is employed. Each of these factors has an impact on the other – for example, the various technologies will achieve different performances depending on the composition and pressure of the process stream. Another consideration which may be important is the target CO<sub>2</sub> purity. Cryogenic processes are capable of achieving the highest purity, giving food grade CO<sub>2</sub> which is over 99.99% pure. However, other examples achieve lower CO<sub>2</sub> purity, close to 99%, which is suitable for CCS.

As well as these more established CO<sub>2</sub> separation technologies, another proposed approach under development is sorption enhancement, in which a solid CO<sub>2</sub> sorbent is placed within the reactor. This performs several functions, not only relating to CO<sub>2</sub> capture. Further details are given in the section on advanced reforming technologies (**Section 2.5**).

## 2.5 Advanced reforming technologies

### 2.5.1 Sorption enhancement

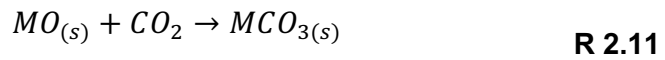
The hydrogen purity in the product gas is limited by stoichiometry of the steam reforming reaction. By the stoichiometry shown in the steam reforming and WGS reactions (R 2.1 to R 2.3), when any oxygenated hydrocarbon C<sub>n</sub>H<sub>m</sub>O<sub>k</sub> undergoes steam reforming, the maximum theoretical H<sub>2</sub> purity is:

$$\% \max H_2 \text{ purity} = 100\% \times \frac{m/2 + 2n - k}{m/2 + 3n - k} \quad \text{Eq. 2.2}$$

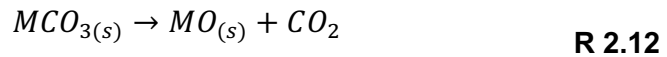
For example, one mole of pure acetic acid CH<sub>3</sub>COOH, when completely converted via steam reforming, could theoretically produce 4 moles of H<sub>2</sub> and 2 moles of CO<sub>2</sub>. This would result in a product which is 66.7% hydrogen

One means of improving the hydrogen purity without the need for downstream separation units is the addition of a CO<sub>2</sub> sorbent into the reactor. The sorbent selectively removes CO<sub>2</sub> from the reaction zone. This not only increases product purity, but also drives the water gas shift reaction (R 2.2) forward by shifting the equilibrium [36]. In addition, the carbonation reaction is highly exothermic and contributes heat to the endothermic reforming reactions, reducing the external heat requirement [71,89,155]. The

sorbent is typically a metal oxide (MO) which binds the CO<sub>2</sub> during the fuel feed step. A carbonate is formed:



When the sorbent is heated, or pressure is reduced, it undergoes calcination and releases the CO<sub>2</sub>:



When sorption enhancement is added to the chemical looping process, the process can be described as SE-CLSR. Calcination can occur during one of the cycle stages in SE-CLSR, for example during oxidation or reduction. In this way, the CO<sub>2</sub> sorbent is regenerated within the reactor, without the need for a separate regenerator [103]. **Chapter 6** discusses different operating strategies for calcination.

A commonly used sorbent in literature is calcium oxide, as it is cheap and readily available material with high CO<sub>2</sub> carrying capacity [156,157]. One challenge observed during experimentation is that the activity tends to decay over multiple sorbent cycles, thus there are ongoing efforts to improve long-term stability [158,159]. Other potential sorbents which are less well-developed include hydrotalcites, magnesium oxide or natural dolomites [156,157].

Antzara et al. [155] carried out a thermodynamic analysis on SE-CLSR with methane as feed. The study found that the optimal temperature range for the process was in the range 550-650°C. An elevated temperature increased hydrogen yield from the process, but at temperatures above 650°C, the partial pressure of CO<sub>2</sub> reduced below its equilibrium partial pressure, and therefore desorption was favoured.

In the same study, Antzara et al. [155] examined air, pure stoichiometric O<sub>2</sub>, CO<sub>2</sub> and H<sub>2</sub>O as potential oxidants. The analysis suggested that only the use of O<sub>2</sub> ensures that the SE-CLSR process saves energy when compared to conventional SMR or SE-SMR. If CO<sub>2</sub> or H<sub>2</sub>O are used, the nickel re-oxidation reactions are highly endothermic, increasing the total thermal requirements. If air is used, two separate reactors must be used for nickel re-oxidation and sorbent regeneration, otherwise the sorbent regeneration stage produces a CO<sub>2</sub> stream which is highly diluted with nitrogen. An alternative approach to eliminate this issue, studied in this thesis, is to carry

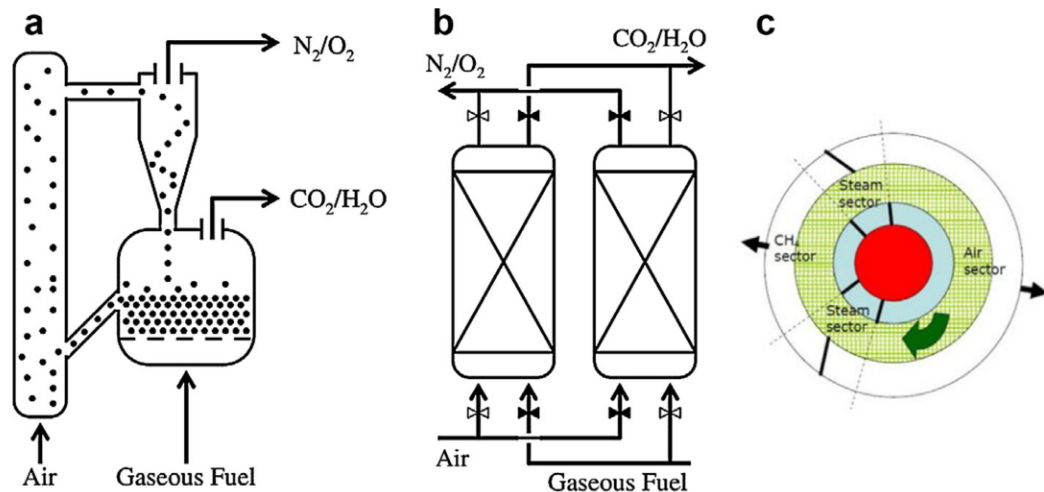
out simultaneous reduction and calcination, rather than oxidation with calcination (**Chapter 6**).

### 2.5.2 Chemical looping steam reforming

As described in **Chapter 1**, chemical looping utilises an oxygen transfer material, or OTM, to provide a source of undiluted oxygen to the reforming process, producing ready-separated gas streams and eliminating the need for external heating (**Figure 1.2**).

Chemical looping technology is not only used in steam reforming, but can also be used in other processes such as combustion. In their review on the topic, Adanez et al. [26] describe the difference between the many different types of chemical looping process. Two of these relate specifically to steam reforming, and it is important to distinguish between them. The first, Steam Reforming with Chemical Looping Combustion (SR-CLC), uses chemical looping combustion to provide the heat required for a typical steam reforming process. The second is Chemical Looping Reforming (CLR), in which chemical looping is used to produce  $H_2$  and CO directly. Where steam is used, it may be described as Chemical Looping Steam Reforming (CLSR). The process has also been referred to as Unmixed Reforming [103,160].

Three potential reactor configurations are illustrated in **Figure 2.16**. The conceptual diagram in **Figure 1.2** illustrates two reactors. In practice, this can be performed in an interconnect fluidised bed reactor (IFBR) or a single packed bed reactor (PBR). In a packed bed, the stages of the cycle are not managed by physical transfer of OTM from one reactor to the other, but by having different steps for fuel-steam feed and oxygen feed, controlled by gas switching valves [37,161,162]. Continuous production of hydrogen can be achieved by having two PBRs operating in parallel and alternating between the two feed steps [160]. An alternative reactor configuration is the rotating reactor, in which the OTM is rotated between the two air and fuel gas streams [75].



**Figure 2.16 – Reactor configurations for chemical looping reforming (a) Interconnected fluidized bed reactor (b) alternating fixed bed reactors (c) rotating reactor [75]**

An advantage of a PBR when compared to a circulating fluidized bed is that a PBR minimises particle attrition, and reduces the need for gas/particle separation [163]. A packed bed system could also ensure more simplicity, and therefore easier scalability for a range of applications. However, this configuration requires a high-pressure, high-temperature gas switching system which introduces complexity and would require a system of switching valves [75], the cost impact of which is explored further in **Chapter 5**.

CLSR may be combined with sorption enhancement to create the SE-CLSR process. The combination of the two together has several advantages [160]:

- i. Production of high purity  $H_2$  (around 90% dry  $H_2$ ) in a single reactor
- ii. Autothermal operation without the requirement for pure oxygen
- iii. Possibility for down-scaling due to improved heat transfer characteristics
- iv. Hotter reactor centre and cooler walls allow for less expensive reactor materials
- v. Coupled exothermic and endothermic reactions remove the need for external heating and thus make a compact process
- vi. Insensitivity to coking and sulphur
- vii. Feedstock flexibility: fuel may be gas or liquid.

### 2.5.3 Oxygen transfer materials

Chemical looping reforming requires a metal oxide, which provides an unmixed source of oxygen directly in to the reforming reactor. A number of studies have examined the development of oxygen transfer materials (OTMs) which are suitable for use in chemical looping. A review by Adanez et al. [26] found that over 700 OTMs have been developed and tested for CLC and CLR processes. These are typically synthetic materials, comprised

of a metal oxide such as Cu, CoO, Fe<sub>2</sub>O<sub>3</sub>, NiO, or Mn<sub>3</sub>O<sub>4</sub> supported on an inert material such as Al<sub>2</sub>O<sub>3</sub>, MgAl<sub>2</sub>O<sub>4</sub>, SiO<sub>2</sub>, TiO<sub>2</sub> or ZrO<sub>2</sub>.

The materials must be capable of performing well at high temperatures, enabling reproducible kinetics over a number of cycles. Key characteristics used to screen potential OTMs include cost, resistance to attrition, toxicity, reversibility and thermal stability. Reactivity is another important consideration. Its thermodynamic properties should enable high conversion, while other features such as particle size, shape structure and specific surface area define reaction kinetics [75].

Protasova and Snijkers [164] note that the OTMs which are suitable for CLSR are generally different to those which are most suitable for CLC. The CLSR process requires an OTM with high selectivity to syngas and high methane conversion. Fe-based and Cu-based systems have also shown promising results for the CLSR of methane [164–166]. However, of all types of OTMs, Ni-based is the type most extensively analysed in literature [26]. Benefits of nickel-based OTMs include their high reactivity and stability at high temperatures, as well as their high selectivity towards hydrogen production [33,75,167,168]. Other advantages of Ni-based catalysts include their relatively low cost and commercial availability [169].

Of the various supports used for Ni-based OTMs, Al<sub>2</sub>O<sub>3</sub> has been shown to have a number of favourable characteristics. Ni/Al<sub>2</sub>O<sub>3</sub> OTMs have demonstrated relatively high reactivity, low attrition rates in fluidized beds, no agglomeration problems and limited carbon deposition [26].

Wang et al. [170] investigated different supports for Ni-based oxygen transfer materials. Of the supports which were tested, Ni/Al<sub>2</sub>O<sub>3</sub> demonstrated mediocre performance while Ni/SBA-15 and lamellar Ni/MMT demonstrated superior activity and stability. Ni/Al-MCM-41 exhibited a high level of activity in the initial cycle, but its thermal instability led to a collapse of its structure.

Ni/ZrO<sub>2</sub> is another potential candidate. Silvester et al. [34] compared alumina and zirconia supports for Ni-based OTMs in CLSR of methane. The Ni-Zr OTM demonstrated superior stability over 20 cycles at 650°C and 850°C. The Ni-Al OTM reduced in performance during the first 12 cycles, after which the performance became stable. Overall, its deactivation reached around 23%. Another comparative study of supports found that ZrO<sub>2</sub> demonstrated high activity and stability [31]. This support was subsequently used in an experimental demonstration of SE-CLSR [171].

Another factor which can influence the suitability of a given OTM is the reactor configuration, i.e. whether the reactor is a PBR or an interconnected fluidized bed (IFBR). It is likely that in a PBR the material will undergo significantly less reduction/oxidation cycles per unit time. However, In an IFBR, only part of the oxidation potential of material is realised, whereas in a PBR the material must remain stable over the entire oxidation range [163].

Much of the literature in OTM development focusses on methane as a feedstock. By comparison, relatively few studies focus on OTMs for bio-oil or other bioenergy alternatives. An experimental study by Cheng and Dupont [128] examined the auto-reduction of a Ni/Al<sub>2</sub>O<sub>3</sub> catalyst with acetic acid followed by acetic acid steam reforming. At 750°C and S/C of 3, this achieved an acetic acid conversion of 88.97%, and a H<sub>2</sub> yield equal to 76.4% of the equilibrium value [128]. A subsequent kinetic study of the direct reduction of a NiO/ $\alpha$ -Al<sub>2</sub>O<sub>3</sub> catalyst with model bio-compounds found that the pre-exponential factors decreased in the following order: CH<sub>4</sub> > ethanol  $\approx$  acetone > acetic acid > furfural > glucose [172].

There is, however, a considerable body of research on catalysts for the steam reforming of bio-oil and its constituent compounds, which can provide useful information for identifying potential OTM candidates. As well as their activity for the steam reforming reaction, the catalysts should be capable of breaking C-C bonds in bio-compounds [119,173,174].

Ni-based catalysts have been extensively studied for acetic acid reforming [114,115,125,175–178]. Such studies have found a number of advantages of Ni-based catalysts. Hu and Lu [179] carried out a comparative study of acetic acid steam reforming on alumina-supported transition metal catalysts. The Ni-based catalyst demonstrated a high level of catalytic activity and other favourable characteristics, such as slower coke formation and sintering rates, and higher stability. At mild temperatures, the Ni-based catalyst showed high selectivity towards CH<sub>4</sub>. However, at higher temperatures, the CH<sub>4</sub> was reduced to trace level, thanks to its high activity for SMR.

A range of other catalyst types have been studied for bio-oil reforming, including different transition metals [179,180], as well as platinum [181–183] and other noble metals [127,184,185], and bio-char [186]. The work of Hu et al. [187] suggests that noble metal catalysts tend to demonstrate less carbon formation than Ni-based metal catalysts. Bimetallic catalysts have also been studied, typically Ni-Al in molar ratios of around 1:2 [125,126,169]. However, as discussed above, these catalysts tend to be more costly than the Ni-based catalysts already widely used in industry.

Different catalyst supports have also been examined for bio-oil reforming, with respect to carbon deposition and catalytic performance. Basagiannis and Verykios [176] studied  $\gamma$ -Al<sub>2</sub>O<sub>3</sub>, La<sub>2</sub>O<sub>3</sub>/Al<sub>2</sub>O<sub>3</sub>, MgO/Al<sub>2</sub>O<sub>3</sub> as supports for nickel and noble metals, concluding that the addition of basic oxides improved catalytic activity. Matas Güell et al. [183] studied ZrO<sub>2</sub> and CeO<sub>2</sub> as supports for platinum, suggesting that CeO<sub>2</sub> improved catalyst lifetime.

## **2.6 Process modelling of steam reforming processes**

### **2.6.1 Modelling conventional steam reforming**

A number of studies have used process modelling software Aspen Plus to perform conceptual studies on the steam reforming of bio-based feedstocks. These include thermodynamic studies for the reforming of bio-oil and its model compounds [188–194]. Other feedstocks include beef tallow [195], glycerol [105], vegetable oil [196], and bioethanol [197]. Such studies do not model the entire process but are used to understand the feasibility, equilibrium yields, and optimal conditions for novel feedstocks.

Aspen Plus is also a powerful tool for simulating whole processes, and so has been used to analyse proposed steam reforming plants. This includes whole process modelling of the reforming of bioenergy feedstocks including bio-oil [198,199], biodiesel [200], poultry tallow [201], bio-ethanol [202], and glycerol [28]. The process models have been used for a range of analyses, including heat integration and optimisation, techno-economic evaluation and the comparison of different scales of production. A more detailed review of techno-economic evaluations of hydrogen from bio-oil is given in **Chapter 5**. While there is a variety of process modelling to evaluate the SR of bio-oil and other bioenergy feedstocks, a notable omission is the role of CO<sub>2</sub> capture in such processes, so there is scope for novel research in this area.

### **2.6.2 Modelling advanced steam reforming**

As above, early work on the modelling of advanced reforming has used thermodynamic studies for proof of concept, and to identify optimal operating conditions. Many of these studies use Aspen Plus to develop simple models of the process, using interconnected reactors. For example, Tzanetis et al. [203] modelled SMR and SE-SMR using equilibrium reactors, in order to complete a exergy analysis and analyse the benefits of sorption enhancement. Antzara et al. [155], used the software to compare SE-CLSR

with conventional and sorption-enhanced SMR. Their analysis concluded that sorption enhancement leads to higher CH<sub>4</sub> conversion and H<sub>2</sub> purity at low temperatures, and that SE-CLSR leads to further improvements in performance.

Yahom et al. [41] used Aspen Plus to model CLSR and SE-CLSR of methane. CLSR was modelled as a two-reactor process, while the SE-CLSR was a three-reactor process as it incorporated a calcination reactor. According to this study, the optimum reactor operating conditions for CLSR of methane are a temperature of 800°C, a S/C ratio of 3, and a NiO/CH<sub>4</sub> ratio of 1. These conditions resulted in an approximate yield of 2.5 moles of H<sub>2</sub> per mole of CH<sub>4</sub> and an approximate H<sub>2</sub> purity of 75%. With the addition of sorption enhancement, higher hydrogen purity and yield were achieved (3 moles of H<sub>2</sub> per mole of CH<sub>4</sub> and >90% purity). Rydén and Ramos [168] used Aspen Plus to model SE-CLSR in a similar way. This study estimated that, at 1 bar, the process could achieve purity above 98 vol% H<sub>2</sub> with a yield of 2.8 moles of H<sub>2</sub> per mole of CH<sub>4</sub>.

Khan and Shamim [204] used Aspen Plus to perform an exergetic analysis on methane SE-CLSR. They found that overall exergetic efficiency decreases with steam, air and oxide flow rates, and increases with higher flow rates and higher fraction of inert material. Zhu & Fan [205] used Aspen Plus to model SE-SR reforming thermally coupled with chemical looping combustion – a similar but slightly different principle to SE-CLSR.

Recent studies have begun to complete more rigorous numerical models for the advanced reforming of methane, which take kinetics into account. Such studies are important to our understanding of CLSR and SE-CLSR, as these are dynamic processes in which sequencing can play an important role.

Diglio et al. [206] developed a 1D numerical model of CLSR in a non-isothermal PBR. By introducing several cycles to the model, the authors were able to simulate the dynamic behaviour of the cyclical process. This emphasised the strong influence of several key parameters: duration of oxidation and reduction phases, initial temperature, and feed pre-heating. Another important factor was the degree of oxidation obtained in the air feed phase, to ensure enough heat is supplied while ensuring that there is not too much oxygen stored, which is detrimental during the reaction phase.

Some studies have focussed instead on the IFBR configuration. For instance, Diglio et al [207] developed a numerical simulation of CLSR in a dual fluidized bed, in which 1D steady-state heat and mass balances were



coupled with a hydrodynamic model of the fluidized beds. The model was used to assess the impacts of operating conditions on process performance, concluding that key factors are the operating temperature and the amount of oxygen transported by the OTM. Wang et al [208] modelled a similar system, using a CFD simulation with kinetics incorporated into the code.

More recently, authors have begun to use rigorous reactor models of within a more complete process scheme, in order to assess design and operation parameters more holistically. For example, Spallina et al. [209] developed a 1D reactor model for methane CLSR in a PBR with 8% Ni/CaAl<sub>2</sub>O<sub>4</sub>. The process uses a cycle consisting of three steps: reforming, oxidation, and reduction. The later of these is carried out by syngas containing CO, H<sub>2</sub> and CO<sub>2</sub>. Following validation, the reactor model was used to simulate heat management in an industrial-scale process. Sanchez et al. [210] modelled methane reforming in fluidized bed reactors with a downstream PSA column for hydrogen separation. The study examined different types of reforming: SMR, SE-SMR, non-autothermal CLSR and autothermal CLSR. These models were used to perform an energy analysis and comparison of the different reforming processes.

Notably, these rigorous models of CLSR do not include sorption enhancement. The PhD thesis of Abbas [211] describes a method for rigorous modelling of SE-CLSR in a single packed bed. This involves a 1-D heterogeneous reactor model, which incorporates both sorption and steam reforming reactions. The proposed process consists of two steps: fuel feed and air feed. Both reduction and reforming are included within the fuel feed step. There have also been a number of studies of Ca-Cu systems for SE-CLSR of methane [59,212–214]. The principles applied within such work may also be applied to other feedstocks. In the case of this project, it could serve as the foundation for a model of the SE-CLSR of bio-oil.

With regards to the advanced reforming of bio-oils, there have been a number of conceptual thermodynamic studies, reviewed in more detail in **Chapter 4**. If advanced reforming of bio-oil is to be developed further, it will be necessary to evaluate a complete process, including aspects such as purification and auxiliary energy requirements. Such aspects are vital to the understanding of SE-CLSR of bio-oil, in particular how it might compare to conventional reforming techniques from an economic, environmental and efficiency perspective.

## Chapter 3 – Methodology

### 3.1 Introduction

This study uses a range of modelling and experimental techniques to evaluate technical, environmental and economic aspects of bio-oil steam reforming. The following sections provide a summary of these methodologies.

The thermodynamic analysis (**Chapter 4**) was based upon process modelling, as described in Section 3.2. Techno-economic analysis (**Chapter 5**) used a similar process modelling approach, combined with the economic methodology outlined in Section 3.3. In **Chapter 6**, a more detailed model of the SE-CLSR reactor has been created using a system of differential equations, as described in Section 3.3.5. Finally, an experimental study was carried out to determine reaction kinetics. The methods and materials for the kinetic study are described in **Section 3.5**, with details of the methodology for kinetic parameter estimation in **Section 3.6**.

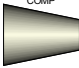







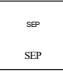
### 3.2 Process modelling

For the thermodynamic and techno-economic studies, steady-state process models were developed in Aspen Plus software. Aspen Plus is a widely used commercial modelling software that can be used for whole plant simulations. The software uses fundamental engineering relationships such as mass and energy balances, phase and chemical equilibria, and reaction kinetics, in order to predict the behaviour of a process [215].

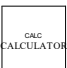
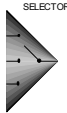


#### 3.2.1 Aspen Plus flowsheets

Process stages were modelled using blocks to represent unit operations, as detailed in **Table 3.1**. A number of manipulator blocks (**Table 3.2**) were used to automate certain calculations within the process.

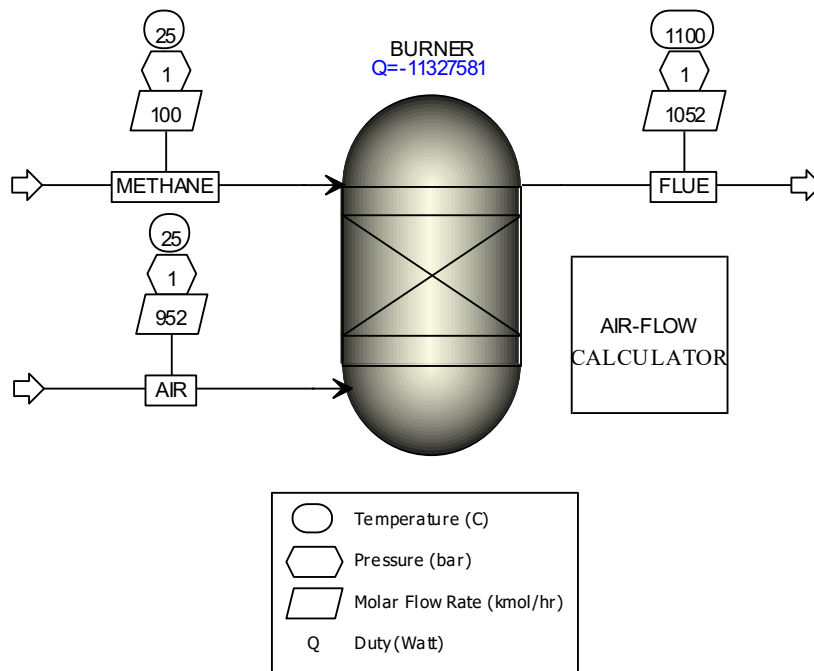
**Table 3.1 – Unit operation blocks in Aspen Plus software**

Symbol	Name	Description
	Compr	Represents compressors or turbines, by modelling the compression or expansion of a fluid stream and associated power requirement.
	Flash2	A two-outlet flash separator. On the basis of the defined outlet conditions, the block carries out a flash calculation to determine the thermal and phase conditions of outlet streams.
	Heater	Represents the heating or cooling of a material stream via the input or output of energy.
	HeatX	Represents the heating or cooling of a material stream via exchanging heat with another material stream.
	Mixer	Combines multiple material streams into a single stream.
	Pump	Models a pressure change in a liquid, and calculates the power input required.
	REquil reactor	Calculates simultaneous phase and chemical equilibrium of one- and two-phase reactions. Used when reaction stoichiometry is known.
	RGibbs reactor	Calculates simultaneous phase and chemical equilibrium of one- and two-phase reactions. Can be used when reaction stoichiometry is not known.
	Sep	A simple separator block, in which the user specifies what proportion of each component is split into each output stream.

**Table 3.2 – Manipulator blocks in Aspen Plus software**

Symbol	Name	Description
	Calculator	Used to insert Fortran statements or Excel spreadsheet calculations into the computations. For example, it has been used to calculate the quantity of oxygen required for completion combustion, and to set the flow rate of air accordingly.
	Selector	Allows the user to switch between different material stream inputs, so that the same model can be used with different inputs. For example, it has been used to select between different bio-oil model compounds in the thermodynamic analysis.
	Design-Spec	Specifies a target value for a flowsheet variable, and adjusts a control variable until the specification is reached. For example, it has been used to set the flowrate of air to a gas turbine, such that it does not exceed a maximum temperature.
	Transfer	Copies flowsheet variables from one part of the flowsheet to another. For example, it can be used to ensure the properties of the solid bed at the end of one SE-CLSR step are copied to the start of the next step.

The blocks are connected together with streams, in order to simulate the flow of material and energy. **Figure 3.1** shows an example flowsheet, containing a methane burner where the air flow required for complete combustion is set by a calculator block. Full flowsheets for thermodynamic and techno-economic studies are detailed in **Chapters 4 and 5** respectively.



**Figure 3.1 Example Aspen Plus flowsheet**

A key definition in the process simulation is the ‘property method’, which is the collection of methods used to compute thermodynamic and transport properties [215]. The selected property method was Peng-Robinson. Aspen Plus guidance suggests this method for H<sub>2</sub>-rich and high-temperature, high-pressure applications such as reformers [216]. Models of similar systems in the literature have used the same property method [190,217,218].

### 3.2.2 Thermodynamic equilibrium

In **Chapters 4, 5 and 7**, reactors are modelled using equilibrium reactor blocks. These reactors calculate the products of a reaction on the basis of thermodynamic equilibrium, using the minimisation of Gibbs free energy. The Gibbs function describes the following relationship between enthalpy, temperature and entropy [219]:

$$G = H - TS \quad \text{Eq. 3.1}$$

where  $G$  is the Gibbs function,  $H$  is enthalpy,  $T$  is temperature, and  $S$  is entropy.

According to the first and second laws of thermodynamics, a chemical reaction at a specified temperature and pressure proceeds in the direction of a decreasing Gibbs function [219]. Thus chemical equilibrium is obtained when the Gibbs reaches a minimum value, expressed as follows:

$$(dG)_{T,P} = \sum (\bar{g}_i dn_i)_{T,P} = 0 \quad \text{Eq. 3.2}$$

where  $\bar{g}_i$  is the molar Gibbs function of component  $i$ , and  $dn_i$  is the differential change in the number of moles of the same component.

Aspen Plus software uses this criterion to estimate the outputs of a chemical reactor at chemical equilibrium, even when the reaction stoichiometry is not known [215]. This is particularly useful for complex systems, such as the bio-oil processes in this study.

### 3.2.3 Feedstock

Bio-oil has a complex composition, which varies between different feedstocks and processes [109]. This study uses two approaches to represent bio-oil. The first approach is to use a single model compound, in order to simplify the analysis. Acetic acid (AcOH) is selected as the first model compound. It has been widely used in experimental and modelling studies, as it is one of the most abundant compounds found in compositional

analysis [119,124–126]. All three of the main groups in biomass (cellulose, hemicellulose and lignin) can thermally decompose to give acetic acid [220]. Resende et al [221] used a thermodynamic analysis to show that the use of AcOH as a model compound is suitable from a thermodynamic standpoint.

Furfural was also selected because its molecular formula ( $C_5H_4O_2$ ) closely matches that of the moisture-free bio-oil model mixture shown in Table 3.3. Furfural has been used as a model compound by several authors [101,123]. Remón et al. [222] used a statistical analysis to identify that acetic acid and furfural were the compounds which had the most significant effect on bio-oil reforming performance.

The second approach is to use a surrogate mixture of components, in order to more closely model the composition of a real bio-oil. The literature contains a variety of approaches to surrogate bio-oil mixtures. Plou et al. [223] used mixtures of acetic acid, methanol and acetol to represent three major groups in bio-oil (acids, alcohols and ketones). Other authors have matched their mixture composition to a detailed compositional analysis, using around 10 different compounds [68,199]. An alternative approach involves using a selection of model compounds, in combinations that give an elemental composition ( $C_nH_mO_k$ ) matching that of a real bio-oil [118,224].

In this study, the composition of the bio-oil surrogate mixture is based on the work of Dupont et al. [225]. The bio-oil is represented as a mixture of the 6 macro-families identified by Garcia-Perez et al. [226]. The mass fraction of each compound was selected using curve fitting procedures, in order that the elemental composition and differential thermogravimetric (DTG) curve closely matches that of a real Palm Empty Fruit Bunch (PEFB) bio-oil [227]. A sensitivity analysis on PEFB bio-oil model mixtures has previously shown that the equilibrium results are not sensitive to the exact mixture composition, provided that the elemental composition is known [228]. The composition used in this study is shown in **Table 3.3**.

**Table 3.3 - PEFB bio-oil model mixture composition [225]**

		C	H	O
Ultimate analysis, mol fraction <sup>a</sup>		0.286	0.491	0.223
Model mixture, mol fraction		0.268	0.519	0.213
Percentage of error, %		6.2	5.8	4.8
Water, wt.% <sup>a</sup>		24.3		
Model water, wt.%		24.0		
Family <sup>b</sup>	Family wt.%	Model compounds		Mass fraction
1	F1=10%	Formaldehyde, CH <sub>2</sub> O		0.08
		Acetaldehyde, C <sub>2</sub> H <sub>4</sub> O		0.01
		1-hydroxy-2-butanone, C <sub>4</sub> H <sub>8</sub> O <sub>2</sub>		0.01
2	F2=30%	Acetic acid, C <sub>2</sub> H <sub>4</sub> O <sub>2</sub>		0.07
		Water, H <sub>2</sub> O		0.23
3	F3=15%	Furfural, C <sub>5</sub> H <sub>4</sub> O <sub>2</sub>		0.13
		Phenol, C <sub>6</sub> H <sub>6</sub> O		0.01
		Water, H <sub>2</sub> O		0.01
4	F4=15%	Creosol, C <sub>8</sub> H <sub>10</sub> O <sub>2</sub>		0.14
		Guaiacol, C <sub>7</sub> H <sub>8</sub> O <sub>2</sub>		0.01
5	F5+F6=30%	Catechol, C <sub>6</sub> H <sub>6</sub> O <sub>2</sub>		0.24
6		Palmitic acid, C <sub>16</sub> H <sub>32</sub> O <sub>2</sub>		0.01
		Levogluconan, C <sub>6</sub> H <sub>10</sub> O <sub>5</sub>		0.05
<sup>a</sup> Composition of real PEFB bio-oil is from Pimenidou and Dupont [227]				
<sup>b</sup> Macro-families are based on Garcia-Perez[226]				

In the thermodynamic analysis in **Chapter 4**, bio-oil was represented by the two model compounds, as well as a surrogate mixture. **Chapter 5** focusses only on the surrogate mixture, in order to provide a more realistic approximation for techno-economic analysis.

### 3.3 Economic analysis

#### 3.3.1 Design basis

An important aspect of the design basis is the product specification for H<sub>2</sub>, which varies with the intended application. In this project, it is assumed that the plant is located in an industrial area, and takes advantage of CCS and H<sub>2</sub> pipeline infrastructures such as those proposed by the Teesside

Collective and the H21 Leeds City Gate project [21,229]. The specifications are therefore the same as those proposed for a UK H<sub>2</sub> grid by the H21 Leeds City Gate project [21], shown in **Table 3.4**. Given that the pressure (40 bar) is within the range for an industrial hydrogen pipeline [230], this could also represent hydrogen for an industrial network. For water content, it is assumed the dew point specifications would be the same as those defined for natural gas in the Gas Safety (Management) Regulations 1996, which state that the water dew point:

*“shall be at such levels that they do not interfere with the integrity or operation of pipes or any gas appliance...which a consumer could reasonably be expected to operate”* [231].

**Table 3.4 – Hydrogen specifications** [21,231]

<b>H<sub>2</sub> export properties</b>	
H <sub>2</sub> export pressure	40 bar
Export temperature	25°C
<b>Composition</b>	
H <sub>2</sub>	>99.98%
CO	< 15 ppmv
CH <sub>4</sub>	< 100 ppmv
CO <sub>2</sub>	< 10 ppmv
Water dew point	-30°C at 45 bar (8.3 ppmv)

Where CO<sub>2</sub> capture was considered, it was necessary to meet CO<sub>2</sub> specifications that ensure the integrity of transportation and storage infrastructure. For example, it is necessary to minimise species that can cause pipeline corrosion or fouling, or those that pose a health hazard [232]. The base case CO<sub>2</sub> purity specification (**Table 3.5**) was taken from the recommendations of the CO<sub>2</sub> Europe project, in which CCS stakeholders created a set of guidelines for European CCS infrastructure [233]. However, as there is not yet any standardised specification for CCS, studies in the literature have used a range of different purity targets [234–237]. The feasibility of achieving these CO<sub>2</sub> purity specifications in SE-CLSR is discussed further in **Chapter 6**. The specified CO<sub>2</sub> pressure was assumed to be 110 bar, for transportation in the supercritical phase [136,238–240].



**Table 3.5 – CO<sub>2</sub> purity specifications [233]**

Component	Limit in CO <sub>2</sub>
CO <sub>2</sub>	>95 vol%
Ar	Total non-condensables
CH <sub>4</sub>	<5 vol%
H <sub>2</sub>	
N <sub>2</sub>	
O <sub>2</sub>	
H <sub>2</sub> O	No free water (< 500 ppm <sub>v</sub> )
CO	4750 ppm <sub>v</sub>
NH <sub>3</sub>	550 ppm <sub>v</sub>
H <sub>2</sub> S	235 ppm
COS	235 ppm <sub>v</sub>
SO <sub>2</sub>	75 ppm <sub>v</sub>
NO <sub>2</sub>	75 ppm <sub>v</sub>
HCN	70 ppm <sub>v</sub>

A further consideration is the production capacity. A typical industrial scale steam reformer may have a capacity in the region of 200,000 Nm<sup>3</sup> h<sup>-1</sup> [73]. A plant that uses bio-compounds as feedstock would be considerably smaller, due to feedstock limitations. For this study it is assumed that the reformer is a centralized plant that accepts feedstock from multiple pyrolysis plants, as proposed in literature [14,90]. In this way, the plant is not limited to the capacity of a single pyrolysis facility, so it may take advantage of economies of scale. A range of 5,000 Nm<sup>3</sup> h<sup>-1</sup> to 100,000 Nm<sup>3</sup> h<sup>-1</sup> was selected for consideration, representing bio-oil input from 1 to 20 medium-sized fast pyrolysis plants. The basis for this figure is given in **Appendix A**.

### 3.3.2 Process performance indicators

A number of performance indicators were used to provide a quantitative analysis of process performance. One indicator of performance is the hydrogen yield, on a molar basis:

$$Yield (molar) = \frac{\dot{n}_{H_2}}{\dot{n}_{feed,m.f.}} \quad \text{Eq. 3.3}$$

where  $\dot{n}_{H_2}$  and  $\dot{n}_{bio-oil,m.f.}$  represent the molar flow rates of hydrogen and moisture-free fuel respectively.

Alternatively, the H<sub>2</sub> yield can be described on a mass basis, either based on wet or moisture-free bio-oil:

$$Yield (wt\%, .wet) = \frac{\dot{m}_{H_2,actual}}{\dot{m}_{feed,wet}} \times 100\% \quad \text{Eq. 3.4}$$

$$Yield (wt\%, .m.f.) = \frac{\dot{m}_{H_2,actual}}{\dot{m}_{feed,m.f.}} \times 100\% \quad \text{Eq. 3.5}$$

The H<sub>2</sub> yield may also be expressed as a percentage of the stoichiometric potential, i.e. how the yield compares to the maximum yield determined by stoichiometry of the relevant reaction (defined in **Table 4.2**):

$$\% \text{ stoichiometric potential} = \frac{\dot{n}_{H_2,actual}}{\dot{n}_{H_2,stoichiometric}} \times 100\% \quad \text{Eq. 3.6}$$

H<sub>2</sub> purity was calculated as the molar percentage of H<sub>2</sub> in the product:

$$H_2 \text{ purity (mol\%)} = \frac{\dot{n}_{H_2,product}}{\dot{n}_{total,product} - \dot{n}_{H_2O,product}} \times 100\% \quad \text{Eq. 3.7}$$

The thermal efficiency of the process was calculated as follows [241]:

$$\eta_{th,process} = \frac{\sum_i \dot{Q}_{prod,i} + (P_{el}^- - P_{el}^+) + (\dot{Q}_{th}^- - \dot{Q}_{th}^+)}{\sum_j \dot{Q}_{fuel,j} + (P_{el}^+ - P_{el}^-) + (\dot{Q}_{th}^+ - \dot{Q}_{th}^-)} \times 100\% \quad \text{Eq. 3.8}$$

where  $\dot{Q}_{prod,i}$  and  $\dot{Q}_{fuel}$  are the energy values of the products and fuel inputs respectively. Both were calculated on a lower heating value (LHV) basis. The LHVs of bio-oil and model compounds were taken from Aspen Plus. The LHV of CH<sub>4</sub> was assumed to be 800 kJ mol<sup>-1</sup>, and H<sub>2</sub> was 240 kJ mol<sup>-1</sup>.  $P_{el}$  represents the electricity, and  $\dot{Q}_{th}$  represents the heat that is imported (superscript “+”) or exported (“superscript “-“). For heat and electricity, only the net flows are included, so that the terms appear either in the numerator (net exports) or denominator (net imports).

The heat export took the form of low pressure (LP) steam at 6 bar and 160°C [242]. The equivalent heat from steam export was thus calculated by:

$$\dot{Q}_{th}^- = \dot{m}_{steam}(h_{s@6 \text{ bar},160^\circ\text{C}} - h_{liq,sat@6 \text{ bar}}) \quad \text{Eq. 3.9}$$

where  $\dot{m}_{steam}$  is the mass flow rate of steam export.  $h_{s@6 \text{ bar},160^\circ\text{C}}$  is the specific enthalpy of the exported steam, and  $h_{liq,sat@6 \text{ bar}}$  is the specific enthalpy of saturated water at the same pressure.

### 3.3.3 Capital cost methodology

Cost estimates were calculated using the method outlined in Turton et al. [243]. This uses a module costing approach, first introduced by Guthrie

[244,245] and later modified by Ulrich [246]. It is a widely used approach, considered to be an effective method for preliminary cost estimates [243].

### 3.3.3.1 Bare module costs

As far as possible, bare module costs were taken from Turton et al. [243], in which data from a survey of manufacturers have been used to formulate cost correlations in the following form:

$$\log_{10}C_p^o = K_1 + K_2\log_{10}(A) + K_3[\log_{10}(A)]^2 \quad \text{Eq. 3.10}$$

where  $C_p^o$  is the purchased cost of equipment at base case conditions (ambient operating pressure and carbon steel construction) and  $A$  is the size parameter.

Size parameters were taken from the Aspen Plus model and used to calculate the purchased cost of equipment for some base conditions. The purchased cost ( $C_p^o$ ) was then multiplied by a series of factors that account for deviations from the base conditions, including specific equipment type, system pressure, and materials of construction. **Table 3.6** summarises how these factors are applied to each type of equipment.

**Table 3.6 – Equations for bare module cost of equipment [243]**

Equipment type	Equation for bare module cost
Process vessels	$C_{BM} = C_p^o F_{BM} = C_p^o (B_1 + B_2 F_M F_P)$
Heat exchangers	$C_{BM} = C_p^o F_{BM} = C_p^o (B_1 + B_2 F_M F_P)$
Pumps	$C_{BM} = C_p^o F_{BM} = C_p^o (B_1 + B_2 F_M F_P)$
Fans with electric drives	$C_{BM} = C_p^o F_{BM} F_P$
Fired heaters and furnaces	$C_{BM} = C_p^o F_{BM} F_P F_T$
Power recovery equipment	$C_{BM} = C_p^o F_{BM}$
Compressors and blowers without drives	$C_{BM} = C_p^o F_{BM}$
Drives for compressors and blowers	$C_{BM} = C_p^o F_{BM}$

$F_M$  is the material factor, given for each equipment type in [243]. Those parts of the process that were exposed to bio-oil were assumed to be stainless steel, due to the corrosive nature of bio-oil [247,248]. Remaining parts of the process were assumed to be carbon steel.  $F_{BM}$  is the bare module factor, also given in [243].  $F_T$  is a superheat correction factor for steam boilers.  $F_T = 1$  for other heaters and furnaces.

For process vessels, the pressure factor  $F_P$  was based on the ASME code for pressure vessel design:

$$F_{P,vessel} = \frac{\frac{(P_{vessel} + 1)D}{2[850 - 0.6(P_{vessel} + 1)]} + 0.00315}{0.0063} \text{ for } t_{vessel} > 0.0063m \quad \text{Eq. 3.11}$$

where  $P_{vessel}$  is the operating pressure in barg,  $D$  is vessel diameter, and  $t_{vessel}$  is the wall thickness.

For remaining process equipment,  $F_P$  was calculated by:

$$\log_{10}F_P = C_1 + C_2 \log_{10}(P_{vessel}) + C_3 [\log_{10}(P_{vessel})]^2 \quad \text{Eq. 3.12}$$

where the constants  $C$  were taken from [243].

For certain units, such as WGS reactors, PSA systems, or CO<sub>2</sub> capture plants, bare module costs were estimated using single point cost data from literature. This allowed estimates for complex systems without detailed design. Cost data were adjusted to the relevant sizes via the scaling formula:

$$C_{mod} = C_{mod,0} \left( \frac{S_{mod}}{S_0} \right)^f \times I \quad \text{Eq. 3.13}$$

where  $f$  is the scaling exponent,  $C_{mod}$  is the bare module cost of the unit with size  $S_{mod}$ , and  $C_{mod,0}$  and  $S_{mod,0}$  are the cost and size of the reference case respectively. The value  $I$  is the installation factor (where given).

**Chapter 5** gives details of the single point data applied in this study.

In the SE-CLSR study, the refractory-lined reactor vessels were identified as a key component that could have a large influence on the overall cost. These vessels were designed in more detail, based on the methods in Peters et al. [249] and Hamers et al. [249]. A reactor volume was estimated from the catalyst weight hourly space velocity (WHSV) and sorbent quantity. On the basis of this reactor volume, the mass of steel and refractory material were calculated, and converted to a cost. Full details are in **Appendix B**

Cost data was updated using the Chemical Engineering Plant Cost Index (CEPCI). As 2018 is the most recent year for which there is an annual value, data was updated to 2018 as follows:

$$C_{BM,2018} = C_{BM,base} \left( \frac{CEPCI_{2018}}{CEPCI_{base}} \right) \quad \text{Eq. 3.14}$$

where  $C_{BM,2018}$  is the 2018 cost, and  $C_{BM,base}$  is the cost in the base year.  $CEPCI_{2018}$  is the annual index for 2018, equal to 603.1.  $C_{base}$  is the CEPCI for the base year. For data from Turton, this was equal to 397 [243]. For single point cost data from literature, a relevant CEPCI was selected.

### 3.3.3.2 Total capital costs

The total cost of a new facility ('grassroots cost') was calculated in two stages. First the total module cost ( $C_{TM}$ ) was found by applying a factor for fees, as well as a contingency to account for uncertainty. Fees are assumed to be 3% of the bare module costs [243]. The contingency is 30%, as recommended by NETL for a concept with bench-scale data [48].

$$C_{TM} = 1.33 \sum_{i=1}^n C_{BM,i} \quad \text{Eq. 3.15}$$

A further addition was made for auxiliary facilities, such as site development and buildings. This was equal to 50% of the bare module cost for the base case conditions. The total fixed capital investment (FCI) was thus:

$$FCI = C_{TM} + 0.50 \sum_{i=1}^n C_{BM,i}^o \quad \text{Eq. 3.16}$$

where  $C_{BM,i}^o$ , the bare module cost for base case conditions, was found by setting  $F_M$  and  $F_P$  to unity.

It was assumed that working capital was equal to 15% of the fixed capital investment [243]. The total capital investment was calculated as follows:

$$TCI = 1.15FCI \quad \text{Eq. 3.17}$$

### 3.3.4 Operating cost methodology

Operating costs were calculated using the method of Turton et al. [243]. The overall cost of manufacture was estimated as a sum of direct, fixed and general manufacturing expenses, as outlined in **Table 3.7**.

**Table 3.7 – Methodology for cost of manufacture [243]**

Cost item	Value
1. Direct manufacturing costs	-
a. Raw materials	$C_{RM}$
b. Waste treatment	$C_{WT}$
c. Utilities	$C_{UT}$
d. Operating labour	$C_{OL}$
e. Direct supervisory and clerical labour	18% of $C_{OL}$
f. Maintenance and repairs	6% of Fixed Capital Investment ( $FCI$ )
g. Operating supplies	0.9% of $FCI$
h. Laboratory charges	15% of $C_{OL}$
i. Patents and royalties	3% of total cost of manufacture ( $COM$ )

Cost item	Value
2. Fixed manufacturing costs	
a. Depreciation	Included in cash flow – 20 year straight line.
b. Local taxes and insurance	3.2% of $FCI$
c. Plant overhead costs	60% of lines d, e and f
3. General manufacturing expenses	
a. Administration costs	15% of lines d, e and f
b. Distribution and selling costs	11% of $COM$
c. Research & development	5% of $COM$

By summing together the terms and rearranging, the total cost of manufacture without depreciation ( $COM_d$ ) is found to be:

$$COM_d = 0.18FCI + 2.73C_{OL} + 1.23(C_{UT} + C_{WT} + C_{RM}) \quad \text{Eq. 3.18}$$

**Chapter 5** gives further detail of the specific economic assumptions applied in each case, such as the operating costs, and single point cost data.

### 3.3.5 Levelised cost of hydrogen

To compare processes on a consistent basis, the levelised cost of hydrogen (LCOH) was used. The LCOH gives an estimate of the value of hydrogen that is required to recoup the lifetime costs of a project. By combining all the lifetime costs into a single value, it enables simple analysis. LCOH was calculated as follows [250]:

$$LCOH = \frac{\sum_{Y=1}^n \frac{TCI_Y + COM_{d,Y}}{(1+r)^Y}}{\sum_{Y=1}^n \frac{H_t}{(1+r_D)^Y}} \quad \text{Eq. 3.19}$$

where  $n$  is the lifetime of the project,  $TCI_Y$  is the capital investment and  $COM_{d,t}$  is the cost of manufacture in year  $Y$ .  $H_t$  is the hydrogen generated in year  $Y$ .  $r_D$  is the discount rate. A 22 year lifetime was assumed, including 2 years of construction and commissioning, followed by 20 years of operation. The discount rate was set at 10%.

### 3.3.6 Carbon emissions and cost of CO<sub>2</sub> avoided

As emissions reduction is a key driver for the study, another important metric was the GHG emissions emitted by the process. The total emissions include

not only CO<sub>2</sub> emissions in the flue gases, but also those associated with imports and exports of electricity and steam. The specific emissions (kg<sub>CO2</sub> kg<sub>H2</sub><sup>-1</sup>) were calculated as follows:

$$E_{H_2} = \frac{\dot{m}_{CO_2} + (\dot{Q}_{th}^+ - \dot{Q}_{th}^-)E_{th} + (\dot{P}_{el}^+ - \dot{P}_{el}^-)E_{el}}{\dot{m}_{H_2}} \quad \text{Eq. 3.20}$$

where  $\dot{m}_{CO_2}$  is the flowrate of CO<sub>2</sub> in the flue gases, and  $\dot{m}_{H_2}$  is the mass flowrate of H<sub>2</sub>.  $E_{th}$  and  $E_{el}$  are the emissions factors for thermal energy and electricity, respectively.  $\dot{Q}_{th}$  and  $\dot{P}_{el}$  are the thermal energy and electrical power, while subscripts + and – signify imports and exports, respectively. Emission factors are taken from European Union data [53].  $E_{el}$  is assumed to be 0.391 kg kWh<sup>-1</sup>, and  $E_{th}$  is 0.224 kg kWh<sup>-1</sup>, assuming a natural gas boiler with 90% efficiency.

To quantify the economic impact of CO<sub>2</sub> capture, the cost of CO<sub>2</sub> avoided (CCA) was calculated. CCA is defined as the value of carbon that would make the plant with CO<sub>2</sub> capture competitive with a benchmark plant [251]:

$$CCA = \frac{LCOH - LCOH_{ref}}{E_{H_2,ref} - E_{H_2}} \quad \text{Eq. 3.21}$$

where  $LCOH$  and  $LCOH_{ref}$  are the levelized cost of hydrogen (\$ kg<sub>H2</sub><sup>-1</sup>) in the plant with without CO<sub>2</sub> capture, respectively.  $E_{H_2}$  and  $E_{H_2,ref}$  are the specific emissions (kg<sub>CO2</sub> kg<sub>H2</sub><sup>-1</sup>) of the plant with and without CO<sub>2</sub> capture, respectively.

A further consideration was the origin of the carbon emissions. There are three main sources of carbon to the process: bio-oil, methanol (for bio-oil stabilisation), and methane. The bio-oil contributes biogenic emissions, whereas it was assumed that methane and methanol originate from fossil-based sources. This important distinction would affect the overall life cycle emissions of the process, particularly when considering the potential for negative emissions via BECCS.

This study does not contain a full life cycle assessment, but nonetheless it is useful to examine the balance of fossil and biogenic carbon sources. CO<sub>2</sub> emissions may be allocated to different sources via a carbon balance on the process inputs:

$$Y_{fossil} = \frac{\dot{n}_{CH_4} + \dot{n}_{CH_3OH}}{\dot{n}_{CH_4} + \dot{n}_{CH_3OH} + \alpha_{bio-oil}\dot{n}_{bio-oil}} \times 100\% \quad \text{Eq. 3.22}$$

$$Y_{biogenic} = 100\% - Y_{fossil} \quad \text{Eq. 3.23}$$

$Y_{fossil}$  and  $Y_{biogenic}$  are the percentage allocations of fossil-based and biogenic emissions, respectively.  $\dot{n}_{CH_4}$ ,  $\dot{n}_{CH_3OH}$  and  $\dot{n}_{bio-oil}$  are the inlet molar

flow rates of methane, methanol and bio-oil. The constant  $\alpha_{bio-oil}$  is the number of moles of carbon in each mole of bio-oil, equal to 4.057 in this case (Table 3.3).

### 3.4 Dynamic reactor modelling

In Chapter 6, a stage of SE-CLSR is simulated by developing a detailed mathematical model of a packed bed reactor (PBR). This model was created by combining a system of mass, energy and momentum balances, as well as reaction kinetics, and solving these as a system of differential and algebraic equations. The approach is described in the following sections.

#### 3.4.1 Modelling packed bed reactors

Within a catalytic PBR, a number of complex phenomena occur simultaneously, including chemical reactions and mass-, heat- and momentum-transfer. Reactor models are developed by formulating mass and energy balances over a discrete volume element, an example of which is shown in Figure 3.2.

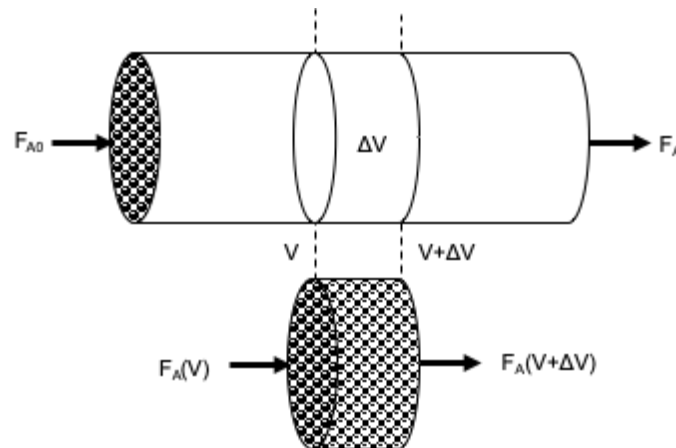


Figure 3.2 Plug flow reactor schematic (adapted from [252])

To simulate what is occurring within the reactor, it is necessary to define a set of equations to describe the system mathematically. These systems of equations can have varying levels of complexity, commonly described by the classifications in Table 3.8. Pseudo-homogeneous models do not distinguish between the fluid and solid phase, whereas heterogeneous models consider the fluid and solid phases separately [253]. A basic, or ideal, model assumes plug flow, meaning that concentration and temperature gradients occur only in the axial direction. Further detail may be included by considering mixing in the radial direction. In heterogeneous models, interfacial and intra-particle gradients may also be included.



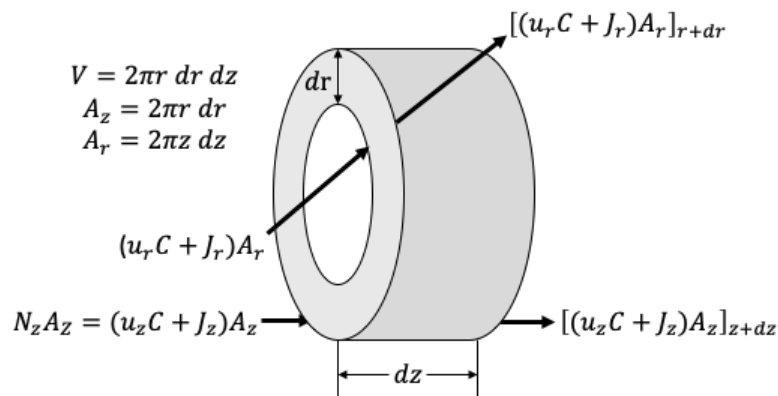
**Table 3.8 – Classification of packed bed reactor models [253]**

	<b>A. Pseudo homogeneous models</b> $T = T_s, C = C_s$	<b>B. Heterogeneous models</b> $T \neq T_s, C \neq C_s$
One-dimensional	A.I: Basic, ideal → ↓ A.II: + axial mixing	B.I: + interfacial gradients ↓ B.II: + intraparticle gradients
Two-dimensional	↓ A.III: + radial mixing	↓ B.III: + radial mixing

Adding detail to a model can provide a more accurate depiction of a system. However, it also introduces further complexity, and increase in computation time, that may not be justified by the improvement in accuracy. In this case, the selected modelling approach was an ideal pseudo-homogeneous model. This assumption has been used widely in literature on hydrogen production, including accurate models of steam methane reforming [173,254,255], sorption-enhanced reforming [59,212,256] and chemical looping [165,214,257,258].

### 3.4.2 Governing equations

To model mass transfer in both the axial and radial directions, the volume element is an annular ring with length  $dz$  and width  $dr$ , shown in **Figure 3.3**.



**Figure 3.3 Annular differential ring continuity equations, based on [259]**

According to the law of conservation of mass, the continuity equation for species  $i$  over this volume may be written as:

$$\left( \begin{array}{c} \text{Rate of} \\ \text{accumulation} \\ \text{of moles of } i \end{array} \right) = \left( \begin{array}{c} \text{Rate of} \\ \text{change in} \\ \text{z direction} \\ \text{due to} \\ \text{flow and} \\ \text{diffusion} \end{array} \right) + \left( \begin{array}{c} \text{Rate of} \\ \text{change in} \\ \text{r direction} \\ \text{due to} \\ \text{flow and} \\ \text{diffusion} \end{array} \right) + \left( \begin{array}{c} \text{Generation} \\ \text{of } i \text{ due to} \\ \text{reaction} \end{array} \right) + \left( \begin{array}{c} \text{Generation} \\ \text{of } i \text{ due to} \\ \text{interphase} \\ \text{addition} \end{array} \right)$$

Mathematically, this is expressed as [259]:

$$\frac{\partial VC}{\partial t} + \frac{\partial(N_z A_z)}{\partial z} dz + \frac{\partial(N_r A_r)}{\partial r} dr = g_c + g_a \quad \text{Eq. 3.24}$$

The molar flux due to flow and diffusion in direction  $j$  is given by:

$$N_j = u_j C_i + J_j \quad \text{Eq. 3.25}$$

where molar flux due to diffusion,  $J_j$ , is given by Fick's law:

$$J_j = -D_j \frac{\partial C}{\partial j} \quad \text{Eq. 3.26}$$

Substituting and dividing through by  $V = 2\pi r dr dz$  gives:

$$\frac{1}{V} \frac{\partial VC}{\partial t} + \frac{\partial A_z u C}{A_z \partial z} dz - D_z \frac{\partial^2 C}{\partial z^2} - \frac{D_r}{r} \frac{\partial}{\partial r} \left( r \frac{\partial C}{\partial r} \right) = \frac{g_c}{V} + \frac{g_a}{V} \quad \text{Eq. 3.27}$$

where radial velocity  $u_r$  is zero and diffusion coefficients  $D_z$  and  $D_r$  are independent of position.

Given the rate of reaction  $R_c = \frac{g_c}{V}$  and rate of addition  $R_a = \frac{g_a}{V}$ , further simplification gives:

$$\begin{array}{cccccc} \frac{\partial C}{\partial t} & + & \frac{\partial u C}{\partial z} dz & - & D_z \frac{\partial^2 C}{\partial z^2} & - & \frac{D_r}{r} \frac{\partial}{\partial r} \left( r \frac{\partial C}{\partial r} \right) & = & R_c + R_a & \text{Eq. 3.28} \\ \text{(1)} & & \text{(2)} & & \text{(3)} & & \text{(4)} & & \text{(5)} & \end{array}$$

The terms in the continuity equation include (1) the accumulation in moles of  $i$  with time in a volume  $V$  in terms of (2) change with volume traversed; (3) axial diffusion or dispersion; (4) radial dispersion; and (5) generation via reaction and addition from another phase [259].

An analogous derivation for energy yields the following energy balance:

$$\frac{\partial T}{\partial t} + \frac{\partial u T}{\partial z} dz - \lambda_z \frac{\partial^2 T}{\partial z^2} - \frac{\lambda_r}{r} \frac{\partial}{\partial r} \left( r \frac{\partial T}{\partial r} \right) = \frac{q_c}{\rho C_p} + \frac{q_a}{\rho C_p} \quad \text{Eq. 3.29}$$

where  $\lambda_r$  and  $\lambda_z$  are the thermal conductivity in the axial and radial directions, respectively.  $q_c$  is the heat liberated or abstracted by reaction, and  $q_a$  is the rate of heat addition or removal.  $\rho$  is the mass density, and  $C_p$  is the specific heat capacity.

For a PBR, it is assumed that there are no radial gradients in temperature, concentration or reaction rate. The following assumptions were also applied:

- Adiabatic operation
- Ideal gas behaviour
- Constant bed porosity

Based on **Eq. 3.28** and **Eq. 3.29**, the balances for a one-dimensional (1D) heterogeneous packed bed reactor are expressed in in **Table 3.9**.

**Table 3.9 – Mass and energy balances for 1D heterogeneous PBR [254]**

<b>Mass and energy balances in the gas phase:</b>	
$\varepsilon_b \left( \frac{\partial C_i}{\partial t} \right) + \frac{\partial(uC_i)}{\partial z} + k_{g,i}a_v(C_i - C_{i,s}) = \varepsilon_b D_z \frac{\partial^2 C_i}{\partial z^2}$	<b>Eq. 3.30</b>
$\varepsilon_b \rho_g C_{p,g} \left( \frac{\partial T}{\partial t} \right) + u \rho_g C_{p,g} \frac{\partial T}{\partial z} = h_f a_v (T_s - T) + \lambda_z^f \frac{\partial^2 T}{\partial z^2}$	<b>Eq. 3.31</b>
<b>Mass and energy balances in the solid phase:</b>	
$k_{g,i}a_v(C_i - C_{i,s}) + \left( \frac{\partial C_{i,s}}{\partial t} \right) = \eta(1 - \varepsilon_b)\rho_{bed}r_i$	<b>Eq. 3.32</b>
$\rho_{bed}C_{p,bed} \left( \frac{\partial T_s}{\partial t} \right) + h_f a_v (T_s - T) = (1 - \varepsilon_b)\rho_{bed} \sum \eta_j (-\Delta H_{rxn,j})R_j$	<b>Eq. 3.33</b>

A pseudo-homogeneous model does not distinguish between solid and fluid phases, therefore:

$$C_i = C_{i,s} \quad \text{Eq. 3.34}$$

$$T_i = T_{i,s} \quad \text{Eq. 3.35}$$

The balances for solid and gas phases are thus simplified into the pseudo-homogenous balances in **Table 3.10**.

**Table 3.10 – Mass and energy balances for 1D adiabatic axially dispersed pseudo-homogeneous packed bed reactor [212]**

<b>Mass balance:</b>	
$\varepsilon_b \left( \frac{\partial C_i}{\partial t} \right) + \frac{\partial(uC_i)}{\partial z} = \varepsilon_b D_z \frac{\partial^2 C_i}{\partial z^2} + \eta(1 - \varepsilon_b)\rho_{bed}r_i$	<b>Eq. 3.36</b>
<b>Energy balance:</b>	
$\varepsilon_b \rho_g C_{p,g} \left( \frac{\partial T}{\partial t} \right) + (1 - \varepsilon_b)\rho_{bed}C_{p,bed} \left( \frac{\partial T}{\partial t} \right) + u \rho_g C_{p,g} \frac{\partial T}{\partial z} = \lambda_z^f \frac{\partial^2 T}{\partial z^2} + (1 - \varepsilon_b)\rho_{bed} \sum \eta_j (-\Delta H_{rxn,j})R_j$	<b>Eq. 3.37</b>

Pressure drop across the bed was calculated via a steady state momentum balance, known as the Ergun equation [260]:

$$-\frac{\partial P}{\partial z} = \frac{150}{d_p^2} \left[ \frac{(1 - \varepsilon_b)^2}{\varepsilon_b^3} \right] \mu_g u + \left( \frac{1.75}{d_p} \right) \left( \frac{1 - \varepsilon_b}{\varepsilon_b^3} \right) \rho_g u^2 \quad \text{Eq. 3.38}$$

The axial mass dispersion coefficient was given by [261]:

$$D_z = 0.73D_m + \frac{0.5ud_p}{1 + 9.49 \frac{D_m}{ud_p}} \quad \text{Eq. 3.39}$$

Effective thermal conductivity was given by [262]:

$$\frac{\lambda_z^f}{\lambda_g} = \frac{\lambda_z^o}{\lambda_g} + 0.75PrRe_p \quad \text{Eq. 3.40}$$

$$\frac{\lambda_z^o}{\lambda_g} = \varepsilon_b + \frac{1 - \varepsilon_b}{0.139\varepsilon_b - 0.0339 + \left( \frac{2}{3} \right) \frac{\lambda_g}{\lambda_s}} \quad \text{Eq. 3.41}$$

The particle Reynolds number ( $Re_p$ ) and Prandtl number ( $Pr$ ) are:

$$Re_p = \frac{\rho_g u d_p}{\mu_g} \quad \text{Eq. 3.42}$$

$$Pr = \frac{C_{p,g} \mu_g}{\lambda_g} \quad \text{Eq. 3.43}$$

At reactor inlet ( $z = 0$ ), the boundary conditions were defined as:

$$C_i = C_{i,0} \quad T = T_0 \quad P = P_0$$

At reactor outlet ( $z = L$ ), the boundary conditions were:

$$\left. \frac{\partial C_i}{\partial z} \right|_{z=L} = 0 \quad \left. \frac{\partial T}{\partial z} \right|_{z=L} = 0$$

Initial conditions were:

$$C_i = C_{i,0} \quad T = T_0$$

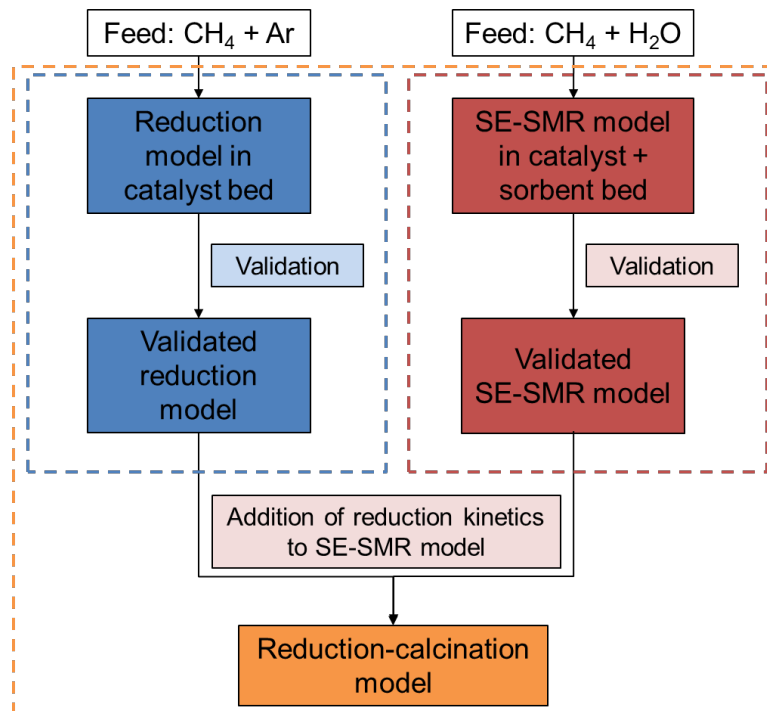
The mass and energy balances require details of chemical kinetics that are relevant to the system. In the model of reduction-calcination (**Chapter 5**), the kinetics for reduction, reforming, sorption and calcination were taken from the literature. In **Chapter 6**, kinetics for acetic acid steam reforming were derived by the experimental study. The generalised mass and energy balances given above were also adjusted in some cases, for example to model a mixed catalyst/sorbent bed. Further details of kinetics and model adjustments are given in the relevant chapters.

### 3.4.3 Mathematical modelling methodology

The system of equations described above was solved using gPROMS ModelBuilder 4.1.0®, an advanced process modelling platform from Process Systems Enterprise. The software allows the user to construct models from first principles, offering a high level of customisation and complexity. It also has parameter estimation capabilities that can be used to fit experimental data, further details of which are given in **Section 3.6.2**.

The reactor bed was described as a distributed model, in which properties varied with respect to the axial dimension as well as to time. The system of equations in **Section 3.4.2** was solved using the differential algebraic solver (DASOLV). DASOLV implements a Backward Differentiation Formulae (BDF) algorithm for efficiently solving large systems of differential algebraic equations (DAEs) [263,264]. The reactor was discretized in the axial direction using the backward finite difference method (BFDM). Models were checked for sensitivity to discretization, with the number of intervals ranging from 50 – 1000 shown to have minimal effect.

The study in **Chapter 6** focusses on the simultaneous reduction and calcination stage of the SE-CLSR cycle. The model was created in stages, by creating a validated model of reduction, and a validated model of SE-SMR, before combining the two into a single model (**Figure 3.4**).



**Figure 3.4 Modelling methodology hierarchy for reduction-calcination**

## 3.5 Experimental methods and materials for kinetic study

**Chapter 7** outlines the results of a kinetic study on the steam reforming of a bio-oil model compound. In order to derive kinetic parameters, it was necessary to carry out a number of experiments to determine how reactant conversion is affected by temperature and space velocity. The following sections give details of the experimental methods and materials that were used to obtain this data.

### 3.5.1 Bio-oil model compound

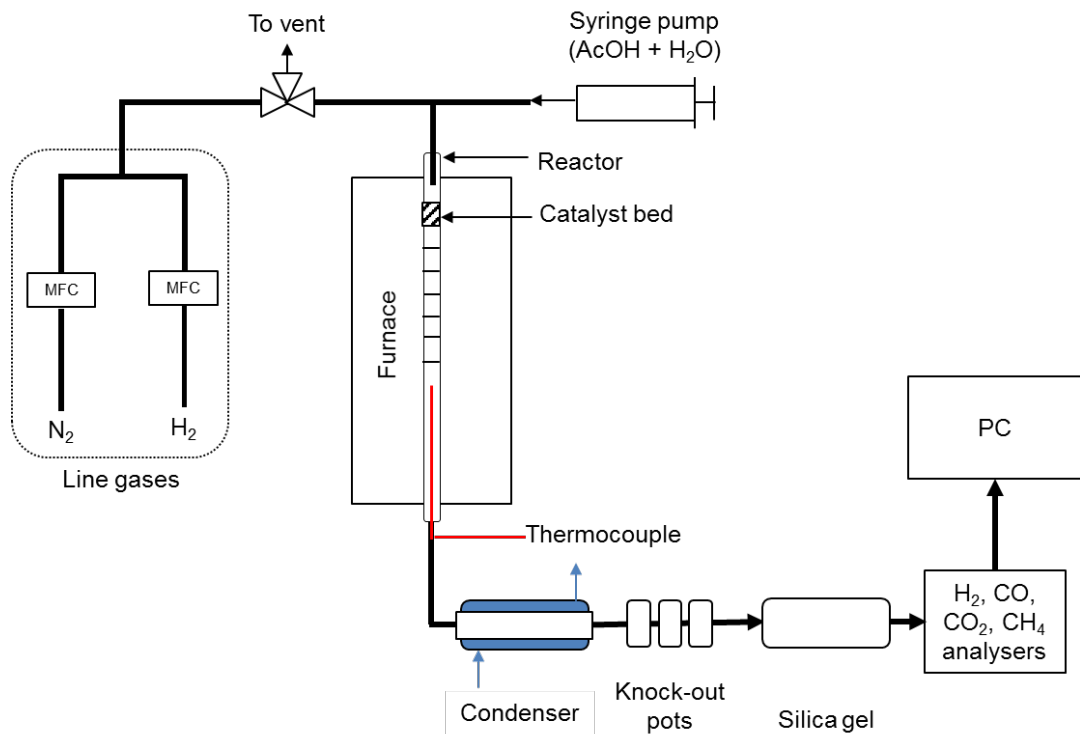
As discussed in **Section 3.2.3**, bio-oil contains a complex mix of organic compounds. A common experimental approach is to use a single model compound to represent bio-oil [122,123,181,194,265]. While this does not fully represent the behaviour of a real bio-oil, this approach has certain other benefits. For example, it simplifies the analysis, and makes it easier to form comparative studies [119]. It also enables a more fundamental understanding of what is occurring within the system.

In addition, the model compound approach provides information that is transferable to other systems, without the variation observed in real bio-oils. For example, studies by Arregi et al [266], Bakhtiari et al. [267] and Gayubo et al. [268] showed the derivation of kinetics for whole bio-oils. While these provide useful information on real bio-oil, their transferability is limited because the empirical observations apply to specific bio-oils whose compositions may not easily be replicated. In the longer term, it may be possible to combine data from individual compounds into versatile models of mixtures.

For this work, acetic acid was selected as the bio-oil model compound. The acetic acid used for experimentation was reagent grade ( $\geq 99.0\%$ ) from Fluka Analytical. Acetic acid steam reforming has been extensively studied, as it is one of the most abundant compounds present in bio-oil [119,125,127,128,193,269]. Resende et al [221] demonstrated that acetic acid is a satisfactory model compound for bio-oil, from a thermodynamic standpoint. Galdámez et al [126] proposed simple first-order kinetics on bimetallic Ni-Al catalysts, but kinetic data is otherwise limited. A review of kinetic studies is given in **Chapter 7**.

### 3.5.2 Packed bed reactor configuration

Acetic acid steam reforming was carried out in the packed bed reactor set-up illustrated in **Figure 3.5**.



**Figure 3.5 – Reactor set-up for acetic acid steam reforming experiments**

The reactor was a 316 stainless steel tube, 750mm long, with inside diameter 13.2mm. It was placed within an Elite Thermal Systems vertical furnace (TSVH12/30/450), controlled by a Eurotherm 3216 temperature controller. To enable monitoring of the reaction temperature, a K-type thermocouple was placed inside the reactor. To minimise heat losses, gaps at the top and base of the reactor were covered with thermal insulation (Superwool® 607 HT paper).

A solution of acetic acid and deionised H<sub>2</sub>O, mixed to the required S/C ratio, was fed from a programmable syringe pump. The rig was also connected to a supply of N<sub>2</sub> and H<sub>2</sub> (BOC, purity 99.995%). A Bronkhorst MASS-VIEW mass flow controller (0 – 2000 sccm) controlled the flow of N<sub>2</sub>, while a Bronkhorst EL-FLOW (0.1 – 200 sccm) controlled H<sub>2</sub> flow.

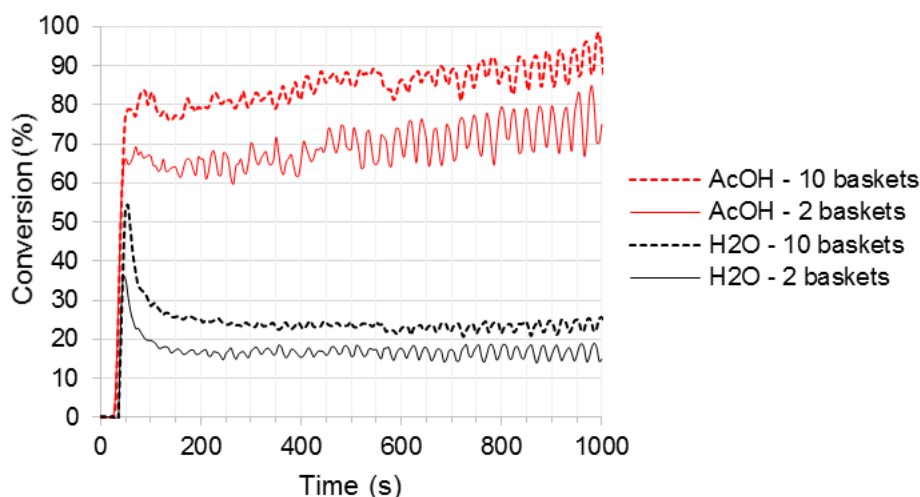
A catalyst bed was created by placing 1g of catalyst into a cylindrical mesh basket (1.25 cm<sup>3</sup>). To raise the catalyst bed as close as possible to the inlet tubing, it was placed on top of nine empty baskets. These rested on a thin steel bar welded across the tube. The total length of baskets was 200mm, ensuring there was sufficient distance from the ends of the furnace to

maintain a constant temperature from the top of the catalyst bed to the thermocouple.

To protect the gas analysers, moisture was removed from the gas in two stages. The bulk of the moisture was removed in a condenser, consisting of a jacketed heat exchanger cooled by a 1:1 mix of water and ethylene glycol at 4°C, followed by a series of three knock-out pots. Remaining traces of water were removed by a moisture trap filled with silica gel.

The dry gas was passed through an ABB Advanced Optima analyser. CO, CO<sub>2</sub> and CH<sub>4</sub> were measured by a Uras 14 module, using infrared absorption. H<sub>2</sub> was measured with a Caldos 15 module, using thermal conductivity.

As the feed was a liquid solution, a key consideration was the vaporisation of reactants. The configuration of 10 baskets described above retained a small space (18 mm) between the end of the feed tube and the catalyst bed, to allow time for vaporisation. To ensure this was sufficient space for vaporisation, a test was carried out during which an experiment was replicated with 10 baskets (1 full and 9 empty) and with 2 baskets (1 full and 1 empty). The composition gas profiles are shown in **Figure 3.6**.



**Figure 3.6 – Vaporisation test, showing the comparison between a 10-basket configuration and 2-basket configuration.**

**S/C = 2.5, T = 620°C, N<sub>2</sub> = 600 sccm, liquid flow = 0.479 ml min<sup>-1</sup>**

**Figure 3.6** shows that when there were fewer baskets, i.e. the catalyst bed was located further from the inlet tubing, the fluctuations in gas composition were more pronounced. This suggests the fluctuations did not result from vaporisation issues caused by the catalyst bed being located too close to the inlet. It is more likely that the fluctuations resulted from the pulsating flow of



the syringe pump. The fluctuations had implications for data processing, which are discussed in **Section 3.5.5**.

In **Figure 3.6** it is also notable that the conversion was reduced in the 2-basket configuration. This may have been because there was a longer residence time before reaching the catalyst bed, enabling more time to undergo non-catalytic reactions (such as pyrolysis). Another potential cause is reduced back-pressure, leading to lower reactant partial pressure. It highlights the importance of retaining the same number of baskets in all experiments. On the basis of the test, the 10-basket configuration was deemed acceptable for reactant vaporisation, and 10 baskets were retained for all experiments.

### **3.5.3 Packed bed reactor operation**

The steps in the operation procedure were as follows:

- (1) The mesh basket was filled with 1g of catalyst and loaded into the reactor tube, before the reactor was fitted into the furnace.
- (2) The reactor was heated to the reaction temperature at  $10^{\circ}\text{C min}^{-1}$  with a flow of 100 sccm  $\text{N}_2$ .
- (3) Once the reactor had reached the desired temperature, the catalyst was reduced with  $\text{H}_2$  gas. This converted  $\text{NiO}$  to  $\text{Ni}$ , ensuring the catalyst bed was catalytically active. A mixture of 5 vol%  $\text{H}_2$  in  $\text{N}_2$  was flowed at 200 sccm for around 2 hours, until the catalyst was fully reduced. The end of reduction was confirmed by the outlet gas composition matching the inlet gas.
- (4) The reactor was purged with 500 sccm  $\text{N}_2$  until  $\text{H}_2$  was no longer detected at the outlet.
- (5) The  $\text{N}_2$  flow was set to the rate required for the experiment. The syringe pump was switched on, and data sampling commenced.
- (6) The system was left to run until it reached steady state. When the feed syringe was nearly empty, data sampling ended and the syringe pump and furnace were switched off. The reactor was purged with  $\text{N}_2$ , and left to cool.
- (7) Once the reactor had cooled to ambient temperature, samples of condensate were collected from the knock-out pots, and the catalyst was retained for analysis. The reactor, knock-out pots and baskets were then cleaned in preparation for the next experiment.

### 3.5.4 Catalyst

OTMs for chemical looping reforming are typically comprised of a metal oxide such as Cu, Fe<sub>2</sub>O<sub>3</sub>, NiO, or Mn<sub>3</sub>O<sub>4</sub> supported on an inert material such as Al<sub>2</sub>O<sub>3</sub>, MgAl<sub>2</sub>O<sub>4</sub>, SiO<sub>2</sub>, TiO<sub>2</sub> or ZrO<sub>2</sub> [75]. Nickel-based OTMs are the most extensively analysed in literature and have the crucial advantage of being effective steam reforming catalysts in their reduced, metallic form [26]. Studies with methane and Ni/NiO have demonstrated high reactivity and stability at high temperatures, as well as high selectivity towards hydrogen production [33,75,167,168]. More recent work have demonstrated successful application of Ni-based OTMs to the reforming of bio-oil model compounds, including acetic acid [38,123,270]. The reforming catalyst selected for study was therefore a commercial Ni-based catalyst.

In the work of Omoniyi et al. [270–272], Ni/Ca/Al<sub>2</sub>O<sub>3</sub> exhibited a more stable performance than Ni/Al<sub>2</sub>O<sub>3</sub> during the SE-CLSR of acetic acid. This is potentially because the calcium aluminate support is less acidic and is therefore less prone to carbon deposition. For this reason, Ni/Ca/Al<sub>2</sub>O<sub>3</sub> was selected for the kinetic experiments. The catalyst used for experimentation was 15 wt% NiO/Ca/Al<sub>2</sub>O<sub>3</sub> (TST 8466), provided by Twigg Scientific Ltd. The large catalyst pellets were ground to particle size 150 – 250 μm using a pestle and mortar.

This study does not contain detailed catalyst characterisation, as the thesis of Omoniyi [271] contains extensive characterisation of this catalyst in acetic acid SE-CLSR at similar conditions. However, in order to evaluate the impacts of carbon deposition, a selection of catalyst samples were subjected to CHN elemental analysis

CHN analysis is a technique to quantify the amount of carbon, hydrogen and nitrogen in a sample. Samples are combusted at very high temperatures (1000 - 1800°C) in an oxygen-rich atmosphere. A thermal conductivity detector within a chromatography column detects the combustion products (CO<sub>2</sub>, H<sub>2</sub>O and N<sub>2</sub>/NO<sub>x</sub>). These measurements are then used to determine the quantity of carbon, hydrogen and nitrogen within the sample [273].

For the CHN analysis, around 15mg of catalyst was placed into a tin capsule. The capsule was compressed to eliminate air before being placed onto an auto-sampler for analysis in a Flash EA 2000 elemental analyser. Oxygen (BOC, purity 99.99%) was used as the oxidant, while helium (BOC, purity 99.99%) was used as carrier gas.

### 3.5.5 Process outputs and material balance

Data from the analyser and thermocouple were recorded on a computer, with a sample interval of 5 seconds. The information required for the kinetic study was then derived via two stages of data processing: H<sub>2</sub> measurement correction, and material balances.

#### 3.5.5.1 H<sub>2</sub> measurement correction

The concentration of H<sub>2</sub> in the product gas was measured by a Caldos 15 analyser, which uses thermal conductivity to measure the concentration of H<sub>2</sub> in N<sub>2</sub>. Other species present in the gas, such as CH<sub>4</sub>, CO<sub>2</sub> and CO, alter the thermal conductivity measurements and thus affect the H<sub>2</sub> reading. A correction factor was applied to account for the effect of these other gases:

$$y_{H_2,out} = \sum \left( \frac{\lambda_i}{\lambda_{H_2}} y_i \right) + y_{H_2} \quad \text{Eq. 3.44}$$

where  $y_i$  is the concentration of species  $i$  detected by the analyser, and  $\lambda_i$  is its thermal conductivity at STP (20°C, 101.325 kPa). In cases where  $\lambda_i > \lambda_{N_2}$ , then  $\lambda_i$  is multiplied by -1. However, in this study, N<sub>2</sub> was always the component with the highest vol%.

This correction was applied to the same analyser in the work of Bloom [274], wherein the correction was tested and shown to improve accuracy.

#### 3.5.5.2 Material balance

The conversions of reactants (AcOH and H<sub>2</sub>O) were calculated via a series of mass balances. As the carrier gas (N<sub>2</sub>) was inert, it could be assumed that the flow of N<sub>2</sub> remained the same at the inlet and outlet. The number of moles of each component was calculated on the basis on N<sub>2</sub> concentration:

$$n_{dry,out} = \frac{n_{N_2,in}}{y_{N_2,out}} \quad \text{Eq. 3.45}$$

where  $n_{dry,out}$  is the total molar flow of dry product gas,  $n_i$  is the molar flow of species  $i$ , and  $y_i$  is its molar fraction in the dry product gas.

The outlet flow of AcOH was calculated by a carbon balance, while the outlet flow of H<sub>2</sub>O was calculated by a hydrogen balance:

$$n_{AcOH,out} = n_{AcOH,in} - n_{dry,out} \times \left( \frac{y_{CO,out} + y_{CO} + y_{CH_4,out}}{2} \right) \quad \text{Eq. 3.46}$$

$$n_{H_2O,out} = \frac{4n_{AcOH,in} - 4n_{AcOH,out} + 2n_{H_2O,in} - n_{dry,out}(2y_{H_2} + 4y_{CH_4})}{2} \quad \text{Eq. 3.47}$$

The conversions of AcOH and water were then calculated as follows:

$$X_{AcOH} = \frac{n_{AcOH,in} - n_{AcOH,out}}{n_{AcOH,in}} \times 100\% \quad \text{Eq. 3.48}$$

$$X_{H_2O} = \frac{n_{H_2O,in} - n_{H_2O,out}}{n_{H_2O,in}} \times 100\% \quad \text{Eq. 3.49}$$

### 3.5.5.3 Steady state results

The aim of the experiments was to obtain steady state conversion data to enable fitting of kinetic parameters (Section 3.6). As seen in **Figure 3.6**, experiments displayed dynamic behaviours that had to be accounted for in data processing. Each experiment initially underwent a transient period before reaching steady state. To obtain data for the kinetic study, AcOH and H<sub>2</sub>O conversions were taken only from the steady state period, typically starting around 600s after the start of each run.

**Figure 3.6** also shows fluctuations in the composition of the product gas, even during the ‘steady state’ period. This was caused by intermittent (dripping) flow from the syringe pump at low flow rates. The flow rates could not be increased further, as tests showed that this led to low conversions and high carbon deposition. Instead, the fluctuations were minimised by using feed tubing with the smallest diameter available (1/16 in. OD).

Nonetheless, some fluctuations still occurred, further emphasised by the short sample time (5s). In data processing, it was assumed that the conversion was an average of the measured fluctuations. The conversion was found by taking the mean of the values over the selected steady state time period. In each case, the standard deviation of the readings was calculated and found to be ≤6% of the mean value.

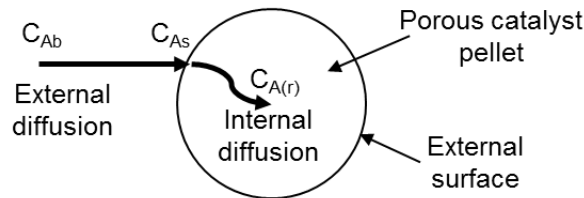
## 3.6 Determination of reaction kinetics

The aim of the kinetic study was to obtain kinetic parameters to describe the reactions involved in the steam reforming of the bio-model compound acetic acid on the Ni-Ca/Al<sub>2</sub>O<sub>3</sub> catalyst used previously in studies of CLSR and SE-CLSR of acetic acid in a packed bed reactor configuration [270–272]. As such, the conversion data from the lab-scale reactor had to undergo further analysis and parameter fitting. The steps in this analysis are outlined in the following sections.

### 3.6.1 Mass transfer limitations

To obtain an accurate estimate of reaction kinetics, it is necessary to ensure that the measured data represent only the rate of chemical reaction, and are not affected by transport phenomena.

In heterogeneous catalysis, the reaction sequence consists of a number of steps. First, mass transfer occurs from the bulk fluid to the external surface of the particle (external diffusion). Second, reactants diffuse from the external surface and through the pores of the catalyst particle (internal diffusion). Once the reactants reach the catalytic surface of the pores, they undergo chemical reaction. The steps are illustrated in **Figure 3.7** for a spherical particle (or pellet).



**Figure 3.7 – Mass transfer and reaction steps for a spherical catalyst particle [252]**

To obtain kinetic data it is necessary to ensure that mass transfer steps do not affect the measured rate, i.e. chemical reaction is the rate-limiting step. To verify that the experiment is operating in a region of kinetic control, the effects of mass transfer can be quantified using the criteria detailed below.

#### 3.6.1.1 External mass transfer

The Mears criterion was used to examine external diffusion [252]. According to this criterion, mass transfer from the bulk gas phase to the particle's external surface can be neglected when the following equation is satisfied:

$$\frac{-r_A \rho_{bed} R n}{k_c C_{Ab}} < 0.15 \quad \text{Eq. 3.50}$$

where the symbols are defined as follows:

- $-r_A$  Measured rate of reaction,  $\text{mol kg}_{\text{cat}}^{-1} \text{s}^{-1}$
- $\rho_{bed}$  Bulk density of catalyst bed,  $\text{kg m}^{-3}$ .
- $R$  Catalyst particle radius, m
- $n$  Reaction order
- $k_c$  Mass transfer coefficient,  $\text{m s}^{-1}$
- $C_{Ab}$  Bulk reactant concentration,  $\text{mol m}^{-3}$

The mass transfer coefficient  $k_c$  can be found by using a relevant correlation. In this case, the Ranz and Marshall equation for mass transfer in laminar flow around a sphere was used [275]:

$$k_c = \frac{D_{AcOH,N_2} Sh}{d_p} \quad \text{Eq. 3.51}$$

where  $D_{AcOH,N_2}$  is the molecular diffusivity of AcOH in  $N_2$  in  $m^2 s^{-1}$ , and  $d_p$  is the particle diameter.  $Sh$  is the Sherwood number, defined as:

$$Sh = 2 + 0.6Re^{1/2}Sc^{1/3} \quad \text{Eq. 3.52}$$

$Re$  is the Reynolds number for a packed bed and  $Sc$  is the Schmidt number:

$$Re = \frac{d_p u_s \rho_g}{\mu} \quad \text{Eq. 3.53}$$

$$Sc = \frac{\mu_g}{\rho_g D_{AcOH,N_2}} \quad \text{Eq. 3.54}$$

where  $d_p$  is the particle diameter,  $u_s$  is the superficial velocity.  $\rho_g$  is the gas density, and  $\mu_g$  is gas viscosity.

$D_{AcOH,N_2}$  is the molecular diffusivity of AcOH in  $N_2$ , where  $N_2$  represents the bulk gas mixture's dominant species, calculated as follows [276]:

$$D_{AcOH,N_2} = \frac{1.00 \times 10^{-3} T^{1.75} \left( \frac{1}{M_{AcOH}} + \frac{1}{M_{N_2}} \right)^{1/2}}{P \left[ (\sum_{AcOH} v_i)^{1/3} + (17.9)^{1/3} \right]^2} \quad \text{Eq. 3.55}$$

$M_{AcOH}$  and  $M_{N_2}$  are the molar mass of acetic acid and nitrogen respectively.  $P$  is the system pressure, in atmospheres.  $v_i$  are the special atomic diffusion volumes given in [276], which are summed over the atoms, groups and structural features of the diffusing species.

### 3.6.1.2 Internal mass transfer

One way to quantify mass transfer effects is the effectiveness factor, a ratio that signifies the relative importance of mass transfer and reaction limitations [252]. The internal effectiveness factor  $\eta$  focusses on the internal diffusion:

$$\eta = \frac{\text{Actual overall rate of reaction}}{\text{Rate of reaction that would result if entire interior surface were exposed to the external particle's surface conditions } C_{As}, T_s}$$

$$\eta = \frac{-r_A}{-r_{As}} \quad \text{Eq. 3.56}$$

when  $\eta$  is close to 1, this signifies that internal diffusion has a minimal effect on the overall rate, i.e. internal diffusion is not limiting.

Another parameter is the Thiele modulus, which describes the ratio of surface reaction rate to diffusion rate. The Thiele modulus for a reaction with order  $n$  is defined as:

$$\phi_n^2 = \frac{k_n R^2 C_{As}^n}{D_e C_{As}} \quad \text{Eq. 3.57}$$

where  $k_n$  is the rate constant,  $R$  is the particle radius, and  $C_{As}$  is the concentration of a species A (e.g. acetic acid) at the external surface.  $D_e$  is the effective diffusivity, calculated as follows:

$$D_e = \frac{D_{AcOH,N_2} \varepsilon_p \sigma_c}{\tau} \quad \text{Eq. 3.58}$$

$\varepsilon_p$  is the particle porosity,  $\sigma_c$  is the constriction factor and  $\tau$  is tortuosity. A large Thiele modulus signifies that internal diffusion is limiting the reaction, whereas a small Thiele modulus ( $\phi_n \ll 1$ ) suggests that the surface reaction is rate-limiting. For a first order reaction, the internal effectiveness factor  $\eta$  can be expressed as a function of the Thiele modulus  $\phi_n$ :

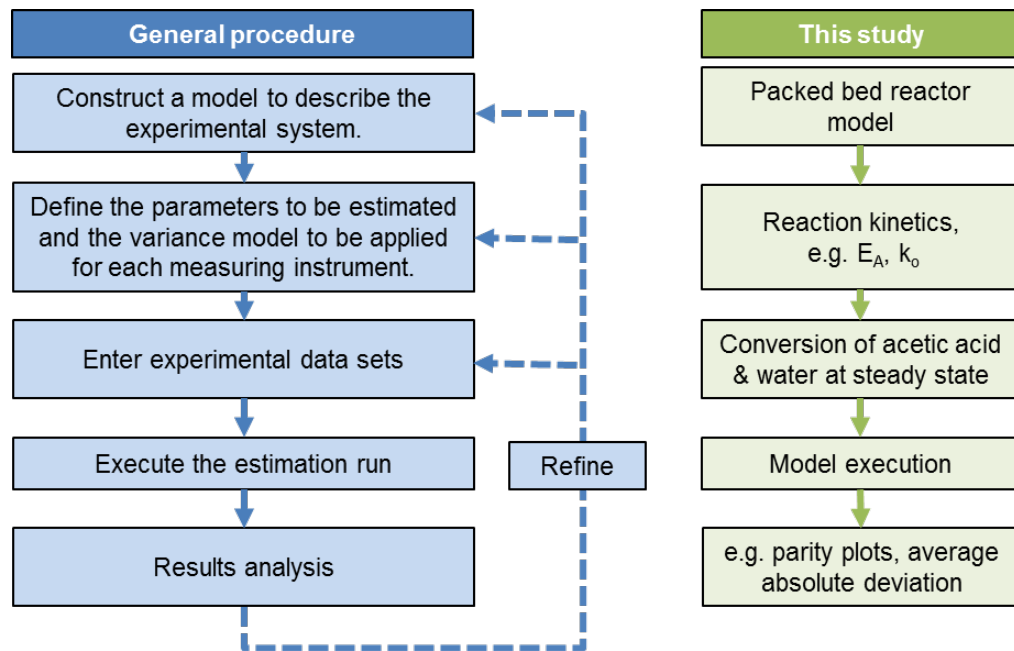
$$\eta = \frac{3}{\phi_1^2} (\phi_1 \coth \phi_1 - 1) \quad \text{Eq. 3.59}$$

To evaluate the effect of internal diffusion, the Weisz-Prater parameter  $C_{WP}$  was used [252]. The Weisz-Prater criterion states that internal diffusion is not limiting when the Weisz-Prater parameter is very small, i.e. when  $C_{WP} \ll 1$ .  $C_{WP}$  is a function of effectiveness factor and Thiele modulus:

$$C_{WP} = \eta \phi_1^2 = \frac{-r_A \rho_c R^2}{D_e C_{As}} \quad \text{Eq. 3.60}$$

### 3.6.2 Parameter fitting

Kinetic parameters of the reactions at work during the steam reforming of acetic acid were calculated using the parameter estimation facility in gPROMS. This facility enables the user to estimate a set of unknown parameters, such as kinetic data, by fitting model predictions to measured reality. **Figure 3.8** outlines the steps in the parameter estimation procedure.



**Figure 3.8 – Procedure for parameter estimation in gPROMS.**  
Adapted from [277]

During set-up, the user describes the system with a mathematical model, defines which parameters are to be estimated, and enters a set of experimental data. **Chapter 5** gives further detail of the modelling approach used to describe the experimental system. To account for experimental error, the user also defines the variance model for the measuring instruments [264]. This can be either:

- Constant variance, such as a thermocouple with accuracy  $\pm 1^\circ\text{C}$ ;
- Constant relative variance, such as a gas concentration analyser with error  $\pm 5 \text{ vol}\%$ ; or
- Heteroscedastic variance, which combines both of the above.

Based on this information, gPROMS uses advanced mathematical analysis to determine unknown parameters. It uses a ‘maximum likelihood’ approach. This seeks to determine values that maximise the probability that the mathematical model will predict measured values. This maximum likelihood goal is described by an objective function [264]:

$$\Phi = \frac{N}{2} \ln(2\pi) + \frac{1}{2} \min_{\theta} \left\{ \sum_{i=1}^{NE} \sum_{j=1}^{NV_i} \sum_{k=1}^{NM_{ij}} \left[ \ln(\sigma_{ijk}^2) + \frac{(\hat{z}_{ijk} - z_{ijk})^2}{\sigma_{ijk}^2} \right] \right\} \quad \text{Eq. 3.61}$$

where the symbols are defined as follows:

- $N$  Total number of measurements taken during all experiments
- $\theta$  Model parameters to be estimated. Acceptable values may be subject to lower and upper bounds,  $\theta^l < \theta < \theta^u$
- $NE$  Number of experiments performed



$NV_i$	Number of variables measured in the $i^{\text{th}}$ experiment
$NM_{ij}$	Number of measurements of the $j^{\text{th}}$ variable in the $i^{\text{th}}$ experiment
$\sigma_{ijk}^2$	Variance of the $k^{\text{th}}$ measurement of variable $j$ in experiment $i$ , determined by the measured variable's variance model
$\tilde{z}_{ijk}$	$k^{\text{th}}$ measured value of variable $j$ in experiment $i$
$z_{ijk}$	$k^{\text{th}}$ (model-) predicted value of variable $j$ in experiment $i$

## Chapter 4 – Thermodynamic analysis of advanced reforming of bio-oil

### 4.1 Introduction

**Chapter 2** introduced advanced techniques, such as sorption enhancement and chemical looping, that could improve the steam reforming process. This chapter explores how these techniques may be applied to the steam reforming of bio-oil, using thermodynamic analysis to assess theoretical energy flows, purities and yields of products.

Early studies such as those by Fathi et al. [30] and Rydén et al. [29] demonstrated the feasibility of methane-based chemical looping steam reforming (CLSR). Over 700 OTMs have since been developed and tested for combustion and reforming [26], aiming to produce materials with high catalytic activity and stability [31–34].

The CLSR concept has also been applied to alternative fuels from bioenergy sources, including glycerol [35,36], waste lubricating oil [37], and bioethanol [39]. This also includes the CLSR of bio-oil and its model compounds on nickel-based OTMs [38,123,270]. Recent work has demonstrated the performance of acetic acid in sorption-enhanced CLSR (SE-CLSR), as a model compound for bio-oil [271]. Over 20 successive cycles at 650°C, the yield remained above 78% of the equilibrium value.

These results suggest that there is an opportunity to combine advanced reforming techniques with bio-based feedstocks. The advantages of advanced reforming techniques, such as improved yields, efficiencies and flexibility of scale, could strengthen the technical and economic case for the uptake of alternative feedstocks. However, further work is required to understand the viability of such a process.

In this chapter, a thermodynamic analysis is carried out to evaluate hydrogen production from bio-oil. Thermodynamic analysis is an informative tool used to evaluate key process parameters such as equilibrium yields, conversions and the energy balance. It is a first step towards more realistic, dynamic models, capable of simulating real processes in detail.

Thermodynamic analysis is also to support experimental studies, by calculating equilibrium yields at experimental conditions [125,126,128]. This technique has been used to investigate advanced reforming of several feedstocks, including methane [41,155], shale gas [278] and glycerol [279].

Thermodynamic analysis has also been carried out on bio-oil model compounds in conventional steam reforming, SE-SR and CLSR [194,218,269,280]. For example, a thermodynamic analysis on acetic acid steam reforming by Goicoechea et al. [269] found that, for a steam-to-fuel ratio of 2 (equivalent to a S/C ratio of 1), the maximum hydrogen production was achieved at 700°C and pressure of 1 bar. The parameter with the highest influence was temperature, followed by S/C ratio and pressure. Vagia and Lemonidou [193] suggested that the optimum conditions are 630°C, atmospheric pressure and S/C ratio of 3. They also showed that the effects of elevated pressure can be managed by using high temperatures.

Tian et al. [218] used Aspen Plus to simulate SR and SE-SR of acetic acid. The models were used to carry out an exergy analysis, which found that the exergy efficiencies were 61.8% and 66.8% for acetic SR and SE-SR respectively. In both cases, the largest exergy destruction was in the burner, where around 32% of the exergy is destroyed. Udomchoke et al. [281] investigated a three-reactor SE-CLSR process for corn stover bio-oil. This included a modification to the process in which a fraction of the solids stream is recirculated from the air reactor back to the reforming reactor. Their results suggested that the modification led to a higher hydrogen yield and hydrogen purity, although the conversion of bio-oil was reduced. The thesis of Cheng includes a thermodynamic analysis of CLSR of a number of bio-compounds in a nickel-based system [280].

Two opportunities have been identified to improve understanding of the advanced reforming of bio-oil. First is the study of SE-CLSR in a packed bed configuration, which has not previously been examined for bio-oil. Second is the modelling of bio-oil as a mixture of compounds, rather than a single model compound, to give a more realistic assessment of its potential. This chapter examines three feedstocks relating to bio-oil: a bio-oil surrogate mixture, and two model compounds. The steam reforming techniques studied include conventional steam reforming (C-SR), sorption-enhanced steam reforming (SE-SR), chemical looping steam reforming (CLSR), and sorption-enhanced chemical looping steam reforming (SE-CLSR).

Thermodynamic analysis is applied to evaluate an approximate energy balance of bio-oil reforming processes, as well as the hydrogen yield, product purity, and potential for carbon deposition. The autothermal operation of SE-CLSR is assessed, to identify opportunities for optimisation. Given the high oxygen content of bio-oils and lower calorific value, there are

two important questions relating to the viability of cyclical operation. First is whether sufficient heat can be generated by the unmixed oxidation of the bio-oil surrogate mixture and the two model compounds to supply the heat demand for steam reforming. A further consideration is the effect of large quantities of CO<sub>2</sub> generated, and whether the amount of sorbent required could overwhelm the heat balance.

## 4.2 Methodology

### 4.2.1 Process description

In conventional steam reforming (C-SR), a hydrocarbon or other organic feedstock reacts with steam to produce hydrogen and carbon dioxide (R1 to R3 in **Table 4.1**). In industry, the reaction typically occurs in two reactor stages: a reforming stage and a WGS stage. The reforming reactor performs the endothermic R1 at high temperature, producing syngas. The WGS (in one or two reactors) reduces the carbon monoxide content via the exothermic R2, increasing H<sub>2</sub> yield and purity [59]. This study focusses on the high temperature reforming stage.

Three advanced reforming processes are also considered: chemical looping steam reforming (CLSR), sorption-enhanced steam reforming (SE-SR), and sorption-enhanced chemical looping steam reforming (SE-CLSR).

In CLSR, an oxygen transfer material (OTM), typically a metal oxide, provides oxygen for partial oxidation of the fuel (R9). In its reduced form, the OTM acts as a catalyst for the reforming reaction, so that feedstock oxidation in the absence of air occurs simultaneously with reforming. The release of heat from feedstock oxidation reduces energy demand, so that the reformer may be autothermal, and no longer requires indirect heating from a furnace. The OTM provides oxygen in an undiluted form, thereby eliminating the need for costly air separation [282]. It is closely related to other chemical looping processes proposed for hydrogen production, such as steam reforming with chemical looping combustion (SR-CLC), or chemical looping water splitting [26,283–286].

In SE-SR, the steam reforming reactions are enhanced by the addition of a solid CO<sub>2</sub> sorbent [203]. The sorbent removes CO<sub>2</sub> from the reactor, enhancing purity and enabling in situ CO<sub>2</sub> capture. At the same time, it shifts the chemical equilibria of both steam reforming and water gas shift, thereby improving feedstock conversion and hydrogen yield and thus further improving H<sub>2</sub> purity. The advantages of sorption enhancement and chemical

looping can be combined into SE-CLSR, to give high purity hydrogen in an autothermal process [41,168,171,278].

OTMs are typically comprised of a metal oxide such as Cu, Fe<sub>2</sub>O<sub>3</sub>, NiO, or Mn<sub>3</sub>O<sub>4</sub> supported on an inert material such as Al<sub>2</sub>O<sub>3</sub>, MgAl<sub>2</sub>O<sub>4</sub>, SiO<sub>2</sub>, TiO<sub>2</sub> or ZrO<sub>2</sub> [75]. Nickel-based OTMs are the most extensively analysed in literature [26]. They have the crucial advantage in packed bed configuration of being the catalysts with best combination of activity for steam reforming and low cost in their reduced, metallic form, which is why nickel based catalysts are the preferred catalysts in the steam reforming industry [287]. Studies with methane and Ni/NiO have demonstrated high reactivity and stability at high temperatures, as well as high selectivity towards hydrogen production [33,75,167,168]. A range of sorbents have also been studied, including MgO, hydrotalcite, Li<sub>2</sub>O<sub>3</sub> and alkaline ceramics. CaO has been identified as a promising sorbent with high capacity and low cost, although long-term stability remains a challenge [156,288]. On the basis of the literature review, the OTM selected for study is Ni/NiO. The selected CO<sub>2</sub> sorbent is CaO<sub>(s)</sub>.

In these processes, steam reforming occurs alongside reactions of the OTM and sorbent. In addition, a number of reactions lead to coke formation [289].

**Table 4.1** shows the generalised reaction scheme for an organic compound  $C_nH_mO_k$ .

**Table 4.1 - Main reactions in sorption-enhanced and chemical looping reforming of an organic compound  $C_nH_mO_k$**

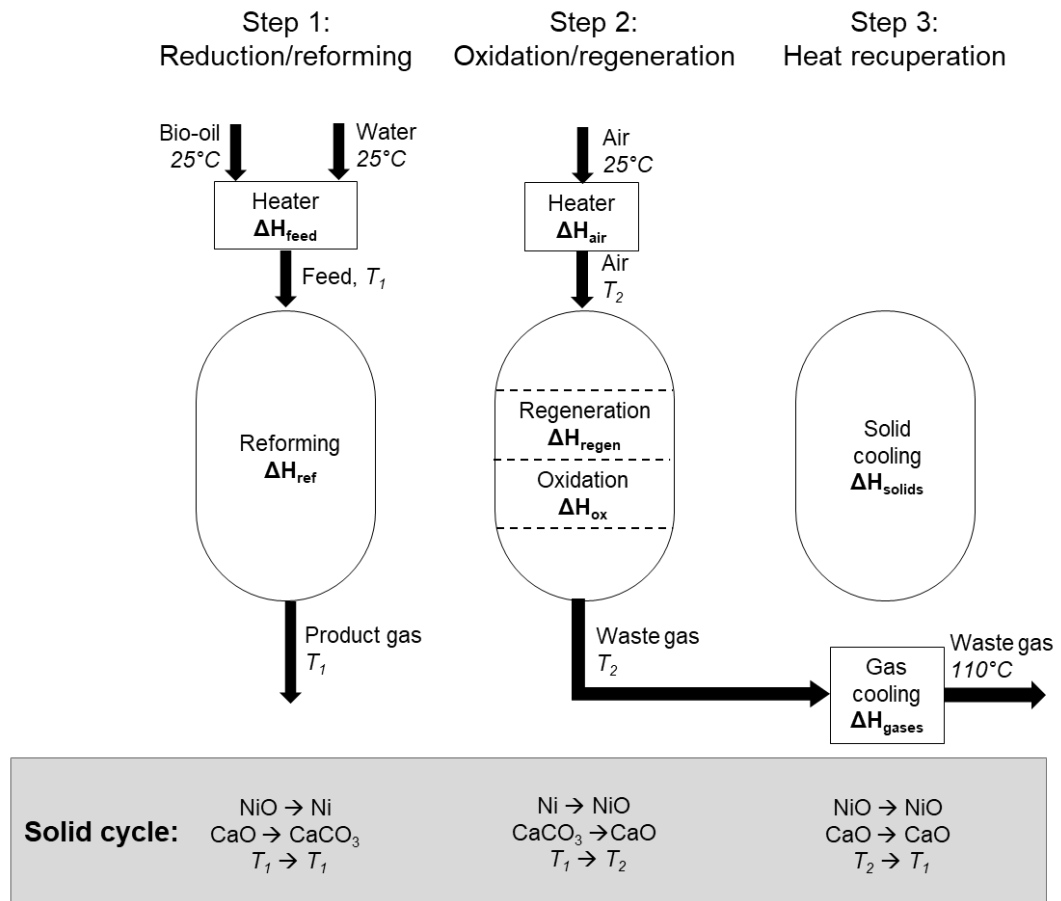
No.	Reaction	Description
R1	$C_nH_mO_k + (1 - k)H_2O \leftrightarrow nCO + (\frac{m}{2} - k + 1)H_2$	Steam reforming
R2	$CO + H_2O \leftrightarrow CO_2 + H_2$	Water gas shift
R3	$C_nH_mO_k + (2n - k)H_2O \leftrightarrow nCO_2 + (2n + \frac{m}{2} - k)H_2$	Global steam reforming
R4	$CO + 3H_2 \leftrightarrow CH_4 + H_2O$	Methanation
R5	$CO_2 + 4H_2 \leftrightarrow CH_4 + 2H_2O$	Methanation
R6	$CaO_{(s)} + CO_2 \leftrightarrow CaCO_{3(s)}$	Carbonation of $CaO_{(s)}$
R7	$CaO_{(s)} + H_2O \leftrightarrow Ca(OH)_{2(s)}$	Hydration of $CaO_{(s)}$
R8	$C_nH_mO_k + (2n - k)H_2O + nCaO \rightarrow nCaCO_3 + (2n + \frac{m}{2} - k)H_2$	Sorption-enhanced steam reforming
R9	$C_nH_mO_k + (2n - k)NiO \rightarrow (2n - k)Ni + nCO_2 + \frac{m}{2}H_2$	NiO reduction/ fuel combustion
R10	$C_nH_mO_k + (n - k)NiO \rightarrow (n - k)Ni + nCO + \frac{m}{2}H_2$	NiO reduction/ fuel partial oxidation
R11	$C_nH_mO_k + (n - \frac{2k}{3})NiO + (n - \frac{k}{3})H_2O \rightarrow (n - \frac{2k}{3})Ni + nCO_2 + (n + \frac{m}{2} - \frac{k}{3})H_2$	CLSR (NiO reduction + steam reforming)
R12	$C_nH_mO_k + (n - \frac{2k}{3})NiO + (n - \frac{k}{3})H_2O + nCaO \rightarrow (n - \frac{2k}{3})Ni + nCaCO_3 + (n + \frac{m}{2} - \frac{k}{3})H_2$	SE-CLSR (NiO reduction + sorption-enhanced steam reforming)
R13	$Ni_{(s)} + 0.5O_2 \rightarrow NiO_{(s)}$	Oxidation of Ni
R14	$C_nH_mO_k \leftrightarrow C_xH_yO_z + gases (H_2, H_2O, CO, CO_2, CH_4 \dots) + coke$	Thermal pyrolysis reaction
R15	$2CO \leftrightarrow CO_2 + C$	Boudouard reaction
R16	$CO + H_2 \leftrightarrow C + H_2O$	Coke formation from CO
R17	$CH_4 \leftrightarrow C + 2H_2$	Coke formation from $CH_4$

To enable regeneration of sorbent and re-oxidation of the OTM, these processes are cyclical. The cycle steps can occur in a series of fluidised beds, or within a packed bed with sequenced flows [75,160]. Simplified

process flow diagrams of SE-SR, CLSR and SE-CLSR in a packed bed have previously been illustrated in S G Adiya et al [278].

## 4.2.2 Energy balance

**Figure 4.1** illustrates the main components in the energy balance for the SE-CLSR process. As well as the heat associated with reactions, the balance also includes heating of reactants, and heat recuperation from the solids and waste gases.



**Figure 4.1 - Schematic description of SE-CLSR, showing key energy terms and temperature assumptions.**

In C-SR, SE-SR and CLSR, the absence of OTM or sorbent was modelled by setting the flow of the corresponding stream to zero.

The  $\Delta H$  terms were based on the definitions given in [278]. In this study, they are defined as:

$\Delta H_{\text{feed}}$  is the enthalpy change required to raise liquid reactants from 25°C to reforming temperature ( $T_1$ ).

$\Delta H_{\text{ref}}$  is the enthalpy associated with the reactions in the reduction/reforming step, occurring isothermally at  $T_1$ .

$\Delta H_{\text{regen}}$  is the enthalpy associated with sorbent regeneration, including the heating of the sorbent from  $T_1$  to  $T_2$ , and the enthalpy of reaction. For a

1.013 bar system, the regeneration temperature was set at 897°C. For higher pressure systems, the temperature was raised to ensure full regeneration of the sorbent.  $T_2$  is 967°C, 1027°C and 1147°C for a 5 bar, 10 bar and 30 bar system respectively.

$\Delta H_{air}$  is the enthalpy change required to heat air from 25°C to regeneration/oxidation temperature ( $T_2$ ).

$\Delta H_{ox}$  is the enthalpy released by oxidation of Ni, at  $T_2$ . Where there is solid carbon present in the equilibrium products,  $\Delta H_{ox}$  also includes the oxidation of this carbon.

$\Delta H_{solids}$  is the enthalpy change associated with heating or cooling the regenerated solids (NiO and CaO) from  $T_2$  to reformer temperature ( $T_1$ ), so that they are returned to the starting point of the next cycle.

$\Delta H_{gas}$  is the heat recuperated from cooling the waste gas from step 2. This includes unreacted  $N_2$  from the air, and the  $CO_2$  released by sorbent regeneration. Gases are cooled from  $T_2$  to 110°C.

$\Delta H_{total}$  is the overall energy balance, calculated as the sum of all the energy terms.

For C-SR:

$$\Delta H_{total} = \Delta H_{feed} + \Delta H_{ref} \quad \text{Eq. 4.1}$$

For SE-SR:

$$\Delta H_{total} = \Delta H_{feed} + \Delta H_{ref} + \Delta H_{regen} + \Delta H_{solids} + \Delta H_{gases} \quad \text{Eq. 4.2}$$

For CLSR:

$$\Delta H_{total} = \Delta H_{feed} + \Delta H_{ref} + \Delta H_{air} + \Delta H_{ox} + \Delta H_{solids} + \Delta H_{gases} \quad \text{Eq. 4.3}$$

For SE-CLSR:

$$\Delta H_{total} = \Delta H_{feed} + \Delta H_{ref} + \Delta H_{air} + \Delta H_{ox} + \Delta H_{regen} + \Delta H_{solids} + \Delta H_{gases} \quad \text{Eq. 4.4}$$

Where a unit was exothermic, this was signified by a negative energy term. Where  $\Delta H_{total}$  was equal to or less than zero, the process as a whole is autothermal.

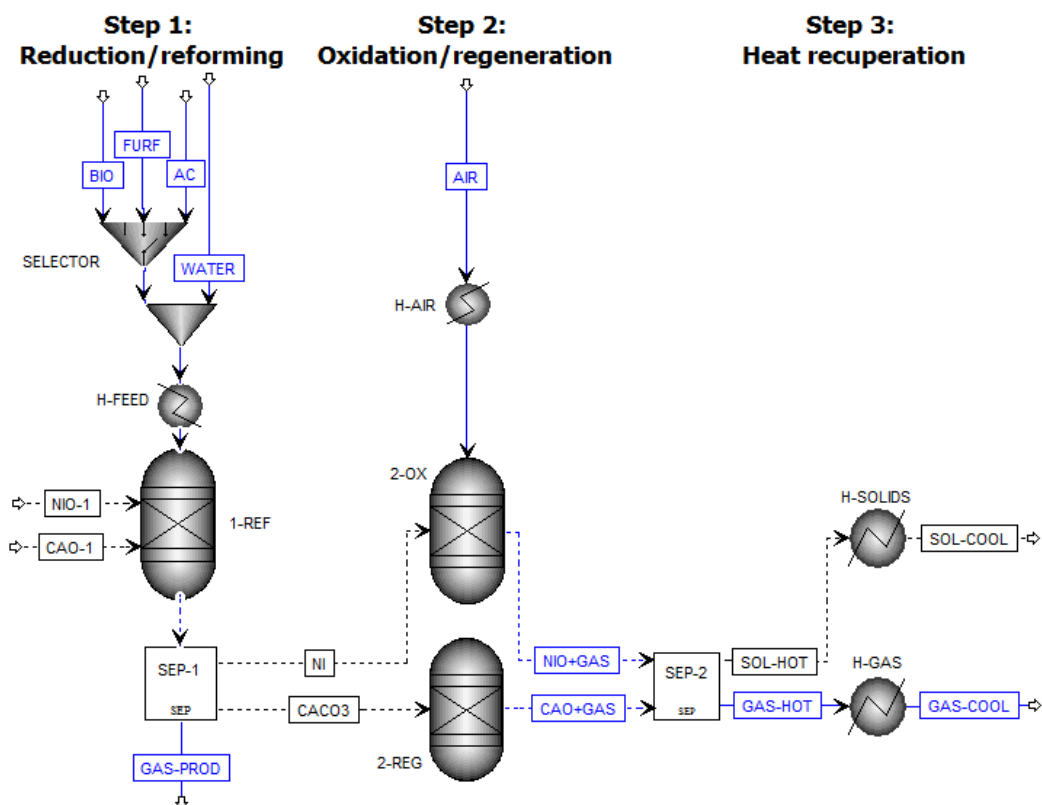
An Aspen Plus simulation was used to calculate the terms in the energy balance. Reactors were modelled using RGibbs reactor blocks, which calculate thermodynamic equilibrium by the minimisation of Gibbs free energy (**Section 3.2.2**).

The Aspen Plus flowsheet is shown in **Figure 4.2**. A series of reactors and heat exchangers was used to represent the cycle stages. A combination of gaseous reactants and solids entered each reactor. Both the solids and the



gases exited the reactor, before the stream was separated into solid and gaseous products by a separator block. The solid stream was connected to the next stage, while the gas flowed out as a product or waste gas. The second stage was represented as two reactors, so that oxidation and regeneration energy could be evaluated separately.

This flowsheet can represent either a circulating fluidised bed reactor (CFBR) or packed bed system. For a CFBR system, the reactors and streams represent different reactors and the movement of solids between them. For a packed bed system, the solid material streams do not represent the physical movement of solids between different reactors. Instead, the reactor blocks represent different stages (time intervals with different feed streams) within the same reactor. The solid material streams represent the retention of solids from one stage to the next, essentially modelling a ‘semi-batch’ process in which the solid reactants remain in the reactor.



**Figure 4.2 – Aspen Plus flowsheet for advanced reforming energy balances. Solid blue lines represent fluid streams, dashed blacked lines represent solid streams, and dashed blue streams represent mixed solids and fluids.**

To assess the potential for carbon deposition, solid carbon (graphite) was included as a component within Aspen Plus. Fluid inputs (organic feedstock, water, air) enter the system at 25°C, and at operating pressure. The energy balance did not include the energy required to raise the fluids to this pressure, or any other electrical or auxiliary energy. The flow of air was set

by a calculator block, which calculated the stoichiometric quantity of air required to completely oxidise the nickel. The composition of air was assumed as 79% N<sub>2</sub> and 21% O<sub>2</sub>.

Key process parameters are the feed molar steam-to-carbon (S/C) ratio, NiO to carbon (NiO/C) molar ratio and sorbent to feed carbon (CaO/C) molar ratio. The flow of steam, Ni and CaO were set using a calculator block, which multiplied the molar carbon flow by the relevant ratio. For S/C ratio, the calculation took account for the water content in the bio-oil:

$$n_{steam} = \left( \sum \alpha_i n_{C,bio-oil} \times S/C \right) - y_{H_2O} n_{bio-oil} \quad \text{Eq. 4.5}$$

where  $n_{steam}$  and  $n_{bio-oil}$  are the molar flow rates of steam and bio-oil respectively.  $S/C$  is the molar steam-to-carbon ratio,  $y_{H_2O}$  is the molar fraction of water in bio-oil,  $n_{C,bio-oil}$  represents the number of moles of carbon species in the bio-oil, and  $\alpha_i$  is the number of carbon atoms in the carbon species.

The hydrogen yield was expressed as wt% of the feedstock. As the bio-oil has a high moisture content (**Table 3.3**), the yield was expressed on a wet basis and moisture-free (m.f.) basis:

$$\begin{aligned} H_2 \text{ yield (wt\%, wet)} & \quad \text{Eq. 4.6} \\ & = \frac{n_{H_2} \times M_{H_2}}{n_{fuel,wet} \times M_{fuel,wet}} \times 100 \end{aligned}$$

$$\begin{aligned} H_2 \text{ yield (wt\%, m. f. )} & \quad \text{Eq. 4.7} \\ & = \frac{n_{H_2} \times M_{H_2}}{n_{fuel,m.f.} \times M_{fuel,m.f.}} \times 100 \end{aligned}$$

where  $n_{H_2}$  is the number of moles of hydrogen produced, and  $M_{H_2}$  is the molecular weight of hydrogen.  $n_{fuel,wet}$  represents the number of moles of fuel including moisture content, and  $M_{fuel,wet}$  is its molecular mass.  $n_{fuel,m.f.}$  is the number of moles of the organic fraction of the fuel, and  $M_{fuel,m.f.}$  is its molecular mass.

The yield was also expressed as a percentage of the theoretical potential from the SE-CLSR global reaction (R12):

$$\begin{aligned} \% \text{ stoich. potential} & \quad \text{Eq. 4.8} \\ & = \frac{\text{mol } H_2 \text{ produced}}{\text{mol } H_2 \text{ from SE-CLSR stoichiometry}} \times 100 \end{aligned}$$

Purity was calculated as the molar percentage of hydrogen in the product gas, on a dry basis:

$$H_2 \text{ purity (mol \%)} = \frac{n_{H_2,product}}{n_{total,product} - n_{H_2O,product}} \times 100 \quad \text{Eq. 4.9}$$

where  $n_{i,product}$  is the number of moles of component  $i$  in the product gas.

### 4.2.3 Feedstocks

Three different feedstocks were considered. This includes two model compounds, acetic acid and furfural, as well as a bio-oil surrogate mixture. Further details of these feedstocks are given in **Chapter 3**.

**Table 4.2** shows the key stoichiometric information for each feedstock in SE-CLSR (R12). Methane is also included for comparison, as it is a common steam reforming feedstock. The stoichiometry illustrates some key constraints, such as the potential hydrogen yield, required S/C ratio and appropriate quantities of OTM and sorbent.

**Table 4.2 –Stoichiometry for SE-CLSR of methane, bio-oil model compounds, and PEFB bio-oil surrogate mixture (Reaction 11)**

		CH <sub>4</sub>	Acetic acid	Furfural	PEFB bio-oil (moisture-free)
Composition (C <sub>n</sub> H <sub>m</sub> O <sub>k</sub> )	n	1	2	5	4.057
	m	4	4	4	4.977
	k	0	2	2	1.776
Molar mass (kg kmol <sup>-1</sup> )		16.05	60.06	96.09	82.17
Reactants (mol <sub>i</sub> mol <sub>feedstock</sub> <sup>-1</sup> )	NiO	1.000	0.667	3.667	2.873
	H <sub>2</sub> O	1.000	1.333	4.333	3.465
	CaO	1.000	2.000	5.000	4.057
Products (mol <sub>i</sub> mol <sub>feedstock</sub> <sup>-1</sup> )	Ni	1.000	0.667	3.667	2.873
	CaCO <sub>3</sub>	1.000	2.000	5.000	4.057
	H <sub>2</sub>	3.000	3.333	6.333	5.954
S/C ratio		1.000	0.667	0.867	0.854
NiO/C ratio		1.000	0.333	0.733	0.708
CaO/C ratio		1.000	1.000	1.000	1.000
mol <sub>H<sub>2</sub></sub> /mol <sub>carbon</sub>		3.000	1.667	1.267	1.468

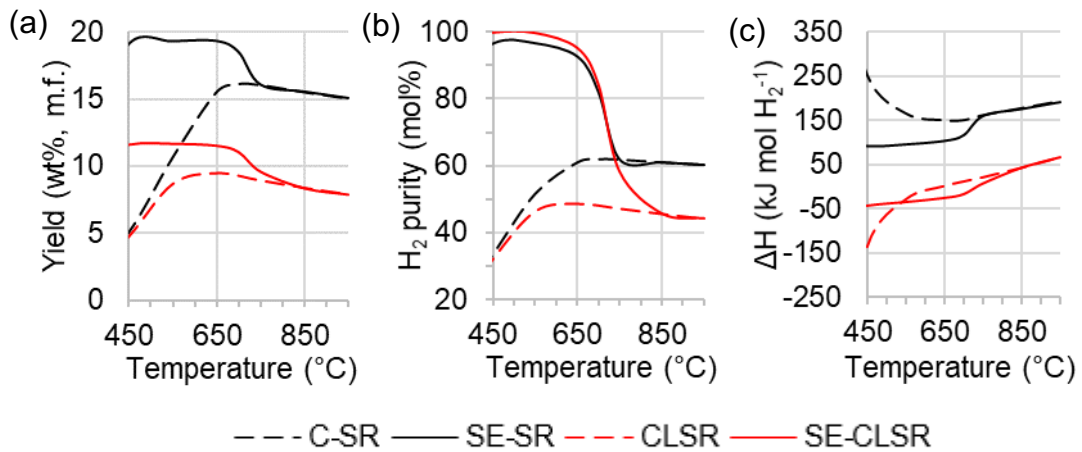
## 4.3 Results and discussion

### 4.3.1 Process comparison and effect of temperature

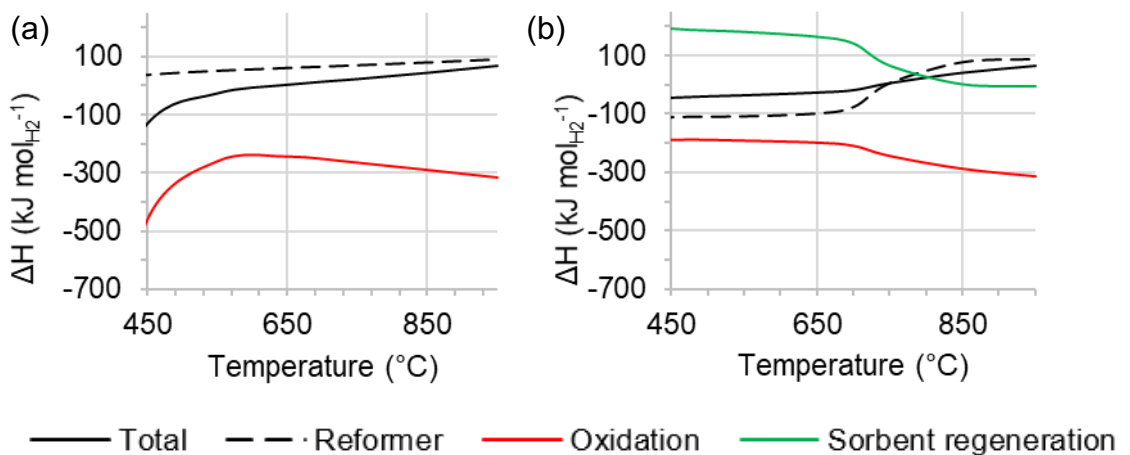
**Figure 4.3** shows the performance of each process over a range of temperatures and at atmospheric pressure. **Figure 4.3a** and **Figure 4.3b** indicate that the sorbent enhances the yield and purity of C-SR and CLSR, until the sorbent becomes ineffective at around 780°C. At certain temperatures, the sorption enhanced processes achieve purity over 99 mol%, while C-SR and CLSR only reach 60 mol% purity, and would require extensive downstream processing.

In SE-CLSR with S/C ratio of 2, maximum H<sub>2</sub> yield (11.7 wt%) is achieved at 823K, at which point the purity is 99.6 mol% H<sub>2</sub>, with 0.2 mol% CO<sub>2</sub>, 0.1 mol% CH<sub>4</sub> and 0.05 mol% CO. However, maximum purity (99.7 mol%) is achieved at 450°C, where yield is slightly lower than the maximum (11.6 wt%). The remaining 0.3% is methane, and other impurities are negligible (<1ppm). To reduce the requirement for downstream processing, the optimal operating point is likely to be the point of maximal purity, where yield will be slightly lower than the maximum.

As result of the enhanced yield, SE-SR has a lower net energy balance than C-SR, despite the requirement for heat to regenerate the sorbent (**Figure 4.3c**). At atmospheric pressure, SE-CLSR has a lower net energy balance than CLSR only between the range of around 500 – 700°C. This can be explained by the individual energy terms, shown in **Figure 4.4**. Below 550°C, the CLSR energy balance is dominated by the oxidation term. Both CLSR and SE-CLSR release the same quantity of heat in oxidation but CLSR has a very low yield in this region, so that the energy released per mole of H<sub>2</sub> is higher. While CLSR appears to have a thermodynamic advantage over SE-CLSR at this point, it is unlikely that the process would be operated in this region as the yield is low. Above around 780°C, the calcium sorbent becomes ineffective and so both CLSR and SE-CLSR have the same net energy balance. The design of advanced reforming processes should consider these interactions between yield and heating burden in order to find an optimal balance.



**Figure 4.3 - The effect of reduction/reforming temperature (T1) for PEFB bio-oil surrogate mixture in C-SR, CLSR, SE-SR and SE-CLSR with S/C ratio of 2 at 1.013 bar. For SE-SR and SE-CLSR, CaO/C = 1 and NiO/C = 1. (a) mass yield, moisture-free basis, (b) H<sub>2</sub> purity, (c) net process energy balance.**



**Figure 4.4 - The effect of reduction/reforming temperature (T1) on the main energy terms in advanced reforming of PEFB bio-oil surrogate mixture with S/C = 2 at 1.013 bar (a) CLSR, with NiO/C = 1 and CaO/C = 0, (b) SE-CLSR, with NiO/C = 1 and CaO/C = 1.**

The equilibrium yields for the PEFB bio-oil mixture are similar to yields observed in experimental studies. Remón et al. [222] measured steam reforming yields in the range of 10 to 18 wt% from various bio-oils at S/C = 7.6 and 650°C. At the same conditions, the C-SR equilibrium model gives 11.6 wt% m.f. For a real PEFB bio-oil, Zin et al. [290] measured a yield of 9.5 wt% m.f. with S/C = 2.75 at 600°C. Sorption enhancement increased the yield to 10.4 wt%, with H<sub>2</sub> purity of 97%. At the same conditions, the model gives 16.2 wt% m.f and 21.1 wt% m.f. in SR and SE-SR respectively. A direct comparison is not applicable as the molecular composition was

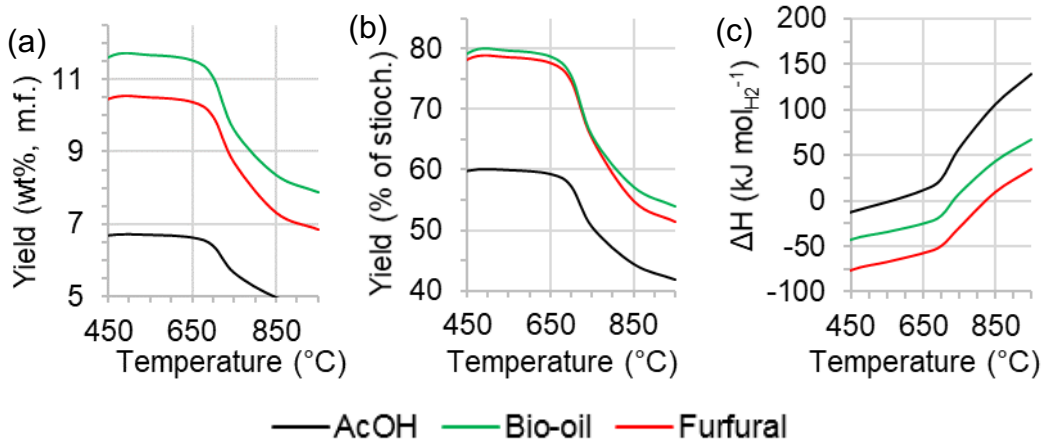
different in each case. Nonetheless, these figures indicate that the model gives predictions within a reasonable range.

Experimental demonstration of advanced reforming of bio-oil is more limited, but there is some evidence of model compounds achieving close to equilibrium yield in CLSR. In CLSR at 650°C, acetic acid achieved 7.13 wt%, or 61.27% of equilibrium yield, while furfural achieved 12.6 wt%, or 71.86% of equilibrium yield [280].

One limitation of thermodynamic analysis is that it does not represent the deactivation of OTM and sorbent over multiple cycles. Acetic acid has displayed stable performance over at least 10 successive cycles in CLSR and SE-CLSR, with carbon deposits being removed during the oxidation stage [270,271]. However, a whole bio-oil may display different deactivation behaviour. Catalyst stability is not within the scope of this study, but it is an important consideration for future work on process feasibility.

#### 4.3.2 Feedstock comparison in the SE-CLSR process

The previous section focussed on bio-oil surrogate mixture, but it is also useful to understand how common model compounds perform in the same analysis. **Figure 4.5** shows the yield and net energy balance for each feedstock in SE-CLSR.



**Figure 4.5 - The effect of reduction/reforming temperature (T1) in SE-CLSR of acetic acid, bio-oil and furfural at 1.013 bar with S/C = 2, NiO/C = 1, CaO/C = 1 (a) mass yield, moisture-free basis, (b) yield in % of stoichiometric potential from the SE-CLSR global reaction, (c) net process energy balance.  $\Delta H < 0$  signifies an exothermic process**

**Figure 4.5a** shows the mass yield, as this parameter is commonly used for reporting experimental results in bio-oil reforming. The mass yield from bio-oil peaks at 11.7 wt% m.f., while acetic acid achieves only 6.7 wt% m.f. This

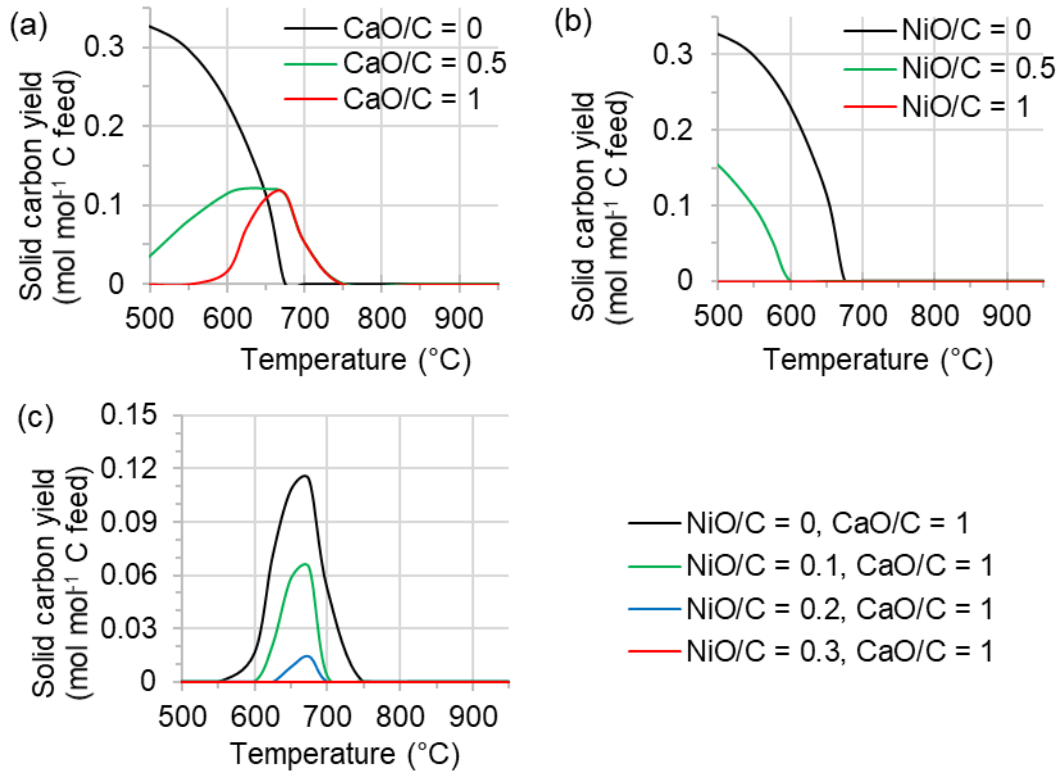
is explained by the stoichiometry in **Table 4.2**. Although bio-oil has a higher molar mass (i.e. a higher denominator), this is balanced by a high molar yield. When the stoichiometric yield is used (**Figure 4.5b**), bio-oil and furfural are closely matched due to the similarity in their chemical formula ( $C_nH_mO_k$ ), shown in **Table 4.2**. The behaviour of furfural more closely models that of the bio-oil, suggesting that it is a more suitable model compound for representing the performance of bio-oil.

**Figure 4.5c** shows the wide variation in net energy balance between the different feedstocks. At the range of conditions considered, the furfural energy balance is lower than that of bio-oil, by 32 to 37  $\text{kJ mol}_{\text{H}_2}^{-1}$ . The net energy balance for acetic acid is higher than that of bio-oil, by 30 to 72  $\text{kJ mol}_{\text{H}_2}^{-1}$ . In the optimal region, both model compounds are a similar distance from the bio-oil mixture. This highlights that variations in bio-oil composition could have a large impact on the energy balance, and the autothermal nature of the plant, so that feedstock variation would be an important factor in process design and control.

These results were generated using the same NiO/C ratio ( $\text{NiO/C} = 1$ ). In practice, each feedstock will have a different optimal NiO/C ratio, according to the reaction stoichiometry (**Table 4.2**). For example, acetic acid appears to be performing well beneath its stoichiometric potential in **Table 4.4b**, but this is because NiO/C of 1 represents a large excess of NiO above the required level (0.333). Thus, it is not appropriate to make a direct comparison of feedstocks at a single set of conditions. Instead, the process should be optimised, and the different optimal solutions compared. **Section 4.3.4** examines this optimisation.

### 4.3.3 Carbon deposition

At S/C ratio of 2 and above, the results showed no carbon deposition in bio-oil steam reforming. A high excess of steam inhibits carbon deposition and enables steam gasification of carbon deposits [278]. However, operating with a lower S/C ratio may be preferable as it reduces the process energy balance. **Section 4.3.4** contains further detail on the influence of S/C ratio on yield and energy balance. To understand the risk of carbon deposition at low S/C ratios, **Figure 4.6** shows solid carbon yields with  $\text{S/C} = 1$ .



**Figure 4.6 - Equilibrium carbon product in advanced reforming of PEFB bio-oil surrogate mixture with S/C = 1 at 1.013 bar (a) SE-SR, with NiO/C = 0, (b) CLSR, with CaO/C = 0, (c) SE-CLSR, with CaO/C = 1.**

In SE-SR, the presence of sorbent changes the limit for carbon deposition (**Figure 4.6a**). The upper temperature limit is increased, but a minimum temperature is also introduced, to give an envelope in which equilibrium carbon product occurs. As more sorbent is introduced, the lower limit increases so that the envelope for carbon deposition is narrowed. In SE-SR with a stoichiometric quantity of sorbent (CaO/C = 1), carbon deposition occurs between 550 °C and 700 °C. Previous thermodynamic studies have similarly found that carbon deposition is suppressed by CO<sub>2</sub> sorption, as the enhanced WGS reaction reduces CO content, and thereby shifts the equilibrium for the Boudouard reaction (R15) backwards [188,291].

**Figure 4.6b** shows the effect of OTM content in CLSR. Increasing the amount of NiO moves the temperature boundary for carbon, so that carbon is eliminated at lower temperatures. By increasing NiO/C to 1, carbon product is eliminated at any temperature over 450 °C. This is the result of introducing oxygen into the reactor, which enables the oxidation of carbon.

The combined effects of both OTM and sorbent in SE-CLSR are shown in **Figure 4.6c**. With CaO/C = 1, and S/C = 1, carbon product is eliminated with NiO/C of 0.3 or above. These results highlight a potential advantage of SE-



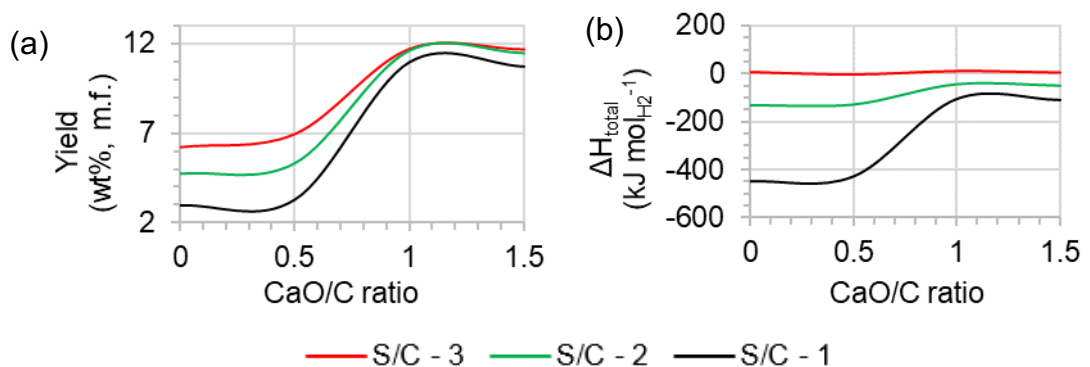
CLSR: by combining the effects of the sorbent and OTM, carbon can be suppressed to very low levels across a wide operating range.

#### 4.3.4 Optimisation and autothermal operation in SE-CLSR

The analysis has highlighted that the process is affected by several interacting parameters which should be considered together. As well as temperature and pressure, other key parameters for consideration are the ratios S/C, NiO/C and CaO/C. These parameters can be manipulated to enhance yield and purity, reduce energy demand and eliminate carbon deposition.

In this optimisation study of H<sub>2</sub> production from bio-oil, three parameters are initially fixed: pressure, temperature, and CaO/C ratio. According to Le Chatelier's principle, the reaction is favoured by low pressures, so the pressure is fixed at atmospheric pressure, 1.013 bar. Temperature is fixed at 450°C. The earlier analysis identified that this temperature maximises purity and gives close to maximum yield at this pressure.

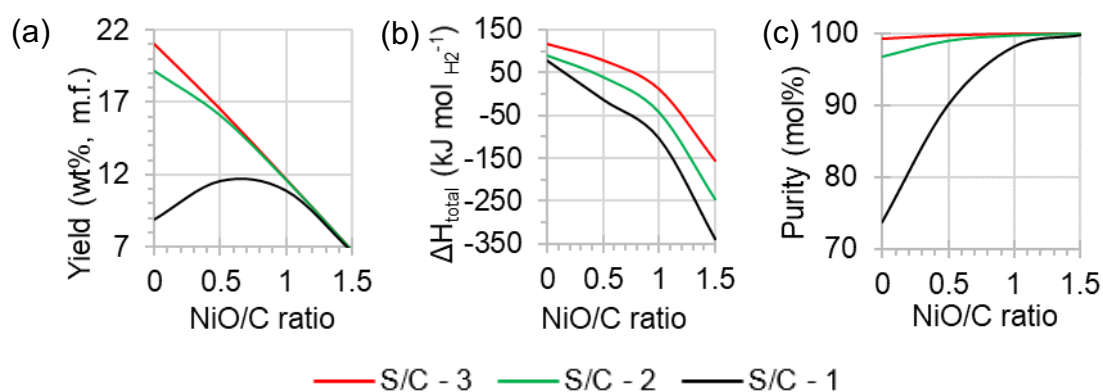
**Figure 4.7** shows the effect of the CaO/C ratio in SE-CLSR. According to the stoichiometry in **Table 4.2**, CaO/C = 1 provides enough sorbent to capture all of the CO<sub>2</sub>. Increasing CaO/C beyond this point does not increase the yield (**Figure 4.7a**), but simply increases the net energy balance and the expense associated with excess sorbent. For this reason, the amount of sorbent is fixed at CaO/C = 1.



**Figure 4.7 - Effect of CaO/C ratio in SE-CLSR of bio-oil at 1.013 bar, 450°C with NiO/C = 1. (a) mass yield, moisture-free basis, (b) net process energy balance.**

The effects of NiO/C ratio and S/C ratio are illustrated in **Figure 4.8**. **Figure 4.8b** shows that the net energy balance can be reduced by increasing NiO/C ratio, as more heat is released from the oxidation of fuel and Ni. Above a

certain NiO/C ratio, autothermal operation ( $\Delta H \leq 0$ ) is theoretically possible. However, the reduced energy balance comes at the cost of lower H<sub>2</sub> yield (**Figure 4.8a**). Similarly, lower S/C ratio reduces heat demand, but also decreases H<sub>2</sub> yield and purity. For S/C = 1, the purity is considerably reduced due to methanation. The selection of NiO/C and S/C ratios should balance the conflicting objectives.



**Figure 4.8 - Effect of NiO/C ratio in SE-CLSR of bio-oil at 1.013 bar, 450°C, with CaO/C = 1. (a) mass yield, moisture-free basis, (b) net energy balance, (c) hydrogen purity.**

**Table 4.3** shows the autothermal point for the bio-oil surrogate mixture, as well as the model compounds acetic acid and furfural at 450°C. In autothermal SE-CLSR of bio-oil, CO<sub>2</sub> and CO are reduced to a negligible level, so that downstream purification requirements are minimised.

A low quantity of steam (S/C = 1) allows a small NiO inventory in autothermal operation, but also supports methanation, so that H<sub>2</sub> purity is low and more than 12 mol% of the product gas is CH<sub>4</sub>. By increasing the S/C ratio to 2, autothermal operation can be achieved alongside a high yield (13.6 wt%) and minimal methanation.

When comparing feedstocks, it is notable that the optimal solution for a bio-oil mixture is different to that of the model compounds. As seen in earlier results, furfural is a closer match to bio-oil and thus is a more suitable model compound for understanding thermodynamic potential. However, process development should aim to consider realistic bio-oil mixtures wherever possible.

**Table 4.3 - Parameters for autothermal operation in SE-CLSR of bio-oil, acetic acid and furfural at 1.013 bar, 450°C, with CaO/C = 1. In all cases, solid carbon and CO are negligible (<1ppm)**

Feedstock	S/C	Minimum NiO/C	Yield (wt%, m.f.)	Yield (wt%, wet)	H <sub>2</sub> purity (mol%)	CO <sub>2</sub> (mol%)	CH <sub>4</sub> (mol%)
Bio-oil	3	1.050	11.2	8.51	99.95	0	0.054
	2	0.785	13.6	10.3	99.52	0	0.48
	1	0.419	11.3	8.59	87.91	0	12.1
Acetic acid	3	1.210	5.31	-	99.94	0.063	0
	2	0.949	7.04	-	99.99	0	0
	1	0.679	8.49	-	98.86	0	1.14
Furfural	3	0.940	11.1	-	99.91	0.019	0.076
	2	0.675	13.6	-	99.43	0.015	0.55
	1	0.267	9.22	-	80.36	0	19.6

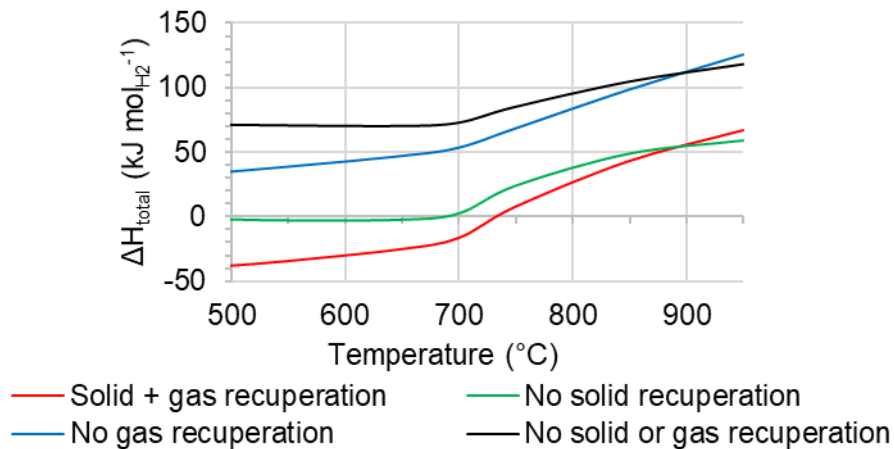
While it may be possible to design an autothermal process, this comes at the expense of a reduced yield (**Figure 4.8**). Hence the preferred operating regime will depend on whether autothermal operation is a priority, which will depend on plant-specific constraints such as required capacity, and the availability and cost of heat. Techno-economic analysis would be required to find the optimal solution for a given plant, but the above method of thermodynamic analysis could be a valuable starting point for such an evaluation.

#### 4.3.5 Heat recuperation

The analysis above assumes that usable heat is recovered from both solids and gases after the oxidation/regeneration stage. **Figure 4.9** shows the impact on the energy balance if the heat recuperation terms are not included. Recuperation of heat from the gas has the largest impact. The impact of heat recuperation from solids decreases when the temperature of reduction/reforming approaches the same temperature as regeneration/oxidation (900°C). When combined, both types of recuperation reduce the net energy balance by 60 to 115 kJ mol<sub>H<sub>2</sub></sub><sup>-1</sup>.

This highlights the importance of heat integration in SE-CLSR. As the process is cyclical, parts of the process are repeatedly heated and cooled, and there is the potential to waste a large amount of heat if process design does not consider heat integration. Previous work has highlighted that the

catalyst support can introduce a large additional heating burden [278], which would further increase the impact of heat recuperation from the solids.



**Figure 4.9 - Effect of heat recuperation in SE-CLSR of bio-oil at 1.013 bar, with S/C = 1, CaO/C = 1, NiO/C = 1.**

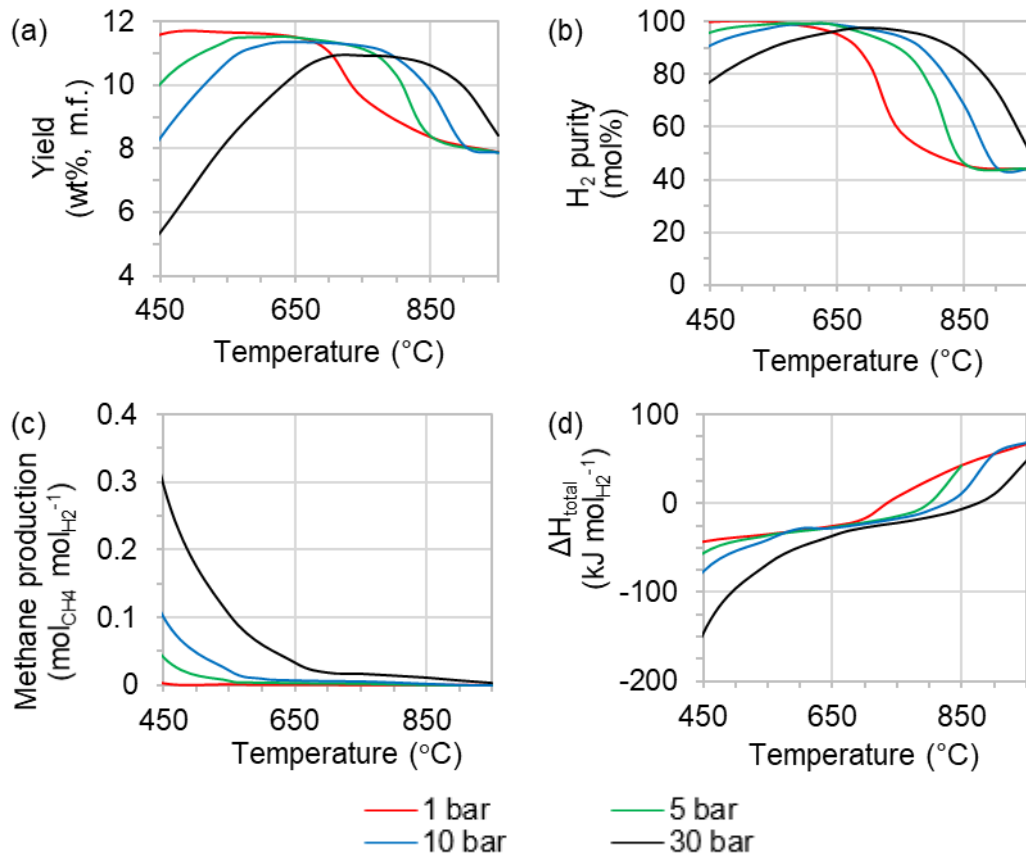
#### 4.3.6 The effect of pressure on SE-CLSR

Low pressure favours the production of hydrogen in the steam reforming reaction. However, industrial reforming processes are typically operated at higher pressures, in the region of 20 bar or higher, to enable efficient processing of large gas flows in reduced reactor and pipe volumes [89]. Figure 4.10a illustrates how the various reforming processes are affected by elevated pressures. As pressure is increased, the maximum H<sub>2</sub> yield is slightly decreased, and occurs at a higher temperature. At atmospheric pressure, the maximum yield is 11.6 wt% at 450°C. At 30 bar, the maximum yield is 10.9 wt% at 750°C (**Figure 4.10a**)

**Figure 4.10b** shows that purity over 90 mol% is achievable at all the studied pressures, due to the CO<sub>2</sub> sorbent. However, as pressure increases the maximum purity is lowered, and the region of maximum purity is narrowed. In a 30 bar system, H<sub>2</sub> purity peaks at 96.7 mol%. The main impurity is CH<sub>4</sub> (1.8 mol%), as the high pressure conditions are favourable for methanation (R4 and R5). The level of methanation is illustrated in **Figure 4.10c**.

To achieve a given H<sub>2</sub> yield, the high pressure system requires a higher reformer temperature. However, **Figure 4.10d** shows that the net process energy balance remains similar. In the low temperature region, higher pressure leads to more methanation (**Figure 4.10c**), which releases heat into the reformer. In the high temperature region, the energy balance is affected by the sorption reaction – as the sorbent becomes ineffective, it no

longer provides heat for sorption. This effect is observed at lower temperatures in low pressure systems.



**Figure 4.10 - Effect of pressure in SE-CLSR of bio-oil, with S/C = 2, NiO/C = 1, CaO/C = 1 (a) mass yield, moisture-free basis, (b) H<sub>2</sub> purity, (c) methane production, (d) net process energy balance.**

**Table 4.4** gives parameters for autothermal operation at elevated pressures. Autothermal operation remains a possibility at industrial reforming pressures, but the higher pressure leads to a higher NiO inventory, reduced yield, and more impurities.

**Table 4.4 - Parameters for autothermal operation in SE-CLSR of bio-oil at various pressures, with CaO/C = 1.  
In all cases, solid carbon yield is negligible.**

P (bar)	S/C (-)	T (°C)	Min. NiO/C	Yield (wt%, m.f.)	Yield (wt%, wet)	H <sub>2</sub> (mol%)	CO (mol%)	CO <sub>2</sub> (mol%)	CH <sub>4</sub> (mol%)
30	3	700	1.19	9.68	7.36	98.7	0.183	0.795	0.37
	2	700	0.87	11.8	8.95	96.9	0.197	0.346	2.57
	1	700	0.42	8.19	6.23	77.6	0.341	0.227	21.9
10	3	600	1.13	10.3	7.82	99.5	0.058	0.232	0.23
	2	600	0.84	12.6	9.55	98.3	0.047	0.094	1.60
	1	600	0.42	9.20	6.99	81.5	0.053	0.053	18.4
5	3	575	1.12	10.5	7.96	99.7	0	0.171	0.11
	2	575	0.83	13.0	9.85	99.1	0.046	0.092	0.78
	1	575	0.43	9.94	7.55	84.1	0.051	0.051	15.8

#### 4.4 Conclusion

In this thermodynamic study, conventional steam reforming (C-SR) is assessed alongside Sorption Enhanced Steam Reforming (SE-SR), Chemical Looping Steam Reforming (CLSR) and Sorption Enhanced Chemical Looping Steam Reforming (SE-CLSR). The selected CO<sub>2</sub> sorbent is CaO and oxygen transfer material (OTM) is Ni/NiO. PEFB bio-oil is modelled as a surrogate mixture and two common model compounds, acetic acid and furfural, are also considered. The operating regime of SE-CLSR is evaluated in order to assess the impact of S/C ratio, NiO/C ratio, CaO/C ratio and temperature.

The evaluation has demonstrated the potential of bio-oil steam reforming and highlighted the role of advanced reforming techniques in enhancing its performance. Sorption enhancement can increase hydrogen yield and purity, while also decreasing the net process energy balance. Chemical looping reduces the net energy balance, although hydrogen yield is reduced due to the partial oxidation of the feedstock. When both techniques are combined in SE-CLSR, bio-oil can be converted to hydrogen in a process with purity over 99% and a low net energy balance.

A PEFB bio-oil surrogate mixture has been compared to model compounds acetic acid and furfural. Due to the similarity in molecular formula, furfural is a more representative model compound for whole PEFB bio-oil. The

comparison also highlighted that the feedstock has a considerable impact on process energy balance, and as such process design should consider the variability of bio-oil compositions.

The SE-CLSR of bio-oil can achieve autothermal operation with yields over 13 wt% and purity over 99.5 mol%, so that it may be possible to develop small bio-oil reforming plants which are energy self-sufficient and require minimal product purification. Autothermal operation is also achievable at industrial reforming pressures, although the product yield and purity are reduced. In autothermal operation at 30 bar, S/C ratio of 2 gives a yield of 11.8 wt%, and hydrogen purity of 96.9 mol%. Alternatively, if autothermal operation is not a priority, the yield can be improved by reducing the quantity of OTM. The recuperation of heat from solid materials and waste gases is a major contributor to the energy balance. Heat integration is therefore a key consideration for process development.

Carbon deposition is present when S/C ratio is low ( $S/C = 1$ ), but the risk of carbon product can be reduced by increasing the quantity of OTM or sorbent. The autothermal operating regimes for SE-CLSR showed no solid carbon in the equilibrium products.

Thermodynamic analysis demonstrates how advanced reforming techniques can improve the potential of bio-oil as a low carbon feedstock for hydrogen, in theory improving cost-effectiveness and flexibility of scale in low carbon hydrogen production. This study used a high-level overview of reactor thermodynamics, but further work is required to assess the feasibility of a real process, taking into account practical aspects such as kinetic constraints, and heat management. Economic constraints are another important consideration. The following chapters address some of these challenges through the use of techno-economic analysis and detailed reactor modelling.

## Chapter 5 – Techno-economic analysis of advanced reforming of bio-oil

### 5.1 Introduction

To date, the literature on bio-oil steam reforming has largely focussed on experimental studies that have tested a range of catalysts and operating conditions [118,122,179,272,292–295], as well as thermodynamic studies that seek to optimise reformer performance [191–194,221,224,296]. However, for hydrogen production from bio-oil to be realised at an industrial scale, it is important that future development is supported by techno-economic assessment of the process as a whole.

A number of authors have applied techno-economic assessment to the different upgrading pathways of bio-oil, including Fischer-Tropsch synthesis [198,297] and bio-oil upgrading [298,299], but a limited number focus on hydrogen production. In a 2014 study based in Canada, Brown et al [198] estimated the cost of hydrogen production from bio-oil steam reforming to be 3.25 to 5 \$ kg<sub>H<sub>2</sub></sub><sup>-1</sup>. A second study in Canada focused on the autothermal reforming route [68]. This analysis estimated hydrogen prices ranging from 2.40 to 4.55 \$ kg<sub>H<sub>2</sub></sub><sup>-1</sup>, with a carbon cost of 133 to 356 \$ t<sub>CO<sub>2,eq</sub></sub><sup>-1</sup>. Zhang et al. [199] carried out a techno-economic analysis that compared bio-oil steam reforming to gasification. The study concluded that reforming was the more cost-effective route, with lower capital costs and higher H<sub>2</sub> yields.

While there are some relevant techno-economic assessments in literature, there is scope for more detailed analysis, to identify areas of future research focus. In particular, it would be useful to have a quantitative analysis of how certain aspects of process design and operation could affect performance and cost. For example, a review by Trane et al. [119] highlights that many experimental studies have applied very high S/C ratios, in order to alleviate carbon deposition issues. However, the review also highlight that the high S/C ratios would increase cost. Another aspect to consider is operating pressure. The analysis in **Chapter 4** showed that low pressures lead to favourable thermodynamic performance. However, industrial steam reformers are typically operated at higher pressures to enable higher production flows and improve economies of scale [45]. A techno-economic study could quantify the effects of these operating parameters, in order to better understand the trade-offs, and aid decision-making for process development.

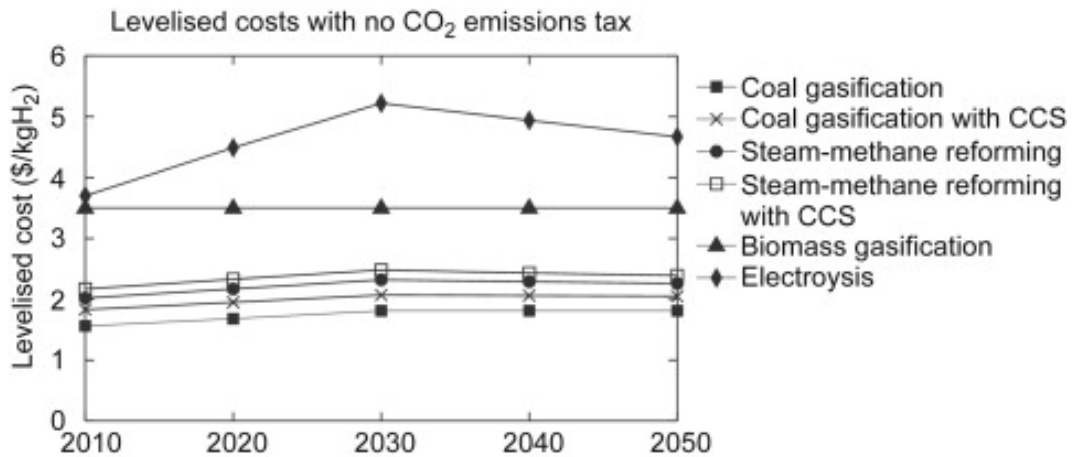


In addition, Trane et al. [119] have highlighted that the risk of sulphur poisoning in bio-oil reforming is an area that requires further research, as reforming catalysts are readily poisoned by H<sub>2</sub>S. For example, in SMR, the feed gas is often pre-treated to remove sulphur to levels as low as 0.1 ppmv (dry) [130].

Bio-oils typically contain very low levels of sulphur- 0.05 wt% sulphur or less, depending on feedstock [101,107,119,300]. This is considerably lower than a typical naphtha (1.5 wt%) [101]. Previous techno-economic studies on bio-oil reforming have therefore assumed that desulphurisation is not required [68,129,199]. In practice, the optimum level of sulphur input to a bio-oil reformer would need to be determined by an economic trade-off between the costs of desulphurisation and the benefits of improved catalyst performance and lifetime. At present there is limited information on bio-oil reforming and deactivation mechanisms to support such a judgement, especially considering the parallel issue of carbon deposition. However, a techno-economic assessment could help to quantify the costs and benefits of desulphurisation capabilities.

An additional area of interest is the role of CO<sub>2</sub> capture in bio-oil steam reforming. As discussed in **Chapter 2**, several features of the steam reforming process make it an attractive candidate for CO<sub>2</sub> capture [16]. Bio-oil reforming has the additional benefit of providing a potential route to negative emissions. A recent report by H2FC Supergen has identified the important potential for bio-based H<sub>2</sub> to provide negative emissions, but focussed on biomass gasification rather than the bio-oil reforming route [98]. Thus there is scope to further develop the evidence base on bio-oil reforming and CO<sub>2</sub> capture as an alternative route to hydrogen.

Various techno-economic studies have explored the potential for CO<sub>2</sub> capture in steam methane reforming [236,251,301]. A review in 2015 [302] produced costs projections of different routes to hydrogen production, shown in **Figure 5.1**. These cost projections show minimal difference in the levelised cost of hydrogen with and without CCS. However, other work has estimated that CO<sub>2</sub> capture facilities in SMR increase the cost of hydrogen by 25-30% [20]. Meerman et al. [136] estimated that absorption-based CO<sub>2</sub> capture at SMR plants costs in the range of 29 to 93 \$ t<sup>-1</sup> CO<sub>2</sub> captured. This is similar to the range for post-combustion capture at natural gas-fired power plants, estimated to be between 50 and 105 \$ t<sup>-1</sup> CO<sub>2</sub>. Similar studies on bio-oil reforming with CCS could be a valuable tool for comparison.



**Figure 5.1 – Levelised cost projections for hydrogen production (expressed as 2013 \$ kg<sub>H2</sub><sup>-1</sup>) [302]**

There is also scope to assess the potential of alternative process designs. Other techno-economic studies have demonstrated that sorption enhancement and chemical looping lead to increased efficiencies and reduced cost of CO<sub>2</sub> capture compared to benchmark absorption-based processes [162,209,242,303–306]. Cormos [307] has demonstrated similar advantages in the chemical looping of solid biomass. The thermodynamic analysis in **Chapter 4** highlighted that SE-CLSR has certain thermodynamic advantages, such as improved H<sub>2</sub> purity and an autothermal energy balance. The next step is to assess these advantages from an economic perspective, including SE-CLSR as another route to CO<sub>2</sub> capture.

The following chapter seeks to address these research questions with a techno-economic analysis in two phases. The first stage is an assessment of how operating parameters may affect the technical performance and cost of three different bio-oil steam reforming processes: C-SR, C-SR with CO<sub>2</sub> capture, and SE-CLSR with CO<sub>2</sub> capture. This study examines the effects of S/C ratio, pressure and operating temperature on process performance indicators such as product yield, thermal efficiency and direct CO<sub>2</sub> emissions.

The second stage is a cost analysis of these three bio-oil reforming routes, including the cost impacts of CO<sub>2</sub> capture facilities as a route to negative emissions. The study considers an absorption-based CO<sub>2</sub> capture process, as well as SE-CLSR, in order to assess whether the promising thermodynamic properties of SE-CLSR could have economic benefits. Sensitivity analyses are carried out to assess the impacts of operating and capital costs, as well as the potential costs and benefits of desulphurisation capabilities. Taken together, these technical and economic assessments can

be used to evaluate the feasibility of different bio-oil reforming technologies, and identify areas for optimisation and research focus.

## 5.2 Methodology

An overview of the process modelling and techno-economic methodology is given in **Chapter 3**. The following sections detail specific assumptions about the process and economic factors that were applied to the study.

### 5.2.1 Bio-oil feedstock

Bio-oil is modelled using a surrogate mixture that closely matches the elemental composition and differential thermogravimetric (DTG) curve of a real Palm Empty Fruit Bunch (PEFB) bio-oil [225,227]. For consistency, the composition is the same as that used in the thermodynamic study in the previous chapter. The full composition is given in **Chapter 3**.

Bio-oil has a number of challenging properties, such as its thermodynamic instability, viscosity, and density [110,111,300]. For this techno-economic study, it is assumed that the bio-oil is mixed with 10 wt% methanol in order to reduce its viscosity and density [68]. Due to its corrosive nature, it is stored in stainless steel tanks [308].

### 5.2.2 Desulphurisation

As discussed in the introduction, the sulphur content in bio-oils is a key area for consideration. In this study, the base case technical and economic evaluations do not include desulphurisation. This is in alignment with existing techno-economic studies on bio-oil reforming, which assumed the low sulphur content in bio-oils was sufficiently low to avoid the requirement for desulphurisation [68,129,199]. However, as this is a potentially important sensitivity for reforming catalysts, the role of desulphurisation are considered in **Section 5.4.4**.

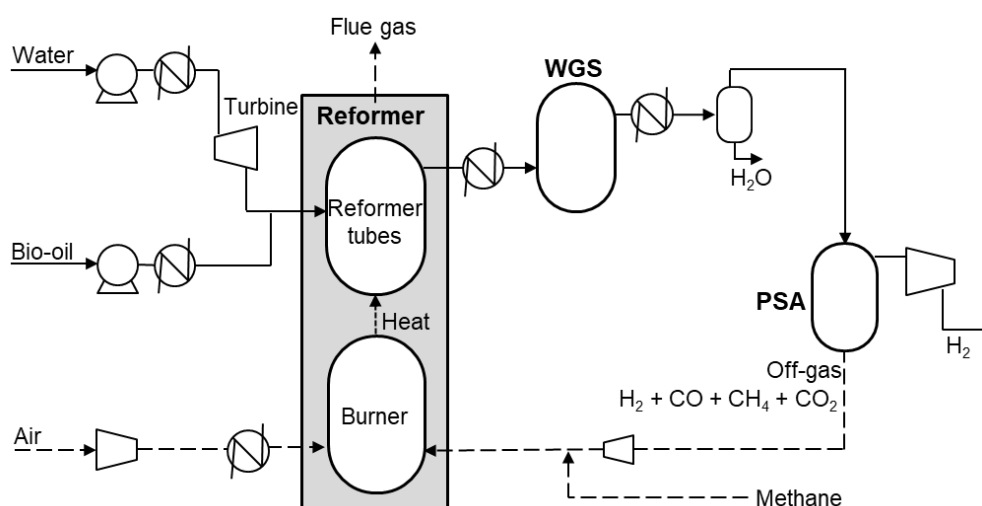
As bio-oil is a liquid feedstock, the desulphurisation methods are likely to be similar to those used in petroleum refining, such as hydrodesulphurisation (HDS), biodesulphurisation, oxidative desulphurisation or desulphurisation by extraction [309,310]. For this assessment, desulphurisation assumptions are based upon the data available for naphtha HDS, a common approach in refining [311]. Transition metal catalysts, such as sulphided CoMo/Al<sub>2</sub>O<sub>3</sub> and NiMo/Al<sub>2</sub>O<sub>3</sub>, convert sulphur compounds in the liquid into H<sub>2</sub>S, via reaction with hydrogen [312]. Technical and economic assumptions are detailed in **Sections 5.2.5** and **5.2.6**. Resulting sulphur levels are assumed to be the

same as those used for the inlet to naphtha reforming, around 0.5 to 1 ppmwt [311,313].

As sulphur levels are lower than in a typical naphtha, HDS may not be the most suitable route to desulphurisation. A simpler method, such as metal oxide beds, may be more cost-effective. Sulphur guard beds, consisting of ZnO or mixed metal oxides, are used for a range of liquid and gas hydrocarbon applications [314–317]. Metal oxides react with sulphurous species, reducing sulphur to below ppb levels. Multiple beds are operated in a lead-lag configuration so that, depending on the adsorbent type and the application, the spent chemisorbent can be regularly regenerated or replaced [318,319]. **Section 5.4.4** includes a discussion on sulphur levels in the reformer feed, the applicability of different desulphurisation methods, the costs of implementation, and the benefits of extending catalyst lifetime.

### 5.2.3 Steam reforming process description

**Figure 5.2** shows a simplified process flow diagram of the conventional steam-reforming (C-SR) process. For simplicity, this version does not show any heat integration, which is discussed in **Section 5.2.5.2**. The process is closely based on steam reforming process designs used in industry, discussed in **Chapter 2**. Descriptions of each stage of the process are given in the sections below. **Section 5.2.5** defines how these processes were modelled in Aspen Plus, including the complete process flowsheets.



**Figure 5.2 – Process flow diagram for bio-oil C-SR without CO<sub>2</sub> capture. Solid lines represent the flow path of feedstocks and products, while dashed lines show flows associated with the burner**

### 5.2.3.1 Bio-oil reformer

Water and bio-oil are pre-heated before they are fed to the reformer, where they react to form a syngas comprised of  $H_2$ ,  $CO_2$ ,  $CO$ ,  $CH_4$ , and water. The reformer consists of a series of reformer tubes containing catalyst, housed within a furnace that supplies heat to the reforming tubes by external firing. The furnace is fuelled by PSA off-gas [200,320], which is topped up with methane to ensure there is sufficient heat to sustain an isothermal reactor. The fuel is combusted to give a flue gas at  $1100^\circ C$  [29].

While hydrogen production is favoured at lower pressure, industrial reforming is commonly operated at high pressures, to manage the large volumes of gas and to improve PSA performance [89]. A high reforming temperature is applied to balance the elevated pressure. A range of reforming temperatures between  $800$  and  $1000^\circ C$  is used in the performance study, before selecting an optimal temperature for the economic analysis. The suitability of the temperature range was determined in the earlier thermodynamic study in **Chapter 3**, as well as thermodynamic analyses in literature [193,269].

Some steam reforming processes include an adiabatic pre-reformer, which can aid feedstock flexibility [91]. In pre-reforming, higher hydrocarbons undergo thermal decomposition, steam reforming and methanation, so that the feed to the main reformer has a higher methane content. At the right conditions, the net energy balance for pre-reforming is only slightly endothermic or even exothermic, so that this pre-processing can occur without external firing. Previous studies have proposed pre-reformers for novel liquid feedstocks, such as bio-oil [119] and bio-ethanol [197]. However, adiabatic pre-reformers are typically operated at low S/C ratios and low catalyst exit temperatures [91], both of which are likely to cause carbon deposition issues with bio-oil. A pre-reformer was not included in this study, but could be included in later work if there was experimental data to determine operational feasibility.

### 5.2.3.2 Water gas shift reactor

The syngas produced by the steam reformer flows to a water gas shift (WGS) reactor, where  $CO$  and water react to produce more  $H_2$  and  $CO_2$ . As WGS is an exothermic reaction, the stream is cooled to  $300^\circ C$  before the WGS reactor [200]. Some industrial reforming processes feature a second stage of WGS at lower temperature, in order to reduce  $CO$  content to a

sufficiently low level [62,133]. However, in this case, as the gas is purified downstream, it is assumed that this second stage is not required [66]. In addition, given the small throughput, it is likely that investment in additional WGS is not worthwhile [69].

### **5.2.3.3 Hydrogen purification**

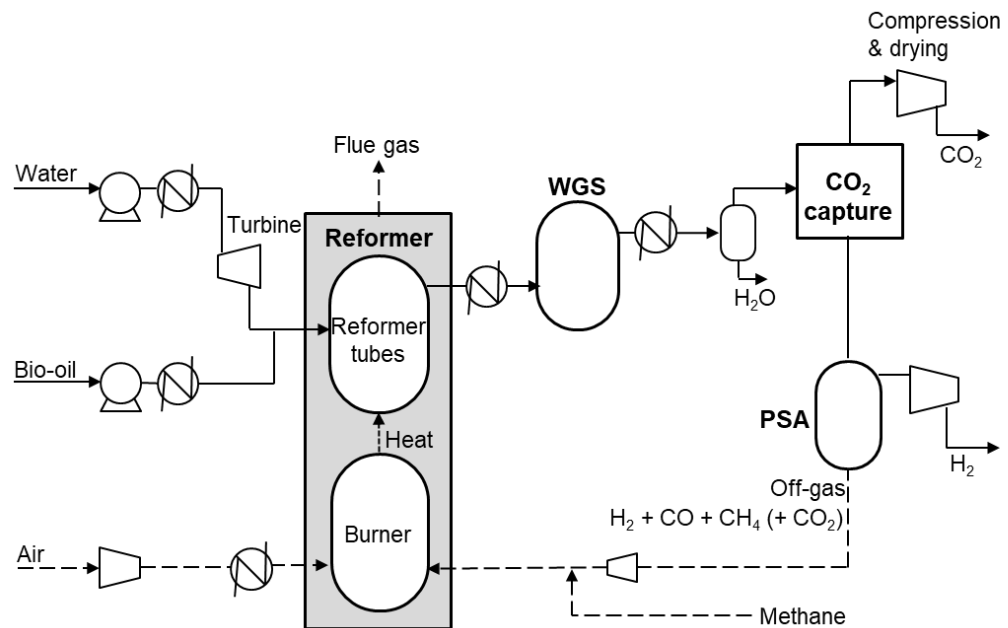
After the WGS reactor, the shifted syngas is cooled and condensed water is removed. The gas is purified in a pressure swing adsorption (PSA) unit, which includes a moisture guard that removes the remaining traces of water. PSA systems can achieve hydrogen recovery between 70 and 90% [66,321]. Recovery is dependent on many variables such as gas composition, operating pressure, the number of beds, and process sequencing [93,322]. A recovery of 90% has been used in several techno-economic assessments of chemical looping and C-SR processes [242,251,323]. As described in Martínez et al. [213], 90% recovery can be achieved when the pressure ratio between feed and off-gas remains above 15. In all cases with this study, this pressure criteria is met, and so 90% recovery is assumed. The changes in syngas composition resulting from bio-oil feedstock, and from sorption enhancement, would have impacts on PSA performance. PSA is not modelled in detail at this stage, but its cost is examined in the sensitivity analysis (**Section 5.4.3**).

### **5.2.3.4 CO<sub>2</sub> capture and compression**

As discussed in the literature review, three potential locations within the steam reforming process are candidates for CO<sub>2</sub> capture: the flue gas, the high-pressure syngas upstream of the PSA, and the low-pressure PSA off-gas [16]. The overall CO<sub>2</sub> capture efficiency would be greatest in the flue gas stream, as all the CO<sub>2</sub> from both bio-oil and the furnace fuel gas passes into this stream. Depending on the capabilities of the capture system, around 90 to 95% of the total process CO<sub>2</sub> could be captured. However, this stream is at low pressure, and is heavily diluted by nitrogen from furnace combustion air, leading to low CO<sub>2</sub> partial pressures, and thus a larger, more expensive capture process. In addition, the combustion flue gases introduce contaminants such as O<sub>2</sub>, SO<sub>2</sub> and NO<sub>2</sub>, which can degrade amines and increase operating costs [141].

For these reasons, the CO<sub>2</sub> capture location selected for this study is the syngas upstream of the PSA. According to IEAGHG, this is the current industry standard for SMR plants [236]. Soltani et al. [16] identified that the

high partial pressure of CO<sub>2</sub> in the stream provides a strong driving force for CO<sub>2</sub> absorption, reducing the cost and size of the absorption-based capture process. In addition, the removal of CO<sub>2</sub> at this location has positive impacts on downstream parts of the process. For example, it reduces the inlet flow to the PSA system. It also reduces the level of dilution of the PSA off-gas, making it a more effective fuel for the burner. After the CO<sub>2</sub> is captured, it is compressed and dried to CO<sub>2</sub> pipeline specifications. **Figure 5.3** shows the process flow diagram for steam reforming with CO<sub>2</sub> capture on syngas.



**Figure 5.3 – Process flow diagram of bio-oil C-SR with CO<sub>2</sub> capture. Solid lines represent the flow path of feedstocks and products, while dashed lines show fluid flows associated with the furnace and CO<sub>2</sub> capture.**

### 5.2.3.5 Steam turbine

The C-SR process contains a large amount of heat in the furnace flue gases, making it possible to raise high pressure steam for power generation. Steam is raised to 100 bar, before being passed through a back-pressure turbine with an outlet pressure 0.1 bar above reformer inlet pressure. This produces sufficient power to meet the demand of the process. Excess power above process requirements is assumed to be a saleable export (**Section 5.2.6**).

## 5.2.4 SE-CLSR process description

### 5.2.4.1 SE-CLSR process stages

The SE-CLSR process contains four key elements:

- 1) sorption-enhanced reforming
- 2) oxidation of the oxygen carrier,
- 3) calcination of the sorbent; and
- 4) reduction of the oxygen carrier.

These elements can be combined into simultaneous stages, reducing the total number of reaction stages, and therefore footprint and cost. These combinations can take different forms, depending on the objectives of the process. For example, where oxidation and calcination are combined in the same step, the exothermic oxidation step can provide heat to enable calcination without a pressure swing [155]. However, this approach is not well-suited to a carbon capture, as the  $N_2$  in air dilutes the  $CO_2$ .

As an alternative, oxidation can occur without calcination, so that in a subsequent step the bed can be simultaneously reduced and calcined. This is the approach selected for the techno-economic study, as it has several advantages for  $CO_2$  capture. A pure stream of wet  $CO_2$  is produced, undiluted by  $N_2$  and low in other contaminants, which are converted by reduction [242,258,324]. If PSA off-gas is used as the reducing gas, overall  $CO_2$  capture efficiency can be improved, as carbon-containing compounds are converted to  $CO_2$  and captured. In addition, the use of PSA off-gas as the source of reduction eliminates the need to use valuable feedstock or  $H_2$  product. **Chapter 6** examines simultaneous reduction-calcination in more detail.

Based on this approach to cycle steps, the simplified process flow diagram for SE-CLSR is shown in **Figure 5.4**. Heat integration is not shown in this simplified diagram, but is shown in the full Aspen Plus flowsheet (**Figure 5.9**). Each of the steps are described in more detail in the following sections.



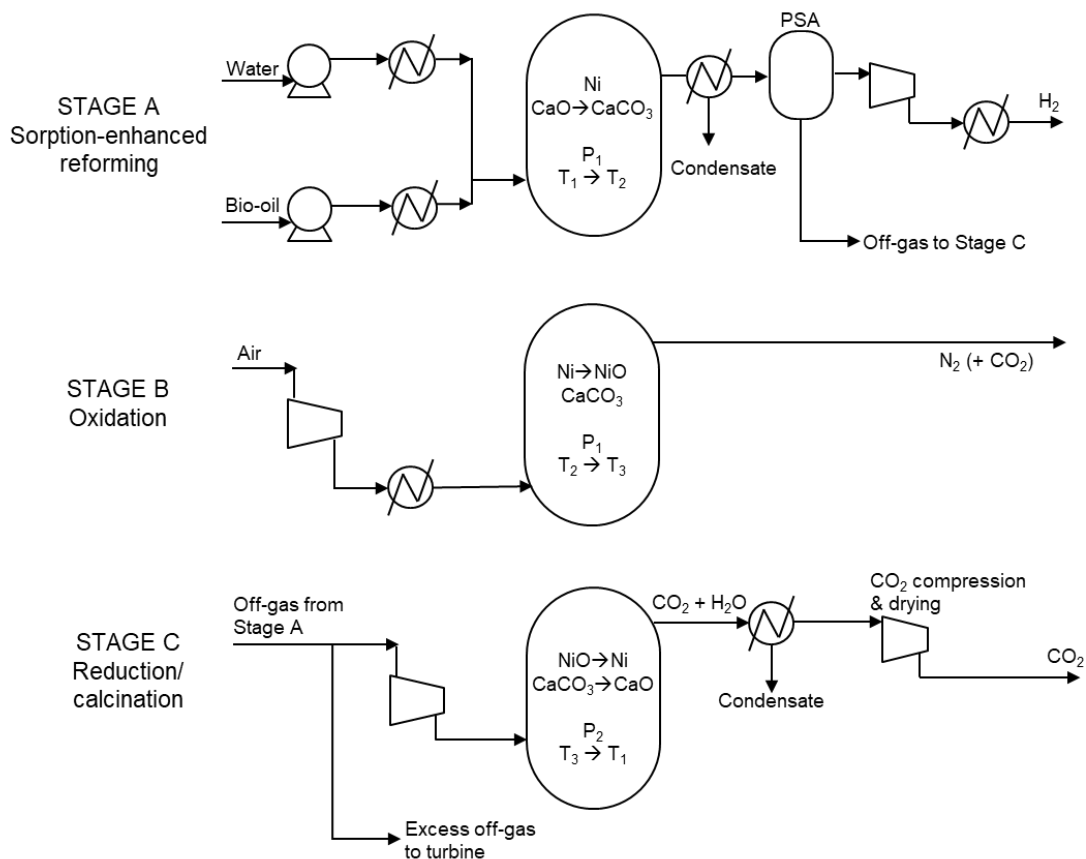


Figure 5.4 – Simplified process flow diagram of bio-oil SE-CLSR

Each sequence of three steps forms an autothermal cycle, in which the temperature at the end of reduction/calcination (Stage C) is equal to the temperature at the start of the reforming step (Stage A). This is illustrated on a temperature-pressure diagram in Figure 5.5.

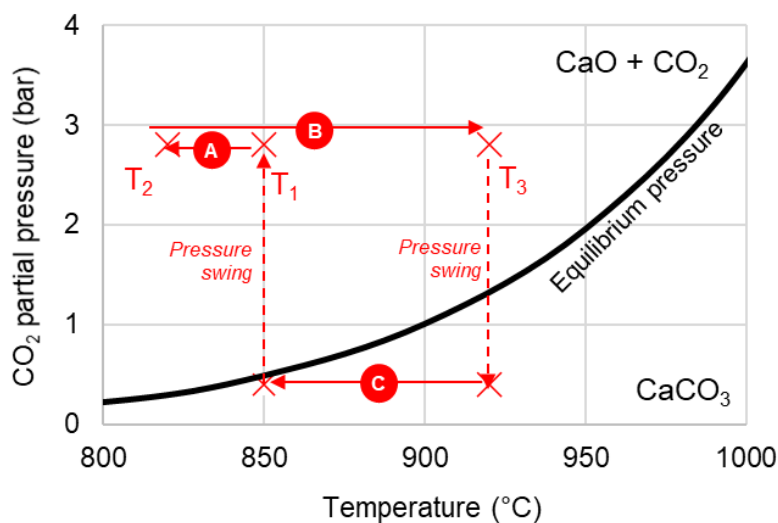


Figure 5.5 – Example SE-CLSR operating conditions on  $\text{CO}_2$  equilibrium partial-pressure diagram.  $\text{CaO}/\text{CO}_2$  equilibrium properties from [325]

#### 5.2.4.2 Sorption-enhanced reforming stage

Bio-oil and water are pre-heated, before they are fed to the reactor containing oxygen carrier in its reduced state ( $\text{Ni}/\text{Al}_2\text{O}_3$ ) and  $\text{CO}_2$  sorbent, both at the initial temperature of  $T_1$  (**Figure 5.5**). The bio-oil undergoes steam reforming, enhanced by the sorption of  $\text{CO}_2$ . The reforming reactor is not externally fired, so depending on the net energy balance, the solids are either cooled or heated to a temperature of  $T_2$ .

The syngas, which is low in  $\text{CO}_2$ , due to the presence of  $\text{CO}_2$  sorbent, is fed to the treatment and purification section. The syngas is cooled and water is condensed out, before the gas is passed through a PSA system to produce pure  $\text{CO}_2$ . PSA recovery is assumed to be 90%, aligning with the assumptions for C-SR (**Section 5.2.3.3**). Pure  $\text{H}_2$  is compressed to the specified export pressure for a  $\text{H}_2$  pipeline (40 bar).

#### 5.2.4.3 Oxidation stage

Air is compressed in three stages to the operating pressure of the oxidation reactor (which is equal to the pressure of the reforming stage, see **Figure 5.5**), and is fed into the Stage B reactor. Oxygen oxidises the Ni, while  $\text{N}_2$  passes through. The exothermic process of oxidation increases the solid bed temperature. This causes a small amount of calcination to occur, so that some  $\text{CO}_2$  enters the flue gas. However, the elevated pressure minimises the level of calcination, so that as much  $\text{CO}_2$  as possible can be captured in the next stage.

#### 5.2.4.4 Reduction/calcination stage

In Stage C, the  $\text{NiO}$  is reduced by PSA off-gas while the  $\text{CaCO}_3$  is calcined. The hot bed, which has been heated by oxidation during Stage B, is subjected to a pressure swing. Calcination is thereby achieved by a combination of high temperature and low pressure (**Figure 5.5**). The wet  $\text{CO}_2$  stream is cooled to  $30^\circ\text{C}$ , and water is condensed out in a flash drum, before the  $\text{CO}_2$  is compressed and dried to pipeline specifications.

#### 5.2.4.5 Off-gas turbine

As described in **Section 5.2.3.5**, the flue gases in the C-SR process contain sufficient heat to generate high pressure steam for a steam turbine. In SE-

CLSR process, the capability to raise excess stream is more limited. Instead, a gas turbine is used, fed by excess PSA off-gas.

In some cases, the supply of off-gas can exceed the requirements of the reduction stage. The excess off-gas is not fed to the Stage C reactor, as the unreacted components (H<sub>2</sub>, CH<sub>4</sub>, CO) would contaminate the CO<sub>2</sub>. Instead, a design specification block (Section 5.2.5.3) determines the amount of off-gas that is required for reduction, and the excess off-gas is directed to a gas turbine. This turbine is represented in Aspen Plus by a compressor, combustor and expander [326]. The gas turbine power output is then assumed to be:

$$\text{Gas turbine output} = \text{expander output} - \text{compressor input} \quad \text{Eq. 5.1}$$

This provides power, while also converting the PSA off-gas components, including CH<sub>4</sub>, H<sub>2</sub> and CO, into a flue gas which can be safely emitted. Where the gas turbine power output is not sufficient to meet process power demands, any deficit is met by power import.

#### 5.2.4.6 Vessel purging

To prevent the creation of an explosive mixture containing syngas and air, a short purge step is included before and after each oxidation stage [209,327]. The purging step is not modelled in Aspen Plus, but the economic model includes certain assumptions to account for purging. Two additional reactor beds are included for the purge stages, taking the total number of reactor beds to five. To estimate the steam flow rate for rinsing, the purge flow was assumed to fill 4 reactor volumes within a 10 minute purging step.

#### 5.2.4.7 Switching valves

In a fixed bed chemical looping process, the stages in the sequence can be managed by three-way switching valves. A techno-economic assessment by Nazir et al. [162] highlighted that high temperature switching valves are an important contributor to total equipment cost, and so this techno-economic study includes the price of these valves.

**Figure 5.6** illustrates the proposed approach to flow switching. Four valves are required for each reactor: two on the inlet, and two on the outlet. The design flow rate of each valve is then equal to the largest flow experienced by the valve during the two stages in which it is in operation. As the Aspen Plus model is a steady state flowsheet, it does not represent flow rate

variations during a stage. Given this constraint in valve design capability, the effect of valve costs are included in the sensitivity analysis (**Section 5.4.3**).

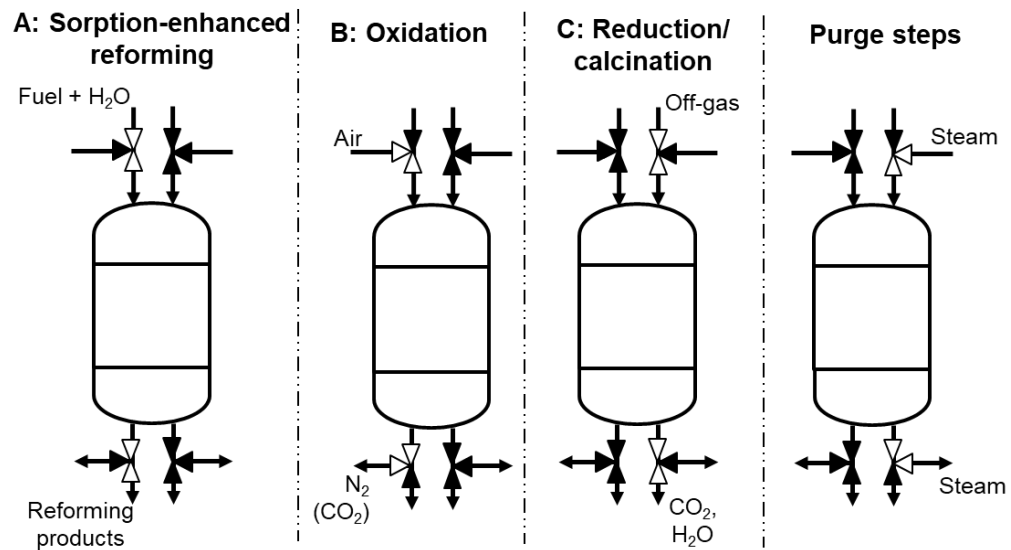


Figure 5.6 – Switching valves in SE-CLSR process

## 5.2.5 Process modelling approach

### 5.2.5.1 Modelling assumptions

The bio-oil steam reforming process has been modelled in Aspen Plus software. Previous studies on bio-oil steam reforming have achieved bio-oil conversion and hydrogen yields close to 100% [119]. Thus an equilibrium-based approach is used as a simplifying assumption for this feasibility study. This enables simple analysis where there is a complex reaction scheme, or where the kinetics are not yet known. Further details are given in **Chapter 3**. The selected property method was Peng-Robinson, as suggested for hydrogen-rich applications [216], and used for similar applications in the literature [190,217,218].

Reforming reactors were modelled using RGibbs reactors, which use the minimisation of Gibbs free energy to calculate the equilibrium product of reactions [215]. In C-SR, an isothermal reforming reactor is connected to a isothermal burner by an energy stream, representing external firing on reformer tubes ('Q-REF', **Figure 5.7**). SE-CLSR was modelled using adiabatic RGibbs blocks, where the outlet temperature is determined by Aspen Plus on the basis of chemical equilibrium and the resulting heat balance. The WGS reactor was an adiabatic REquil reactor in which the WGS reaction is specified.

C-SR can be modelled as a continuous, steady-state process, a common use for an Aspen Plus flowsheet. SE-CLSR is more complex to model as it is a packed bed system, in which different stages are initiated by switching gas inputs. As described in **Chapter 4**, this can be simulated in Aspen Plus as a set of reactor blocks, each with a different gas input. Each reactor block in the process flowsheet (**Section 5.2.5.3**) represents a different stage in the same vessel. At the outlet of each reactor block in Aspen Plus, solid components are separated from product gas via a simple separator. A transfer block automatically copies the pertinent information about the solid bed, such as temperature and composition, to a corresponding solids stream in the next stage. This does not represent the movement of solids between different reactors. Instead, it represents the retention of solids in the same reactor, a type of semi-batch process. This approach does not evaluate dynamic elements of SE-CLSR. However, it is sufficient to provide details for a preliminary techno-economic evaluation, as it identifies key flows of heat and material. **Chapters 6 and 7** discuss the first steps towards a more rigorous process model.

The PSA system was modelled as a separator block that splits a stream on the basis of split fractions and purities. As H<sub>2</sub> recovery was set at 90%, the separator block sent 90% of H<sub>2</sub> in the syngas stream to the product section, while 10% of H<sub>2</sub> and all other components remain in the off-gas.

Detailed modelling of CO<sub>2</sub> compression and drying would not be justified in relation to the aims of this study. The absorption-based capture process was modelled as a separator block in Aspen Plus that recovers 95% of the CO<sub>2</sub> and returns the remainder of the stream to the process. Energy usage for capture and compression was taken from the work of Meerman et al. [136], who modelled an activated MDEA process in syngas at similar conditions to those in this study (**Table 5.1**).

**Table 5.1 – Syngas conditions for absorption-based CO<sub>2</sub> capture**

	Meerman et al.	This work
Syngas pressure (bar)	30	28.5
CO <sub>2</sub> concentration (mol% dry)	25	30
Partial pressure (bar)	7.5	8.6

Similarly, the sensitivity analysis on desulphurisation did not include detailed design, but rather is an order of magnitude estimate of the potential impacts of such a plant. Proposed process schemes for bio-refineries commonly include a hydrotreating step, in which HDS occurs alongside denitrogenation

and deoxygenation, for improved bio-oil stability. A number of studies have evaluated these processes in detail [107,108,328,329]. However, the target product in these hydrotreater designs is an upgraded bio-oil, intended as a drop-in replacement for diesel or naphtha, and so they are not necessarily transferable to bio-oil reforming. Future work could consider desulphurisation that is more specifically targeted to a standalone bio-oil reforming plant. For this study, utility requirements were based on those required for naphtha hydrodesulphurisation, taken from Maples [311]. The hydrogen requirements were derived from a correlation between sulphur content and hydrogen requirements in naphtha desulphurisation, from the same reference.

**Table 5.2 – Utilities consumption for desulphurisation [311]**

Utility	Requirement per m <sup>3</sup> bio-oil/methanol feed
Power	12.58 kWh
Steam	42.79 kg
Fuel gas	55.30 kWh

Performance indicators, such as direct yield, thermal efficiency and CO<sub>2</sub> emissions were calculated according to the methods outlined in **Chapter 3**. Pressure drops in heat exchangers and efficiencies of turbomachines are given in **Table 5.3** and **Table 5.4**. Other assumptions were as follows:

- Where gas volumes are given in Nm<sup>3</sup>, normal conditions are 20°C and 1.01325 bara;
- Air is composed of 79% N<sub>2</sub> and 21% O<sub>2</sub>;
- To ensure storage in liquid form, the bio-oil/methanol mixture is stored above its vapour pressure (around 3bara);
- All other fluid inputs enter the system at 25°C and 1.01325 bara;
- Reactor pressure drop is 5% of inlet pressure; and
- Heat exchanger minimum approach of 10°C.

**Table 5.3 - Pressure drop assumptions for heat exchangers [330]**

Type of service	Pressure drop (bar)
Liquid with no phase change	0.7
Vapour with no phase change	0.14
Condensing	0.14
Boiling	0.07

**Table 5.4 - Efficiencies for the modelling of turbomachines [242]**

Type	Isentropic efficiency	Mechanical-electric efficiency
Compressors	0.85	0.95
Blowers	0.75	0.95
Pumps	0.85	0.95
HP steam turbine	0.85	0.99
Expander	0.85	0.99

### 5.2.5.2 Heat integration and steam export

All three processes have opportunities for heat integration, as hot product or flue gas streams can exchange heat with cool feed streams. This can be used to generate steam and to pre-heat fuel, thereby reducing the energy demands within the reforming reactor. It was assumed that flue gases from the furnace and gas turbine are cooled to 180°C before being emitted to the atmosphere [331]. Excess heat from the process was used to produce low pressure (LP) steam at 6 bar and 160°C, which is sold as a by-product [242].

The heat integration philosophy was determined by first developing a process without any heat integration. All cooling and heating duties were identified, and suitable locations for heat exchange were identified by matching heat exchanger thermal duties and operating temperatures. Some aspects were determined by trial and error, whereby Aspen Plus identified temperature crossovers, so an alternative option was selected.

This approach resulted in processes that do not require any heat import, with the exception of fuel gas for C-SR and C-SR-CCS. Future work may improve heat integration via a pinch analysis. However, initial work identified that heat exchangers were relatively minor contributors to overall cost (**Section 5.4.1**). As heat exchanger optimisation is not a focus of this study, a pinch analysis is not included at this stage.

### 5.2.5.3 Aspen Plus process flowsheets

Given below are the Aspen Plus flowsheets for all three processes, including heat integration. The flowsheets contained a number of manipulator blocks that enable Aspen Plus to automatically define certain input variables. There are various types, as described in **Chapter 3**. The manipulator blocks for each process are summarised in **Table 5.5** and **Table 5.6**.

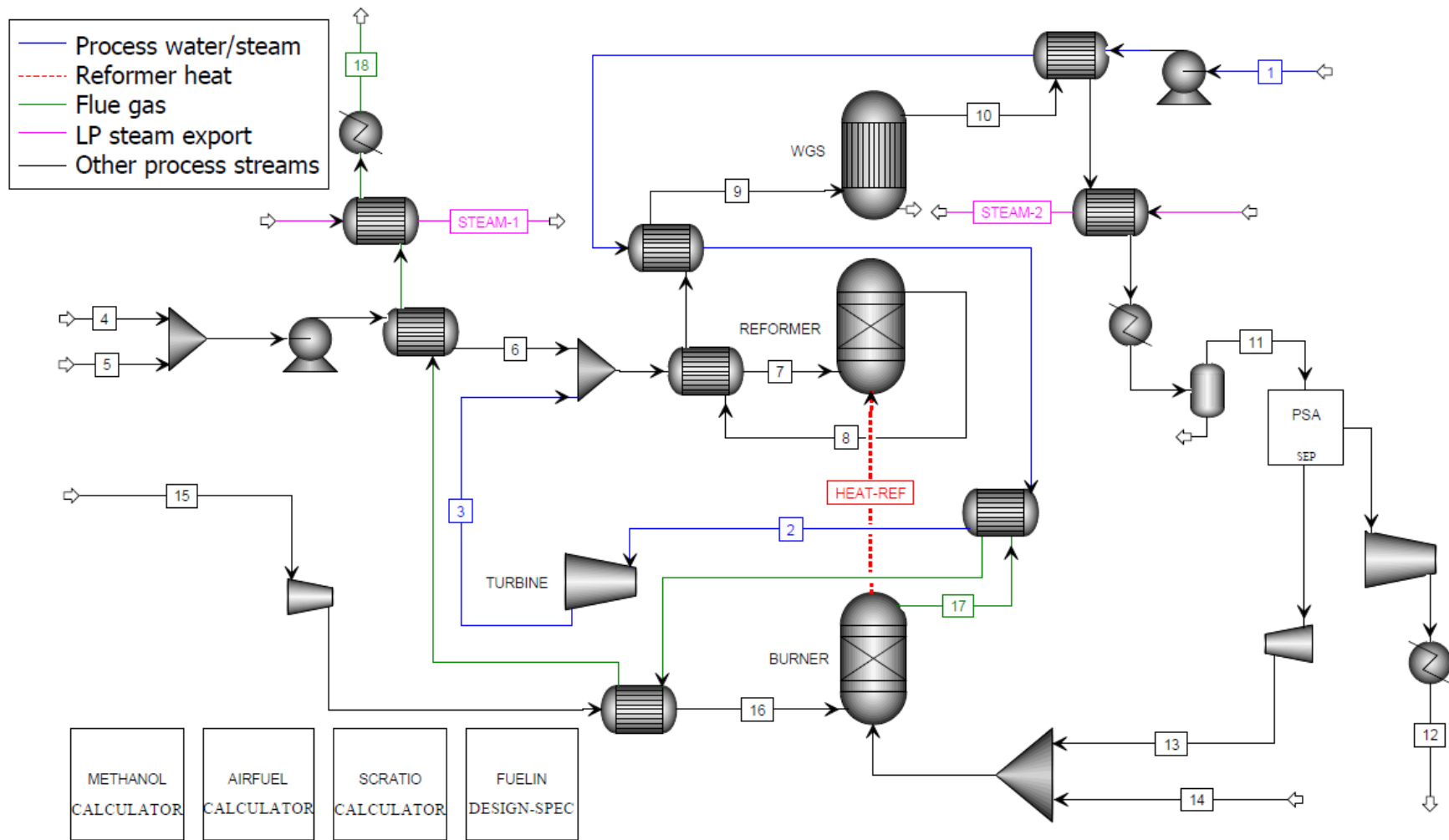


Figure 5.7 – Aspen Plus flowsheet for bio-oil C-SR without CO<sub>2</sub> capture



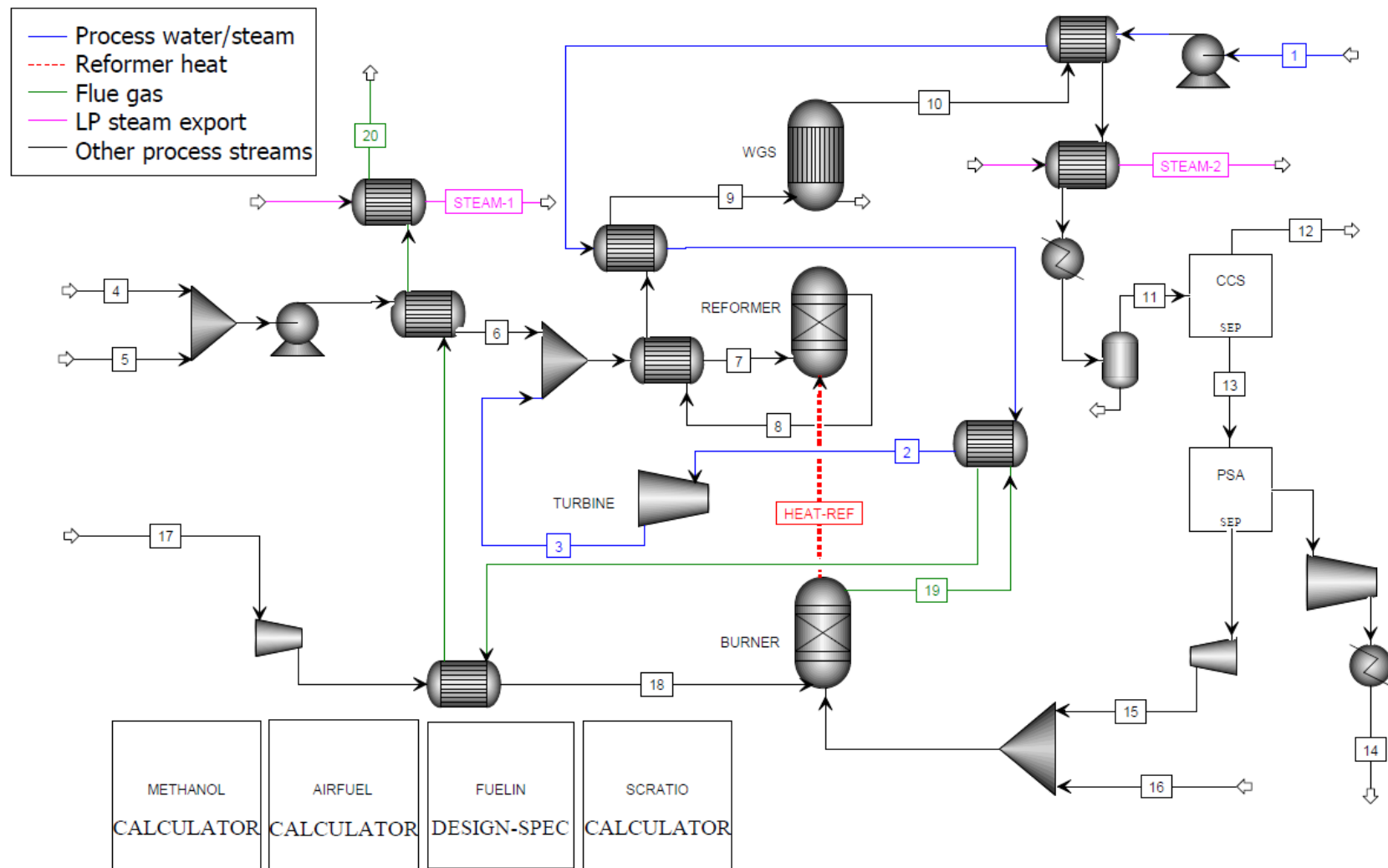


Figure 5.8 – Aspen Plus flowsheet for bio-oil C-SR with CO<sub>2</sub> capture

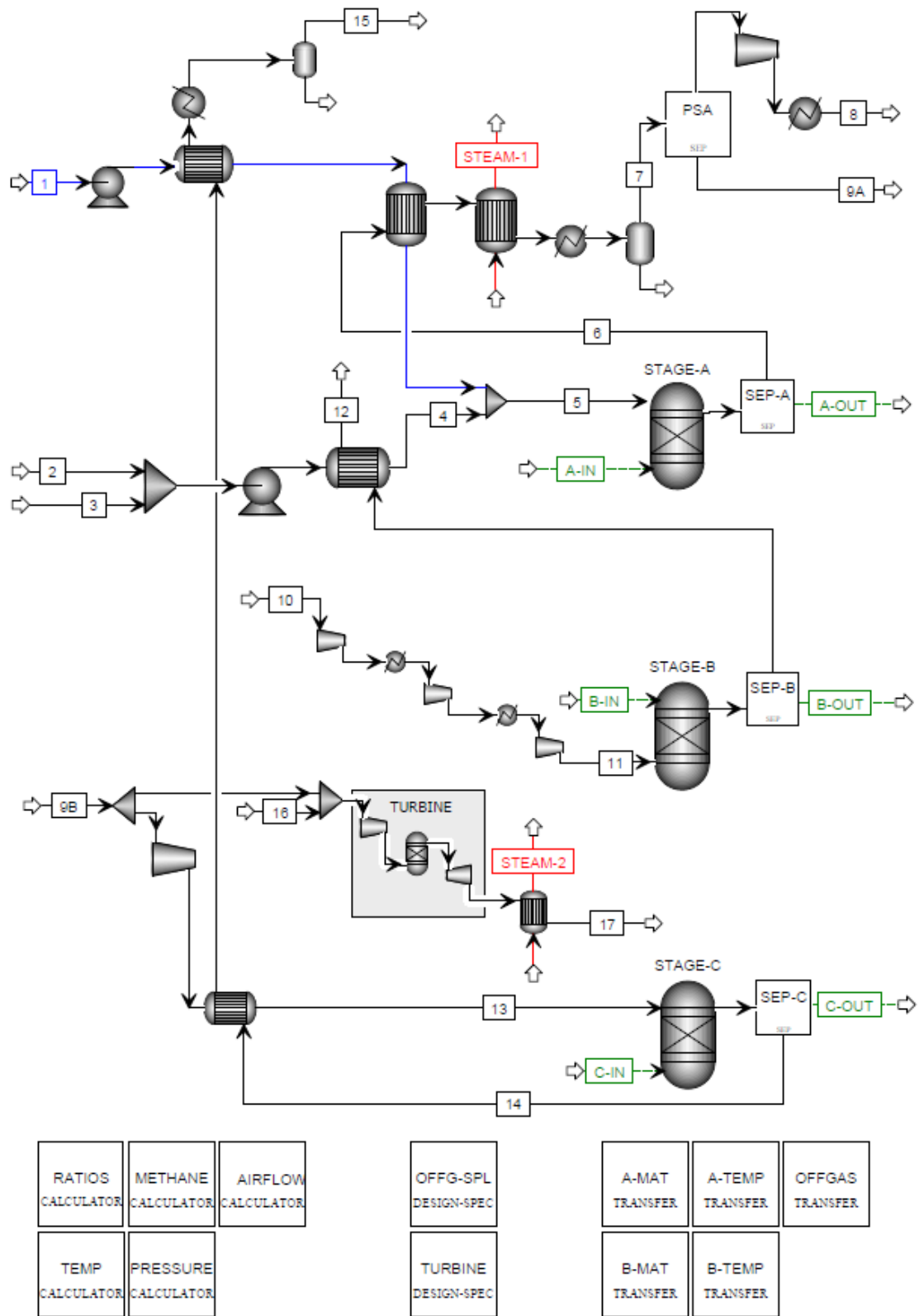


Figure 5.9 – Aspen Plus flowsheet for bio-oil SE-CLSR

**Table 5.5 – Manipulator blocks in Aspen Plus models of C-SR with and without CO<sub>2</sub> capture**

<b>Name</b>	<b>Description</b>	<b>Block specifications</b>
METHANOL	Calculator block that sets the methanol input such that the total mixed fuel contains 10wt% methanol, the conditions assumed for storage.	Import variable: Mass flow of bio-oil input  Export variable: Mass flow of methanol input
SCRATIO	Calculator block that sets the quantity of steam when the user defines a molar S/C ratio. Moisture content in the bio-oil is also factored in, using the equation in Chapter 4 (Eq 4.5).	Import variables: Molar flow of each carbon containing component in bio-oil. Molar flow of methanol. Molar flow of water in bio-oil.  Export variable: Molar flow of steam feed
AIRFUEL	Calculator block that sets the air flow to the burner, based on the quantity of oxygen required for complete combustion of all burner fuel gas, plus a 10% oxygen excess.	Import variables: Molar flow of methane top-up Molar flow of H <sub>2</sub> in off-gas Molar flow of CH <sub>4</sub> in off-gas Molar flow of CO in off-gas  Export variable: Molar flow of air
FUELIN	Design Spec block that determines the methane top-up flow required to sustain the reformer operating temperature.	Design specification: Reformer outlet temperature  Manipulated variable: Flow of methane top-up

**Table 5.6 – Manipulator blocks in Aspen Plus model of SE-CLSR**

<b>Name</b>	<b>Description</b>	<b>Block specifications</b>
METHANOL	Calculator block that sets the methanol input such that the total mixed fuel contains 10wt% methanol, the conditions assumed for storage.	Import variable: Mass flow of bio-oil input  Export variable: Mass flow of methanol input
RATIOS	Calculator block that sets the quantity of steam when the user defines the molar S/C ratio. Carbon content and moisture content in the bio-oil is accounted for, using the equation in Chapter 4 (Eq 4.5). Also allows the user to set the molar NiO/C ratio and CaO/C ratio, using the same carbon basis.	Import variables: Molar flow of each carbon containing component in bio-oil. Molar flow of methanol. Molar flow of water in bio-oil.  Export variable: Molar flow of steam feed Molar flow of Ni in stream A-IN Molar flow of CaO in stream A-IN
AIRFLOW	Calculator block that sets the air flow for oxidation in Stage B, based on the quantity of oxygen required for oxidation of all NiO in the system.	Import variables: Molar flow of Ni in stream B-IN  Export variable: Molar flow of air
OFF-SPL	Design Spec block that adjusts the flow of off-gas to Stage C, until full reduction is achieved.  The remaining off-gas is sent by a flow splitter to the gas turbine.	Design specification: NiO content in stream C-OUT to reach zero.  Manipulated variable: Split fraction in the off-gas flow splitter.
TURBINE	Design Spec block that adjusts the flow of air to the turbine, to achieve 1350°C at the outlet of the combustor.	Design specification: Temperature of combustor outlet  Manipulated variable: Molar flow of air (stream 15)

Name	Description	Block specifications
A-MAT/ B-MAT	Transfer blocks that transfers the flow and composition of solids from stage A to stage B, or Stage B to Stage C.	Transfer from: stream flow of A-OUT/ B-OUT  Transfer to: Stream flow of B-IN/C-IN
A-TEMP/ B-TEMP	Transfer blocks that transfers the temperature of solids from Stage A to Stage B, or Stage B to Stage C.	Transfer from: temperature of A-OUT/B-OUT  Transfer to: temperature of B-IN/C-IN
OFFGAS	Transfer block that transfers all information about PSA off-gas from Stage A to Stage B.	Transfer from: All stream information for 8A  Transfer to: All stream information for 8B.

#### 5.2.5.4 Summary of process variables

**Table 5.7** summarises the key operating parameters for the process models of C-SR, both with and without CO<sub>2</sub> capture. The design variables with CO<sub>2</sub> capture were largely the same as those for the benchmark plant. However, as CO<sub>2</sub> capture reduces the quantity of flue gas, certain temperatures were revised to make heat integration feasible.

**Table 5.7 – Process variables for bio-oil C-SR with and without CO<sub>2</sub> capture**

Variable		Without capture	With capture
<i>Reformer</i>	S/C ratio	3 - 7	
	Inlet pressure	20 - 40 bar	
	Outlet temperature	800 - 1000°C	
	Inlet temperature (outlet of gas/gas exchanger)	300°C below outlet	400°C below outlet
<i>Burner</i>	Air pre-heat temperature	200°C	-
	Oxygen excess	10%	
	Inlet pressure	1.1 bar	
	Outlet pressure	1.01325 bar	
	Flue gas temperature	1100°C	
<i>WGS</i>	Inlet temperature	300°C	
<i>Syngas flash drum</i>	Inlet temperature	30°C	
	Pressure drop	0 bar	
<i>PSA</i>	H <sub>2</sub> recovery	90%	
<i>Steam turbine</i>	Inlet pressure	100 bar	
	Outlet pressure	Reformer inlet pressure	
	Inlet temperature	400°C	340°C
<i>H<sub>2</sub> compression</i>	Product pressure	40 bar	
	Product temperature	30°C	
<i>CO<sub>2</sub> capture</i>	Type	-	a-MDEA, from syngas
	CO <sub>2</sub> capture efficiency	-	95% [136]
	Thermal requirement	-	2.1 MJ kg <sub>CO2</sub> <sup>-1</sup> [136]
	Power requirement	-	0.04 MJ kg <sub>CO2</sub> <sup>-1</sup> [136]
<i>CO<sub>2</sub> compression &amp; drying</i>	Outlet pressure	-	110 bar [136,242,251]
	Power requirement	-	0.3 MJ kg <sub>CO2</sub> <sup>-1</sup> [136]

The process variables for SE-CLSR are summarised in **Table 5.8**. The range of operating temperatures was constrained by the requirement to control sorbent calcination (**Figure 5.5**). The performance evaluation focused on the temperature of solids at the start of reforming, marked  $T_1$  on the diagram.

The NiO/C required to achieve the autothermal temperature cycle was found by trial and error, by manipulating the ratio until the complete temperature cycle is observed in the Aspen Plus model. Other checks on the cycle included confirmation that the OTM and sorbent are fully reverted to their initial state (NiO and CaO, respectively) at the end of Stage C.

A CaO/C ratio of 1 was assumed, as per the thermodynamic analysis in **Chapter 3**, and an additional correction was applied for sorbent capacity:

$$CaO \text{ quantity} = \frac{\text{molar carbon flow}}{X_{sorb}} \quad \text{Eq. 5.2}$$

where  $X_{sorb}$  was the sorbent capacity. According to the work of Martinez et al. [159], this decreases during the first 100 cycles, after which it remains relatively constant at around 0.08. Therefore  $X_{sorb}$  is set at 0.08.

The evaluation of SE-CLSR used a lower range of S/C ratios, as initial analysis identified that high S/C ratios made it difficult to achieve heat integration. As there was no furnace, the process did not contain a large amount of hot flue gases with which to generate steam. The thermodynamic analysis in **Chapter 4** suggested a lower S/C ratio may be acceptable in SE-CLSR, as the presence of NiO and CaO reduces the potential for carbon deposition. In addition, the work of Omoniyi has demonstrated that the oxidation step can burn off carbon deposits [271], and consequently help to retain catalyst activity.

**Table 5.8 – Process variables for SE-CLSR of bio-oil**

	Variable	SE-CLSR process variable
<i>Reforming stage</i>	S/C ratio	2 - 3
	Inlet pressure ( $P_{ref}$ )	20 - 40 bar
	Pressure drop	5% of inlet
	Solids initial temperature ( $T_1$ )	850 - 950°C
	NiO/C ratio	Set to meet autothermal cycle
	NiO catalyst loading	20 wt% [282]
	Sorbent capacity	0.08
	Bio-oil vapour fraction at inlet	1
	Water vapour fraction at inlet	1

Variable		SE-CLSR process variable
<i>Oxidation stage</i>	Reactor pressure	P <sub>ref</sub>
	Air pressure	P <sub>ref</sub>
	Inter-stage cooling temperature	30°C
<i>Reduction/calcination</i>	Solids outlet temperature	T <sub>1</sub>
	Reactor pressure	1.2 bar
	Off-gas pre-heat temperature	100°C below T <sub>1</sub>
<i>Syngas flash drum</i>	Inlet temperature	30°C
	Pressure drop	0 bar
<i>PSA</i>	H <sub>2</sub> recovery	90%
<i>Gas turbine</i>	Compressor outlet pressure	17 bar
	Expander outlet pressure	1.013 bar
	Combustor outlet temperature	1350°C
<i>H<sub>2</sub> compression</i>	Product pressure	40 bar
	Product temperature	30°C
<i>CO<sub>2</sub> compression &amp; drying</i>	Outlet pressure	110 bar [136,242,251]
	Power requirement	0.085 kWh kg <sub>CO2</sub> <sup>-1</sup> [136]

## 5.2.6 Economic assumptions

The levelised cost of hydrogen (LCOH) and cost of carbon avoided (CCA) were calculated according to the equations given in **Chapter 3**. This requires the estimation of capital costs and the cost of manufacture (operating costs). Capital costs were estimated using the method of Turton et al. [243], as described in **Chapter 3**. As far as possible, equipment costs were taken from the cost curves in Turton et al. [243]. For certain systems, where cost curve data was not available, single point cost data were taken from literature (**Table 5.9**) and scaled using the scaling formula:

$$C_{mod} = C_{mod,0} \left( \frac{S_{mod}}{S_0} \right)^f \times I \quad \text{Eq. 5.3}$$



**Table 5.9 – Single point cost data for bare module cost**

Unit	Base size	Base cost (m\$)	f	Installation factor	Year	Ref
WGS	15.6 Mmol h <sup>-1</sup> CO + H <sub>2</sub>	36.9	0.85	1	2001	[332]
PSA	9600 kmol h <sup>-1</sup> throughput	28	0.7	1.69	2001	[332]
CO <sub>2</sub> capture (MDEA)	62.59 kg s <sup>-1</sup> CO <sub>2</sub> captured	104.2	0.8	-	2017	[251]
CO <sub>2</sub> compression & drying	13 MW compressor power	17.9	0.67	-	2017	[251]
High temperature three-way valve	2 m <sup>3</sup> s <sup>-1</sup>	0.1695	0.6	-	2014	[327]
HDS plant	30,000 BPD	16	0.65	-	1991	[311]

As described in **Chapter 3**, the cost of manufacture is defined as follows:

$$COM_d = 0.18FCI + 2.73C_{OL} + 1.23(C_{UT} + C_{WT} + C_{RM}) \quad \text{Eq. 5.4}$$

The terms in this equation were estimated using the data in **Table 5.10**.

The price of bio-oil was based upon a review of literature, including bio-oil from various feedstocks and locations. However, variations or uncertainty in bio-oil cost could have a strong influence on the economics analysis, examined in the sensitivity analysis (**Section 5.4.3**).

Reforming catalyst lifetime was assumed to be low, due to carbon deposition issues associated with bio-oil. For this study, the lifetime was assumed to be 1 year. The WGS catalyst lifetime was assumed to be 5 years, similar to a current industrial process [328], as the feed to the WGS is syngas, rather than bio-oil. In SE-CLSR, OTM lifetime was assumed to be slightly longer, at 2 years, as the thermodynamic analysis in **Chapter 4** concluded that the presence of OTM and sorbent materials would reduce the tendency for coke deposition. In addition, the oxidation step of SE-CLSR enables the oxidation of carbon deposits [271]. The sorbent lifetime is also assumed to be 2 years, as the bed of sorbent and catalyst would be changed out at the same time. Power generated by turbines was off-set against total power requirements, to give a net power import or export, with the associated cost in **Table 5.10**.

**Table 5.10 – Assumptions for calculation of operating cost**

Materials		
Bio-oil price	0.2 \$ kg <sup>-1</sup>	[90,333,334]
Methanol price	0.37 \$ kg <sup>-1</sup>	[335]
Reforming catalyst/oxygen carrier price	20 \$ kg <sup>-1</sup>	[202,336]
WGS catalyst price	60 \$ kg <sup>-1</sup>	[242]
CaO sorbent	1.1 \$ kg <sup>-1</sup>	[162]
WHSV for steam reforming	1 h <sup>-1</sup>	[119]
GHSV for WGS	3000 h <sup>-1</sup>	[202,337]
Reforming WHSV (SE-CLSR)	0.8 h <sup>-1</sup>	[190]
Reforming catalyst lifetime (C-SR)	1 year	Assumed
Oxygen carrier lifetime (SE-CLSR)	2 years	Assumed
WGS catalyst lifetime	5 years	[328]
CaO sorbent lifetime	2 years	Assumed
CO <sub>2</sub> solvent	0.04 m\$ yr <sup>-1</sup> per kg <sub>CO2</sub> s <sup>-1</sup>	[251]
Waste treatment		
Waste water disposal	0.538 \$ t <sup>-1</sup>	[338]
Catalyst recovery	-0.11 \$ kg <sup>-1</sup>	[328]
Utilities		
Process water	0.2 \$ t <sup>-1</sup>	[339]
Electricity (purchase)	100 \$ MWh <sup>-1</sup>	[340]
Electricity (export)	50 \$ MWh <sup>-1</sup>	[340]
Steam (purchase/export)	20.9 \$ MWh <sup>-1</sup>	Calculated <sup>b</sup>
Natural gas	25 \$ MWh <sup>-1</sup>	[340]
Cooling water	0.4 \$ m <sup>-3</sup>	[339]
Other assumptions		
Plant availability	360 days yr <sup>-1</sup>	-
Conversion £ to \$	1.29	[341]
Conversion € to \$	1.13	[341]
Labour cost in UK industry	40,000 £ yr <sup>-1</sup>	[342]
Shifts worked per worker per week	5	-
Shifts per day	3	-
Weeks worked per year	47	-
<sup>a</sup> MDEA solvent cost estimated from [251], pro-rated to process size		
<sup>b</sup> based on natural gas boiler with 90% efficiency [251]		

## 5.3 Technical assessment

### 5.3.1 Heat and material balances

The following heat and material balances illustrate an example design case for each of the three processes: C-SR, C-SR-CCS and SE-CLSR. Stream numbers correspond to the flowsheets in **Section 5.2.5.3**.

**Table 5.11 – Example heat and material balance for C-SR without CO<sub>2</sub> capture. Reforming operating conditions: 900°C, 30 bar, S/C = 5.**

Description Number	Water feed 1	Steam to turbine 2	Steam turbine outlet 3	Bio-oil 4	Methanol 5
Temperature (°C)	25	400	241	25	25
Pressure (bara)	1.013	100.1	31	3.013	3.013
Mass flow (kg/h)	17814	17814	17814	5159.4	573.26
Molar flow (kmol/h)	988.8	988.8	988.8	116.5	17.89
Bio-oil organic fraction (mol%) (Note 1)	0	0	0	41.0	0
(mol%) Methanol	0	0	0	0	100
H <sub>2</sub> O	100	100	100	59.0	0

Description Number	Heated bio-oil/ methanol 6	Feed to reformer 7	Reformer product 8	WGS inlet 9	WGS outlet 10
Temperature (°C)	329	600	900	300	393
Pressure (bara)	30.14	30	28.5	28.2	26.8
Mass flow (kg/h)	5732.6	23547	23547	23547	23547
Molar flow (kmol/h)	134.4	1123	1420	1420	1420
Bio-oil organic fraction (mol%) (Note 1)	35.52	4.21	Trace	Trace	Trace
Methanol (mol%)	13.32	1.59	Trace	Trace	Trace
H <sub>2</sub> O (mol%)	51.16	94.2	57.7	57.7	52.6
H <sub>2</sub> (mol%)	0	0	27.41	27.41	32.5
CH <sub>4</sub> (mol%)	0	0	0.11	0.11	0.11
CO (mol%)	0	0	5.55	5.55	0.45
CO <sub>2</sub> (mol%)	0	0	9.21	9.21	14.3

<b>Description</b>	<b>PSA inlet</b>	<b>Hydrogen product</b>	<b>PSA off-gas</b>	<b>Furnace fuel</b>
<b>Number</b>	<b>11</b>	<b>12</b>	<b>13</b>	<b>14</b>
Temperature (°C)	30	25	33	25
Pressure (bara)	26.5	40	1.1	1.1
Mass flow (kg/h)	10105	837.62	9267.5	1303.0
Molar flow (kmol/h)	674.2	415.5	258.7	81.22
Bio-oil organic fraction (mol%)	Trace	0	0	0
Methanol (mol%)	Trace	0	0	0
H <sub>2</sub> O (mol%)	0.15	0	0.4	0
H <sub>2</sub> (mol%)	68.48	100	17.85	0
CH <sub>4</sub> (mol%)	0.24	0	0.62	100
CO (mol%)	0.94	0	2.45	0
CO <sub>2</sub> (mol%)	30.15	0	78.58	0

<b>Description</b>	<b>Furnace air</b>	<b>Heated furnace air</b>	<b>Furnace flue gas</b>	<b>Cooled flue gas</b>
<b>Number</b>	<b>15</b>	<b>16</b>	<b>17</b>	<b>18</b>
Temperature (°C)	25	200	1100	180
Pressure (bara)	1.013	1.1	1.013	0.943
Mass flow (kg/h)	28998	28998	39569	69870
Molar flow (kmol/h)	1005	1005	1319	1319
H <sub>2</sub> O (mol%)	0	0	16.16	16.16
CO <sub>2</sub> (mol%)	0	0	22.19	22.19
O <sub>2</sub> (mol%)	21	21	1.44	1.44
N <sub>2</sub> (mol%)	79	79	60.21	60.21

**Table 5.12 – Example heat and material balance for C-SR with CO<sub>2</sub> capture.  
Reforming operating conditions: 900°C, 30 bar, S/C = 5.**

Description Number	Water	Steam	Steam turbine	Bio-oil	Methanol
	feed 1	to turbine 2	outlet 3	4	5
Temperature (°C)	25	340	235	25	25
Pressure (bara)	1.013	100.1	31	3.013	3.013
Mass flow (kg/h)	17814	17814	17814	5159.4	573.26
Molar flow (kmol/h)	988.8	988.8	988.8	116.5	17.89
Bio-oil organic fraction (mol%)	0	0	0	41.0	0
Methanol (mol%)	0	0	0	0	100
H <sub>2</sub> O (mol%)	100	100	100	59.0	0

Description Number	Heated	Feed to	Reformer	Inlet to	WGS
	bio-oil/ methanol 6	reformer 7	product 8	WGS 9	outlet 10
Temperature (°C)	329	600	900	300	393
Pressure (bara)	30.14	30	28.5	28.2	26.8
Mass flow (kg/h)	5732.6	23547	23547	23547	23547
Molar flow (kmol/h)	134.4	1123	1420	1420	1420
Bio-oil organic fraction (mol%)	35.52	4.21	Trace	Trace	Trace
Methanol (mol%)	13.32	1.59	Trace	Trace	Trace
H <sub>2</sub> O (mol%)	51.16	94.2	57.7	57.7	52.6
H <sub>2</sub> (mol%)	0	0	27.41	27.41	32.5
CH <sub>4</sub> (mol%)	0	0	0.11	0.11	0.11
CO (mol%)	0	0	5.55	5.55	0.45
CO <sub>2</sub> (mol%)	0	0	9.21	9.21	14.3

<b>Description</b>	<b>CO<sub>2</sub> capture inlet</b>	<b>CO<sub>2</sub> to drying &amp; compression</b>	<b>PSA inlet</b>	<b>H<sub>2</sub> product</b>	<b>PSA off-gas</b>
<b>Number</b>	<b>11</b>	<b>12</b>	<b>13</b>	<b>14</b>	<b>15</b>
Temperature (°C)	30	30	30	25	34
Pressure (bara)	26.5	26.5	26.5	40	1.1
Mass flow (kg/h)	10105	8497.3	1607.7	837.62	770.19
Molar flow (kmol/h)	674.2	193.1	481.1	415.5	65.57
H <sub>2</sub> O (mol%)	0.15	0	0.22	0	1.59
H <sub>2</sub> (mol%)	68.48	0	95.97	100	70.41
CH <sub>4</sub> (mol%)	0.24	0	0.33	0	2.43
CO (mol%)	0.94	0	1.32	0	9.67
CO <sub>2</sub> (mol%)	30.15	100	2.11	0	15.5

<b>Description</b>	<b>Furnace fuel</b>	<b>Furnace air</b>	<b>Heated furnace air</b>	<b>Furnace flue gas</b>	<b>Cooled flue gas</b>
<b>Number</b>	<b>16</b>	<b>17</b>	<b>18</b>	<b>19</b>	<b>20</b>
Temperature (°C)	25	25	45	1100	180
Pressure (bara)	1.1	1.013	1.1	1.013	0.943
Mass flow (kg/h)	1280.5	28574	28574	30624	30624
Molar flow (kmol/h)	79.82	990.4	990.4	1110	1110
H <sub>2</sub> O (mol%)	0	0	0	18.95	18.95
H <sub>2</sub> (mol%)	0	0	0	0	0
CH <sub>4</sub> (mol%)	100	0	0	0	0
CO (mol%)	0	0	0	0	0
CO <sub>2</sub> (mol%)	0	0	0	8.85	8.85
O <sub>2</sub> (mol%)	0	21	21	1.68	1.68
N <sub>2</sub> (mol%)	0	79	79	70.52	70.52

**Table 5.13 – Example heat and material balance for SE-CLSR.  
Reforming operating conditions: 850°C, 330 bar, S/C = 2.**

Description Number	Water feed 1	Bio-oil 2	Methanol 3	Heated bio-oil/methanol 4	Reformer inlet 5
Temperature (°C)	25	25	25	321	165
Pressure (bara)	1.013	3.013	3.013	20.07	20
Mass flow (kg/h)	8495.7	6867.5	763.06	7630.6	16126
Molar flow (kmol/h)	471.6	155.0	23.81	178.8	650.4
Bio-oil organic fraction (mol%)	0	41.0	0	35.52	9.77
Methanol (mol%)	0	0	100	13.32	3.66
H <sub>2</sub> O (mol%)	100	59.0	0	51.16	86.57

Description Number	Reformer outlet 6	PSA inlet 7	H <sub>2</sub> product 8	PSA off-gas 9A/9B
Temperature (°C)	837	30	25	30
Pressure (bara)	19	18.65	40	1.013
Mass flow (kg/h)	8627.9	4165.3	837.63	3327.6
Molar flow (kmol/h)	821.7	574.0	415.5	158.5
H <sub>2</sub> O (mol%)	30.29	0.20	0	0.73
H <sub>2</sub> (mol%)	56.19	80.43	100	29.13
CH <sub>4</sub> (mol%)	3.54	5.07	0	18.38
CO (mol%)	6.57	9.4	0	34.06
CO <sub>2</sub> (mol%)	3.41	4.89	0	17.70

Description Number	Air 10	Compressed air 11	Flue gas from Stage B 12	PSA off-gas to Stage C 13
Temperature (°C)	25	179	148	750
Pressure (bara)	1.013	20	18.93	1.2
Mass flow (kg/h)	13358	13358	12653	3053.9
Molar flow (kmol/h)	469.3	469.3	422.2	145.4
H <sub>2</sub> O (mol%)	0	0	0	0.73
H <sub>2</sub> (mol%)	0	0	0	29.13
CH <sub>4</sub> (mol%)	0	0	0	18.38
CO (mol%)	0	0	0	34.06
CO <sub>2</sub> (mol%)	0	0	12.20	17.70
O <sub>2</sub> (mol%)	21	21	0	0
N <sub>2</sub> (mol%)	79	79	87.80	0

Description Number	Wet CO <sub>2</sub> from Stage C 14	CO <sub>2</sub> to drying & compression 15	Air to turbine 16	Turbine flue gas 17
Temperature (°C)	850	30	25	180
Pressure (bara)	1.06	0.92	1.013	1.3
Mass flow (kg/h)	11438	9861.0	3356.3	3630.0
Molar flow (kmol/h)	317.7	230.2	116.3	125.3
H <sub>2</sub> O (mol%)	30.34	3.86	0	6.93
H <sub>2</sub> (mol%)	0.16	0.22	0	0
CO (mol%)	0.39	0.54	0	0
CO <sub>2</sub> (mol%)	69.12	95.39	0	7.30
O <sub>2</sub> (mol%)	0	0	21	12.39
N <sub>2</sub> (mol%)	0	0	79	73.38

Description Number	Solids: start of A A-IN	Solids: end of A A-OUT	Solids: start of B B-IN	Solids: end of B B-OUT	Solids: start of B C-IN	Solids: end of B C-OUT
Temperature (°C)	850	837	837	919	919	850
Mass flow (kg h <sup>-1</sup> ) <sup>a</sup>	267805	267805	267805	267805	267805	267805
Molar flow (kmol/h) <sup>a</sup>	4294	4294	4294	4294	4294	4294
Ni (mol%)	4.59	4.59	4.59	0	0	4.59
NiO (mol%)	0	0	0	4.59	4.59	0
Al <sub>2</sub> O <sub>3</sub> (mol%)	13.45	13.45	13.45	13.45	13.45	13.45
CaO (mol%)	81.96	78.00	78.00	79.19	79.19	81.96
CaCO <sub>3</sub> (mol%)	0	3.97	3.97	2.77	2.77	0

<sup>a</sup> In a packed bed gas switching system, mass/molar flows of solids do not represent physical flows through the reactor. Instead the rate represents a rate of conversion within a static bed (Section 5.2.5.3).

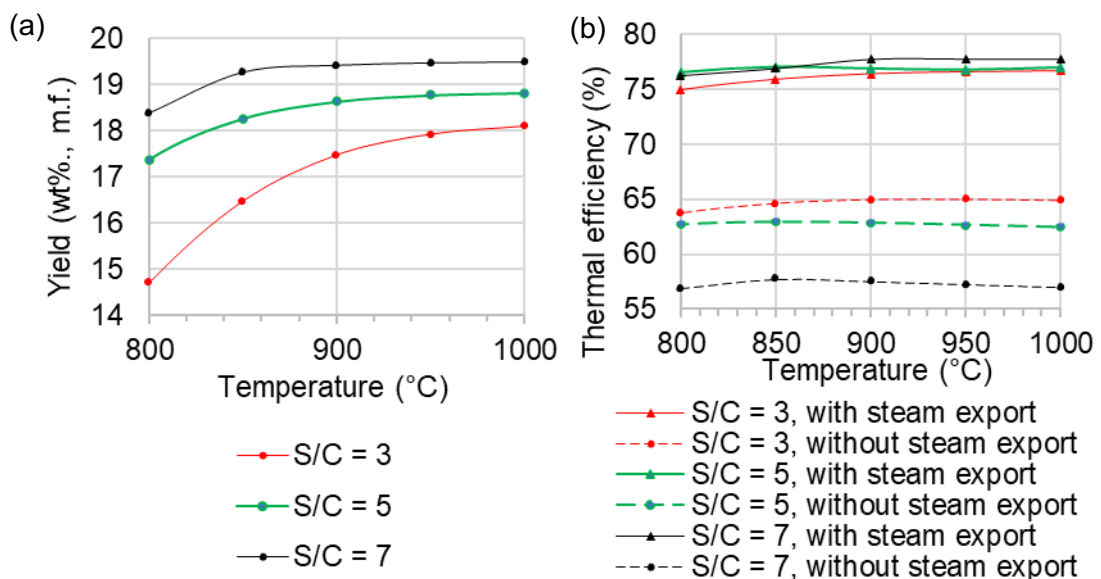
### 5.3.2 C-SR performance without CO<sub>2</sub> capture

**Figure 5.10a** shows the effect on hydrogen yield as the reformer temperature and S/C ratio are varied. H<sub>2</sub> yield is improved by increasing temperature or S/C ratio, although minimal benefit is observed above 950°C. **Figure 5.10b** shows the effect of the same variables on thermal efficiency,



as well as examining the effects of including excess heat as a usable export (streams 'STEAM-1' and 'STEAM-2'). Without steam export, increasing the S/C ratio between 3 and 7 decreases the thermal efficiency. In this range, higher H<sub>2</sub> yield does not outweigh the additional fuel input that is required for higher S/C ratios. However, when LP steam is considered as a useful export, increasing S/C from 3 to 5 leads to a slightly higher thermal efficiency. The additional heat export outweighs the additional fuel input, with the net effect being a small improvement in thermal efficiency.

LP steam export increases the thermal efficiency by around 10%. However, it should be noted that this represents a theoretical efficiency, while in practice there would be a limit to how much steam can be exported. This highlights the importance of selecting the optimal operating regime on a case-by-case basis, for example by using lower S/C ratios if the plant is not co-located with other steam users. This includes the potential to use steam for CO<sub>2</sub> capture, explored further in the following section. Besides these technical performance indicators, higher S/C ratios will have cost implications, explored in **Section 5.4**.

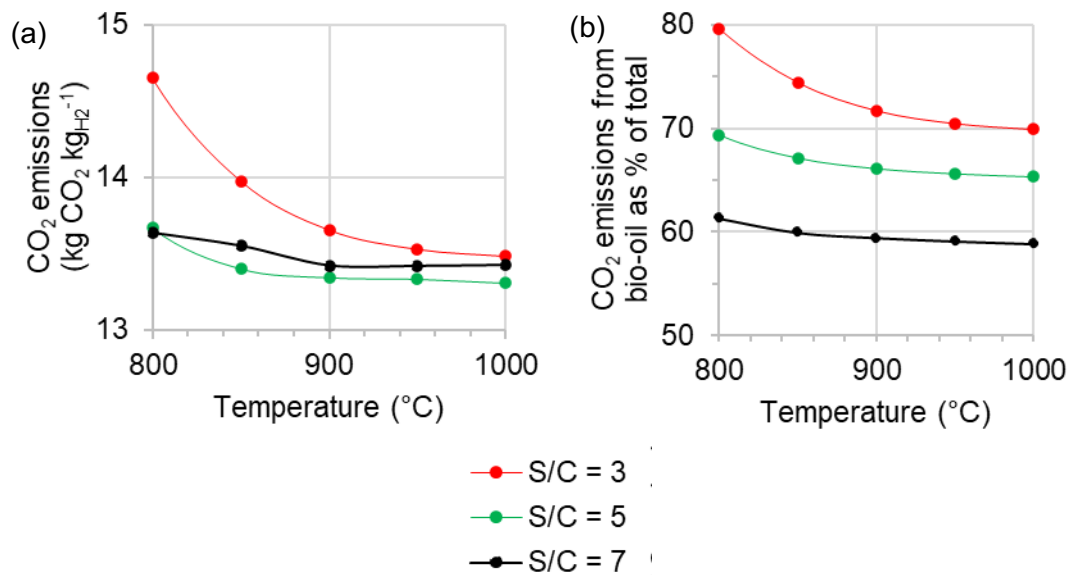


**Figure 5.10 – Effect of reformer temperature and S/C ratio on (a) H<sub>2</sub> yield and (b) thermal efficiency in the C-SR of PEFB bio-oil. Reformer pressure = 30 bar.**

The direct CO<sub>2</sub> emissions are given in **Figure 5.11**, showing the effect of S/C ratio and reformer temperature. Increasing S/C ratio from 3 to 5 reduces the specific emissions (**Figure 5.11a**). With more steam in the reactor, more natural gas combustion is required to sustain the reforming temperature, but this is counterbalanced by an increase in yield (**Figure 5.10a**). As the S/C

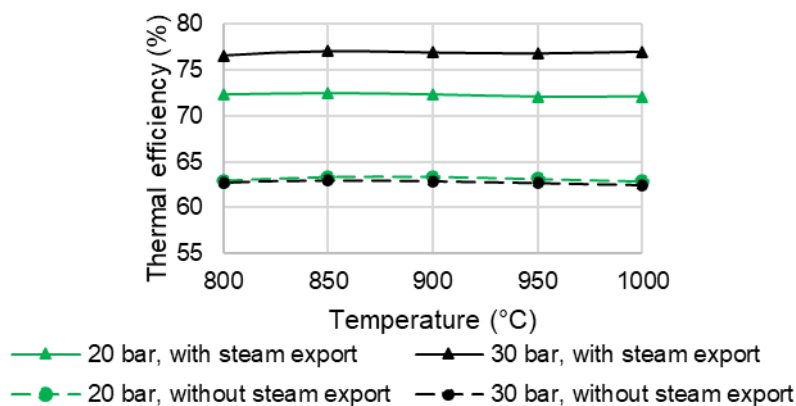
ratio is increased up to 7, the additional CO<sub>2</sub> emissions associated with heat input are not outweighed by the increase in yield. This suggests S/C of 5 is the optimal case for direct CO<sub>2</sub> emissions.

Of these CO<sub>2</sub> emissions, a certain proportion is derived from bio-oil, while the remainder is associated with the methanol (10 wt%) used to stabilise bio-oil, as well as the methane input to the furnace. In **Figure 5.11b**, biogenic emissions contribute the largest share when the S/C ratio and temperature are low, i.e. when less methane is required to support the process. These trends are the inverse of the yield graphs (**Figure 5.10a**), suggesting there is a trade-off between the H<sub>2</sub> yield and the share of biogenic emissions. This could be an important distinction for the economic viability for the plant, especially if there are different price mechanisms for fossil-based emissions and biogenic emissions. This technical and economic trade-off is discussed further in the economic analysis in **Section 5.4**.



**Figure 5.11 – Effect of reformer temperature and S/C ratio on (a) total specific CO<sub>2</sub> emissions and (b) biogenic emissions in the C-SR of PEFB bio-oil. Reformer pressure = 30 bar.**

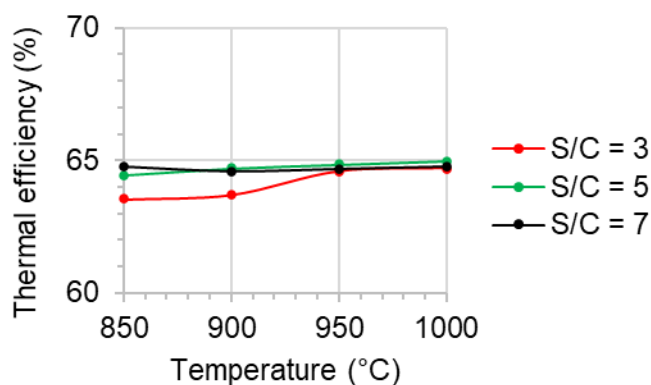
The final parameter to consider is the reformer operating pressure. **Figure 5.12** shows the effect of steam reformer pressure and temperature on the process thermal efficiency. When steam export is not accounted for, the pressure has minimal effect on thermal efficiency. The effects of higher reformer pressure are reduced by the high temperature. In addition, reductions in reformer yield at high pressure are balanced by other efficiency effects, such as reducing hydrogen compression power. The higher pressure (30 bar) process is around 5% more efficient when steam export is included, as this process has more excess heat available in the flue gas.



**Figure 5.12 – Effect of reformer temperature and pressure on thermal efficiency of C-SR, with and without steam export (S/C = 5).**

### 5.3.3 C-SR performance with CO<sub>2</sub> capture

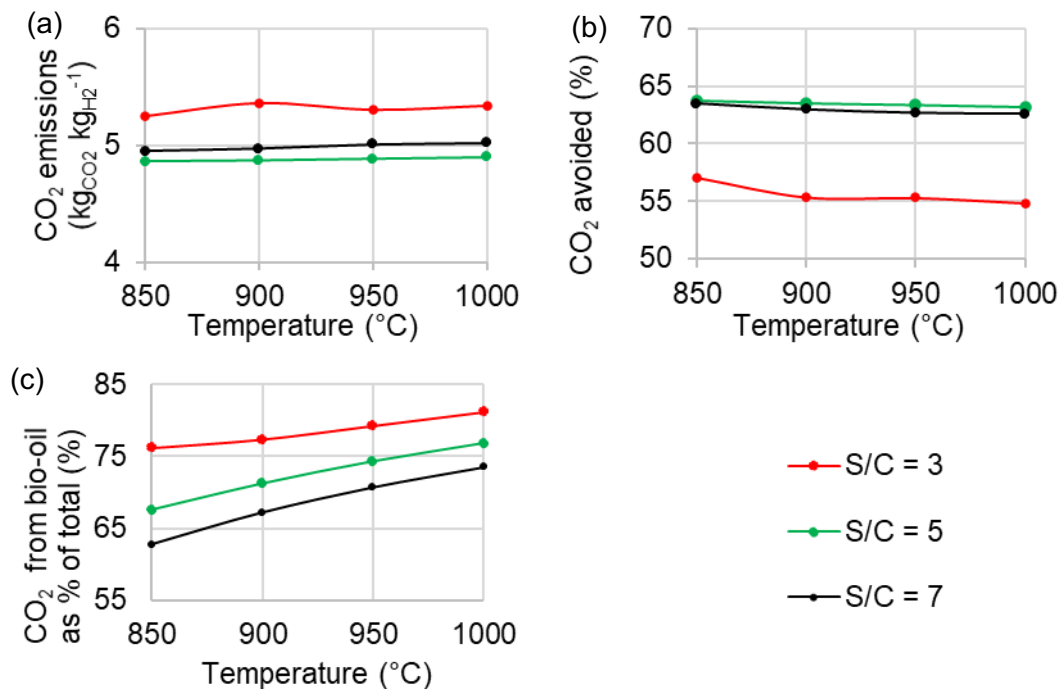
The addition of CO<sub>2</sub> capture does not affect the hydrogen yields from the process, as CO<sub>2</sub> capture is located downstream of the WGS reactor. This can be seen in the example heat and material balances (Table 5.11 and Table 5.12). However, Figure 5.13 shows that the addition of CO<sub>2</sub> capture decreases the thermal efficiency by around 10%, compared to a process with LP steam export, or is similar to the process without steam export (Figure 5.10b). Excess LP steam produced by the process is no longer available for export, and instead is used for regenerating solvent in the CO<sub>2</sub> capture process.



**Figure 5.13 – Effect of reformer temperature and S/C ratio on thermal efficiency in C-SR with CO<sub>2</sub> capture. Reformer pressure = 30 bar.**

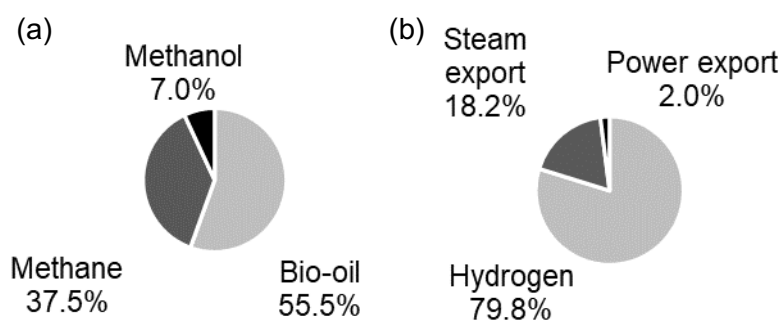
Figure 5.14 shows the direct CO<sub>2</sub> emissions from the process. By the addition of CO<sub>2</sub> capture, the specific emissions are reduced from around 14 kg<sub>CO2</sub> kg<sub>H2</sub><sup>-1</sup> (Figure 5.11a) to around 5 kg<sub>CO2</sub> kg<sub>H2</sub><sup>-1</sup> (Figure 5.14a). This amounts to around 55 to 65% reduction in CO<sub>2</sub> emissions, shown in Figure 5.14b. The reduction in emissions is derived from a dual effect. There is a

95% capture efficiency on the PSA off-gas, which contains about 60% of the total carbon in the process. In addition, the removal of CO<sub>2</sub> from the off-gas makes the off-gas less dilute, so that it is a more effective fuel for the furnace. As a result, the methane input to the furnace is slightly reduced (see the heat and material balances, **Table 5.11** and **Table 5.12**). The latter of these effects reduces the contribution of fossil-based emissions by around 5%, as shown in **Figure 5.14c**.

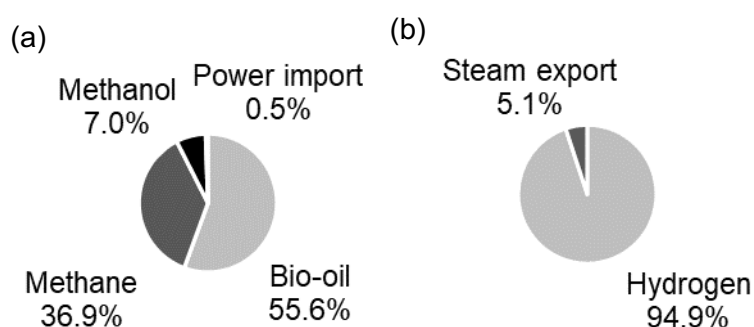


**Figure 5.14 – Effect of reformer temperature and S/C ratio on (a) total specific CO<sub>2</sub> emissions, (b) CO<sub>2</sub> capture efficiency and (c) biogenic emissions in C-SR with CO<sub>2</sub> capture. Reformer pressure = 30 bar.**

**Figure 5.15** and **Figure 5.16** show the impact of CO<sub>2</sub> capture on energy inputs and outputs, on an LHV basis. In **Figure 5.15**, the C-SR plant without CO<sub>2</sub> capture has a net surplus of both steam and electricity. However, the plant with CO<sub>2</sub> capture (**Figure 5.16**) has a large heat requirement for CO<sub>2</sub> capture, as well as power for CO<sub>2</sub> compression. The amount of excess steam and power is considerably reduced, to the extent that power changes from being an export to an import. In both processes, bio-oil contributes around 56% of the total energy input, with the remainder being derived from methanol and methane.



**Figure 5.15 – Breakdown of (a) energy inputs and (b) energy outputs to C-SR without CO<sub>2</sub> capture. S/C = 5 at 900°C, with reformer pressure of 30 bar.**



**Figure 5.16 – Breakdown of (a) energy inputs and (b) energy outputs to C-SR with CO<sub>2</sub> capture. S/C = 5 at 900°C, with reformer pressure of 30 bar.**

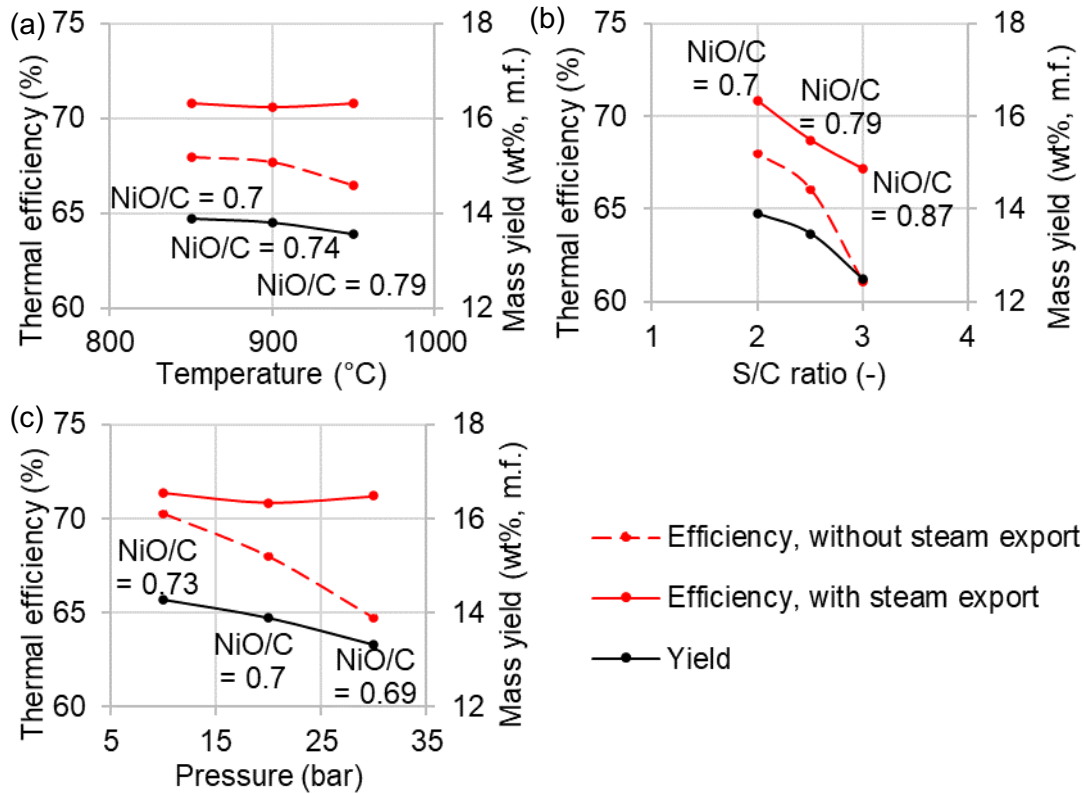
### 5.3.4 SE-CLSR performance with CO<sub>2</sub> capture

**Figure 5.17** shows the effect of temperature, as well as S/C ratio and pressure, on thermal efficiency and hydrogen yield. The NiO/C ratios displayed on **Figure 5.17** are the NiO/C ratios which are required to achieve a full autothermal temperature cycle in each case (**Section 5.2.4.1**). The thermal efficiency of SE-CLSR with CO<sub>2</sub> capture is the same, or slightly higher, than a C-SR process with CO<sub>2</sub> capture (**Figure 5.13**).

Increasing the temperature above 850°C decreases the overall yield (**Figure 5.17a**), as does increasing the S/C ratio (**Figure 5.17b**). This is because a higher NiO/C ratio is required to sustain the autothermal temperature cycle. The higher solids inventory has a number of effects that reduce yield and efficiency, including higher bed heat capacity, more air required for oxidation, and more off-gas used for reduction. This highlights the importance of considering the full autothermal cycle when optimising SE-CLSR, rather than considering a single step in isolation.

Increasing the pressure between 20 and 40 bar leads to approximately 5% drop in efficiency, if steam export is not included (**Figure 5.17c**). However, if

steam export is also considered, the ability to export spare heat compensates for the drop in hydrogen yield, so that efficiency remains fairly constant. As discussed for C-SR, the optimal operating point may be linked to the availability of a nearby steam user.

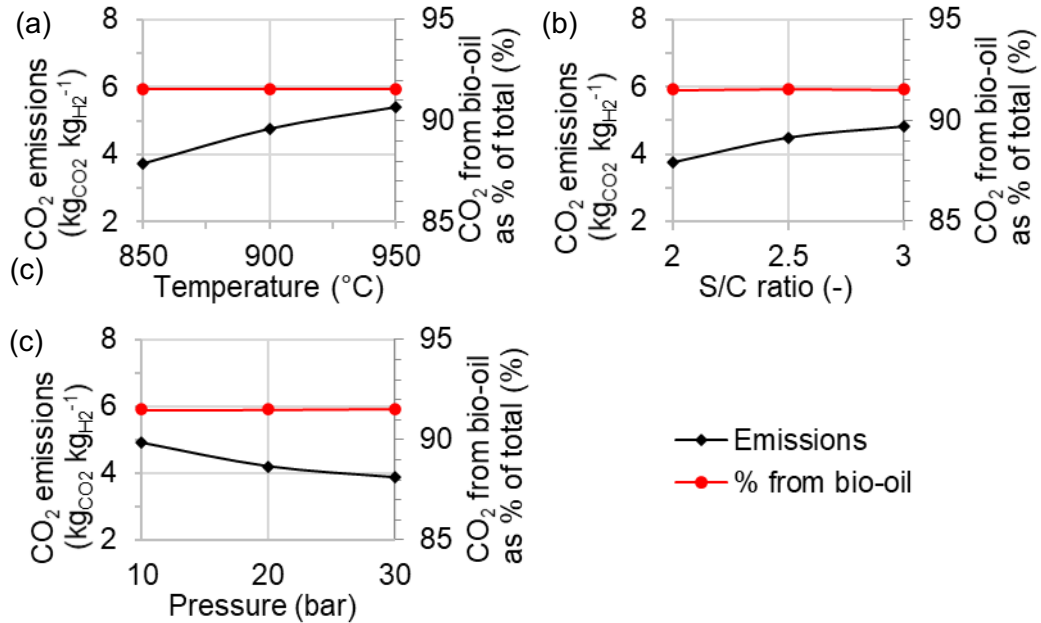


**Figure 5.17 – Thermal efficiency and yield of SE-CLSR, showing the effect of (a) temperature, (b) S/C ratio and (c) pressure. Base conditions are 20 bar, 850°C, S/C = 2.**

One factor not considered here is the amount of inert material in the bed, including both  $\text{Al}_2\text{O}_3$  and inactive  $\text{CaO}$ . Inert materials influence the heat balance as they do not contribute to reaction heats, but do increase the total heat capacity of the bed. On the one hand, this can inhibit product yields by decreasing reformer temperatures. However, keeping temperatures low also have a beneficial effect by ensuring that the sorbent calcination is controlled (**Figure 5.5**). This study assumes 20 wt%  $\text{NiO}/\text{Al}_2\text{O}_3$  as the base case [282], but future work could consider the role of inert materials in optimisation.

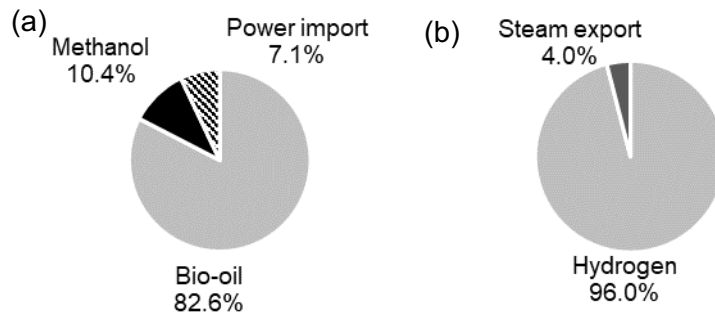
**Figure 5.18** shows the specific  $\text{CO}_2$  emissions, and the proportion of these from bio-oil. As SE-CLSR does not require methane to support a furnace, over 90% of the  $\text{CO}_2$  emissions are from bio-oil, with the remaining 10% derived from electricity import and methanol.  $\text{CO}_2$  emissions can be minimised by operating at lower temperature (850°C) and higher pressure (30 bar) because this provides better control of  $\text{CO}_2$  slip in the oxidation

stage. Specific CO<sub>2</sub> emissions are also reduced by a lower S/C ratio, due to higher H<sub>2</sub> yield.



**Figure 5.18 – Effect of reformer temperature and S/C ratio on (a) total specific CO<sub>2</sub> emissions and (b) biogenic emissions in the SE-CLSR of PEFB bio-oil. Reformer pressure = 20 bar.**

**Figure 5.19** shows the heat inputs and outputs. All heat is provided by the bio-oil/methanol feedstock, without any support from methane combustion. As bio-oil is a more expensive energy source than methane, this has economic implications, discussed in the following section. Also notable is that the SE-CLSR process requires power import, as the gas turbine powered by excess PSA off-gas is not sufficient to meet the process power requirements.



**Figure 5.19 – Breakdown of (a) energy inputs and (b) energy output to SE-CLSR at 20 bar, 850°C, S/C = 2.**

## 5.4 Economic assessment

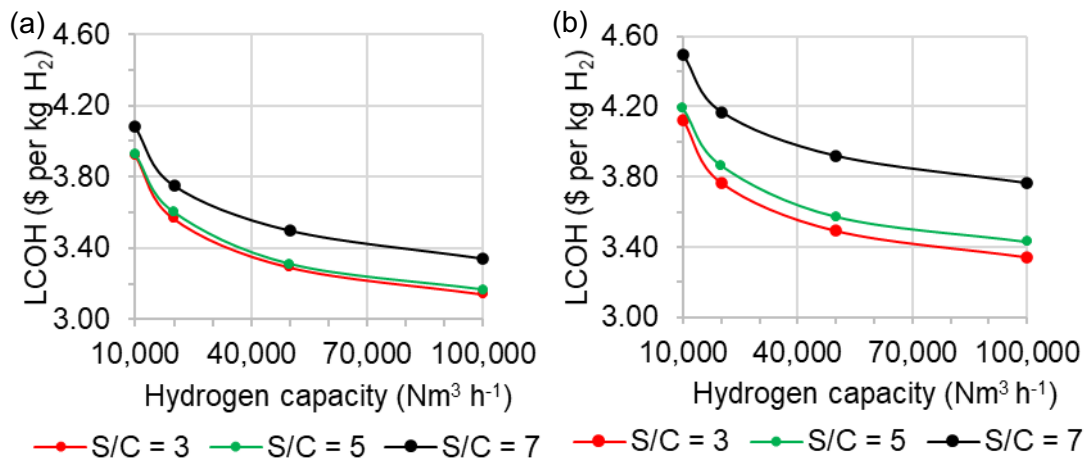
### 5.4.1 Selection of a design basis

The technical evaluation can be used to formulate the basis of design for economic analysis. The temperature selected for the economic study of C-SR and C-SR-CCS is 900°C. At this temperature, the yield and efficiency are close to their maximum, and CO<sub>2</sub> emissions are minimised. The pressure is fixed at 30 bar, as the comparison in **Figure 5.12** showed that this provides a higher thermal efficiency. The impacts of S/C ratio are more complex, and could have significant impact on process cost, and so S/C ratio is retained as a sensitivity in the first part of the economic analysis. All other assumptions are the same as described in **Table 5.7**.

**Figure 5.20** shows the effect of S/C ratio on the levelized cost of hydrogen (LCOH) at different sizes of C-SR. The LCOH with S/C = 3 and S/C = 5 is very similar. This is because the additional capital and operating costs associated with higher S/C ratio are outweighed by increased yield and the ability to export excess heat. However, if S/C is increased further to S/C = 7, there is a larger rise in price. The extra investment is no longer outweighed by increased yield or heat export. This suggests it is possible to apply increase S/C ratio up to 5 in order to mitigate carbon deposition, without a large economic disadvantage. The evaluation does not factor in the potential extension to catalyst lifetime, which may further improve the economic case for high S/C ratios.

Comparing **Figure 5.20a** and **Figure 5.20b**, the ability to export steam reduces the cost of hydrogen by around 10%. This further reinforces the point that opportunities for external heat integration may be an important influence in process optimisation. However, the technical evaluation showed that excess heat from reforming can be used to offset the heat demands of a CO<sub>2</sub> capture process. In this case, excess heat from steam reforming will have an inherent value, regardless of heat export opportunities. For this reason, S/C ratio of 5 is selected as the basis for further economic analysis.

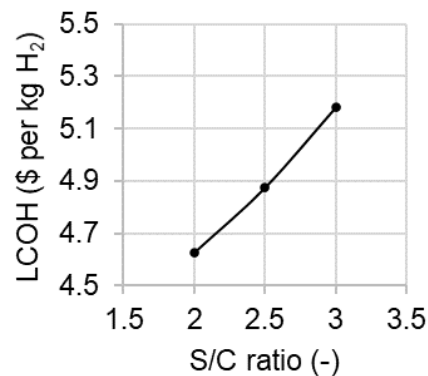




**Figure 5.20 – Effect of S/C ratio and capacity on levelised cost of hydrogen in C-SR at 30 bar and 900°C (a) without steam export (b) with steam export. H<sub>2</sub> production capacity = 10,000 Nm<sup>3</sup> h<sup>-1</sup>**

For SE-CLSR,  $T_1$  is set at 850°C, as this optimises CO<sub>2</sub> emissions (**Figure 5.18**) without having a detrimental effect on thermal efficiency (**Figure 5.17a**). A pressure of 20 bar is assumed, to balance efficiency with CO<sub>2</sub> emissions.

**Figure 5.21** shows the effect of S/C ratio on the cost of hydrogen in SE-CLSR. The SE-CLSR process costs appear to be quite sensitive to S/C ratio. **Section 5.3.4** highlighted that higher S/C ratios require a higher NiO/C ratio to sustain the autothermal temperature cycle, resulting in higher capital and operating costs, while also reducing hydrogen yield and increasing emissions. S/C ratio of 2 was therefore selected as the base case for economic analysis of SE-CLSR. However, this preliminary analysis has highlighted that the economics of bio-oil SE-CLSR are potentially sensitive to S/C ratio. Future experimental work should be used to assess the viability of different S/C ratios over long-term operation and subsequently be used to inform future techno-economic analysis.



**Figure 5.21 – Effect of S/C ratio on the levelised cost of hydrogen from SE-CLSR at 20 bar, with  $T_1 = 850^\circ\text{C}$ .**

The parameters in **Table 5.14** are selected as the design basis on which to compare processes in the economic analysis. The differences in operating conditions represent the optimal conditions for each process type, according to the technical and preliminary economic evaluations outlined above.

**Table 5.14 – Design basis for economic comparisons**

	C-SR	C-SR-CCS	SE-CLSR
Reformer pressure (bar)	30	30	20
Reformer temperature (°C)	900	900	850
S/C ratio	5	5	2
NiO/C ratio	-	-	0.7

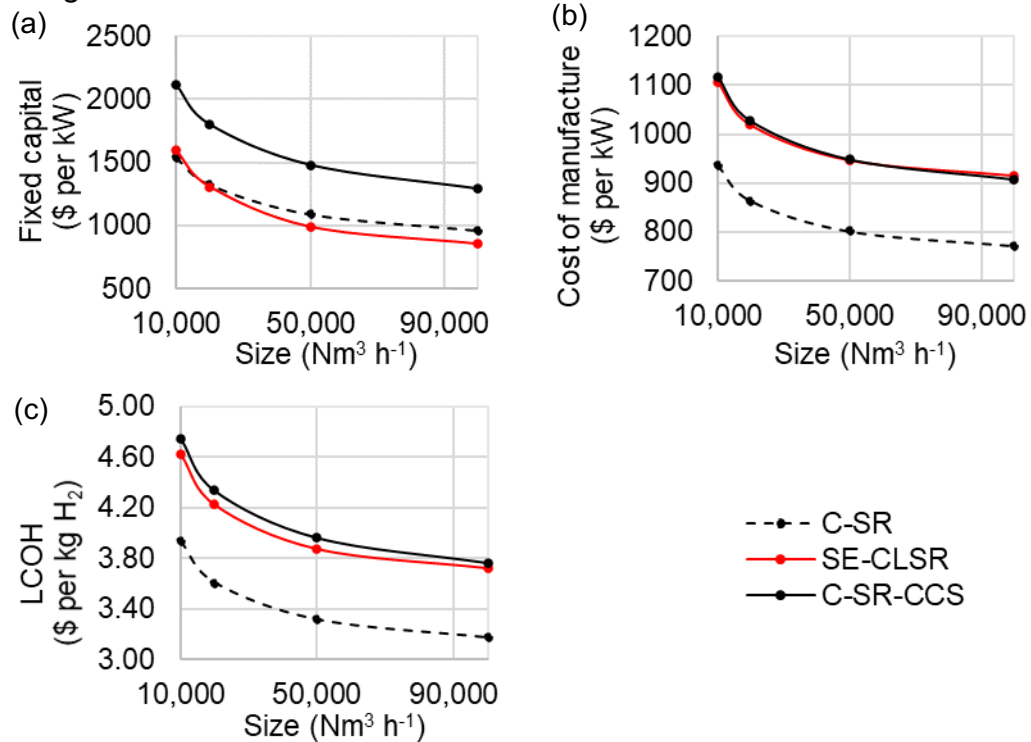
#### 5.4.2 Economic comparison of processes

Following confirmation of the design basis, the three process types are compared for their economic performance. **Figure 5.22** shows the cost comparisons, including fixed capital, cost of manufacture and LCOH. All three processes demonstrate economies of scale. For example, in the case of SE-CLSR, cost of hydrogen reduces from 4.63 to 3.76 \$ kg<sub>H2</sub><sup>-1</sup>, a reduction of 19%, as size increases from 10,000 to 100,000 Nm<sup>3</sup> h<sup>-1</sup>. Both SE-CLSR and C-SR-CCS are more costly than C-SR without CCS, reflecting the costs of CO<sub>2</sub> capture capabilities.

The LCOH is similar to the projections for biomass gasification, shown in **Figure 5.1**, but have the additional benefit of including CO<sub>2</sub> capture. While the prices are higher than other methods of hydrogen production, they may still be viable. The Hydrogen Council has projected that even with H<sub>2</sub> costs at the pump of 6 \$ kg<sub>H2</sub><sup>-1</sup>, H<sub>2</sub> would be cost-competitive for 15% of transport energy demand by 2030 [47]. In addition, these simple LCOH comparisons do not reflect the potential cost of carbon emissions, or value of negative emissions, discussed in further detail below. The capital costs in \$ kW<sup>-1</sup> are in a similar price range to those quoted in the review by Dodds for other production routes, including small SMR, gasification, or electrolysis [302].

SE-CLSR has similar operating costs to C-SR-CCS (**Figure 5.22b**), but a slightly lower capital cost (**Figure 5.22a**). These differences are examined in more detail by cost breakdowns given below. Given the level of uncertainty in these basic cost estimates, it is difficult to say definitively whether SE-CLSR has a lower hydrogen cost than C-SR-CCS. Instead, these cost estimates indicate that the LCOH is a similar magnitude for both processes.

**Section 5.4.3** contains sensitivity analyses that examine which aspects have the greatest influence on cost.

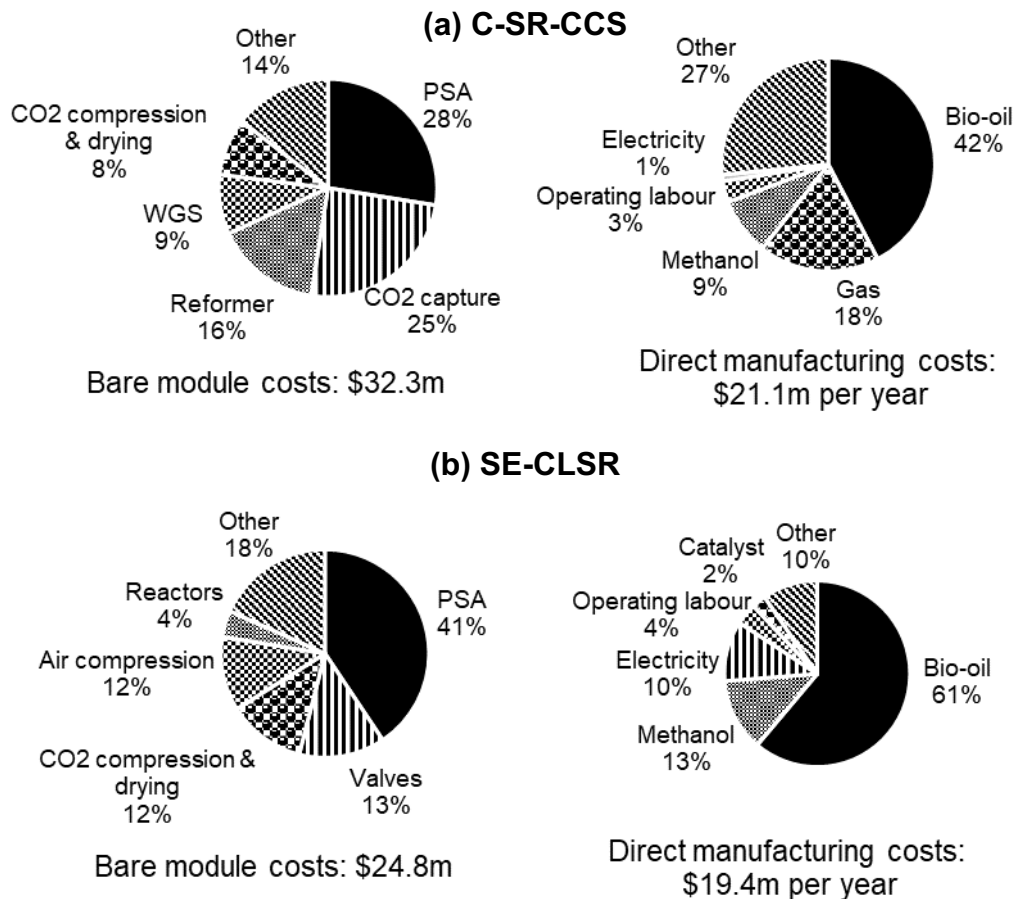


**Figure 5.22 – Cost analysis of base case C-SR and SE-CLSR processes with steam export (a) fixed capital costs (b) cost of manufacture, and (c) LCOH**

**Figure 5.23** shows a breakdown of bare module costs and direct manufacturing costs in C-SR-CCS and SE-CLSR. For both processes, PSA is the largest bare module cost. In C-SR-CCS, the CO<sub>2</sub> capture system is located upstream of the PSA, reducing the size and cost of PSA. However, the CO<sub>2</sub> capture system is an equally large contributor to cost, such that the cost of both separation systems (PSA + CO<sub>2</sub> capture) is 53% of the total.

**Figure 5.23b** shows that, although SE-CLSR does not require the costly CO<sub>2</sub> capture system, three-way valves are potentially a relatively large contributor to cost. These major equipment cost contributors are evaluated in the sensitivity analysis that follows (**Section 5.4.3**).

In both processes, bio-oil is the largest contributor to direct manufacturing costs. This is especially the case in SE-CLSR, as this process derives all its heat from the bio-oil/methanol feedstock, without the support of natural gas. While this has advantages for emissions reduction, it affects the hydrogen price as bio-oil is a more expensive source of energy. Also notable is the cost of electricity in SE-CLSR, highlighting that further SE-CLSR process optimisation may benefit from providing greater self-sufficiency.



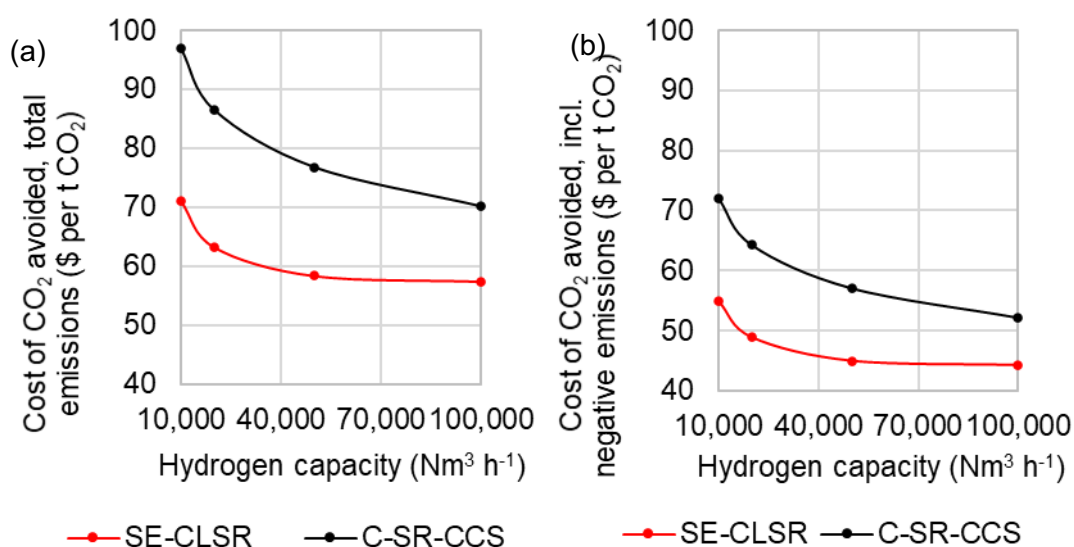
**Figure 5.23 – Breakdown of bare module costs and direct manufacturing costs in a 10,000 Nm<sup>3</sup> h<sup>-1</sup> process for (a) C-SR-CCS and (b) SE-CLSR**

As discussed above, the process have different sources of carbon. If fossil-based and biogenic emissions are treated differently, the net CO<sub>2</sub> balance is changed. When biogenic emissions are accounted for as 'negative emissions', the total carbon avoided is increased by around 30% (**Table 5.15**). This has a considerable effect on the cost of carbon avoided, shown in **Figure 5.24**. A potential route to avoid this complication is to use another biogenic source of heat, such as biogas, or hydrogen product, although these will have potentially high costs. The technical and economic balance between fossil fuel and bioenergy fuel sources is a unique challenge for BECCS processes, and will be an important factor in determining the optimal business models and policy support mechanisms to support negative emissions technologies.

**Figure 5.24** also shows that SE-CLSR has a lower cost of carbon avoided than C-SR-CCS. There are two contributing factors. For SE-CLSR, the cost of hydrogen is slightly lower. In addition, SE-CLSR has a higher CO<sub>2</sub> capture rate (**Table 5.15**).

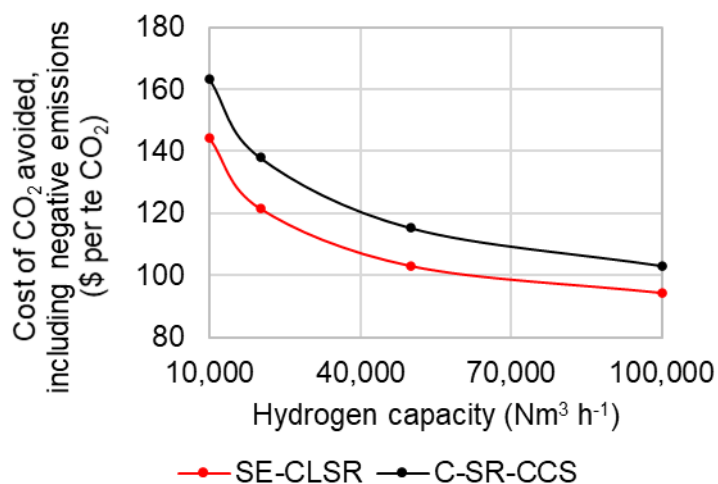
**Table 5.15 – Comparison of total emissions and negative emissions**

Process	Specific emissions from process ( $\text{kg}_{\text{CO}_2} \text{ kg}_{\text{H}_2}^{-1}$ )					
	Without negative emissions		With negative emissions			
	CO <sub>2</sub> emitted	CO <sub>2</sub> avoided	Fossil-based CO <sub>2</sub> emitted	Biogenic CO <sub>2</sub> captured	Net CO <sub>2</sub> emissions	CO <sub>2</sub> avoided
C-SR	13.3	-	3.2	0	3.2	-
C-SR-CCS	4.9	8.5	0.46	8.7	-8.2	11.4
SE-CLSR	3.5	9.8	2.2	10.6	-9.5	12.7



**Figure 5.24 – Cost of carbon avoided in C-SR-CCS and SE-CLSR, compared to bio-oil C-SR base case (a) total direct CO<sub>2</sub> emissions and (b) including negative emissions**

The cases above assume bio-oil steam reforming as the reference case, in order to compare the costs of CO<sub>2</sub> capture. Another useful metric is to find the CCA compared to the current predominant method of hydrogen production, steam methane reforming. To do this comparison, costs and emissions for SMR were taken from Riva et al. [251]. **Figure 5.25** shows that, using SMR as the benchmark, the CCA is increased, because natural gas is a cheap and readily available fuel compared to bio-oil. The influence of bio-oil cost is studied further in the sensitivity analysis (**Section 5.4.3**).



**Figure 5.25 – Cost of carbon avoided (direct emissions) compared to methane C-SR, including negative emissions**

As seen in the graph, economies of scale also have a significant influence. If bio-oil processes are operated at a scale of 100,000 Nm<sup>3</sup> h<sup>-1</sup>, closer to a typical SMR process, the CCA relative to methane is reduced down to 94 \$ kg<sub>H<sub>2</sub></sub><sup>-1</sup>. However, this does not consider the accessibility of bio-oil feedstock. Considering this is a BECCS process with negative emissions, the values are within the range for other forms of BECCS (Table 5.16).

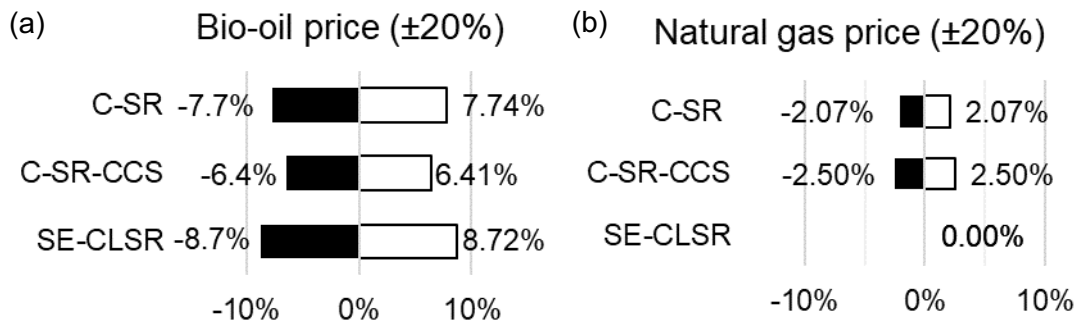
The scope of this feasibility analysis has focussed only on direct CO<sub>2</sub> emissions, and has not considered lifecycle emissions from bio-oil. Future work on bio-oil stream reforming could include a full lifecycle assessment (LCA). While there are LCAs on bio-hydrogen production from bio-oil [129,343], these do not yet include CCS and the potential for negative emissions.

**Table 5.16 – Cost of CO<sub>2</sub> avoided in BECCS processes**

Sector	Cost of CO <sub>2</sub> avoided (\$ t <sub>CO<sub>2</sub></sub> <sup>-1</sup> )	Ref.
Hydrogen from bio-oil – C-SR-CCS	103 – 163	This work
Hydrogen from bio-oil – SE-CLSR	94 – 144	This work
Combustion	88 – 288	[344]
Ethanol	20 – 175	[344]
Pulp and paper mills	20 – 70	[344]
Biomass gasification	30 – 76	[344]

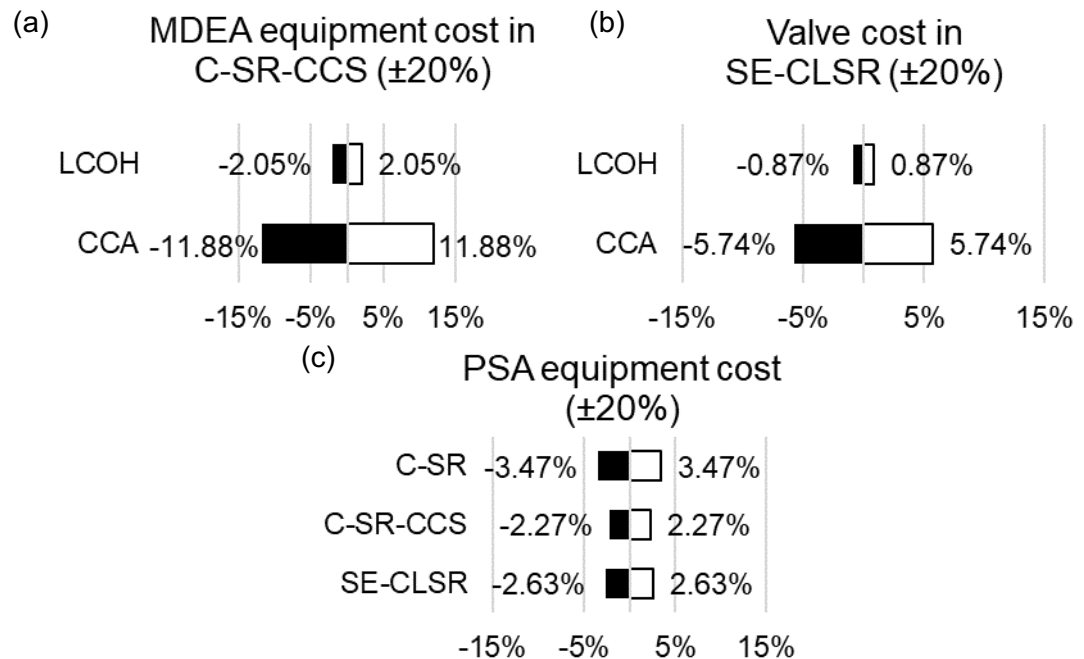
### 5.4.3 Sensitivity analysis

Figure 5.26 shows the effects of the feedstock costs on the levelised cost of hydrogen. Bio-oil price has the largest effect on price. This is particularly true for SE-CLSR, as all heat for the process is provided by bio-oil, without the support of natural gas. Thus SE-CLSR might be more attractive economically at lower bio-oil prices, or increased natural gas prices.



**Figure 5.26 – Effect of feedstock costs on LCOH, showing influence of (a) bio-oil price and (b) natural gas price**

**Figure 5.27** shows the impact of certain equipment costs, focussing on the most significant costs in each process. A 20% change in MDEA process cost has a relatively small impact on LCOH ( $\pm 2\%$ ), but changes the cost of carbon avoided by nearly 12%. Thus an important next step in better defining C-SR-CCS cost could be to study the costs of CO<sub>2</sub> capture from a bio-oil syngas. Similarly, the fixed bed SE-CLSR process could be strongly influenced by the cost of three-way valves, and so the design and cost of these valves warrants further attention.



**Figure 5.27 – Sensitivity analysis on capital costs**

#### 5.4.4 Impacts of desulphurisation and catalyst performance

In SMR, the feed gas is typically pre-treated to reduce sulphur levels to 0.1 ppmv (dry), in order to preserve the steam reforming catalyst [130]. To understand the need for desulphurisation in bio-oil reforming, the

concentration in ppmv at the reformer inlet can be compared to an SMR feed. **Table 5.17** shows the results of this calculation. This shows that the level of sulphur is much higher than 0.1 ppmv (dry), and desulphurisation is likely to be required.

**Table 5.17 – Sulphur levels at reformer inlet conditions in C-SR**

Description	Value
Sulphur in bio-oil (wt%, wet)	0.05
Bio-oil as proportion of reformer feed (wt%, wet)	22
Sulphur in reformer feed (wt%, wet)	0.011
Inlet pressure (bar)	30
Temperature (°C)	900
Molar mass reformer feed (kg kmol <sup>-1</sup> )	20.97
Density reformer feed (kg m <sup>-3</sup> )	6.45
Sulphur, ppmv (wet)	72
Water in feed (vol%)	94
Sulphur, ppmv (dry)	1223

**Table 5.18** summarises the technical and economic impacts of including HDS for sulphur removal. Plant data is based on a naphtha HDS system [311], designed to reduce sulphur from 0.2 wt% to 1 ppmwt. While this exceeds the needs of a bio-oil plant, it provides a conservative estimate for the purposes of feasibility analysis. The comparison shows that the impacts on thermal efficiency and yield are minimal. The low sulphur level means there is a low hydrogen requirement [311]. However, HDS adds around 11% to the bare module costs. As a result, the LCOH increases from 3.93 to 4.13 \$ kg<sub>H2</sub><sup>-1</sup>, a 5% increase.

Using the same conversion as above, 1 ppmwt of sulphur in bio-oil equates to 2.45 ppmv (dry) in the reformer feed, which is still higher than an SMR inlet. Depending on the benefits of deeper desulphurisation, the HDS process could be followed by a sulphur polishing bed [345].



**Table 5.18 – Impact of desulphurisation on C-SR without CO<sub>2</sub> capture (base case scenario, S/C = 5, reformer at 30 bar, 900°C)**

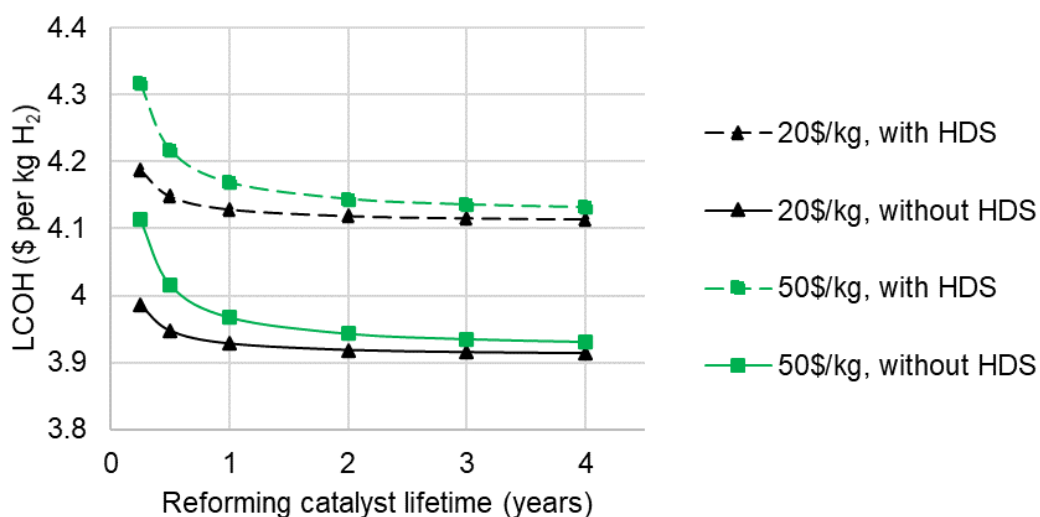
	Without desulphurisation	With desulphurisation
<b>Technical performance</b>		
H <sub>2</sub> production - gross (Nm <sup>3</sup> h <sup>-1</sup> )	10,000	10,000
H <sub>2</sub> for HDS (Nm <sup>3</sup> h <sup>-1</sup> ) <sup>a</sup>	0	88
Steam for HDS (kW)	0	132
Power for HDS (kW)	0	67
Fuel gas for HDS (kW)	0	295
H <sub>2</sub> yield (wt%, m.f.)	18.64	18.61
Thermal efficiency, inc. steam export (%)	76.88	76.16
<b>Economic performance</b>		
Bare module costs C-SR plant (\$m)	23.48	23.48
Bare module costs HDS plant (\$m)	0	2.54
Fixed capital costs (\$ kW <sup>-1</sup> )	1534	1702
Cost of manufacture (\$ kW <sup>-1</sup> )	936	969
LCOH (\$ kg <sub>H<sub>2</sub></sub> <sup>-1</sup> )	3.93	4.13
<sup>a</sup> Based on 0.5 wt% sulphur in feed, using correlation in [311]		

Given that the sulphur content is low compared to a naphtha, HDS may not be the most suitable method for desulphurisation. For example, it may be more cost-effective to use a sulphur guard bed consisting of metal oxides. Recent research has examined novel applications for sulphur guard beds, such as the use of ZnO for treating biogas [346] or biomass syngas [347]. Matheson's Nanochem® GuardBed™ is advertised for its applicability in renewable applications including bio-ethanol, bio-diesel and biogas [316]. However, there is very limited data available to inform a techno-economic assessment of its use for bio-oil. This is an important area for future research, to determine whether metal oxide beds are a feasible and cost-effective route for bulk sulphur removal in bio-oil applications.

This evaluation shows only the costs associated with desulphurisation, and does not illustrate the potential benefits of improving catalyst lifetime and performance. This study assumes low catalyst lifetimes of only 1 year in C-SR, due to the challenging properties of bio-oil. However, this could be lengthened in a number of ways. As well as desulphurisation, this could include operating strategies to reduce carbon deposition, or the development of sulphur- and carbon-resistant catalysts.

As a first step towards understanding the economic trade-offs, **Figure 5.28** shows the impact of catalyst lifetime and price on the LCOH. Low catalyst lifetimes below 2 years cause the LCOH to escalate. Above 2 years lifetime, the benefits of extended catalyst lifetime are less apparent. In practice, the

effects of lifetime would be even greater than shown in this simple analysis. More regular catalyst replacement would lead to high maintenance costs, high downtime, and safety impacts of regular interventions. A full evaluation would require more data on the specific impacts of sulphur in bio-oil reforming, details of which are currently lacking in the literature. This emphasises the importance of better understanding catalyst lifetime in bio-oil reforming, and quantifying the effects of improvement strategies.



**Figure 5.28 – Effect of catalyst lifetime, cost and hydrodesulphurisation on levelised cost of hydrogen from C-SR,  $10,000 \text{ Nm}^3 \text{ h}^{-1}$**

## 5.5 Conclusion

A techno-economic analysis has been used to evaluate three processes for hydrogen production from bio-oil: steam reforming without  $\text{CO}_2$  capture, steam reforming with  $\text{CO}_2$  capture, and SE-CLSR with  $\text{CO}_2$  capture. A performance analysis of the three processes examined the impacts of S/C ratio, temperature and pressure. This performance analysis was used to identify the design basis for an economic evaluation. The analysis identified that bio-oil C-SR or SE-CLSR may be a feasible route to hydrogen production, with potential to provide negative emissions. However, this is dependent upon several factors which would benefit from more detailed research focus.

One area of focus was the utilisation of high S/C ratios, which have been proposed in literature in order to minimise carbon deposition. In C-SR, increasing S/C ratio from 3 to 5 does not have a large influence on hydrogen cost, particularly where excess heat can be exported to a neighbouring

steam user. This suggests that the high S/C ratios required to mitigate carbon deposition may not be prohibitive, if the potential for wider heat integration is favourable. This highlights a useful parallel between bio-oil C-SR and CO<sub>2</sub> capture, if spare heat from high S/C ratio processes can be used to support CO<sub>2</sub> capture heat demand.

SE-CLSR was compared to C-SR-CCS as a route to hydrogen with BECCS. SE-CLSR can improve process thermal efficiency compared to C-SR-CCS. At the same time, the autothermal SE-CLSR does not rely on fuel gas, and so reduces fossil-based CO<sub>2</sub> emissions. However, the cost of SE-CLSR is highly variable with the S/C ratio. At S/C = 2, the levelised cost of hydrogen and cost of carbon avoided is less than that of a C-SR process with amine-based CCS. However, at higher S/C ratios, SE-CLSR does not have a strong economic advantage. Thus, if SE-CLSR is to be advanced further for bio-oil, it would be useful to better understand the viability of operating at high temperatures (> 850°C) with a low S/C ratio, and whether the SE-CLSR cycle can sustain low carbon deposition levels over a long operating period.

Economic analysis shows that SE-CLSR is comparable to C-SR-CCS for the levelised cost of hydrogen, with costs in the region of 3.8 to 4.6 \$ kg<sup>-1</sup>. The costs are similar to projected costs for the biomass gasification route. This is higher than other H<sub>2</sub> production routes, but is within the range that the Hydrogen Council has predicted will make H<sub>2</sub> cost-competitive at the fuel pump, and so bio-oil might have a role in a diversified hydrogen production sector, especially if the potential value of negative emissions is considered.

The cost of carbon avoided (CCA) varies considerably, depending how it is calculated. If all emissions, both biogenic and fossil-based, are considered the same, the cost ranges from 60 to 100 \$ t<sub>CO<sub>2</sub></sub><sup>-1</sup>. If biogenic emissions captured are considered as 'negative emissions', the cost reduces to the region of 40 to 70 \$ t<sub>CO<sub>2</sub></sub><sup>-1</sup>. If a natural-gas based SMR process is used as the reference to calculate CCA, the CCA increases to 90 to 160 \$ t<sub>CO<sub>2</sub></sub><sup>-1</sup>, because methane is a considerably less expensive feedstock. However for larger-scale plants (100 000 Nm<sup>3</sup> h<sup>-1</sup>), the CCA of 95 to 105 \$ t<sub>CO<sub>2</sub></sub><sup>-1</sup> is within the range of BECCS in other industries.

Significant contributors to process cost were the PSA system, CO<sub>2</sub> capture (in the case of C-SR-CCS) and three-way valves (in the case of SE-CLSR). Future process development could provide better cost definitions for these three aspects of process design, taking into account to the specific chemistry and design requirements of bio-oil reforming. Another area for future work could be to compare CO<sub>2</sub> capture locations in bio-oil steam reforming,

similar to previous work on SMR [236], but accounting for the chemistry of the new feedstock.

A further sensitivity relates to the catalyst lifetime, and the impacts of using desulphurisation as a means to extend this. A high-level analysis, based on naphtha hydrodesulphurisation (HDS) data, showed that the high capital cost of HDS could increase the LCOH by around 5%. However, this cost may be justified if required to extend catalyst lifetime, especially considering the potential costs associated with high process downtime. Given the relatively low sulphur content, chemisorption by metal oxide beds may be a more appropriate method for bulk sulphur removal. Further research is needed in this area, as it could be an important sensitivity in process development. This could include research into the mechanisms of catalyst deactivation, HDS processes optimised for bio-oil reforming, and the feasibility and cost of metal oxide beds.

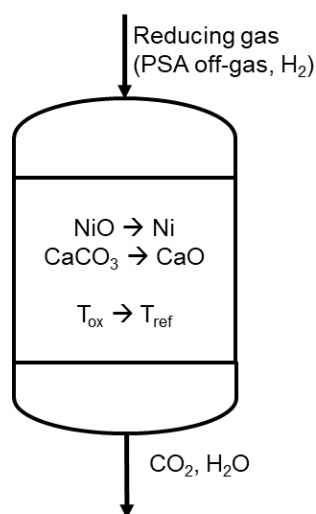
Initial comparisons of direct emissions have identified the important role of negative emissions, but this should be further explored with life cycle assessments. In addition, this work should be supplemented by the development of policy, carbon markets and business models that address the unique aspects of negative emissions. The techno-economic analysis has highlighted how the balance between fossil and biogenic emissions can change with process design, and so the commercial and technical optimisation will be closely interconnected. This highlights a particular challenge for BECCS plants where part of the system heat demand is supported by fossil fuel energy.

Other technical aspects of SE-CLSR feasibility depend upon dynamic aspects of the process, which will affect various aspects such as sequencing and operability, heat management and product stream composition. The following chapters begin to approach this knowledge gap, with the support of dynamic reactor modelling and kinetic analysis.

## Chapter 6 – Reactor modelling of reduction-calcination

### 6.1 Introduction

The techno-economic analysis in **Chapter 5** was based upon a potential operating strategy for SE-CLSR, in which the reactor bed undergoes three cycle stages. This chapter focusses in more detail on the third stage, reduction-calcination, which serves several important functions, illustrated in **Figure 6.1**.



**Figure 6.1 – Illustration of reduction-calcination stage**

During this stage of SE-CLSR, the OTM is reduced from NiO to Ni, restoring its catalytic activity for steam reforming. At the same time, the sorbent is regenerated by calcination. Calcination produces a stream of CO<sub>2</sub> which may be captured and stored. The reactions are summarised in **Table 6.1**, based on the kinetic model of Iliuta et al. [348].

**Table 6.1 – Reactions in reduction-calcination stage [206,207,257]**

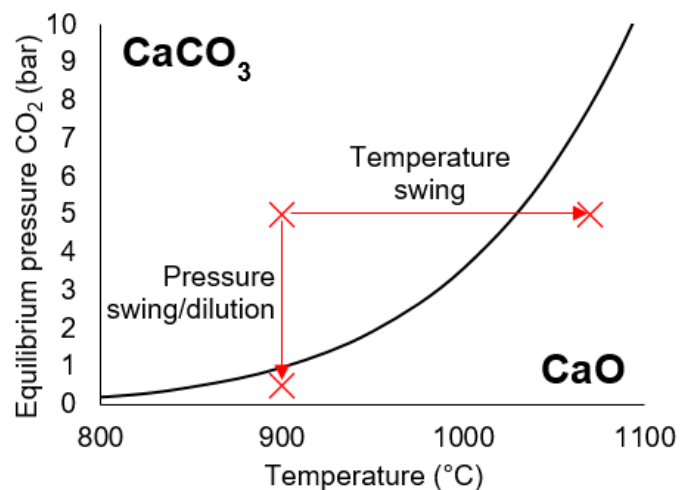
Reaction	Stoichiometry	$\Delta H_{927^\circ\text{C}}$
Reduction by CH <sub>4</sub> (1)	$\text{CH}_4 + 2\text{NiO} \rightarrow 2\text{Ni} + 2\text{H}_2 + \text{CO}_2$	162 kJ mol <sub>CH<sub>4</sub></sub> <sup>-1</sup>
Reduction by H <sub>2</sub>	$\text{H}_2 + \text{NiO} \rightarrow \text{Ni} + \text{H}_2\text{O}$	-16 kJ mol <sub>H<sub>2</sub></sub> <sup>-1</sup>
Reduction by CO	$\text{CO} + \text{NiO} \rightarrow \text{Ni} + \text{CO}_2$	-49 kJ mol <sub>CO</sub> <sup>-1</sup>
Reduction by CH <sub>4</sub> (2)	$\text{CH}_4 + \text{NiO} \rightarrow \text{Ni} + 2\text{H}_2 + \text{CO}$	211 kJ mol <sub>CH<sub>4</sub></sub> <sup>-1</sup>
Calcination	$\text{CaCO}_3 \rightarrow \text{Ca} + \text{CO}_2$	178 kJ mol <sub>CaCO<sub>3</sub></sub> <sup>-1</sup>

Another important function is a change in temperature. The process modelling in **Chapter 5** determined that, in the NiO/CaCO<sub>3</sub> system under study, the energy balance for this stage is net endothermic. This is because

the calcination reaction and most of the reduction reactions are endothermic (**Table 6.1**). Thus the bed material is cooled from the elevated temperature reached at the end of oxidation ( $T_{ox}$ , 919°C), back to the cooler temperature required for sorption-enhanced reforming ( $T_{ref}$ , 850°C).

Through combined reduction, calcination, and bed cooling, the bed material is returned to its original condition, ready to return to the first stage of SE-CLSR, sorption-enhanced reforming. By allowing these functions to occur simultaneously, the number of cycle stages is reduced. This has many advantages, such as reducing the cost and footprint associated with an additional reactor. It also reduces the number of valves, which the techno-economic assessment has highlighted is a significant contributor to cost.

Although there are benefits to the approach, it leads to a complex design and operating strategy with several interacting factors. For example, calcination can only occur if the partial pressure of the system is below the equilibrium pressure of  $CO_2$ . Calcination can be controlled in several ways, illustrated on **Figure 6.2**. One approach is to reduce the partial pressure of  $CO_2$ , either by a pressure swing or by dilution. An increase in temperature can also shift the system to the right of the equilibrium curve, enabling calcination. As previously discussed, the proposed reduction-calcination stage is net endothermic, so temperature swing is not feasible in this case. Thus, this study focusses on the use of pressure swing and composition control to facilitate calcination.



**Figure 6.2 – Equilibrium pressure of CaO/CaCO<sub>3</sub> system, showing strategies for calcination**

Another factor to consider is the outlet gas purity. If the stream of  $CO_2$  is to be captured, it must be of sufficient purity for transportation and storage. As reduction and calcination occur at different rates, their mass & heat transfer

fronts progress at different speeds along the bed [258]. The relative speeds of the reaction fronts have different consequences for outlet gas composition, as well as the time taken to fully regenerate the bed.

A further consideration is the type of gas that is used for reduction. One approach is to use hydrogen [258]. An advantage of this approach is that the reduction of NiO by H<sub>2</sub> produces only water as by-product (**Table 6.1**), which is relatively easy to separate from CO<sub>2</sub>. However, this approach uses valuable H<sub>2</sub> product. Other studies have proposed reduction using feedstocks such as methane [257,349] or bio-oil [123,172], or a stream of CO/H<sub>2</sub> produced by steam reforming with a low S/C ratio [213,350]. However, these approaches consume feedstock which could otherwise be used for hydrogen production.

An alternative approach is to use PSA off-gas. The PSA off-gas contains many useful components, including unconverted CO and CH<sub>4</sub> and around 10% of the total H<sub>2</sub> production. **Table 6.2** shows the properties of off-gas determined by process modelling in Chapter 5.

**Table 6.2 – Properties of PSA off-gas from SE-CLSR, from Chapter 5 (at base case conditions: reforming at 850°C, 20 bar, S/C = 2).**

Property	Value
CO (mol%)	34.1
H <sub>2</sub> (mol%)	29.1
CH <sub>4</sub> (mol%)	18.4
CO <sub>2</sub> (mol%)	17.7
Lower heating value (MJ kg <sup>-1</sup> )	14.97
kg <sub>off-gas</sub> kg H <sub>2</sub> <sup>-1</sup>	3.97

In the conventional steam reforming (C-SR) process in **Chapter 5**, useful energy in PSA off-gas is recovered by using it as fuel gas for the furnace. In SE-CLSR, there is no furnace in which to burn the off-gas. However, H<sub>2</sub>, CO and CH<sub>4</sub> in the off-gas can be used for NiO reduction, yielding easily separated CO<sub>2</sub> and H<sub>2</sub>O end products. Thus the PSA off-gas can still be used, reducing carbon slip from the process while at the same time minimising the need to use H<sub>2</sub> product gas or extra fuel for reduction [161,162,166,351]. However, CO<sub>2</sub> already exists in the off-gas stream, and more is produced by reduction, affecting the partial pressure of CO<sub>2</sub> and therefore its equilibrium limit and the rate of calcination. A further

consideration is the breakthrough of off-gas components, which could reduce CO<sub>2</sub> purity.

Temperature is another important factor. As discussed, the endothermic nature of the stage means that it can cool the bed, returning it to the reforming temperature. Moreover, the drop in temperature slows rates of reaction, or potentially makes calcination thermodynamically infeasible (**Figure 6.2**). The earlier process modelling (**Chapter 5**) identified suitable operating temperatures and NiO/C ratios to achieve a complete temperature cycle. To gain a better understanding of whether this approach is feasible, it is important to also consider the dynamic aspects of heat and mass transfer.

Given the complexity of these dynamic and interacting phenomena, simple equilibrium models are not sufficient to gain a proper understanding of the system. Thus detailed modelling of a dynamic reactor is an invaluable tool to gain insights into the performance of the reduction-calcination stage.

Alarcon and Fernandez [258] created a model of simultaneous reduction-calcination, and the research group have also performed experimental studies of the system [324]. Qin et al. [349] similarly completed a modelling study on matching the kinetics of reduction and calcination. However, these studies used CuO as oxygen transfer material. There is comparatively little work on reduction-calcination with alternative oxygen transfer materials. Nickel-based materials have been widely studied and are considered to be promising candidates, due to nickel's superior performance as a steam reforming catalyst, as well as its low cost and high oxygen transfer capacity [31,33,164,170,352]. While other aspects of Ni-based chemical looping processes have been modelled [206,209,257], there is comparatively little information on simultaneous reduction-calcination.

Copper-based systems have many important differences compared to nickel-based systems. Most notably, reduction by CuO is highly exothermic, meaning that reduction-calcination is exothermic or energy neutral overall. While this assists with calcination, it also means that an extra stage is required for cooling [213]. In addition, as CuO reduction kinetics are different, the relative speeds of reduction and calcination fronts would be managed differently. Thus, while the work on Cu-based systems is informative, further work is needed to model specific aspects of Ni-based systems.

The following study aims to develop a reactor model for simultaneous reduction-calcination in a CaCO<sub>3</sub> + NiO/Al<sub>2</sub>O<sub>3</sub> reactor for SE-CLSR. The



resulting model is used as a tool to evaluate the feasibility and effectiveness of such a system, including the effects of using different feed gases, pressure and flow rates. These findings are then discussed in relation to the wider project aims, assessing the impacts on operating strategy, economics of the process, and the potential for carbon capture.

## 6.2 Methodology

### 6.2.1 Modelling methodology for reduction of NiO

**Chapter 3** gives an overview of the approach to modelling reduction-calcination, with the modelling hierarchy illustrated in **Figure 3.4**. In the first step, a dynamic model was developed to describe the reduction of NiO in a packed bed of Ni/Al<sub>2</sub>O<sub>3</sub>, and subsequently validated against experimental data from Iliuta et al [348].

The mass balances were based upon the generalised balances for a pseudo-homogenous packed bed reactor, derived in **Chapter 3**. Material and energy balances are given in **Table 6.3**. The balances use the apparent density of the catalyst (i.e. the density of catalyst including the particle porosity), as this is the property given in the reference used for validation [348]. As experiments were run at isothermal conditions, an isothermal energy balance was used.

**Table 6.3 – Material and energy balances for model of NiO reduction**

<b>Component mass balance:</b>	
$\varepsilon_b \left( \frac{\partial C_i}{\partial t} \right) + \frac{\partial (uC_i)}{\partial z} = \eta_{cat} (1 - \varepsilon_b) \rho_{cat} r_i$	<b>Eq. 6.1</b>
<b>Oxygen carrier mass and mole balances:</b>	
$\frac{dC_{NiO}}{dt} = (2r_{red,1} + r_{red,2} + r_{red,3} + r_{red,4})M_{NiO}$	<b>Eq. 6.2</b>
$\frac{dC_{Ni}}{dt} = -(2r_{red,1} + r_{red,2} + r_{red,3} + r_{red,4})M_{Ni}$	<b>Eq. 6.3</b>
$\frac{dX_{NiO}}{dt} = (2r_{red,1} + r_{red,2} + r_{red,3} + r_{red,4}) \frac{M_{NiO}}{C_{NiO}^0}$	<b>Eq. 6.4</b>
<b>Carbon mass balance:</b>	
$\frac{dC_C}{dt} = (r_{cd} - r_{g,H_2O} - r_{g,CO_2})C_{Ni}M_C$	<b>Eq. 6.5</b>
<b>Energy balance:</b>	
$\text{Isothermal: } T = T_o$	<b>Eq. 6.6</b>

Axial dispersion was not included, as Iliuta et al. [348] determined that the Peclet number in their experimental system was sufficiently high for a plug flow assumption to be valid. The Peclet number ( $Pe$ ) is a dimensionless number that describes the ratio of the rate of advection to the rate of diffusion, given by:

$$\text{Mass transfer: } Pe_m = \frac{ud_p}{D_m} \quad \text{Eq. 6.7}$$

$$\text{Heat transfer: } Pe_h = RePr \quad \text{Eq. 6.8}$$

The reaction scheme and rate equations were taken from Iliuta et al [348]. The full reaction scheme and corresponding rate equations are summarised in **Table 6.5**. The reaction scheme includes a set of four non-catalytic reactions for the reduction of NiO, as well as a series of catalytic reactions including SMR and WGS, among others. The reaction rate constants, equilibrium constants and adsorption coefficients are given in **Appendix C**.

Iliuta et al. [348] note that, although complete methane combustion is included in the kinetic model as its own reaction (described as “reduction by CH<sub>4</sub> (1)”), in reality this occurs as a combination of two of the other reactions – partial oxidation of CH<sub>4</sub> to CO, followed by CO oxidation to CO<sub>2</sub>. Nonetheless, their proposed kinetic model of four reduction reactions appears to describe the system well, and has been used in several other modelling studies [206,207,212,257,353,354]. All four reduction reactions from the kinetic model of Iliuta et al. [348] are retained in subsequent modelling, for completeness.

The species molar balances combine the reduction and catalytic reactions. For the catalytic reactions, the rate of reaction depends upon the availability of active catalyst, and so the Ni concentration ( $C_{Ni}$ ,  $kg_{Ni}kg_{cat}^{-1}$ ) was included in the molar balance:

$$r_i = \sum_{j,red} \nu_{i,j,red} r_{j,red} + \sum_{j,cat} \nu_{i,j,cat} r_{j,cat} C_{Ni} \quad \text{Eq. 6.9}$$

where  $j, red$  refers to reduction reactions and  $j, cat$  refers to catalytic reactions.  $\nu_{i,j}$  is the stoichiometric coefficient of component  $i$  in reaction  $j$ .

All assumptions regarding physical properties, momentum balances, boundary conditions etc., were the same as described in **Chapter 3**.

Properties of the system are summarised in **Table 6.4**. Initial conditions were:

$$\begin{aligned} C_i &= C_{i,0} & T &= T_0 & C_C &= C_{C,0} \\ C_{Ni} &= C_{Ni,0} & C_{NiO} &= C_{NiO,0} & X_{NiO} &= X_{NiO,0} \end{aligned}$$

**Table 6.4 – Properties applied in model of lab-scale NiO reduction [348]**

Property	Value
Feed gas	10% CH <sub>4</sub> in Ar
$P_{in}$ (bar)	1.01325
$T_{in}$ (°C)	700
$L$ (m)	$7.65 \times 10^{-3}$
$d_p$ (m)	$1.4 \times 10^{-4}$
$G_z$ (kg m <sup>-2</sup> s <sup>-1</sup> )	0.233
$\varepsilon_b$ (-)	0.37
$\rho_{cat,app}$ (kg m <sup>-3</sup> )	1040
$\eta_{cat}$ (-)	1
$C_{NiO,0}$ (kg <sub>NiO</sub> kg <sub>cat</sub> <sup>-1</sup> )	0.15
$C_{Ni,0}$ (kg <sub>Ni</sub> kg <sub>cat</sub> <sup>-1</sup> )	0
$C_{C,0}$ (-)	0
$X_{NiO,0}$ (-)	0

Table 6.5 – Reaction scheme and rate equations for model of NiO reduction [348]

Reaction	Stoichiometry	Rate equation
<b>Reduction reactions</b>		
Reduction by CH <sub>4</sub> (1)	CH <sub>4</sub> + 2NiO → 2Ni + 2H <sub>2</sub> + CO <sub>2</sub>	$r_{red,1} = a_0(1 - X)k_{red,1}C_{CH_4}C_{NiO}C_{Ni}$
Reduction by H <sub>2</sub>	H <sub>2</sub> + NiO → Ni + H <sub>2</sub> O	$r_{red,2} = a_0(1 - X)k_{red,2}C_{H_2}C_{NiO}$
Reduction by CO	CO + NiO → Ni + CO <sub>2</sub>	$r_{red,3} = a_0(1 - X)k_{red,3}C_{CO}C_{NiO}$
Reduction by CH <sub>4</sub> (2)	CH <sub>4</sub> + NiO → Ni + 2H <sub>2</sub> + CO	$r_{red,4} = a_0(1 - X)k_{red,4}C_{CH_4}C_{NiO}C_{Ni}$
<b>Catalytic gas-solid reactions</b>		
Steam reforming of methane	CH <sub>4</sub> + H <sub>2</sub> O ↔ CO + 3H <sub>2</sub>	$r_{rf,H_2O} = \frac{k_{rf,H_2O} \frac{p_{CH_4} p_{H_2O}^{0.5}}{p_{H_2}^{1.25}} \left[ 1 - \frac{p_{CO} p_{H_2}^3}{K_{eq,rf,H_2O} p_{CH_4} p_{H_2O}} \right]}{\left( 1 + K_{CO,rf,H_2O} p_{CO} + K_{H_2,rf,H_2O} p_{H_2}^{0.5} + K_{H_2O,rf,H_2O} \frac{p_{H_2O}}{p_{H_2}} \right)^2}$
Water gas shift	CO + H <sub>2</sub> O ↔ CO <sub>2</sub> + H <sub>2</sub>	$r_{WGS} = \frac{k_{WGS} \frac{p_{CO} p_{H_2O}^{0.5}}{p_{H_2}^{0.5}} \left[ 1 - \frac{p_{CO} p_{H_2}}{K_{eq,WGS} p_{CO} p_{H_2O}} \right]}{\left( 1 + K_{CO,rf,H_2O} p_{CO} + K_{H_2,rf,H_2O} p_{H_2}^{0.5} + K_{H_2O,rf,H_2O} \frac{p_{H_2O}}{p_{H_2}} \right)^2}$
Methanation	CO + 3H <sub>2</sub> ↔ CH <sub>4</sub> + H <sub>2</sub> O	$r_m = \frac{k_m K_{CO,m} K_{H_2,m}^2 p_{CO}^{0.5} p_{H_2}}{\left( 1 + K_{CO,m} p_{CO}^{0.5} + K_{H_2,m} p_{H_2}^{0.5} \right)^3}$

Reaction	Stoichiometry	Rate equation
Decomposition of methane	$\text{CH}_4 + \text{Ni} \leftrightarrow \text{Ni-C} + 2\text{H}_2$	$r_{cd} = \frac{k_{cd}K_{\text{CH}_4,cd} \left( p_{\text{CH}_4} - \frac{p_{\text{H}_2}^2}{K_{eq,cd}} \right)}{\left( 1 + \frac{1}{K_{r,cd}} p_{\text{H}_2}^{3/2} + K_{\text{CH}_4,cd} p_{\text{CH}_4} \right)^2}$
Dry reforming of methane	$\text{CH}_4 + \text{CO}_2 \leftrightarrow 2\text{CO} + 2\text{H}_2$	$r_{rf,CO_2} = \frac{k_{rf,CO_2} p_{\text{CH}_4} p_{\text{CO}_2}}{1 + K_{\text{CO}_2,rf,CO_2} p_{\text{CO}_2}}$
Carbon gasification with steam	$\text{C} + \text{H}_2\text{O} \leftrightarrow \text{CO} + \text{H}_2$	$r_{g,H_2O} = \frac{\frac{k_{g,H_2O}}{K_{\text{H}_2O,g,H_2O}} \left( \frac{p_{\text{H}_2O}}{p_{\text{H}_2}} - \frac{p_{\text{CO}}}{K_{eq,g,H_2O}} \right)}{\left( 1 + K_{\text{CH}_4,g,H_2O} p_{\text{CH}_4} + \right)^2}$
Carbon gasification with CO <sub>2</sub>	$\text{C} + \text{CO}_2 \leftrightarrow 2\text{CO}$	$r_{g,CO_2} = \frac{\frac{k_{g,CO_2}}{K_{\text{CO}_2,g,CO_2} K_{\text{CO},g,CO_2}} \left( \frac{p_{\text{CO}_2}}{p_{\text{CO}}} - \frac{p_{\text{CO}_2}}{K_{eq,g,CO_2}} \right)}{\left( 1 + K_{\text{CO},g,CO_2} p_{\text{CO}} + \frac{1}{K_{\text{CO}_2,g,CO_2} K_{\text{CO},g,CO_2}} \frac{p_{\text{CO}_2}}{p_{\text{CO}}} \right)^2}$

## 6.2.2 Modelling methodology for mixed sorbent/catalyst bed

The next stage in the modelling methodology, described in **Chapter 3**, was to develop and validate of model of a mixed sorbent/catalyst bed. As above, the mass and energy balances are based upon the balances derived in **Chapter 3**. However, as the bed contains a mixture of catalyst and sorbent materials, the balances were adjusted. Based on the work of Grasa et al. [212] and Abbas et al. [257], the balances contain separate terms for catalytic activity in the catalyst and sorption/calcination reactions in the sorbent.

A further adjustment relates to the way in which material density was expressed. The model of reduction used the apparent catalyst density (**Table 6.3**). However, for the mixed bed, the source for experimental data [212] gives the material properties in terms of absolute density and particle voidage. The apparent density was therefore expressed as follows:

$$\rho_{app} = (1 - \varepsilon_p)\rho_{solid} \quad \text{Eq. 6.10}$$

**Table 6.6 – Mass and energy balances for model of mixed sorbent/catalyst bed**

<b>Mass balance:</b>	
$\varepsilon_b \left( \frac{\partial C_i}{\partial t} \right) + \frac{\partial(uC_i)}{\partial z} = \varepsilon_b D_z \frac{\partial^2 C_i}{\partial z^2} + v_{cat} \eta_{cat} (1 - \varepsilon_b)(1 - \varepsilon_{cat}) \rho_{cat} r_{i,cat}$ $+ v_{sorb} \eta_{sorb} (1 - \varepsilon_b)(1 - \varepsilon_{sorb}) \rho_{sorb} r_{i,sorb}$	<b>Eq. 6.11</b>
<b>Energy balance:</b>	
<p>Isothermal: <math>T = T_o</math></p>	<b>Eq. 6.12</b>

Table 6.7 – Reaction scheme and rate equations for model of SE-SMR [212]

Reaction	Stoichiometry	Rate equation
Steam reforming of methane	$\text{CH}_4 + \text{H}_2\text{O} \leftrightarrow \text{CO} + 3\text{H}_2$	$r_{SMR,1} = \frac{1}{\Omega^2} \frac{k_{SMR,1}}{p_{H_2}^{2.5}} \left( p_{CH_4} p_{H_2O} - \frac{p_{H_2}^3 p_{CO}}{K_{eq,SMR,1}} \right)$ $\Omega = 1 + K_{CO} p_{CO} + K_{H_2} p_{H_2} + K_{CH_4} p_{CH_4} + K_{H_2O} \frac{p_{H_2O}}{p_{H_2}}$
Water gas shift	$\text{CO} + \text{H}_2\text{O} \leftrightarrow \text{CO}_2 + \text{H}_2$	$r_{WGS} = \frac{1}{\Omega^2} \frac{k_{WGS}}{p_{H_2}} \left( p_{CO} p_{H_2O} - \frac{p_{H_2} p_{CO_2}}{K_{eq,WGS}} \right)$
Global steam reforming	$\text{CH}_4 + 2\text{H}_2\text{O} \leftrightarrow \text{CO}_2 + 4\text{H}_2$	$r_{SMR,2} = \frac{1}{\Omega^2} \frac{k_{SMR,2}}{p_{H_2}^{2.5}} \left( p_{CH_4} p_{H_2O}^2 - \frac{p_{H_2}^4 p_{CO_2}}{K_{eq,SMR,2}} \right)$
Sorbent carbonation	$\text{CaO} + \text{CO}_2 \leftrightarrow \text{CaCO}_3$	$r_{carb} = \frac{1}{M_{CaO}} \left( \frac{dX_{carb}}{dt} \right)$ $\frac{dX_{carb}}{dt} = \frac{k_{carb}}{pq} (X_{carb,max} - X_{carb})(y_{CO_2} - y_{CO_2,eq})$

For carbonation, the equilibrium concentration of CO<sub>2</sub> was calculated using the CO<sub>2</sub> equilibrium equation from Baker [325]:

$$C_{CO_2,eq} = \frac{5.045 \times 10^{11}}{T} \exp\left(\frac{-20474}{T}\right) \quad \text{Eq. 6.13}$$

The CO<sub>2</sub> carrying capacity of the material ( $X_{carb,max}$ ) was given by [158]:

$$X_{carb,max} = \frac{1}{\frac{1}{(1 - X_r)} + kN} + X_r \quad \text{Eq. 6.14}$$

where  $X_r$  is the residual capacity for an infinite number of cycles, equal to 0.17.  $k$  is the sorbent deactivation constant, equal to 0.5. For experimental validation, the material was in its first cycle, and thus  $X_{carb,max}$  was equal to 0.7566.

The species molar balances were as follows:

$$\text{Catalytic reactions:} \quad r_{i,cat} = \sum_j \beta_{i,j} r_{j,cat} \quad \text{Eq. 6.15}$$

$$\text{Sorbent reactions:} \quad r_{i,sorb} = -r_{carb} \quad (i = CO_2) \quad \text{Eq. 6.16}$$

$$r_{i,sorb} = 0 \quad (i \neq CO_2) \quad \text{Eq. 6.17}$$

All other assumptions regarding physical properties, momentum balances, boundary conditions etc., were the same as described in **Chapter 3**. Initial conditions were:

$$C_i = C_{i,0} \quad T = T_0 \quad X_{carb} = X_{carb,0}$$

When modelling the lab-scale reactor, the effectiveness factor of catalytic and sorbent reactions were initially assumed to be 1, due to the small particle size, and this was later verified by the validation graph (**Figure 6.5**). Other system properties are taken from Grasa et al. [212], summarised in **Table 6.8**.



**Table 6.8 – Properties in model of lab-scale mixed bed reactor [212]**

Property	Value
Feedstock	CH <sub>4</sub>
S/C ratio (-)	3.2
$P_{in}$ (bar)	3 - 9
$T_{in}$ (°C)	650
$L$ (m)	0.15
$d_p$ (m)	$8 \times 10^{-4}$
$G_z$ (kg m <sup>-2</sup> s <sup>-1</sup> )	0.0685
$B$ , sorbent to catalyst mass ratio (-)	5
$\varepsilon_b$ (-)	0.4
$\varepsilon_{cat}$ (-)	0.41
$\varepsilon_{sorb}$ (-)	0.48
$\rho_{cat}$ (kg m <sup>-3</sup> )	3400
$\rho_{sorb}$ (kg m <sup>-3</sup> )	2710
$v_{cat}$ (-)	0.19
$v_{sorb}$ (-)	0.81
$\rho_{bed}$ (kg m <sup>-3</sup> )	1558
$\eta_{cat}$ (-)	1
$\eta_{sorb}$ (-)	1
$X_{carb,max}$ (-)	0.7566
$X_{carb,0}$ (-)	0

### 6.2.3 Modelling methodology for reduction-calcination

The focus of the study was to examine the regeneration stage of the SE-CLSR, during which reduction occurs simultaneously with calcination. A model of the reduction-calcination stage was created by combining the validated models from the previous sections.

The mass and energy balances (**Table 6.9**) were based on the mixed catalyst/sorbent balance for a mixed sorbent bed, given in **Section 6.2.2**. However, as the model includes NiO reduction, it was also important to account for catalytic activity. The changes in NiO/Ni concentration were incorporated via the same approach as **Section 6.2.1**, by using the Ni concentration ( $C_{Ni}$ ) in the molar balance for catalytic reactions:

$$r_i = \sum_{j,red} \beta_{i,j,red} r_{j,red} + \sum_{j,cat} \beta_{i,j,cat} r_{j,cat} C_{Ni} \quad \text{Eq. 6.18}$$

where  $j, red$  refers to reduction reactions and  $j, cat$  refers to catalytic reactions.  $\beta_{i,j}$  is the stoichiometric coefficient of component  $i$  in reaction  $j$ .

A further consideration was the inclusion of axial dispersion effects. For adiabatic reactors, the effects of axial dispersion may be neglected, provided the reactor is long enough [355]. The criterion is as follows:

$$\frac{PeL}{d_p} > 100 - 400 \quad \text{Eq. 6.19}$$

Where the Peclet numbers ( $Pe$ ) are given by:

$$\text{Mass transfer: } Pe_m = \frac{ud_p}{D_m} \quad \text{Eq. 6.20}$$

$$\text{Heat transfer: } Pe_h = RePr \quad \text{Eq. 6.21}$$

In the system under study, the left hand side of **Eq. 6.19** was in the order of several thousand for both heat and mass transfer. Thus axial dispersion could be neglected, and was not included in the mass or energy balance.

**Table 6.9 – Mass and energy balances for model of reduction-calcination**

<b>Mass balance:</b>	
$\varepsilon_b \left( \frac{\partial C_i}{\partial t} \right) + \frac{\partial (uC_i)}{\partial z}$ $= v_{cat} \eta_{cat} (1 - \varepsilon_b) (1 - \varepsilon_{cat}) \rho_{cat} r_i$ $+ v_{sorb} \eta_{sorb} (1 - \varepsilon_b) (1 - \varepsilon_{sorb}) \rho_{sorb} r_{sorb}$	<b>Eq. 6.22</b>
<b>Energy balance:</b>	
$\varepsilon_b \rho_g C_{p,g} \left( \frac{\partial T}{\partial t} \right) + (1 - \varepsilon_b) \rho_{bed} C_{p,bed} \left( \frac{\partial T}{\partial t} \right) + u \rho_g C_{p,g} \frac{\partial T}{\partial z} =$ $v_{cat} \eta_{cat} (1 - \varepsilon_b) (1 - \varepsilon_{cat}) \rho_{cat} \sum \eta_j (-\Delta H_{rxn,j}) R_j$ $+ v_{sorb} \eta_{sorb} (1 - \varepsilon_b) (1 - \varepsilon_{sorb}) \rho_{sorb} (-\Delta H_{sorb}) R_{sorb}$	<b>Eq. 6.23</b>

The reaction scheme (**Table 6.10**) used the same reaction kinetics as the reduction model, which included reduction of NiO together with SMR and WGS, and dry methane reforming. To simplify the model, methane decomposition, carbon gasification and methane dry reforming were assumed to be negligible, as steam was in large excess compared to methane. The kinetics of calcination were taken from the work of Martinez et al. [159]. CO<sub>2</sub> equilibrium partial pressure was found using the equation of Baker [325], as per the previous section.

Table 6.10 – Reaction scheme and rate equations for model of reduction-calcination [159,348,356]

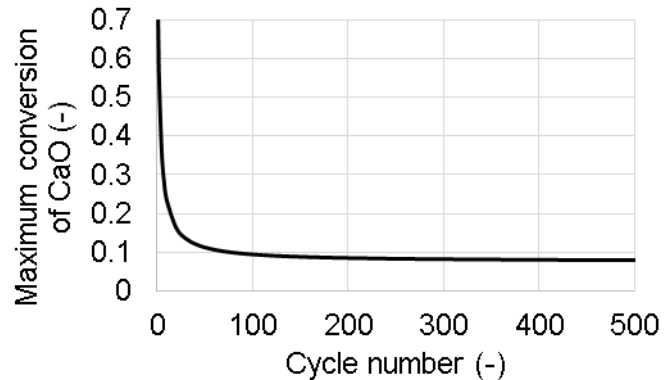
Reaction	Stoichiometry	Rate equation
<b>Reduction reactions</b>		
Reduction by CH <sub>4</sub> (1)	CH <sub>4</sub> + 2NiO → 2Ni + 2H <sub>2</sub> + CO <sub>2</sub>	$r_{red,1} = a_0(1 - X)k_{red,1}C_{CH_4}C_{NiO}C_{Ni}$
Reduction by H <sub>2</sub>	H <sub>2</sub> + NiO → Ni + H <sub>2</sub> O	$r_{red,2} = a_0(1 - X)k_{red,2}C_{H_2}C_{NiO}$
Reduction by CO	CO + NiO → Ni + CO <sub>2</sub>	$r_{red,3} = a_0(1 - X)k_{red,3}C_{CO}C_{NiO}$
Reduction by CH <sub>4</sub> (2)	CH <sub>4</sub> + NiO → Ni + 2H <sub>2</sub> + CO	$r_{red,4} = a_0(1 - X)k_{red,4}C_{CH_4}C_{NiO}C_{Ni}$
<b>Catalytic gas-solid reactions</b>		
Steam methane reforming	CH <sub>4</sub> + H <sub>2</sub> O ↔ CO + 3H <sub>2</sub>	$r_{rf,H_2O} = \frac{k_{rf,H_2O} \frac{p_{CH_4} p_{H_2O}^{0.5}}{p_{H_2}^{1.25}} \left[ 1 - \frac{p_{CO} p_{H_2}^3}{K_{eq,rf,H_2O} p_{CH_4} p_{H_2O}} \right]}{\left( 1 + K_{CO,rf,H_2O} p_{CO} + K_{H_2,rf,H_2O} p_{H_2}^{0.5} + K_{H_2O,rf,H_2O} \frac{p_{H_2O}}{p_{H_2}} \right)^2}$
Water gas shift	CO + H <sub>2</sub> O ↔ CO <sub>2</sub> + H <sub>2</sub>	$r_{WGS} = \frac{k_{WGS} \frac{p_{CO} p_{H_2O}^{0.5}}{p_{H_2}^{0.5}} \left[ 1 - \frac{p_{CO} p_{H_2}}{K_{eq,WGS} p_{CO} p_{H_2O}} \right]}{\left( 1 + K_{CO,rf,H_2O} p_{CO} + K_{H_2,rf,H_2O} p_{H_2}^{0.5} + K_{H_2O,rf,H_2O} \frac{p_{H_2O}}{p_{H_2}} \right)^2}$
<b>Sorbent reactions</b>		
Sorbent calcination	CaCO <sub>3</sub> ↔ CaO + CO <sub>2</sub>	$r_{calc} = \frac{1}{M_{CaCO_3}} \left( \frac{dX_{carb}}{dt} \right)$ $\frac{dX_{carb}}{dt} = k_{calc} \left( \frac{X_{carb}}{X_{carb,max}} \right) (C_{CO_2,eq} - C_{CO_2})$

The maximum sorbent conversion ( $X_{max}$ ) was selected on the basis of the equation given in Martinez et al. [159]:

$$X_{carb,max,N} = \frac{1}{\frac{1}{(1-X_r)} + kN} + X_r \quad \text{Eq. 6.24}$$

$$k = 0.52, X_r = 0.075 (T_{calc} < 950^\circ\text{C}, t_{calc} < 20 \text{ min})$$

This trend is more easily visualised on a graph, shown in **Figure 6.3**. The maximum sorbent conversion decreases rapidly during the first 100 cycles, after which it remains relatively constant at around 0.08. For this reason, 0.08 was selected as the value of  $X_{carb,max}$ . This is lower than the value applied in the section above, using **Eq. 6.14**. This is because the calcination kinetics are taken from Martinez et al., and so the value of  $X_{carb,max}$  from the same reference was the most relevant to use. However, the effect of  $X_{carb,max}$  is considered in the sensitivity analysis.



**Figure 6.3 – Maximum CaO conversion as a function of cycle number**

To ensure the conversion of sorbent ( $X_{carb}$ ) or the concentration of reactants could not go below zero, two 'if' loops were included. The full code for the model is given in **Appendix D**.

Initial conditions were:

$$\begin{aligned} C_i &= C_{i,0} & T &= T_{in} & X_{carb} &= X_{carb,max} \\ C_{Ni} &= C_{Ni,0} & C_{NiO} &= C_{NiO,0} & X_{NiO} &= X_{NiO,0} \end{aligned}$$

The properties and assumptions for the base case are given in **Table 6.11**. Where properties were changed from the base case, in order to carry out sensitivity analysis, this is signified in the text. Gas properties were taken from Aspen Plus, using the Peng-Robinson equation of state to describe the non-ideal behaviour of the gases [216].

For large, industrial-sized pellets, internal diffusion can be limiting, and so the effectiveness of the catalyst is reduced. An effectiveness factor of 0.3 was assumed [256,356]. For calcination the main limiting factor is

temperature, rather than diffusional effects, so the effectiveness factor was assumed to be 1 [258].

**Table 6.11 – Properties for model of reduction-calcination**

Property	Value	Ref
$P_{in}$ (bar)	1.2	-
$T_{in}$ (°C)	919	Techno-economic study (end of oxidation stage)
$L$ (m)	7.8	
$d_p$ (m)	0.01	-
$G_z$ (kg m <sup>-2</sup> s <sup>-1</sup> )	0.3	-
$B$ , sorbent to catalyst mass ratio (-)	3	Techno-economic study
$\varepsilon_{bed}$ (-)	0.4	-
$\varepsilon_{cat}$ (-)	0.41	[212]
$\varepsilon_{sorb}$ (-)	0.48	[212]
$\rho_{cat}$ (kg m <sup>-3</sup> )	3400	[212]
$\rho_{sorb}$ (kg m <sup>-3</sup> )	2710	[212]
$v_{cat}$ (-)	0.19	Techno-economic study
$v_{sorb}$ (-)	0.81	Techno-economic study
$\rho_{bed}$ (kg m <sup>-3</sup> )	1558	Techno-economic study
$C_{p,cat}$ (J kg <sup>-1</sup> °C <sup>-1</sup> )	1992	Aspen Plus
$C_{p,sorb}$ (J kg <sup>-1</sup> °C <sup>-1</sup> )	966	Aspen Plus
$C_{p,bed}$ (J kg <sup>-1</sup> °C <sup>-1</sup> )	1220	Calculated
$\eta_{cat}$ (-)	0.3	[256,356]
$\eta_{sorb}$ (-)	1	[258]
$a_o$ (m <sup>2</sup> g <sup>-1</sup> )	102	[348]
$X_{carb,max}$ (-)	0.08	[159]
$X_{carb,0}$ (-)	0.08	Equal to $X_{carb,max}$
$C_{NiO,0}$ (kg <sub>NiO</sub> kg <sub>cat</sub> <sup>-1</sup> )	0.15	Describes start of reduction
$C_{Ni,0}$ (kg <sub>Ni</sub> kg <sub>cat</sub> <sup>-1</sup> )	0	-
$X_{NiO,0}$ (-)	0	-

For continuity with earlier work, certain properties were based upon the techno-economic study. Reactor length was estimated using the same basis as in **Chapter 5**, assuming a WHSV of 0.8 kg<sub>bio-oil</sub> h<sup>-1</sup> kg<sub>cat</sub><sup>-1</sup> and L/D ratio of 3. These dimensions satisfy the conditions for plug flow conditions in an industrial scale reactor [357,358], defined as :

$$\text{Ratio of bed height to particle size: } L/D_p \geq 50$$

$$\text{Ratio of reactor internal diameter to particle size: } d/d_p \geq 10$$

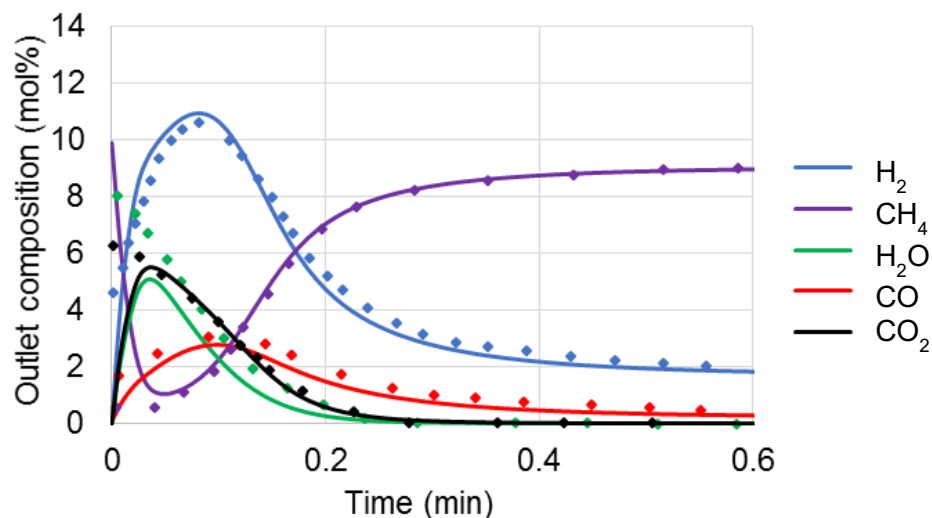
For the process producing  $10\,000\text{ Nm}^3\text{ h}^{-1}$  of  $\text{H}_2$ , this created a reactor of length 7.8m. The sorbent to catalyst mass ratio was based upon the techno-economic study, which also assumed a maximum sorbent capacity of 0.08.

As discussed in the introduction, various different feed gases have been proposed for achieving reduction in SE-CLSR. As the focus of the project is bio-oil, methane or the products of SMR were not examined in further detail. Instead, hydrogen and PSA off-gas were focus of this study. The PSA off-gas composition was the same as given in **Table 6.2**. This was derived from the whole process model in Aspen Plus, using the base case process design for bio-oil SE-CLSR at 20 bar, reforming temperature of  $850^\circ\text{C}$ , with  $\text{S/C} = 2$ .

### 6.3 Results and discussion

#### 6.3.1 Model validation

The model of reduction and the model of SE-SMR were validated against experimental data from literature. **Figure 6.4** demonstrates the evolution of gases during the reduction of NiO. The results of the model closely match the experimental values of Iliuta et al. [348].



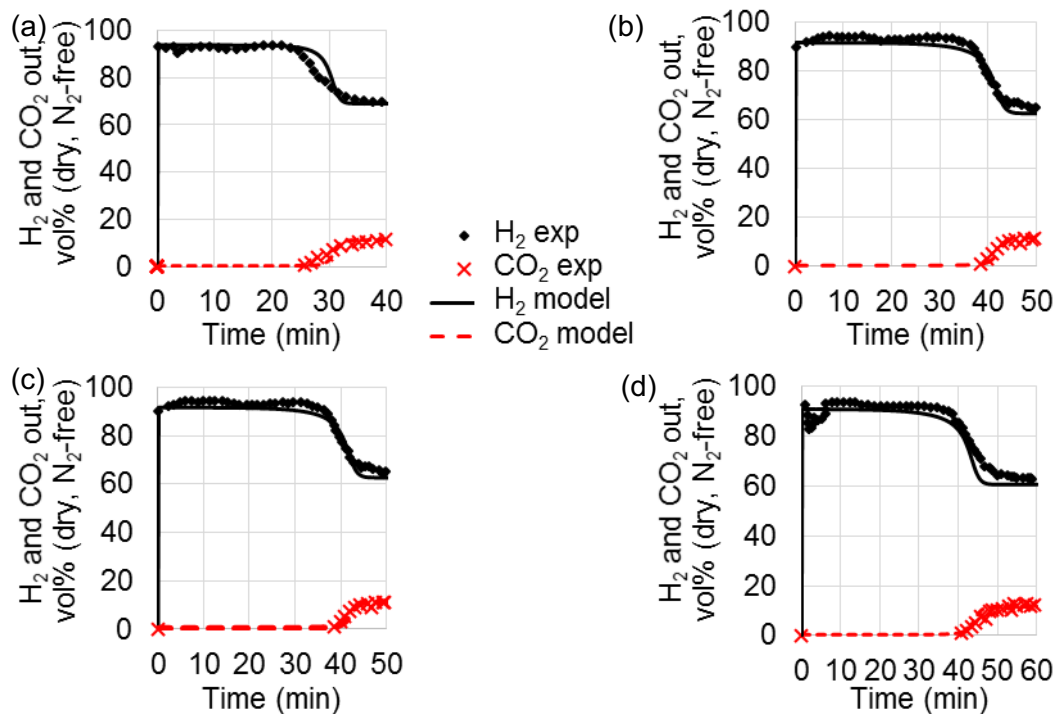
**Figure 6.4 – Product gas composition in reduction of NiO at  $800^\circ\text{C}$ , 1 bar with 10%  $\text{CH}_4$  in Ar as reducing gas. Solid lines represent modelling values, while dots represent experimental values from literature [348]**

During the initial period ( $< 0.05$  min), the  $\text{CH}_4$  content becomes very low, while  $\text{CO}_2$  and  $\text{H}_2\text{O}$  are released in ratios similar to complete methane combustion (reduction reaction 1). This indicates that reduction is occurring rapidly, with  $\text{CO}$  and  $\text{H}_2$  quickly oxidised into  $\text{CO}_2$  and  $\text{H}_2\text{O}$ . After the initial phase, the  $\text{H}_2\text{O}$  and  $\text{CO}_2$  peaks drop, while  $\text{H}_2$  and  $\text{CO}$  levels increase, as

reduction begins to slow. Over time, the NiO is made catalytically active by reduction to Ni, so that SMR and WGS can also occur.

The results of Grasa et al. [212] were used to validate the model of SE-SMR in a mixed catalyst/sorbent bed. The results are shown in **Figure 6.5 (a) to (d)**. All the figures demonstrate a similar pattern including a period of sorption-enhanced reforming, during which H<sub>2</sub> purity is very high, followed by CO<sub>2</sub> breakthrough at around 30 – 40 minutes. The effect of pressure is shown, with increased pressure causing breakthrough to occur later. This effect is most pronounced between 3 bar and 5 bar, where the increase in pressure causes breakthrough to start approximately 10 minutes later.

Both **Figure 6.4** and **Figure 6.5** show excellent agreement between experimental and modelled values. Thus the models were used as the basis for the following work, a combined model of reduction and calcination in a mixed catalyst/sorbent bed.

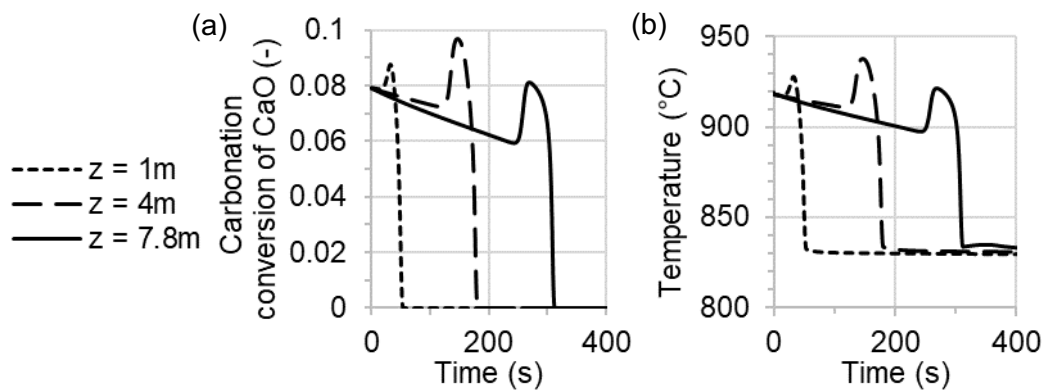


**Figure 6.5 – Effect of pressure on product gas composition (dry, N<sub>2</sub>-free basis) at the outlet of SE-SMR reactor. (a) 3 bar (b) 5 bar (c) 7 bar and (d) 9 bar S/C 3.2, B = 5, 650°C. space velocity 2.5 kg CH<sub>4</sub> h<sup>-1</sup> kg<sub>cat</sub><sup>-1</sup>. Solid lines represent modelling values, while dots are experimental values from [212].**

### 6.3.2 Reduction-calcination with different feed gases

Using the combined reduction-calcination model, an initial sensitivity analysis on feed gas composition determined that a certain amount of steam dilution was required in order to sustain calcination. A number of reactions

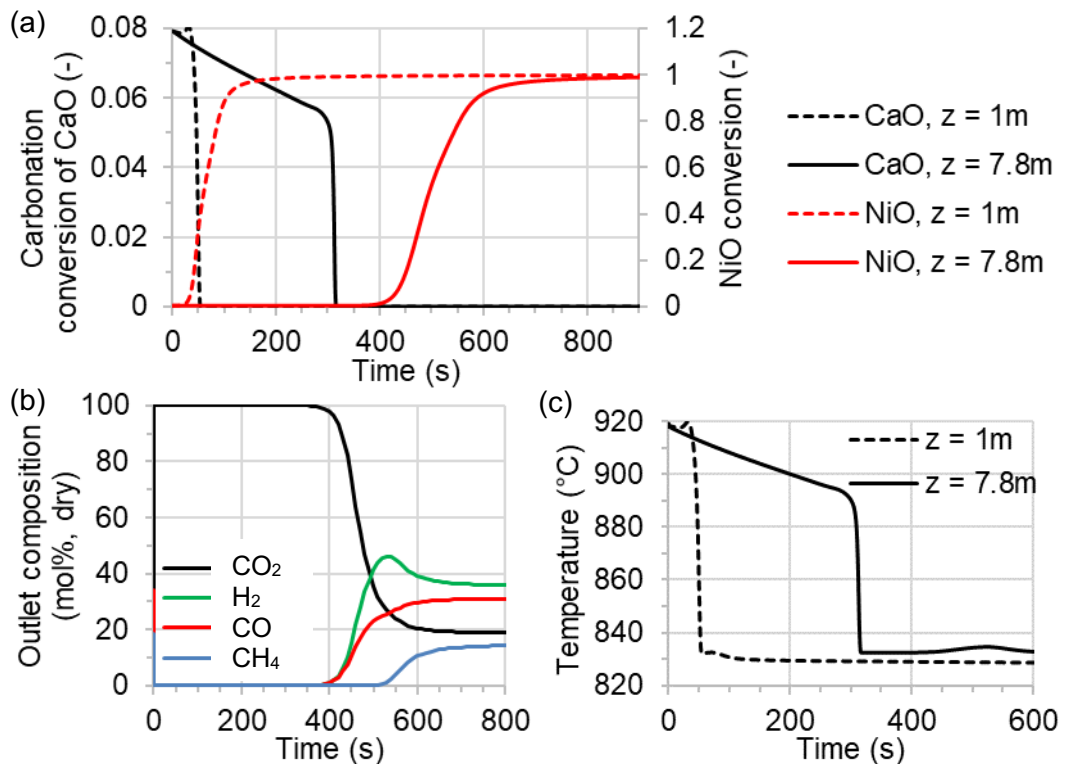
release  $\text{CO}_2$ , which can cause the partial pressure of  $\text{CO}_2$  to exceed the equilibrium pressure, making calcination infeasible (**Figure 6.2**). This effect is illustrated in **Figure 6.6**, which shows the results from a system containing 15% off-gas in 85%  $\text{H}_2\text{O}$ . Initially some calcination occurs, signified by a reduction in CaO conversion. However, at the edge of the calcination front, a large upwards spike in CaO conversion and temperature is observed. This indicates that sorption is occurring because the  $\text{CO}_2$  concentration has become too high. This spike moves along the bed over time, so that a portion of the bed always remains as  $\text{CaCO}_3$ .



**Figure 6.6 – Modelling results from reduction-calcination with 15 mol% off-gas in  $\text{H}_2\text{O}$  a) CaO carbonation conversion, (b) temperature at axial distance  $z$ . Inlet conditions 1.2 bar,  $919^{\circ}\text{C}$ , gas mass flux  $0.3\text{ kg m}^{-2}\text{ s}^{-1}$ ,  $B = 3$ .**

To prevent sorption occurring, the level of steam dilution should be set to the level such that  $\text{CO}_2$  concentration remains sufficiently low, i.e.  $p_{\text{CO}_2} < p_{\text{CO}_2,\text{eq}}$ . While this is not achieved with 85%  $\text{H}_2\text{O}$  (**Figure 6.6**), an increase to 90 mol%  $\text{H}_2\text{O}$  ensures a smooth calcination and temperature front, with no sorption, for the duration of the stage (**Figure 6.7a**).





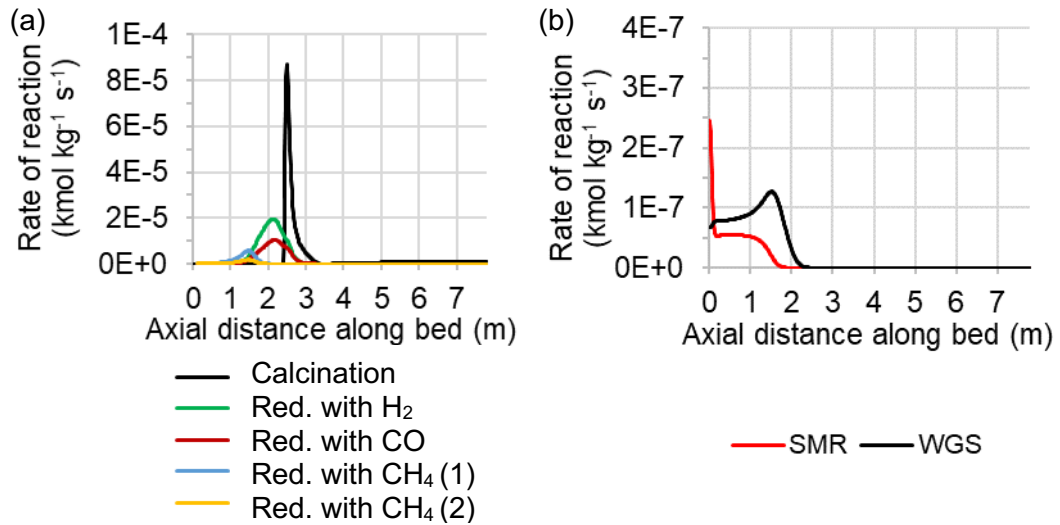
**Figure 6.7 – Modelling results for reduction-calcination with 10 mol% off-gas in H<sub>2</sub>O (a) CaO and NiO conversion at axial distance z, (b) outlet gas composition and (c) temperature at axial distance z. Inlet conditions 1.2 bar, 919°C, gas mass flux 0.3 kg m<sup>-2</sup> s<sup>-1</sup>, B = 3.**

**Figure 6.7a** shows the progress of reduction and calcination fronts along the bed, which can be linked to the outlet gas composition in **Figure 6.7b**. It takes around 300 s for the bed to be fully calcined, during which time the gas output from the bed is wet CO<sub>2</sub> with small levels of impurities. After calcination is complete, the NiO reduction front continues to progress through the bed, with the end of the bed achieving 95% NiO conversion at around 900 s. During this second period, the H<sub>2</sub> and CO concentrations gradually rise to 50% and 40% respectively, while there is very little CH<sub>4</sub>. This indicates that the off-gas (34.1% CO, 29.1% H<sub>2</sub>, 18.4% CH<sub>4</sub>) is being converted via a combination of reduction and reforming reactions. The timings of each stage are discussed in more detail in the following sections.

**Figure 6.7c** shows that, when reduction-calcination is complete, the bed temperature is reduced to 840°C, close to the operating temperature for the next stage, sorption-enhanced reforming. The stage has therefore achieved one of its key functions of cooling the bed to an appropriate temperature.

Rates of reaction are illustrated in **Figure 6.8**, showing a snapshot at 120 s. The most prominent reaction is calcination, showing a large peak at the edge of the calcination front. Reduction with H<sub>2</sub> and CO are the next most prominent, with their peak lagging behind calcination. To a lesser extent,

some steam methane reforming is also occurring in the system, and a small amount of CO and H<sub>2</sub>O is consumed by water gas shift (**Figure 6.8b**).



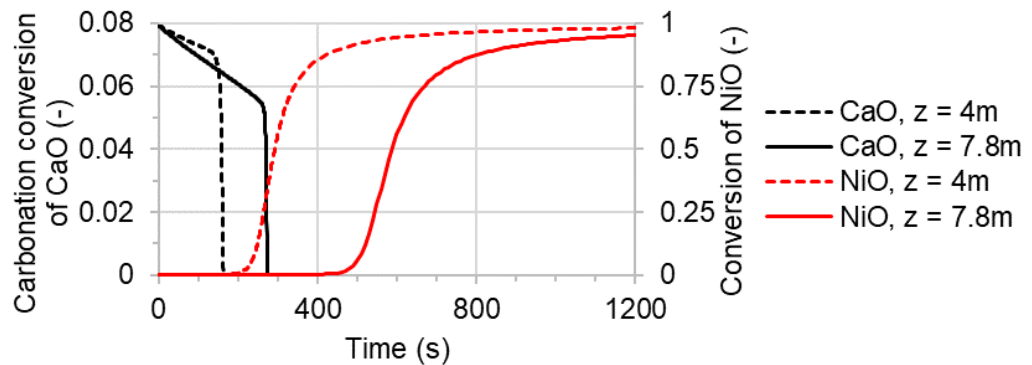
**Figure 6.8 – Rates of reaction at 120s for reduction-calcination with 10 mol% off-gas in H<sub>2</sub>O as reducing gas. (a) calcination and reduction, (b) other reactions**  
**Inlet conditions 1.2 bar, 919°C, 0.3 kg m<sup>-2</sup> s<sup>-1</sup>, B = 3**

In the system under study, steam contents of 90 mol% or higher are required for simultaneous reduction-calcination. The required level of steam would be different for each system, depending on a range of factors that determine the partial pressure of CO<sub>2</sub>. These include the off-gas composition, system pressure and the ratio of sorbent to catalyst. Detailed dynamic reactor modelling is a valuable tool to evaluate these complex interacting factors.

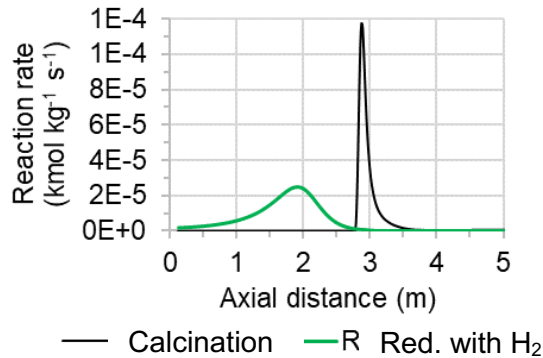
While steam dilution assists with calcination, it also reduces the partial pressure of all other reactants, and therefore reduces the rate of reduction. The operating strategy should aim for the minimum level of steam dilution, sufficient to enable calcination without hindering rates of reduction any further than necessary. The sensitivity analysis in the following sections evaluates methods to improve the relative speeds of calcination and reduction. Steam dilution also has impacts for reactor design and cost, discussed further in **Section 6.3.4**.

For comparison, a feed gas of 10% of H<sub>2</sub> in H<sub>2</sub>O was also examined. **Figure 6.9** shows that the calcination front takes about 300s to reach the end of the bed, similar to the off-gas case. However, it takes 1200s for the end of the bed to achieve 95% NiO conversion, or 50% longer than the off-gas case. In the H<sub>2</sub> system, the only reduction reaction that occurs is reduction with H<sub>2</sub> (**Figure 6.10**), so it takes longer for the NiO to be fully reduced. This

identifies an additional advantage of using off-gas rather than H<sub>2</sub>. It not only reduces H<sub>2</sub> wastage and makes use of the off-gas product, but it also enables faster reduction of the bed.

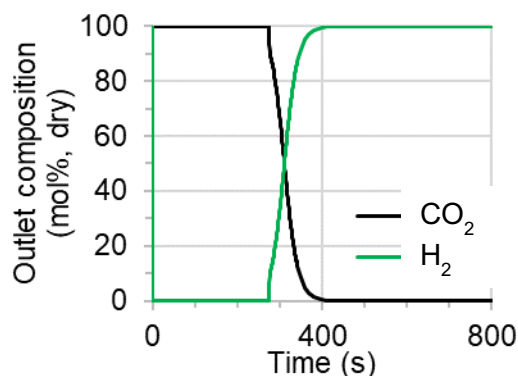


**Figure 6.9 – Model results for reduction-calcination with 10 mol% H<sub>2</sub> in H<sub>2</sub>O, showing carbonation conversion and conversion of NiO. Inlet conditions 1.2 bar, 919°C, 0.3 kg m<sup>-2</sup> s<sup>-1</sup>, B = 3.**



**Figure 6.10 – Rates of reaction at 120s, 10 mol% H<sub>2</sub> in H<sub>2</sub>O. Inlet conditions 1.2 bar, 919°C, 0.3 kg m<sup>-2</sup> s<sup>-1</sup>, B = 3.**

A further consideration is the outlet gas composition, shown in **Figure 6.11**. After calcination ends at 300 s, there is a 100 s transition period where CO<sub>2</sub> concentration falls and H<sub>2</sub> rises, representing the time for the feed gas to begin breaking through. From 400 s to 1200 s, reduction is still occurring in the bed but unreacted H<sub>2</sub> passes through to the outlet gas. This H<sub>2</sub> stream could be recycled to the process, offering a potential advantage compared to the off-gas feed, which produces a mixture of H<sub>2</sub>, CO and CO<sub>2</sub>.



**Figure 6.11 – Outlet gas composition, dry basis in reduction-calcination with 10 mol% H<sub>2</sub> in H<sub>2</sub>O as reducing gas. inlet conditions 1.2 bar, 919°C, 0.3 kg m<sup>-2</sup> s<sup>-1</sup>, B = 3.**

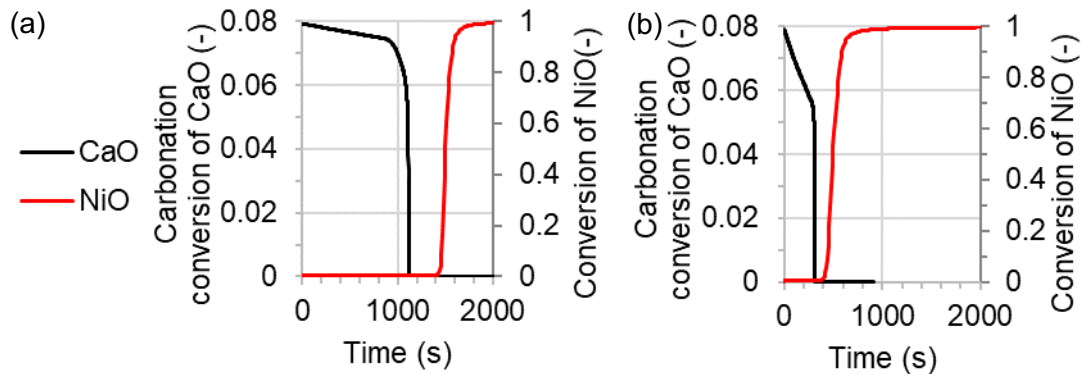
### 6.3.3 Sensitivity analysis

Having identified a suitable level of steam dilution to achieve reduction-calcination, the next stage is to optimise other parameters in the process. The following results examine the influence of a range of parameters, including temperature, mass flux, pressure, and sorbent capacity, in order to identify opportunities to tune the bed for optimal performance.

As discussed above, the results in **Figure 6.7** demonstrate that the reduction and calcination fronts move at different speeds along the bed. During the calcination period (the first 400 s), the outlet gas composition is nearly pure CO<sub>2</sub>. From 400 s to 900 s, the bed continues to undergo NiO reduction, during which time the outlet gas composition is no longer pure CO<sub>2</sub> (**Figure 6.7c**). This has implications for CO<sub>2</sub> capture, as the bed produces on-specification CO<sub>2</sub> for less than 50% of the total stage time. This would increase carbon slip from the process, as less of the carbon content in the off-gas would be captured. It would also influence the operating strategy, as CO<sub>2</sub> capture would not be continuous. Thus a particular focus of the sensitivity study is to identify methods to alter the relative speeds of reduction and calcination, in order to improve continuity of CO<sub>2</sub> production.

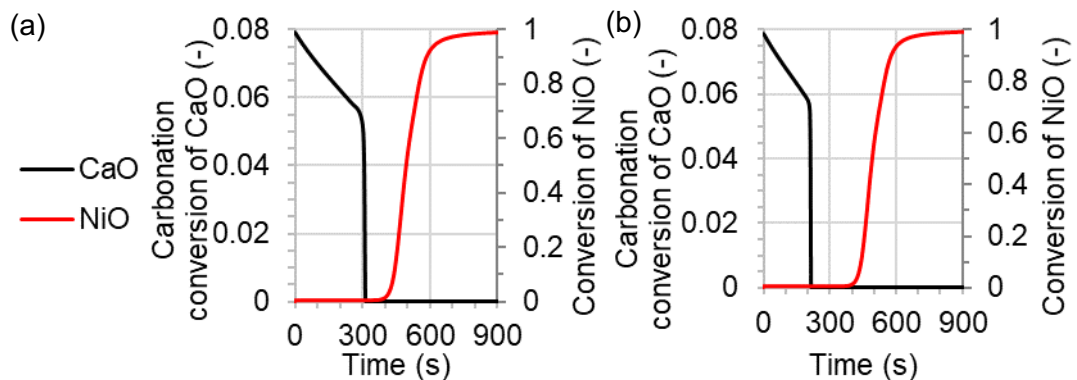
**Figure 6.12** shows the effect of gas mass flux. Increasing the gas mass flux from 0.1 to 0.3 kg m<sup>-2</sup> s<sup>-1</sup> causes both reduction and calcination fronts to progress at a faster rate through the bed. The influence is slightly greater in the case of reduction, so that increased flux brings the two fronts closer together. The reduction reactions depend upon the availability of reactants, and thus are strongly influenced by mass transfer rates. In contrast, the calcination reaction is influenced by CO<sub>2</sub> concentration, temperature and pressure, and so the mass transfer rates have less influence. Bringing the

two fronts closer together reduces the time difference between the calcination and reduction periods. The resulting effect of flux on operation and design is explored in **Section 6.3.4**.

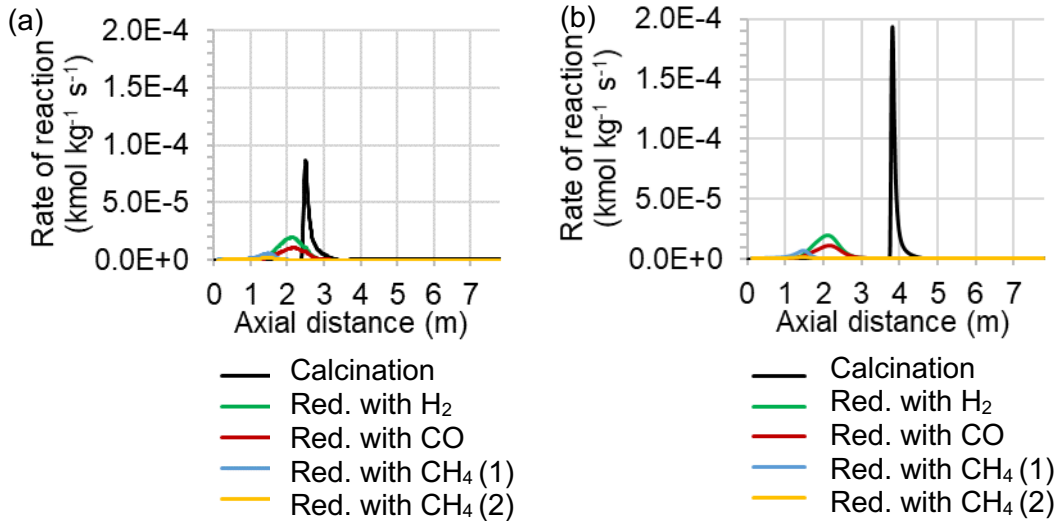


**Figure 6.12 – Effect of gas mass flux in reduction-calcination, showing NiO and CaO conversion at bed outlet ( $z = 7.8\text{m}$ ). (a)  $0.1 \text{ kg m}^{-2} \text{ s}^{-1}$  (b)  $0.3 \text{ kg m}^{-2} \text{ s}^{-1}$ . Inlet conditions 10 mol% off-gas in  $\text{H}_2\text{O}$ , 1.2 bar,  $918^\circ\text{C}$ ,  $B = 3$ .**

**Figure 6.13** shows the effect of increasing the initial bed temperature from  $918^\circ\text{C}$ , the temperature observed at the end of oxidation in the Aspen Plus process model, to a slightly higher temperature of  $950^\circ\text{C}$ . The temperature is not increased beyond this level because the calcination kinetics (Eq. 6.24) are not valid above  $950^\circ\text{C}$ . Despite the relatively small change in temperature, the graph shows that the time to complete calcination decreases by 33% from 300 to 200 s. The reduction front shows little change, with both cases taking around 900 s to achieve 95% NiO conversion. This is explained by the rates of reaction, shown in **Figure 6.14**. The rate of calcination is strongly influenced by the temperature change within this region, being approximately doubled. When compared on the same scale, the reduction reaction rates show little change by comparison. This suggests that increasing temperature would not be an effective method to improve the synchronisation of reduction and calcination.



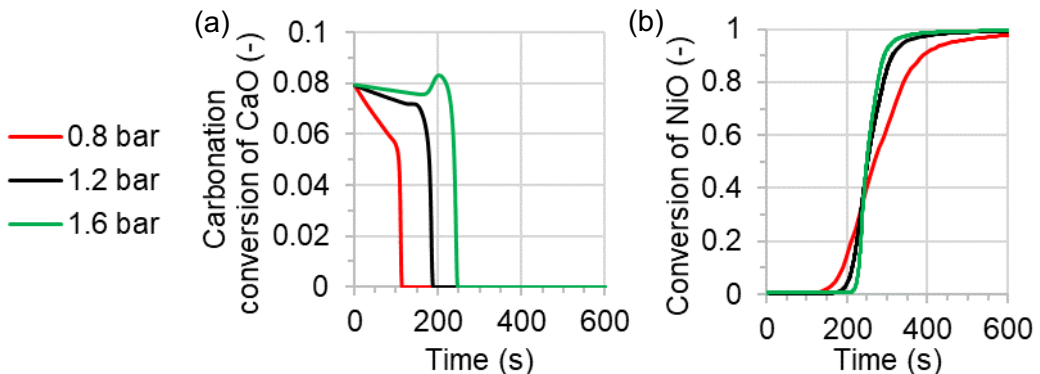
**Figure 6.13 – Effect of initial temperature in reduction-calcination, showing NiO and CaO conversion at bed outlet ( $z = 7.8\text{m}$ ). (a)  $918^\circ\text{C}$  (b)  $950^\circ\text{C}$ . Inlet conditions 10 mol% off-gas in  $\text{H}_2\text{O}$ , 1.2 bar,  $0.3 \text{ kg m}^{-2} \text{ s}^{-1}$ ,  $B = 3$ .**



**Figure 6.14 – Effect of temperature on rates of reaction at t = 120 s. (a) 918°C (b) 950°C**

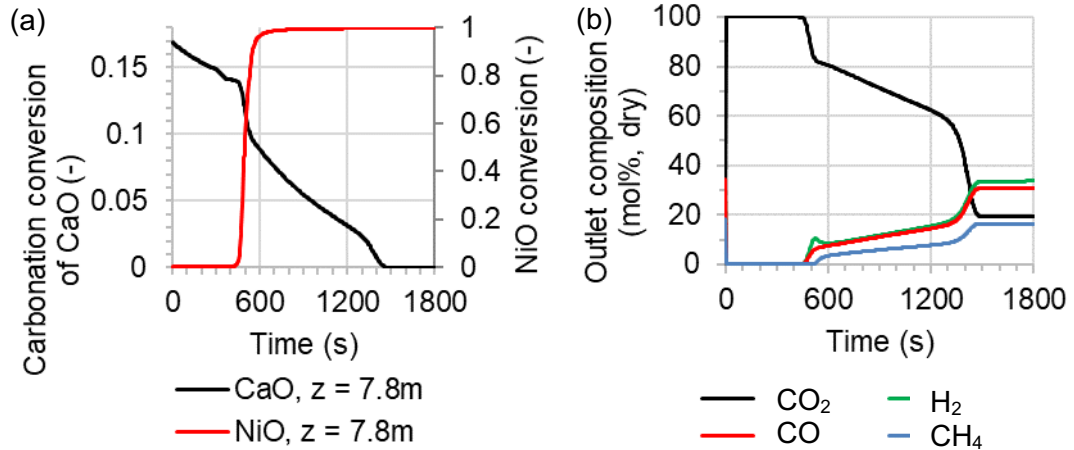
**Inlet conditions 10 mol% off-gas in H<sub>2</sub>O, 1.2 bar, 0.3 kg m<sup>-2</sup> s<sup>-1</sup>, B = 3.**

The effect of pressure is shown in **Figure 6.15**. At the operating conditions considered in this study, small pressure changes have a strong influence on calcination. In contrast, the overall speed of the reduction front sees little change, although the shape of the front becomes sharper as the pressure increases. Operating in vacuum conditions (0.8 bar) increases the speed of calcination. However, as the reduction front does not speed up to the same extent, this would increase the length of time between the end of calcination and the end of the stage, and therefore the length of time with off-specification CO<sub>2</sub>. In the highest pressure case (1.6 bar), there is a spike in the calcination front. As discussed in **Section 6.3.2**, this spike is observed when the partial pressure of CO<sub>2</sub> becomes too high for calcination to occur. Thus operating at higher pressures would require the feed gas to be diluted further, in order to sustain calcination.



**Figure 6.15 – Effect of pressure in reduction-calcination in 10 mol% off-gas in H<sub>2</sub>O. (a) NiO conversion at z = 4m (b) CaO conversion at bed outlet at z = 4m. Inlet conditions 1.2 bar, 919°C, 0.3 kg m<sup>-2</sup> s<sup>-1</sup>, B = 3.**

The final sensitivity to be considered is the sorbent capacity, to show the effects of designing new sorbent materials with different sorption performance. The base case sorbent capacity is 0.08, based on **Eq. 6.24**, originally determined by experiment in Martinez et al. [159]. **Figure 6.16** shows the impact when the maximum NiO sorbent capacity is increased to 0.17.



**Figure 6.16 – Modelling results with higher sorbent capacity ( $X_{\text{carb,max}} = 0.17$ ).**  
**(a) conversion of CaO and NiO at the bed outlet and (b) product gas compositions.**

**Inlet conditions 1.2 bar, 918°C, 0.3 kg m<sup>-2</sup> s<sup>-1</sup>, B = 3.**

Due to the higher quantity of CO<sub>2</sub> stored in the sorbent, the calcination front takes more time to progress through the bed. As a result, the reduction front is faster than the calcination front (**Figure 6.16a**). This changes the shape of the calcination front, showing three distinct periods:

- 1) Reduction-calcination: during the initial 500 s, the reduction front is passing through the bed, releasing CO<sub>2</sub> and slowing the rate of calcination. Nearly pure CO<sub>2</sub> is produced (**Figure 6.16b**).
- 2) Calcination: from around 500 s to 1200 s, reduction is complete and calcination continues, but at a faster rate. As the off-gas components are no longer required to reduce the OTM, they pass through the bed. This produces a mixture of CO<sub>2</sub>, CO, H<sub>2</sub> and CH<sub>4</sub>.
- 3) Off-gas breakthrough: from around 1200 s, both reduction and calcination are complete, so the outlet gas composition mirrors the inlet composition.

This is one example of a case where the reduction front is faster than the calcination front. In such a case, the potential for CO<sub>2</sub> capture is reduced as a large portion of the calcination time produces an impure stream of CO<sub>2</sub>. This confirms that the preferred scenario is for the calcination front to progress faster than the reduction front, albeit with some of the measures discussed above to synchronise the two fronts as far as possible.



It also highlights the importance of considering how sorbent capacity might affect all stages in the process. Higher sorbent capacity is desirable as it reduces the required solids inventory, creating a smaller reactor with more efficient heat transfer. However, this example demonstrates that higher sorbent capacity has implications for simultaneous reduction-calcination that also require consideration.

### 6.3.4 Impacts on reactor design, operation and cost

The modelling results and sensitivity analysis have demonstrated how the reduction-calcination process can be tuned by adjusting a number of factors, including temperature, flux, and pressure. The next stage is to consider the practical implications on operating strategy, reactor design, and cost.

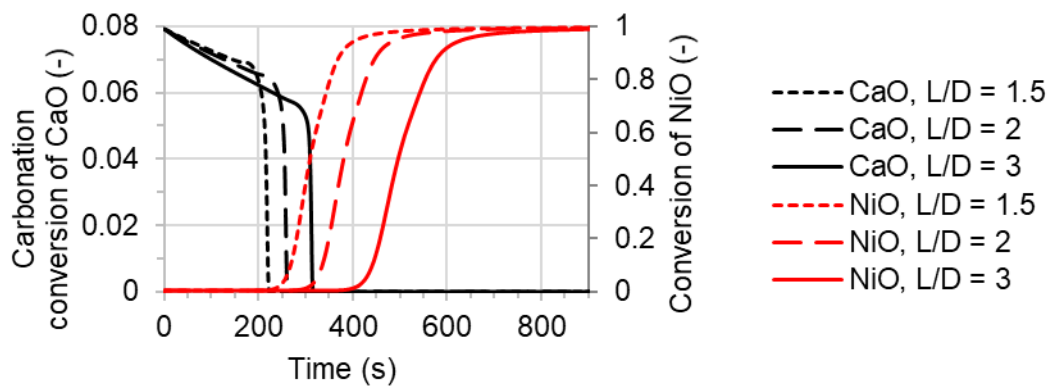
**Table 6.12** summarises the basis of design for this evaluation. Operating temperature and pressure were fixed on the basis of the sensitivity analysis. A range of L/D ratios and gas mass fluxes were considered, to evaluate the effect on operational timings.

**Table 6.12 – Basis of design for reduction-calcination**

Operating conditions			
$P_{in}$ (bar)	1.2		
$T_{in}$ (°C)	919		
Feed gas	10 mol% off-gas in H <sub>2</sub> O		
Reactor sizing			
L/D ratio	1.5	2	3
Length (m)	4.9	6	7.8
Diameter (m)	3.3	3	2.6

**Figure 6.17** illustrates the reduction, calcination and temperature profiles at the end of the bed, when the L/D ratio changes between 1.5 and 3. An increased L/D ratio increases the total length, causing the reduction and calcination fronts to take longer to reach the end of the bed.





**Figure 6.17 – Ca and NiO conversion profiles at the bed outlet, for different reactor L/D ratios.**

**Inlet conditions 10 mol% off-gas in H<sub>2</sub>O, 1.2 bar, 918°C, 0.3 kg m<sup>-2</sup> s<sup>-1</sup>, B =3**

Results such as those shown in **Figure 6.17** can be used to identify the timing of key events in the stage, in order to quantify the effects of varying L/D ratio and gas mass flux. The results are shown in **Table 6.13**. The time for CO<sub>2</sub> to go off-specification was determined by the CO content, as this was observed to be the first component to exceed the specification limits in **Table 3.5** (4750 ppm). Time for calcination was measured at the point at which the end of the bed reaches CaO conversion <0.001. The limit for NiO was less stringent, as the asymptotic nature of the NiO reduction front means it takes a considerable amount of time for NiO conversion to increase from 95% to 100%. While the end of the bed is at 95% conversion, the majority of the rest of the bed will have already reached 100% conversion. Time for reduction is therefore taken as the time taken for the end of the bed to achieve >95% NiO conversion.

**Table 6.13 – Effect of L/D ratio and gas mass flux on key time steps in reduction-calcination at 918°C, 1.2 bar**

	L/D = 1.5	L/D = 2	L/D = 3
<b>G<sub>z</sub> = 0.1 kg m<sup>-2</sup> s<sup>-1</sup></b>			
Duration CO <sub>2</sub> on-spec (s)	805	1018	1350
Time to 95% NiO conversion (s)	1040	1265	1630
Time with CO <sub>2</sub> off-spec (s)	235	247	280
Time with CO <sub>2</sub> off-spec (% of total)	23%	20%	17%
<b>G<sub>z</sub> = 0.2 kg m<sup>-2</sup> s<sup>-1</sup></b>			
Duration CO <sub>2</sub> on-spec (s)	345	427	580
Time to 95% NiO conversion (s)	560	680	870
Time with CO <sub>2</sub> off-spec (s)	215	253	290
Time with CO <sub>2</sub> off-spec (% of total)	38%	37%	30%

	L/D = 1.5	L/D = 2	L/D = 3
<b><math>G_z = 0.3 \text{ kg m}^{-2} \text{ s}^{-1}</math></b>			
Duration CO <sub>2</sub> on-spec (s)	205	255	315
Time to 95% NiO conversion (s)	410	500	640
Time with CO <sub>2</sub> off-spec (s)	205	245	325
Time with CO <sub>2</sub> off-spec (% of total)	50%	49%	51%

The results in **Table 6.13** show that increasing the L/D ratio increases the total time period required for the stage, as well as the time during which the bed is producing off-specification CO<sub>2</sub>. While a higher L/D ratio increases the total time taken for the stage, it also lowers the proportion of time that the CO<sub>2</sub> is off-specification. Increasing the gas mass flux reduces the total time required for the stage, but increases both the time and proportion of time spent with CO<sub>2</sub> off-specification. In terms of CO<sub>2</sub> slip from the process, a longer duration with CO<sub>2</sub> off-specification (i.e. a slower calcination front) is preferable, as this means that a larger proportion of the carbon within the off-gas is also being captured. However, this comes at the expense of slower reduction-calcination step which could have implications for SE-CLSR cycle sequencing. This suggests there is no single solution that is optimal for all factors as there is a trade-off between total stage time, time with off-specification CO<sub>2</sub>, and total CO<sub>2</sub> slip.

Potential operational measures to manage the discontinuity of pure CO<sub>2</sub> production would be to have a CO<sub>2</sub> buffer vessel, or to recycle a slipstream of CO<sub>2</sub>, thereby ensuring a continuous supply to the CO<sub>2</sub> compression and storage system. Reducing the duration of the off-specification period would reduce the cost of this buffer vessel or recycle loop.

Other impacts on the process design include the requirement to generate additional steam, and the length of cycle steps. The resulting changes to performance indicators such as net thermal efficiency, cost of hydrogen and cost of carbon avoided are not considered here, as a full techno-economic analysis is outside the scope of this study. However, this modelling work highlights variations to the design and operating strategy that could be integrated with full process modelling in future work.

## 6.4 Conclusion

The reduction-calcination stage in SE-CLSR performs several vital functions, including simultaneous OTM reduction, sorbent regeneration, bed cooling,

and CO<sub>2</sub> capture. Due to the complexity of the various interacting phenomena, it is difficult to assess the viability of such an approach without a detailed model. Thus this study aimed to develop a dynamic packed bed reactor model, and to use this to evaluate aspects of process design and operating strategy. Packed bed reactor models were developed for NiO reduction and SE-SMR occurring in a mixed bed of NiO/Al<sub>2</sub>O<sub>3</sub> and CaO. Following validation of both models with experimental data from literature, they were combined to create a model of a mixed bed of NiO /Al<sub>2</sub>O<sub>3</sub> and CaO undergoing simultaneous reduction-calcination.

The model confirms that simultaneous reduction-calcination with PSA off-gas is possible in a Ni-based chemical looping process. This is a key finding, as previous studies of simultaneous reduction-calcination have focussed on Cu-based processes. This study used a PSA off-gas composition from bio-oil steam reforming (derived in **Chapter 5**), but the model could be transferable to an off-gas composition from the steam reforming of any feedstock. Future work could also improve the model by validating it with experimental results at a range of conditions.

A sensitivity analysis was carried out to evaluate the effects of feed gas composition, temperature, pressure, flux and sorbent capacity, with a particular focus on improving the synchronicity of reduction and calcination. The evaluation showed that changing these factors can help to tune the bed design to improve sequence timings, for example by increasing the length of time during which CO<sub>2</sub> product is on-specification.

This work demonstrates one approach to process development, whereby whole process equilibrium modelling is linked to detailed kinetic modelling. In the long-term, the ultimate aim would be to have a fully integrated dynamic model for bio-oil SE-CLSR that can model all the sequence steps and their interactions at cyclic steady state, similar to existing models for PSA [93,359,360] or methane-based SE-CLSR [163,165,209,210]. However, at present, there is insufficient data on bio-oil reaction kinetics. This challenge is explored further in **Chapter 7**. Until kinetic data is available, this combined approach of equilibrium and kinetic modelling may serve as interim method to identify opportunities and limitations for process development.

## Chapter 7 – Kinetic study on acetic acid steam reforming

### 7.1 Introduction

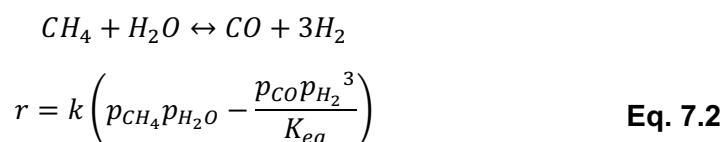
Following the evaluation of the thermodynamic and economic feasibility of bio-oil SE-CLSR, **Chapter 6** used a reactor model to evaluate one stage of SE-CLSR (reduction-calcination). A complete analysis of SE-CLSR would require a similarly detailed model of the other main stage, sorption-enhanced reforming. However, kinetic data on the steam reforming of bio-oil and its constituent compounds is currently lacking, meaning there is limited ability to develop such a model. In order to resolve this gap, this chapter aims to derive kinetic data for a bio-oil model compound, and to use this data for preliminary large-scale reactor modelling.

There have been various kinetic studies on the steam reforming of bio-oil, bio-oil model compounds, and other bio-compounds such as glycerol, summarised in **Table 7.1**. These studies use three main approaches to evaluate reaction kinetics:

- 1) **Power law models** are the simplest form, typically used for non-reversible reactions. Data are fitted to a simple empirical rate equation based on the concentration of partial pressure of reactants, for example:

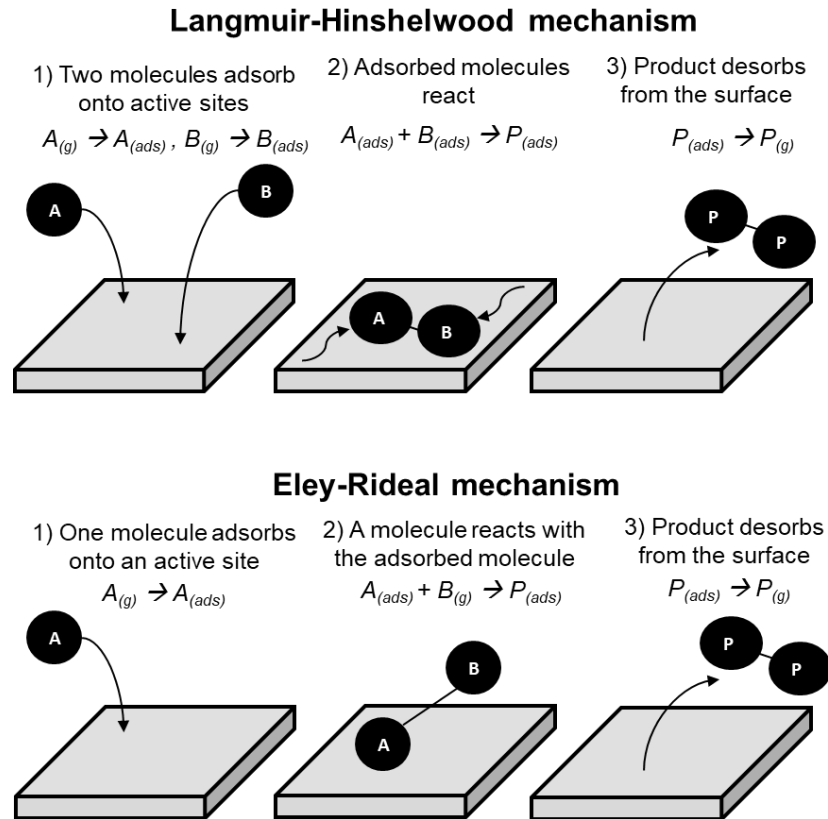
$$R = k(p_A)^\alpha (p_B)^\beta \quad \text{Eq. 7.1}$$

- 2) **Mass action approach** assumes the rate of reaction is directly proportional to reactant concentrations. They are similar to power law models in that the rate of reaction is not linked to a particular reaction mechanism. They can also incorporate an equilibrium constant ( $K_{eq}$ ) to describe the relative rates of forward and backward reactions. For example, for steam methane reforming [361]:



- 3) **Active-site approach**, in which a rate equation is formulated by describing the underlying mechanism. Catalysis is described via three steps: adsorption onto an active site, reaction at the active site, and desorption. Rate expressions are then derived by postulating the surface mechanism, such as a Langmuir-Hinshelwood or Eley-Rideal mechanism (**Figure 7.1**). A rate-determining step (RDS) is then proposed, in order to construct a rate

equation. Several of these mechanisms are tested, in order to determine which provides the closest fit.



**Figure 7.1 – Langmuir-Hinshelwood and Eley-Rideal reaction mechanisms, adapted from [362]**

The intended purpose of a kinetic study will determine which approach is preferable. The active-site approach can shed light on the mechanisms of catalysis. It is also more readily extrapolated, as it uses fundamental principles to describe what is occurring. However, it requires an extensive experimental program and detailed statistical analysis to establish which mechanism provides the best fit. Given the opportunities for experimental error, it can be difficult to determine the true mechanism with any certainty. This level of detail may not always be justified, as power law and mass action models can often provide sufficient detail for reactor design [363].

Another key aspect of kinetic studies is the method that is used to convert experimental data to rate data, which may be one of the following:

- 1) Integral method
- 2) Differential method
- 3) Reactor model

In the integral method, a rate equation is proposed, and integrated. The integrated rate equation is then checked for goodness of fit, usually by manipulating it to give an expression for a straight line. For example, for a first order equation [363]:

$$\frac{dX_A}{dt} = k(1 - X_A) \quad \text{Eq. 7.3}$$

$$\int_0^{X_A} \frac{dX_A}{(1 - X_A)} = k \int_0^t dt \quad \text{Eq. 7.4}$$

$$-\ln(1 - X_A) = kt \quad \text{Eq. 7.5}$$

Thus, if the reaction is first order, a plot of  $\ln(1 - X_A)$  versus  $t$  would yield a straight line. If the data does not fit a straight line, the procedure is repeated with a different rate equation.

In the differential method, the reactor is modelled as a single element [267]. Using the design equation for a packed bed reactor, the rate of reaction can be expressed as [363]:

$$-r_A = \frac{dX_A}{d(W/F_{A0})} \quad \text{Eq. 7.6}$$

where  $W$  is the mass of catalyst, and  $F_{A0}$  is the inlet molar flow rate of  $A$ . The average rate of reaction across the whole reactor can therefore be determined by taking the slope of the curve  $X_A$  vs.  $W/F_{A0}$ . The rates of reaction are then fitted to a rate equation.

The third approach is to use a reactor model. In this case, a model is constructed to describe a reaction system. This can be a simple mass balance [100,268], or can also include mass and heat transfer phenomena and properties such as dispersion and viscosity [267]. Parameter fitting is then carried out, using nonlinear regression, which manipulates the kinetic parameters until the model outputs match observed reality.

Each approach has different advantages and disadvantages. Integral analysis is a rapid procedure for testing simple rate equations. However, in more complex situations, the integration becomes unwieldy, and differential analysis may be more convenient [363]. Differential analysis uses an average rate across the whole reactor, which can introduce inaccuracies, particularly if the conversion is high [267,363]. Reactor simulation requires computer simulations, but can enable more accuracy, for example by including transport phenomena and the change of concentration across the reactor [267].

Table 7.1 – Review of bio-compound kinetic studies in literature

Compound	Catalyst	Type of kinetic model	Analysis	Power law/mass action equation	RDS	Ref
Acetic acid	Ni-Al promoted with lanthanum	First order relation to equilibrium	Differential	$r_i = k_i \left[ \left( \frac{m_i}{m_{AcOH}} \right)_{equil} - \left( \frac{m_i}{m_{AcOH}} \right) \right]$ <p>where <math>i = H_2, CO_2, CH_4</math> and <math>C_2</math> gases</p>		[126]
Acetol	Pt/C	Power law Eley-Rideal Langmuir-Hinshelwood	Differential	$-r_{Ac} = k p_{Ac}^\alpha$ <p><math>\alpha = 0.78 - 0.88</math>, varying with temperature</p>	Surface reaction	[364]
Acetone	Ni/ $\gamma$ -Al <sub>2</sub> O <sub>3</sub> Ni-Rh/ $\gamma$ -Al <sub>2</sub> O <sub>3</sub>	Mass action	Reactor model	<p>Acetone SR:</p> $r_1 = k_1 \left( p_{CH_3COCH_3} - \frac{p_{CO_2}^3 p_{H_2}^8}{K_1 p_{H_2O}^5} \right) P^{-0.5}$ <p>Acetone decomposition:</p> $r_2 = k_2 \left( p_{CH_3COCH_3} - \frac{p_{CH_4} p_{CH_2CO}}{K_2} \right) P^{-0.5}$		[173]
Benzene	Ni/ $\alpha$ -Al <sub>2</sub> O <sub>3</sub>	Power law Langmuir-Hinshelwood	Reactor model	$-r_{Bz} = k p_{Bz}^{0.91} p_{H_2O}^{0.15}$	Benzene adsorption	[365]
Bio-oil (CH <sub>1.93</sub> O <sub>0.92</sub> )	14% Ni/CaO-Al <sub>2</sub> O <sub>3</sub> (commercial)	Power law	Reactor model	$-r_{bio-oil} = k p_{bio-oil} p_{H_2O}$		[266]

Compound	Catalyst	Type of kinetic model	Analysis	Power law/mass action equation	RDS	Ref
<b>Bio-oil</b> (C <sub>2.8</sub> H <sub>7.4</sub> O <sub>1.8</sub> )	Ni/	Power law	Reactor model	$-r_{bio-oil} = kp_{bio-oil}^{0.6}p_{H_2O}^{0.8}$	Bio-compound adsorption	[267]
	Ce <sub>0.5</sub> Zr <sub>0.33</sub> Gd <sub>0.166</sub> O <sub>2</sub>	Eley-Rideal				
<b>Bio-oil</b> (C <sub>3.9</sub> H <sub>6.1</sub> O <sub>3.0</sub> )	Ni/La <sub>2</sub> O <sub>3</sub> - $\alpha$ Al <sub>2</sub> O <sub>3</sub>	Power law	Reactor model	$-r_{bio-oil} = kp_{bio-oil}p_{H_2O}^{0.9}$		[268]
<b>Butanol</b>	Ru/Al <sub>2</sub> O <sub>3</sub>	Power law	Differential	$-r_{But} = kp_{But}^{\alpha}$ $\alpha = 0.92 - 1.12$ , varying with temperature	Surface reaction	[366]
		Langmuir-Hinshelwood				
<b>Ethanol</b>	15% Ni/Al <sub>2</sub> O <sub>3</sub>	Power law Eley-Rideal	Differential	$-r_{EtOH} = kp_{EtOH}^{0.42}$	Dissociation of adsorbed ethanol	[367]
	Ni-based commercial	Power law Langmuir-Hinshelwood Eley-Rideal	Differential	$-r_{EtOH} = kp_{EtOH}^{3.64}$	Molecular adsorption of ethanol	[255]
	Ni-Rh/ $\gamma$ -Al <sub>2</sub> O <sub>3</sub>	Power law	Reactor model	Thermal decomposition of ethanol: $-r_{EtOH} = kp_{EtOH}$		[173]
	Ni-Al	Langmuir-Hinshelwood	Reactor model		Surface reaction	[368]
	Pd/ $\gamma$ -Al <sub>2</sub> O <sub>3</sub>	Power law	Reactor model	Thermal decomposition: $-r_{EtOH} = kp_{EtOH}p_{H_2O}$		[369]
	Rh-Pd/CeO <sub>2</sub>	Power law	Reactor model	Thermal decomposition: $-r_{EtOH} = kp_{EtOH}$		[361]
	Ni-Al	Langmuir-Hinshelwood	Reactor model		Surface reaction	[370]



Compound	Catalyst	Type of kinetic model	Analysis	Power law/mass action equation	RDS	Ref
<b>Ethanol</b>	Pt-Ni/ $\delta$ -Al <sub>2</sub> O <sub>3</sub>	Power law	Initial rate	$-r_{EtOH} = kp_{EtOH}^{1.25} p_{H_2O}^{-0.215}$		[371]
	Pt-Ni/ $\delta$ -Al <sub>2</sub> O <sub>3</sub>	Power law	Differential	$-r_{EtOH} = kp_{EtOH}^{1.01} p_{H_2O}^{-0.09}$		[372]
	15% Ni/ $\gamma$ -Al <sub>2</sub> O <sub>3</sub> (commercial)	Power law Langmuir-Hinshelwood	Differential	$-r_{EtOH} = kp_{EtOH}^{1.52}$	Surface dissociation of methane	[373]
<b>Glycerol</b>	15% Ni/ $\gamma$ -Al <sub>2</sub> O <sub>3</sub>	Power law Langmuir-Hinshelwood	Not given	$-r_{Gly} = kp_{Gly}^{0.48} p_{H_2O}^{0.34}$ $r_{H_2} = kp_{Gly}^{0.34} p_{H_2O}^{0.27}$ $r_{CO_2} = kp_{Gly}^{0.39} p_{H_2O}^{0.41}$ $r_{CO} = kp_{Gly}^{0.74} p_{H_2O}^{-0.39}$ $r_{CH_4} = kp_{Gly}^{0.88} p_{H_2O}^{0.34}$	Surface reaction	[374]
	Ni/10%Nb <sub>2</sub> O <sub>5</sub> /Al <sub>2</sub> O <sub>3</sub>	Power law	Differential	$-r_G = kp_G^{0.9} p_{H_2O}^2$		[375]
	Ni/CeO <sub>2</sub> Ni-ZrO <sub>2</sub> /CeO <sub>2</sub>	Power law	Differential	$-r_G = kp_G^{0.4}$		[376]
<b>Glycerol</b>	5% Pt/C	Power law	Differential	$-r_G = kp_G$		[377]
	Ni/CeO <sub>2</sub>	Power law	Differential	$-r_G = kp_G^{0.233}$		[378]
<b>Phenol</b>	Ni-Co/ZrO <sub>2</sub>	Power law Langmuir-Hinshelwood Eley-Rideal		$-r_p = p_P^{0.9} p_{H_2O}^{0.03}$	Surface reaction	[379]

The review shows there have been numerous kinetic studies on ethanol and glycerol steam reforming, while data on bio-oil and its constituent compounds are more limited. Various experimental studies have examined acetic acid steam reforming [123,127,169,184,190,194,272,380], as it is one of the most abundant compounds in bio-oil [119,124–126]. However, the kinetic data for this compound is still limited. Acetic acid has therefore been selected as the focus of this study. As a continuation from the previous chapters that assumed a Ni/NiO looping cycle, a nickel-based industrial reforming catalyst was used for the kinetic study. A Ni-Ca/Al<sub>2</sub>O<sub>3</sub> was used, after previous work assessed the suitability of this catalyst for acetic acid SE-CLSR [270–272]. **Chapter 3** provides further information on catalyst selection.

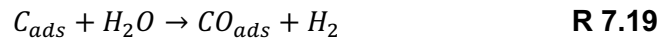
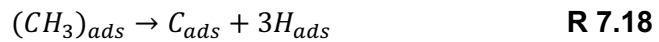
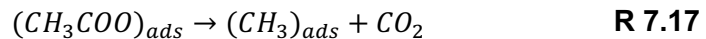
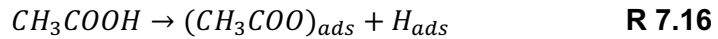
In order to carry out the kinetic study, it was also useful to review existing knowledge of reaction pathways. When acetic acid undergoes steam reforming, the reaction scheme is complex, with multiple possible side reactions. A summary of the key reactions is given in **Table 7.2**.

**Table 7.2 - Summary of reactions in steam reforming of acetic acid** [119,180]

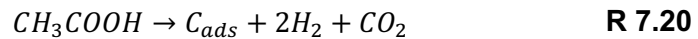
Primary reactions		
R 7.1	SR acetic acid	$CH_3COOH + 2H_2O \rightarrow 2CO_2 + 4H_2$
R 7.2	Ketonization	$2CH_3COOH \rightarrow CH_3COCH_3 + CO_2 + H_2O$
R 7.3	Decomposition 1	$CH_3COOH \rightarrow CH_4 + CO_2$
R 7.4	Decomposition 2	$CH_3COOH \rightarrow 2H_2 + CO_2 + C$
R 7.5	Dehydration	$CH_3COOH \rightarrow CH_2CO + H_2O$
Secondary reactions		
R 7.6	SR acetone	$CH_3COCH_3 + 3H_2O \rightarrow 3CO + 6H_2$
R 7.7	SR ketene	$CH_2CO + H_2O \rightarrow 2CO + 2H_2$
R 7.8	Ketene coupling	$2CH_2CO \rightarrow C_2H_4 + 2CO$
R 7.9	Acetone 1	$2CH_3COCH_3 \rightarrow H_2O + (CH_3)_2CCHCOCH_3$
R 7.10	Acetone 2	$(CH_3)_2CCHCOCH_3 + CH_3COCH_3$ $\rightarrow C_9H_{12} + 2H_2O$
R 7.11	Acetone 3	$C_9H_{12} \rightarrow coke$
R 7.12	SMR	$CH_4 + H_2O \leftrightarrow CO + 3H_2$
R 7.13	Water gas shift	$CO + H_2O \leftrightarrow H_2 + CO_2$
R 7.14	Methanation of CO	$CO + 3H_2 \rightarrow CH_4 + H_2O$
R 7.15	Methanation of CO <sub>2</sub>	$CO_2 + 4H_2 \rightarrow CH_4 + 2H_2O$

Of these reactions, ketonization (R 7.2) and dehydration to ketene (R 7.5) result in products which are precursors to coke formation [119]. Ketonization is particularly prominent at lower temperatures, or in the presence of acidic sites, such as Al<sub>2</sub>O<sub>3</sub> [221,380,381].

Several authors have attempted to describe reaction pathway in greater detail. In 1996, Wang et al [114] proposed a mechanism for the steam reforming reaction on Ni-based catalysts, in which the acetic acid forms adsorbed acetate species that decompose to form CO<sub>2</sub> and H<sub>2</sub>.



R 7.18 and R 7.19 are not elementary steps. Trane et al [119] proposed that the elementary steps for these reactions would be similar to those that occur during steam methane reforming. The overall reaction is as follows:



The adsorbed carbon species, C<sub>ads</sub>, may be removed with steam. The adsorbed methyl species may combine with adsorbed hydrogen molecules to produce methane:

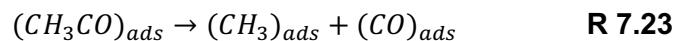
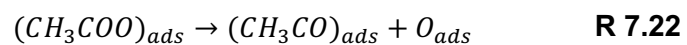


Reaction mechanisms have since been proposed for various other catalysts. For example, Lemonidou et al. [380] examined the reaction pathway on Rh supported on La<sub>2</sub>O<sub>3</sub>/CeO<sub>2</sub>-ZrO<sub>2</sub>, Takanebe et al. [382] proposed a pathway for Pt/ZrO<sub>2</sub> catalysts, and Wang et al [383] examined the mechanism on Co-Fe catalysts. Resende et al. [221] examined steam reforming on a LaNiO<sub>3</sub> perovskite-type catalyst, proposing that acetic acid steam reforming may proceed via two possible reaction pathways:

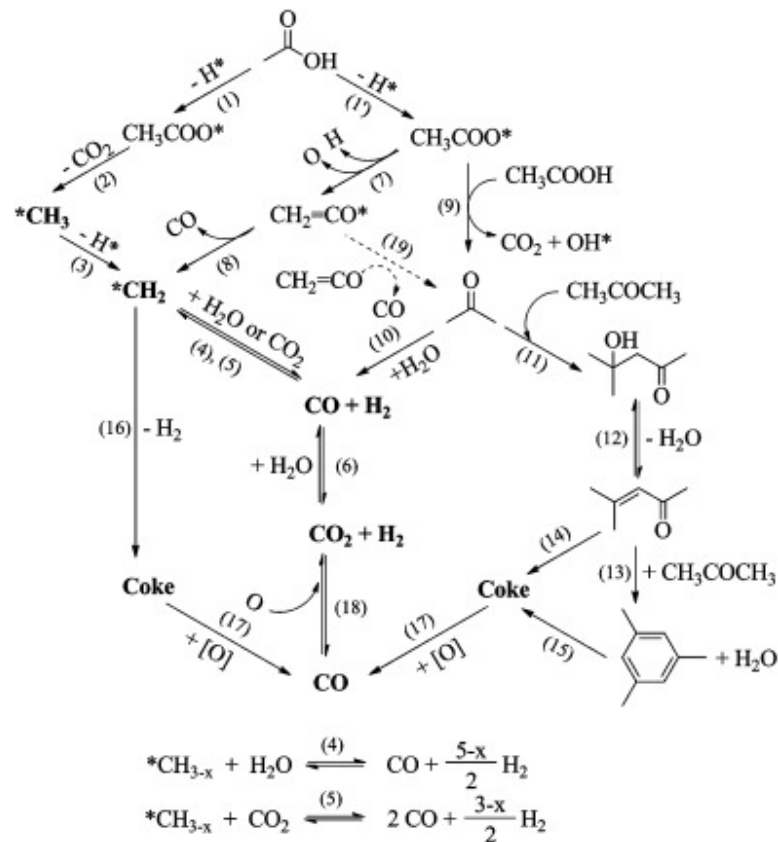
(i) conversion to acetone at intermediate temperatures (between 230 and 600°C)

(ii) transformation into adsorbed acetate species (CH<sub>3</sub>COO\*) followed by decomposition into acetyl species (CH<sub>3</sub>CO\*).

The latter of these is similar to the mechanism proposed by Wang et al [114], with the addition of intermediate steps between R 7.17 and R 7.18:



Hoang et al. [178] reviewed several papers in order to produce a generalized reaction pathway, shown in **Figure 5.2**, in which acetic acid decomposes to H<sub>2</sub>, coke and CO, some of which is converted by WGS.



**Figure 7.2 – Reaction mechanism for acetic acid steam reforming proposed by Hoang et al. [178]**

The following study aims to propose a kinetic model for acetic acid steam reforming. It proposes a simplified reaction scheme, based on the above literature review. Kinetic parameters are estimated by fitting the model to experimental. After testing the model for accuracy, the kinetic model is used to perform preliminary reactor modelling, and to discuss the implications of reaction kinetics for economic feasibility.

## 7.2 Methodology

### 7.2.1 Experimental methodology

The reactor set-up and operating procedure are outlined in **Chapter 3**. The experimental set-up was used to find reactant conversion and outlet compositions at steady state. Reaction conditions were altered by changing the reactor temperature, S/C ratio and flow rates of N<sub>2</sub> and liquid. **Table 7.3** summarises the experimental conditions that were used.

**Table 7.3 – Experimental conditions used for kinetic study**

Design/operating parameter	Value		
Catalyst	15wt% NiO/CaO/Al <sub>2</sub> O <sub>3</sub>		
Catalyst diameter (μm)	150 - 250		
Outlet pressure (bar)	1.01325		
Temperature (°C)	550	620	650
S/C ratio (-)	3	3.5	4
Feed mole fraction (-)	AcOH	H <sub>2</sub> O	N <sub>2</sub>
	0.048	0.342	0.610
	0.058	0.342	0.6
	0.058	0.410	0.531
Feed volumetric flow rate at STP (cm <sup>3</sup> min <sup>-1</sup> )	AcOH + H <sub>2</sub> O solution	N <sub>2</sub>	
	0.109 - 0.921	150 - 800	

To examine carbon deposition, the measured data from CHNS analysis (wt% carbon) were used to estimate the conversion of feedstock to solid carbon. The readings from CHNS were converted to a molar amount using the following equation:

$$n_{C,solid} = m_{catalyst} x_C M_C \quad \text{Eq. 7.7}$$

where  $n_{C,solid}$  is the number of moles of solid carbon and  $m_{catalyst}$  is the mass of catalyst.  $x_C$  is the measured mass fraction of carbon, and  $M_C$  is the molar mass of carbon.

The fractional conversion from AcOH to solid carbon ( $X_{solid}$ ) was found by:

$$X_{solid} = \frac{n_{C,solid}}{\dot{n}_{C,AcOH} t} \quad \text{Eq. 7.8}$$

where  $\dot{n}_{AcOH,in}$  is the molar flow of carbon in acetic acid (2 moles of carbon for each mole of acetic acid) and  $t$  is the total experiment time.

## 7.2.2 Kinetic model

## 7.2.3 Modelling of lab-scale reactor

Kinetic parameters were found via the parameter estimation facility in gPROMS, the process of which is summarised in **Chapter 3**. The parameter fitting operation required a model to describe the laboratory reactor. The model used a simplified version of the generalised mass balance described

in **Chapter 3**. As external mass transfer was not limiting (**Section 7.3.1**), the axial dispersion term was eliminated. Similarly, as the internal mass transfer was not limiting, the effectiveness factor was set to 1. The reactor was isothermal, so the energy balance was also simplified. All other assumptions and governing equations were as outlined in **Chapter 3**.

**Table 7.4 – Mass and energy balances for lab-scale reactor model of acetic acid steam reforming**

<b>Mass balance</b>
$\varepsilon_b \frac{\partial C_i}{\partial t} + \frac{\partial u C_i}{\partial t} = (1 - \varepsilon_b) \rho_{cat,app} r_i$
<b>Energy balance</b>
Isothermal: $T = T_0$

The physical properties of the reactor system are summarised in **Table 7.5**. The inlet pressure was assumed to be slightly above atmospheric pressure, to account for the pressure drop through the system. Apparent density of the catalyst was calculated from the bed size and mass of catalyst, assuming a bed voidage of 0.4.

**Table 7.5 – Parameters for lab-scale reactor model of acetic acid steam reforming**

Description	Value
Inlet pressure (bar)	1.05
Catalyst particle size (m)	$2 \times 10^{-4}$
Apparent catalyst density ( $\text{kg m}^{-3}$ )	1640
Bed voidage (-)	0.4
Bed length (m)	$1.6 \times 10^{-2}$
Bed diameter (m)	$9 \times 10^{-3}$

A gPROMS parameter estimation problem requires the user to define control variables and measured data. In this case, the control variables were those experimental parameters that were altered, namely the inlet concentration, mass flux, and temperature. The measured data were the outlet conversions of acetic acid and H<sub>2</sub>O, described in the model as:

$$X_{AcOH} = \frac{\dot{n}_{AcOH,out} - n_{AcOH,in}}{\dot{n}_{AcOH,in}} \quad \text{Eq. 7.9}$$

$$X_{H_2O} = \frac{\dot{n}_{H_2O,out} - \dot{n}_{H_2O,in}}{\dot{n}_{H_2O,in}} \quad \text{Eq. 7.10}$$

where mass flowrate of component  $i$  is:

$$\dot{n}_i = y_i \times \dot{n}_{total} = y_i \times \frac{G_z A}{M_{av}} \quad \text{Eq. 7.11}$$

where  $\dot{n}_i$  is the molar rate of component  $i$ , and  $y_i$  is its molar fraction.  $G_z$  is the total molar flux,  $M_{av}$  is the average molar mass of the gas, and  $A$  is the cross-sectional area of the reactor.

For Model 2, described in **Table 7.9**, methane was included as a component. Therefore the outlet volume fractions of CH<sub>4</sub> (vol%, dry basis) were also used as measured data for parameter estimation of Model 2.

The absolute average deviation (AAD) was used to assess the accuracy of the model. This was defined as follows:

$$AAD = \frac{|y_{predicted} - y_{measured}|}{y_{measured}} \times 100\% \quad \text{Eq. 7.12}$$

where  $y_{predicted}$  and  $y_{measured}$  represent the measured and predicted values of a parameter, such as reactant conversion or species concentration.

## 7.2.4 Mass transfer limitations

As outlined in **Chapter 3**, kinetic parameter estimation requires that the system is in a region of kinetic control, i.e. mass transfer is not rate-limiting. To establish the absence of mass transfer limitations, a set of experiments was carried out at the highest experimental temperature (650°C), where the rate of reaction would be highest and therefore least likely to be rate-limiting. The rate of reaction was estimated using the differential method. The curve of  $X_{AcOH}$  versus  $W/F$  was fit to a second order polynomial:

$$X_{AcOH} = -a(W/F)^2 + b(W/F) + c$$

The polynomial was differentiated to give an equation for rate of reaction:

$$\frac{dX_{AcOH}}{dW/F} = -r_{AcOH} = -2a(W/F) + b$$

The rate of reaction was then taken from this equation at a single point, using the experiment where average reaction rate was highest, i.e. where reaction was least likely to be limiting.

The absence of external mass transfer limitations was confirmed using the Mears criterion [252]:

$$\frac{-r_A \rho_b R n}{k_c C_{Ab}} < 0.15 \quad \text{Eq. 7.13}$$

The Weisz-Prater criterion, as described in **Chapter 3**, was used to confirm the absence of internal mass transfer limitations [252]:

$$C_{WP} = \eta \phi_1^2 = \frac{-r_A \rho_c R^2}{D_e C_{As}} \quad \text{Eq. 7.14}$$

Internal mass transfer is not limiting if  $C_{WP} < 1$ . The effectiveness factor  $\eta$  and Thiele modulus  $\phi_1^2$  are related by the following:

$$\eta = \frac{3}{\phi_1^2} (\phi_1 \coth \phi_1 - 1) \quad \text{Eq. 7.15}$$

## 7.2.5 Industrial scale reactor modelling

To carry out a preliminary study of an industrial scale reactor, the validated model of SE-SMR from **Chapter 6** was used. However, as no sorbent was present in the reactor, the volume fraction of sorbent was set to zero.

**Table 7.6 – Mass and energy balances for full-scale reactor model**

<b>Mass balance:</b>	
$\varepsilon_b \left( \frac{\partial C_i}{\partial t} \right) + \frac{\partial(uC_i)}{\partial z} = \varepsilon_b D_z \frac{\partial^2 C_i}{\partial z^2} + \eta_{cat} (1 - \varepsilon_b) (1 - \varepsilon_{cat}) \rho_{cat} r_i$	<b>Eq. 7.16</b>
<b>Energy balance:</b>	
Isothermal: $T = T_o$	<b>Eq. 7.17</b>

As discussed in **Chapter 2**, industrial reformers consist of a large number of reactor tubes housed within a furnace. The reactor model was used to simulate a single tube within a furnace, assumed to be isothermal.

The reaction scheme and rate equations for acetic acid were taken from the results of the kinetic study. For methane, the reaction kinetics were the same as those used in the validated model of SE-SMR (**Table 6.7**). The model was adapted to industrial size, and the effectiveness factor of catalyst was reduced accordingly. **Table 7.7** outlines the parameters used in the model.



**Table 7.7 – Parameters for industrial scale reactor model**

Description	Value	Ref
Inlet pressure (bar)	1.2	
Temperature (°C)	700	
S/C ratio (-)	3	
Catalyst pellet size (m)	0.01	
Catalyst density (kg m <sup>-3</sup> )	3400	[212]
Particle voidage (-)	0.41	[212]
Bed voidage (-)	0.4	
Volume fraction catalyst (-)	1	
Volume fraction sorbent (-)	0	
Effectiveness factor (-)	0.3	[256,356]
Tube length (m)	15	[72]
Tube diameter (m)	0.250	[72]

The H<sub>2</sub> production from each tube was estimated by:

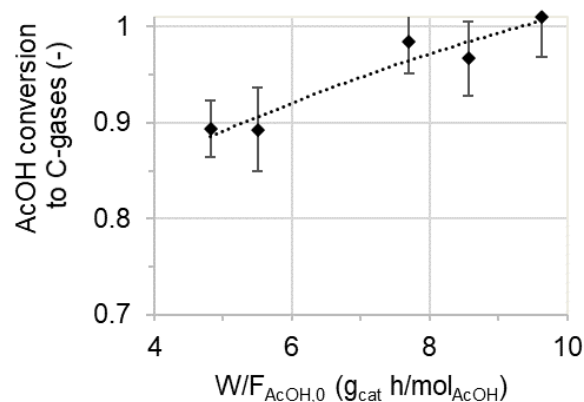
$$\dot{m}_{H_2} = G_z A x_{H_2} \quad \text{Eq. 7.18}$$

where  $\dot{m}_{H_2}$  is the mass flow rate of H<sub>2</sub>,  $G_z$  is total gas mass flux,  $A$  is the tube cross-sectional area, and  $x_{H_2}$  is the mass fraction of H<sub>2</sub> in the outlet gas.

## 7.3 Results and discussion

### 7.3.1 Confirming absence of mass transfer limitations

Mass transfer limitations were assessed using a set of experiments at the highest experimental temperature (650°C), where mass transfer was most likely to be limiting. The results of the experiments are shown on **Figure 7.3**.



**Figure 7.3 – Experimental results used for calculation of mass transfer limitations (650°C, with S/C = 3, y<sub>N2</sub> = 0.6)**

The curve was fit to a second order polynomial, with R<sup>2</sup> = 0.9191:

$$X_{AcOH} = -0.0012(W/F)^2 + 0.0428(W/F) + 0.7082 \quad \text{Eq. 7.19}$$

The polynomial was differentiated to give an equation for rate of reaction:

$$\frac{dX_{AcOH}}{dW/F} = -r_{AcOH} = -0.0024(W/F) + 0.0428 \quad \text{Eq. 7.20}$$

The estimated rate of reaction was used to find the Mears criterion, Weisz-Prater criterion and effectiveness factor. Results are summarised in **Table 7.8**, showing that neither external or internal mass transfer were limiting at the conditions used in this study.

**Table 7.8 – Determination of internal and external mass transfer limitations**

Parameter		Value
	Measured rate of reaction (mol kg <sub>cat</sub> <sup>-1</sup> h <sup>-1</sup> )	31.24
	Particle radius (µm)	100
	Catalyst bulk density (kg m <sup>-3</sup> ) [172]	1200
	$C_{bio,g}$ (mol m <sup>-3</sup> )	0.768
	Diffusion volume $v_{bio}$ [276]	51.88
	$D_{bio,N_2}$ in cm <sup>2</sup> s <sup>-1</sup>	0.878
External mass transfer	Reynolds number (-)	0.465
	Schmidt number (-)	1.28
	Sherwood number (-)	2.44
	Mass transfer coefficient $k_c$ (m s <sup>-1</sup> )	1.07
	Reaction order, assumed	1
	<b>Mears criterion (-)</b>	<b>1.26 x 10<sup>-3</sup></b>
Internal mass transfer	Constriction factor $\sigma_c$ [172]	0.8
	Tortuosity $\tau$ [172]	3.54
	Particle porosity [172]	0.59
	Effective diffusivity $D_e$ (cm <sup>2</sup> s <sup>-1</sup> )	0.117
	Weisz-Prater criterion (-)	1.16 x 10 <sup>-2</sup>
	<b>Effectiveness factor (-)</b>	<b>0.999</b>

### 7.3.2 Experimental measurements of reactant conversion

The following figures summarise the experimental data that was collected, showing how conversions varied as temperature and S/C ratio were changed. The data follows the expected trends, with conversion increasing with pseudo-contact time. Other observed trends are an increase of conversion with temperature (**Figure 7.4**), and increase of conversion as the partial of pressure of AcOH increases (**Figure 7.5**).

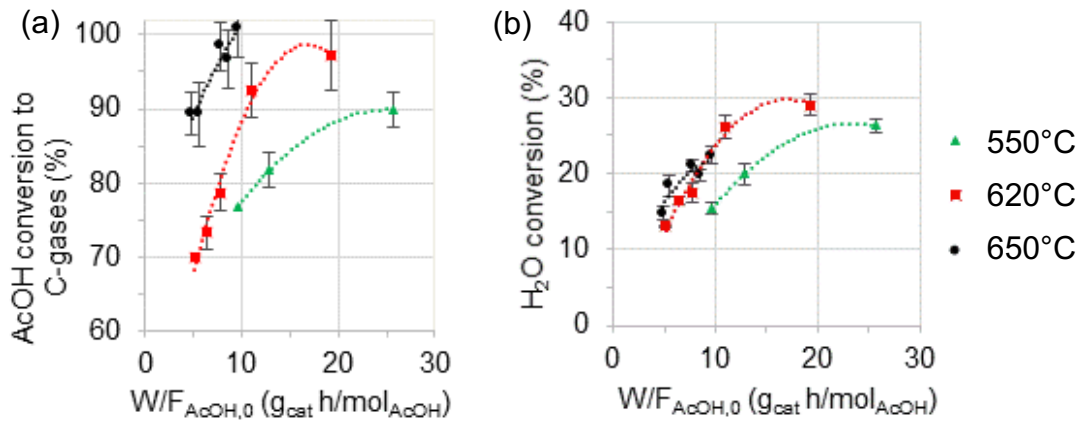


Figure 7.4 – Conversion vs pseudo contact time for different temperatures at  $S/C = 3$ ,  $p_{AcOH} = 5.89$ ,  $p_{H_2O,0} = 34.64$  kPa. (a) AcOH and (b)  $H_2O$

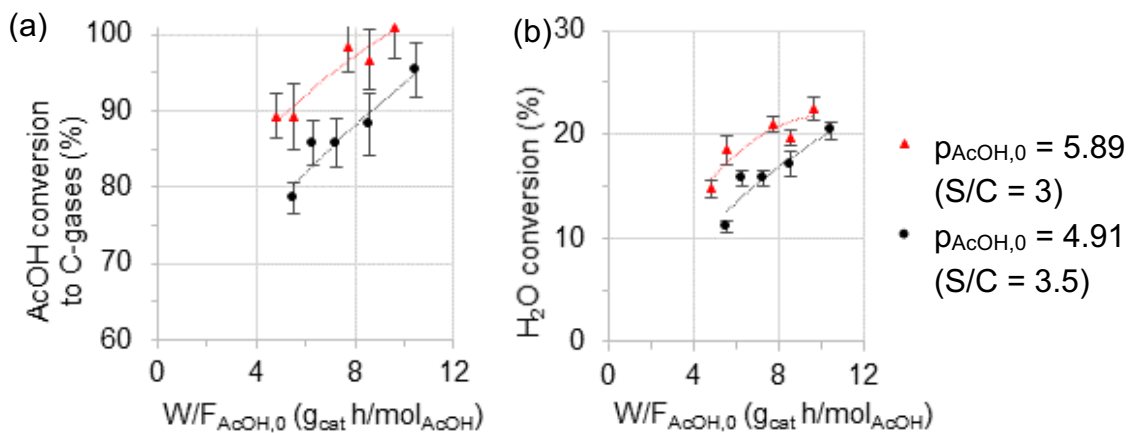


Figure 7.5 – Conversion vs pseudo contact time for different partial pressures of AcOH at  $650^\circ C$ ,  $p_{H_2O,0} = 34.64$  kPa. (a) AcOH and (b)  $H_2O$

Figure 7.6 shows a decrease in AcOH conversion as  $S/C$  ratio increased. As steam was in excess ( $S/C \gg 1$ ), increasing the  $S/C$  ratio did not improve AcOH conversion. Instead, the trend may be explained by the change in flow rates. Increasing  $S/C$  ratio decreases the pseudo-contact time for water ( $W/F_{H_2O,0}$ ) and thus reduces its opportunity to react with AcOH.

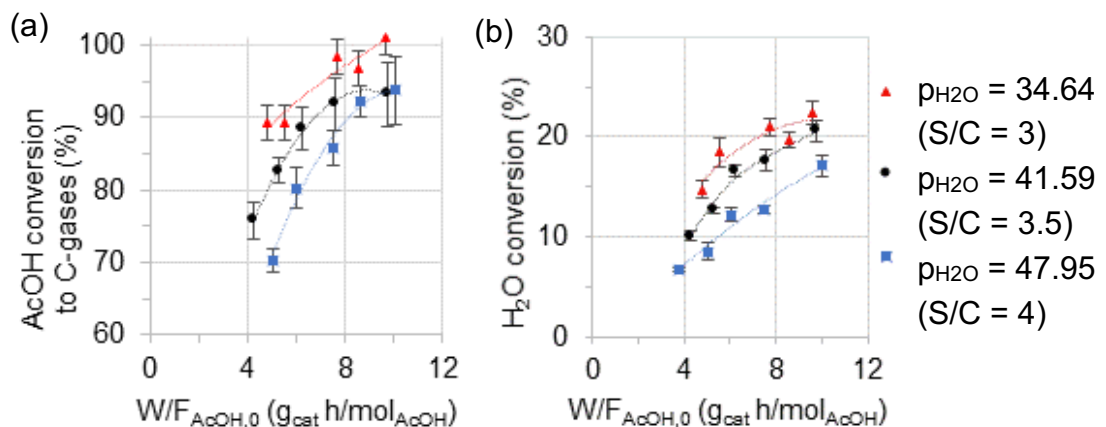
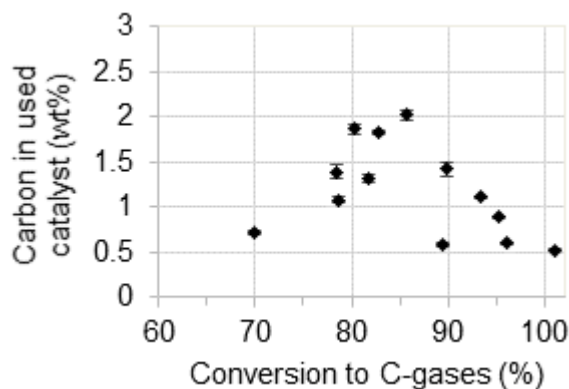


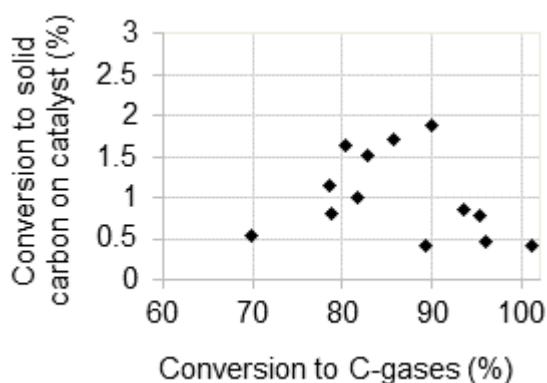
Figure 7.6 – Conversion vs pseudo contact time ( $W/F_{AcOH,0}$ ) for different partial pressures of  $H_2O$  at  $650^\circ C$ ,  $p_{AcOH,0} = 5.89$  kPa. (a) AcOH and (b)  $H_2O$

### 7.3.3 Carbon deposition

Samples of used catalyst were subjected to CHNS analysis, to examine the extent of carbon deposition. **Figure 7.7** shows how the carbon content varied with the conversion to carbon gases. The carbon contents were used to estimate the conversion to solid carbon, shown in **Figure 7.8**.



**Figure 7.7 – Carbon content in used catalyst vs conversion to C-gases. Error bars show standard deviations of duplicate samples.**



**Figure 7.8 – Conversion to solid carbon vs conversion to C-gases**

The results confirm that the level of carbon deposition was low, due to operation at high temperature with an excess of steam. In addition, each experiment was run for only a short time (around 10 – 20 mins), so there was limited time for deactivation to occur. For this study it was assumed that carbon deposition had a minimal impact on catalyst activity. Future work might also consider the rate of catalyst deactivation in its experimental design. For example, the kinetic studies on bio-oil by Arregi et al., Barbarias

et al. and Gayubo et al. [266,268,384] included a term for catalyst activity in each rate equation:

$$r_i = r_j a \quad \text{Eq. 7.21}$$

where  $r_i$  is the rate of reaction including catalyst deactivation, and  $r_j$  is the rate of reaction before deactivation. The term  $a$  signifies the catalyst activity.

By running the experiments for long durations (> 100 minutes), the authors of these studies were able to derive the rate of catalyst deactivation, i.e. the rate of change of  $a$ . A similar method could be applied in a future work in order to improve the model. However, in the SE-CLSR process this should be linked to a corresponding model for catalyst re-activation during the other stages, as a crucial advantage of SE-CLSR is that carbon deposits can be removed by gasification and oxidation [271].

### 7.3.4 Parameter fitting

On the basis of the literature review, two simplified reaction schemes were evaluated. These considered only the major reactions, in order to minimise the number of parameters to be fitted. Model 1 contained three reactions: steam reforming, decomposition to syngas, and WGS. Model 1 did not include reactions relating to methane, as experiments yielded very low CH<sub>4</sub> contents (<1 vol%).

Model 2 also included decomposition to methane, and SMR, in order to examine whether a more detailed mechanism could improve accuracy. The reaction steps in the proposed kinetic models are shown in **Table 7.9**.

**Table 7.9 – Reaction schemes in proposed kinetic models**

	Reaction	Stoichiometry	Model	
			1	2
1	Steam reforming acetic acid	$CH_3COOH + 2H_2O \rightarrow 2CO_2 + 4H_2$	✓	✓
2	Decomposition 1	$CH_3COOH \rightarrow 2CO + 2H_2$	✓	✓
3	Decomposition 2	$CH_3COOH \rightarrow CH_4 + CO_2$		✓
4	SMR	$CH_4 + H_2O \leftrightarrow CO + 3H_2$		✓
5	Water gas shift	$CO + H_2O \leftrightarrow H_2 + CO_2$	✓	✓

**Table 7.10** and **Table 7.11** summarise the reaction schemes used in each of the proposed models. Primary reactions involving acetic acid were modelled via simple power law rate equations. The concentration of water was not

included in the power law rate equations, as water was in large excess ( $S/C \gg 1$ ). SMR and WGS reactions were described using equilibrium rate equations reactions from literature [266,268].

Two different versions of the WGS rate equation were used. Version A, used in Models 1A and 2A, was a more complex form, taken from Xu and Froment [385]. However, initial testing found that Model 2A was not able to converge with this form of the equation. Thus a simplified version of the WGS rate equation was also trialled, based on previous bio-oil kinetic studies [266,384]. The simplified WGS rate equation was used in Models 1B and 2B.

**Table 7.10 – Rate equations for Models 1A and 1B**

Reaction	Rate equation
Steam reforming acetic acid $CH_3COOH + 2H_2O \rightarrow 2CO_2 + 4H_2$	$R_1 = k_1 p_{AcOH}^{\alpha_1}$
Decomposition 1 $CH_3COOH \rightarrow 2CO + 2H_2$	$R_2 = k_2 p_{AcOH}^{\alpha_2}$
Water gas shift $CO + H_2O \leftrightarrow CO_2 + H_2$	<p>Model 1A:</p> $R_{5a} = \frac{k_{5a}}{p_{H_2}} \left( p_{CO} p_{H_2O} - \frac{p_{H_2} p_{CO_2}}{K_{WGS}} \right) \left( \frac{1}{\Omega^2} \right)$ $\Omega = 1 + K_{CO} p_{CO} + K_{H_2} p_{H_2} + K_{CH_4} p_{CH_4} + K_{H_2O} \frac{p_{H_2O}}{p_{H_2}}$ $K_{WGS} = \exp \left( \frac{4400}{T} - 4.036 \right)$ <p>Model 1B:</p> $R_{5b} = k_{5b} \left( p_{CO} p_{H_2O} - \frac{p_{H_2} p_{CO_2}}{K_{WGS}} \right)$ $K_{WGS} = \exp \left( a + \frac{b}{T} + c \log(T) + dT + eT^2 + \frac{f}{T^2} \right)$ $a = -18, b = 5.8 \times 10^3, c = 1.8,$ $d = -2.7 \times 10^{-4}, e = 0, f = -5.8 \times 10^4$

**Table 7.11 – Rate equations for Models 2A and 2B**

Reaction	Rate equation
Steam reforming acetic acid $CH_3COOH + 2H_2O \rightarrow 2CO_2 + 4H_2$	$R_1 = k_1 p_{AcOH}^{\alpha_1}$
Decomposition 1 $CH_3COOH \rightarrow 2CO + 2H_2$	$R_2 = k_2 p_{AcOH}^{\alpha_2}$
Decomposition 2 $CH_3COOH \rightarrow CH_4 + CO_2$	$R_3 = k_3 p_{AcOH}^{\alpha_3}$
SMR $CH_4 + H_2O \rightarrow CO + 3H_2$	$R_4 = k_4 \left( p_{CH_4} p_{H_2O} - \frac{p_{H_2}^3 p_{CO}}{K_{SMR}} \right)$ $K_{SMR} = \exp \left( a + \frac{b}{T} + c \log(T) + dT + eT^2 + \frac{f}{T^2} \right)$ $a = -24.9, b = -2.278 \times 10^4, c = 7.951,$ $d = -4.354 \times 10^{-3}, e = 3.607 \times 10^{-7}, f = 4850$
Water gas shift $CO + H_2O \rightarrow CO_2 + H_2$	<p>Model 2A:</p> $R_{5a} = \frac{k_{5a}}{p_{H_2}} \left( p_{CO} p_{H_2O} - \frac{p_{H_2} p_{CO_2}}{K_{WGS}} \right) \left( \frac{1}{\Omega^2} \right)$ $\Omega = 1 + K_{CO} p_{CO} + K_{H_2} p_{H_2} + K_{CH_4} p_{CH_4} + K_{H_2O} \frac{p_{H_2O}}{p_{H_2}}$ $K_{WGS} = \exp \left( \frac{4400}{T} - 4.036 \right)$ <p>Model 2B:</p> $R_{5b} = k_{5b} \left( p_{CO} p_{H_2O} - \frac{p_{H_2} p_{CO_2}}{K_{WGS}} \right)$ $K_{WGS} = \exp \left( a + \frac{b}{T} + c \log(T) + dT + eT^2 + \frac{f}{T^2} \right)$ $a = -18, b = 5.8 \times 10^3, c = 1.8,$ $d = -2.7 \times 10^{-4}, e = 0, f = -5.8 \times 10^4$

These rate equations were entered into the gPROMs model, and the measured experimental data was used to perform parameter fitting. The results of the parameter fitting are given in **Table 7.12**. No values are given

for Model 2A, as the parameter fitting was unable to converge due to the more complex WGS reaction.

**Table 7.12 – Kinetic parameters estimated by gPROMS parameter fitting**

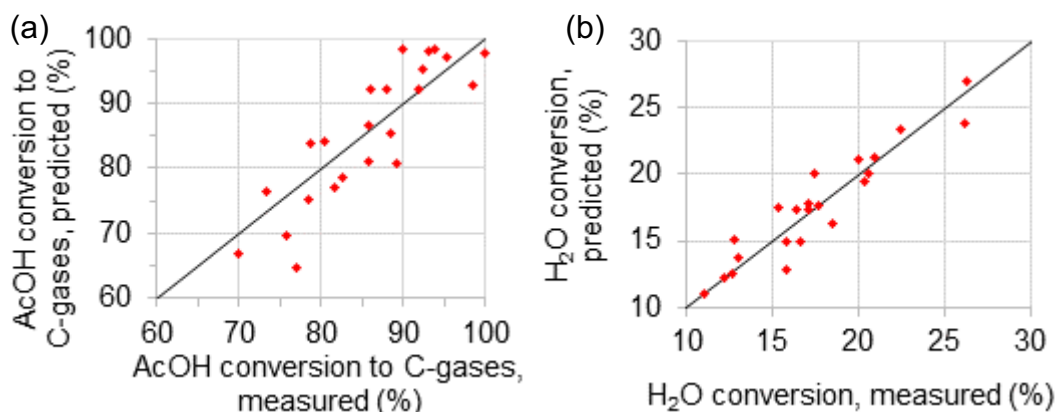
Reaction parameters		Model			Literature
		1A	1B	2B	
$k_{o1}$	$(mol\ kg_{cat}^{-1}\ bar^{-\alpha_1}\ s^{-1})$	0.778	0.867	0.0765	-
$E_{A1}$	$(kJ\ mol^{-1})$	60.85	60.40	122.73	-
$\alpha_1$	(-)	0.958	0.953	1.20	-
$k_{o2}$	$(mol\ kg_{cat}^{-1}\ bar^{-\alpha_2}\ s^{-1})$	0.955	0.648	0.0662	-
$E_{A2}$	$(kJ\ mol^{-1})$	61.25	51.70	40.70	-
$\alpha_2$	(-)	0.636	0.823	0.578	-
$k_{o3}$	$(mol\ kg_{cat}^{-1}\ bar^{-\alpha_3}\ s^{-1})$	-	-	7.994	-
$E_{A3}$	$(kJ\ mol^{-1})$	-	-	83.01	-
$\alpha_3$	(-)	-	-	1.123	-
$k_{o4}$	$(mol\ kg_{cat}^{-1}\ bar^{-2}\ s^{-1})$	-	-	$8.6 \times 10^3$	0.542 [268]
$E_{A4}$	$(kJ\ mol^{-1})$	-	-	194.82	357.50 [268]
$k_{o5,a}$	$(mol\ kg_{cat}^{-1}\ bar^{-1}\ s^{-1})$	4299	-	-	$5.43 \times 10^5$ to $9.9 \times 10^6$ [254,385]
$k_{o5,b}$	$(mol\ kg_{cat}^{-1}\ bar^{-2}\ s^{-1})$	-	607	68.54	5.0 to 360 [266,268,384]
$E_{A5}$	$(kJ\ mol^{-1})$	94.65	86.71	67.13 <sup>a</sup>	30.00 to 89.23 [254,266,268,384,385]
AAD	$X_{AcOH}$ (%)	5.37	4.43	6.01	
	$X_{H_2O}$ (%)	6.36	10.46	8.94	
	$y_{CH_4,dry}$ (%)	-	-	27.5	
R <sup>2</sup>		98.8	99.0	99.3	
<sup>a</sup> Activation energy fixed at the value from Xu and Froment [385], to enable convergence. Further information in text.					

Model 2B was initially unable to converge, due to the large number of unknown parameters. To enable convergence, the activation energy of the WGS reaction ( $E_{A5}$ ) was fixed, using a value from literature. A value of  $67130\ J\ mol^{-1}$  was taken from Xu and Froment [385]. A sensitivity analysis



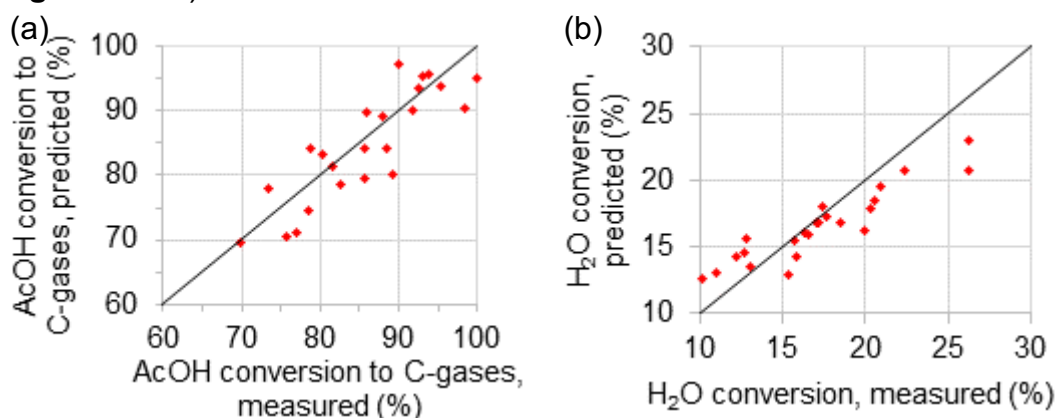
showed that changing this value of  $E_{A5}$  by  $\pm 50\%$  had a minimal impact on overall accuracy (AAD + 2%). Future studies on this catalyst may focus exclusively on the WGS reaction, in order to confirm the most accurate value to use. However, for the purposes of this study, the value from Xu and Froment [385] was deemed suitable.

The goodness of fit for each of the models is shown on the parity plots below. In **Figure 7.9**, Model 1A appears to give a good fit for conversion of both reactants, with results close to the parity line and without any skew.



**Figure 7.9 – Parity plots for Model 1A (a) AcOH conversion, (b) H<sub>2</sub>O conversion**

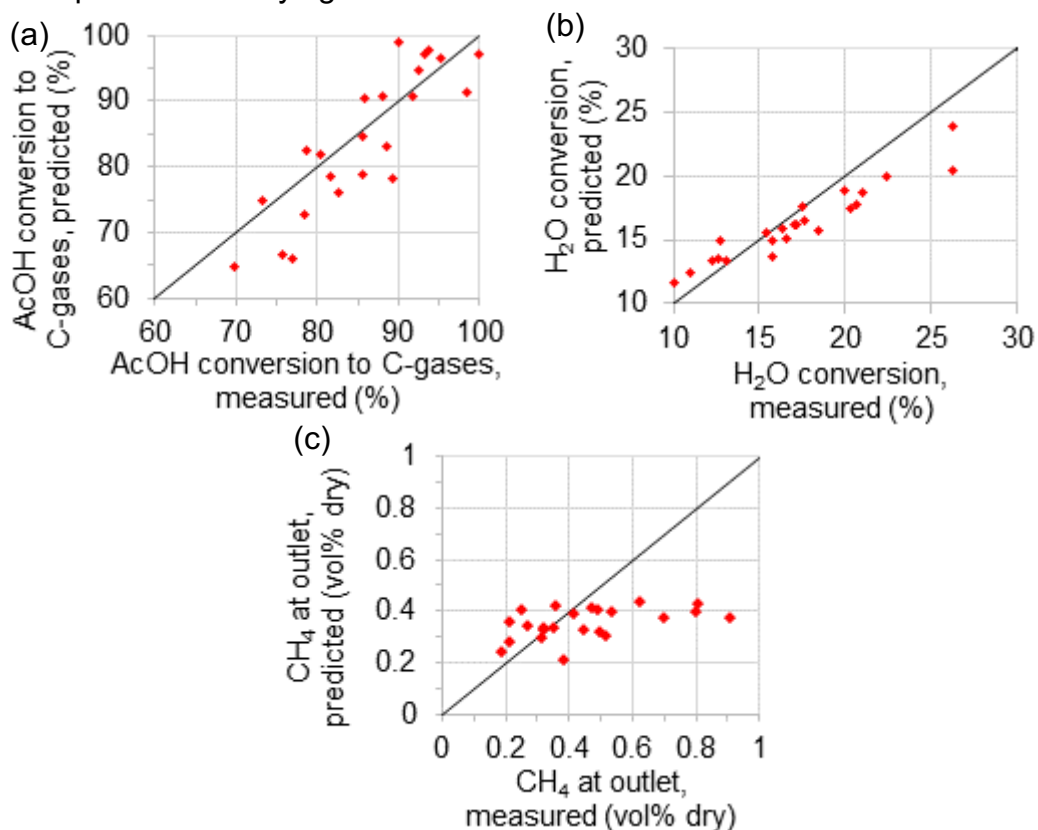
**Figure 7.10a** shows that Model 1B gives a good fit for AcOH conversion, but there is a skew on the H<sub>2</sub>O conversion results in **Figure 7.10b**. This may be associated with the less detailed form of the WGS equation. Model 2B, which used the same form of the WGS equations, had a similar skew (**Figure 7.11b**).



**Figure 7.10 – Parity plots for Model 1B (a) AcOH conversion, (b) H<sub>2</sub>O conversion**

Model 2B appears to give a reasonably good fit for AcOH conversion (**Figure 7.11a**), and some skew for H<sub>2</sub>O conversion (**Figure 7.11b**), similar to Model 1B. However, the poor fit for CH<sub>4</sub> in **Figure 7.11c** suggests that

the model is not providing an accurate description of the underlying mechanisms involving methane. Thus the extra complexity of Model 2B is not justified, either by improved accuracy, or by providing a reliable description of underlying mechanism.



**Figure 7.11 – Parity plots for Model 2B (a) AcOH conversion, (b) H<sub>2</sub>O conversion and (c) CH<sub>4</sub> in outlet gas**

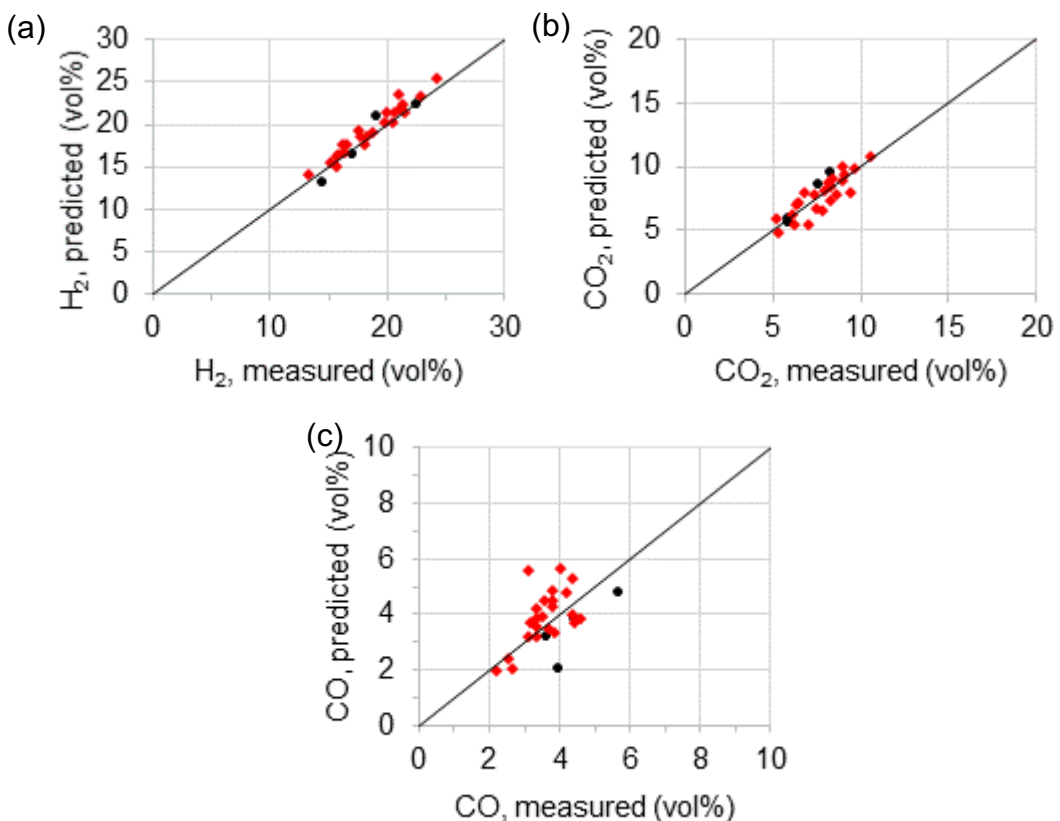
**Table 7.12** gives a quantitative basis for comparison. Model 1A provides the best fit for H<sub>2</sub>O conversion (AAD 5.37%). Model 1B gives a slightly better accuracy for AcOH conversion (AAD 4.43%), but the accuracy of H<sub>2</sub>O conversion is reduced considerably, to give an AAD over 10%. Thus Model 1A gives the best fit when both reactants are considered together. On the basis of these results, Model 1A was judged to give the best fit and was carried forward for further study in the following sections.

### 7.3.5 Kinetic model validation

After Model 1A provided a satisfactory fit for reactant conversions, the model was further tested by comparing predicted outlet compositions to experimental and equilibrium results.

### 7.3.5.1 Model testing away from equilibrium

To test the model at conditions away from equilibrium, the outlet compositions predicted by the reactor model were compared to those measured during experiments. To provide extra validation, four extra experiments were included that were not within the original parameter fitting. The parity plots for outlet composition are given below. **Figure 7.12a** and **Figure 7.12b** demonstrate a good fit for H<sub>2</sub> and CO<sub>2</sub> content, even for those experiments that were not included in the parameter fitting (signified as black dots). **Figure 7.12a** shows there was a tendency towards a small over-prediction of H<sub>2</sub> content. This can be explained by the exclusion of CH<sub>4</sub> from the model, as each molecule of CH<sub>4</sub> contains 2 molecules of H<sub>2</sub>. However, as the measured CH<sub>4</sub> contents were low (<1 vol%), the effect is small. **Figure 7.12c** shows the fitting for CO is also reasonably good, although not as accurate as the other components.



**Figure 7.12 – Parity plots for outlet compositions from Model 1A (a) H<sub>2</sub> vol%, (b) CO<sub>2</sub> vol% and (c) CO vol%.**

**Red dots signify experiments used in parameter fitting, black dots signify experiments not used in the original parameter fitting.**

**Table 7.13** shows the accuracy of predicted outlet concentrations. The model shows good accuracy for H<sub>2</sub> concentration, with AAD around 4%. There is greater error for the compounds that contain carbon, particularly CO. This suggests that there is opportunity to improve the model by refining

reactions involving CO, such as decomposition and WGS. Nonetheless, the average component error is less than 11% AAD, suggesting the model is suitable for preliminary estimates relating to reactor size and H<sub>2</sub> yield.

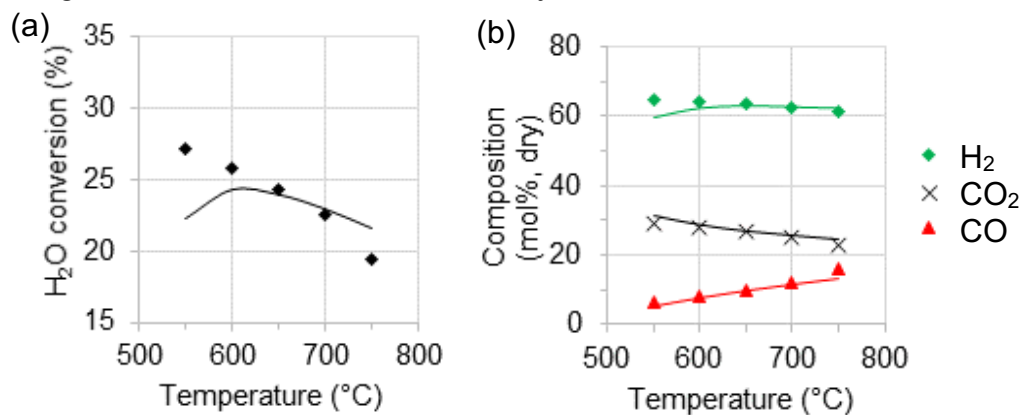
**Table 7.13 – Accuracy of predicted vs measured outlet concentrations**

Component	AAD (%)
$y_{H_2,dry}$	4.34
$y_{CO,dry}$	18.46
$y_{CO_2,dry}$	9.12
Average	10.64

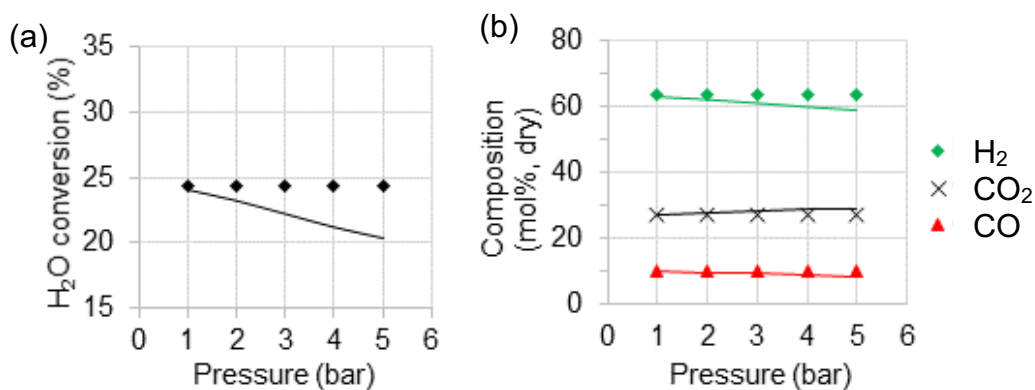
### 7.3.5.2 Model testing at equilibrium

To further test the model, gPROMS model outputs at equilibrium were compared against those from an Aspen Plus equilibrium reactor at the same conditions. The effects of temperature, S/C ratio and pressure were examined. **Figure 7.13** shows that the kinetic model provides a good estimation in the temperature region 600 to 700°C, but outside of this region the model results diverge from equilibrium results. **Figure 7.14** shows that the model is not readily extrapolated to pressures outside the experimental range, as it relies on an empirical power law equation.

For both temperature and pressure, the area of highest accuracy is the region where there is little methane formation, i.e. at high temperature and/or low pressure. This is to be expected, as the simplified kinetic model does not consider methane formation. It highlights that caution is to be advised when extrapolating this kinetic model to low temperature and/or high pressure regions where CH<sub>4</sub> formation is likely.



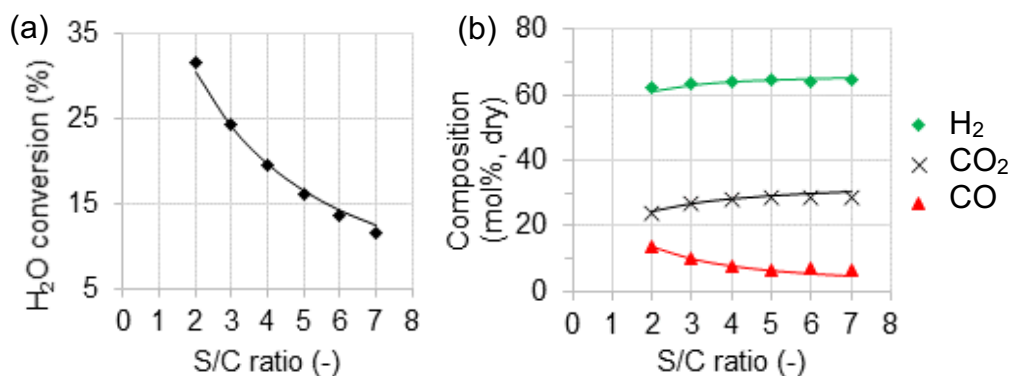
**Figure 7.13 – Effect of temperature on (a) H<sub>2</sub>O conversion, (b) H<sub>2</sub>,CO and CO<sub>2</sub> content at equilibrium. Inlet conditions are 1 bar, S/C = 3. Points represent kinetic model results, while solid lines represent Aspen Plus equilibrium results.**



**Figure 7.14 – Effect of pressure on (a) H<sub>2</sub>O conversion, (b) H<sub>2</sub>, CO and CO<sub>2</sub> content at equilibrium.**

**Inlet conditions S/C = 3, 650°C. Points represent kinetic model results, while solid lines represent Aspen Plus equilibrium results.**

**Figure 7.15** shows the kinetic model provides a good match to equilibrium results at a range of S/C ratios. As the experiments used an excess of steam, the model remains valid when this excess is increased further.



**Figure 7.15 – Effect of S/C ratio on (a) H<sub>2</sub>O conversion, (b) H<sub>2</sub>, CO and CO<sub>2</sub> content at equilibrium.**

**Inlet conditions are 1 bar, 650°C. Points represent kinetic model results, while solid lines represent Aspen Plus equilibrium results.**

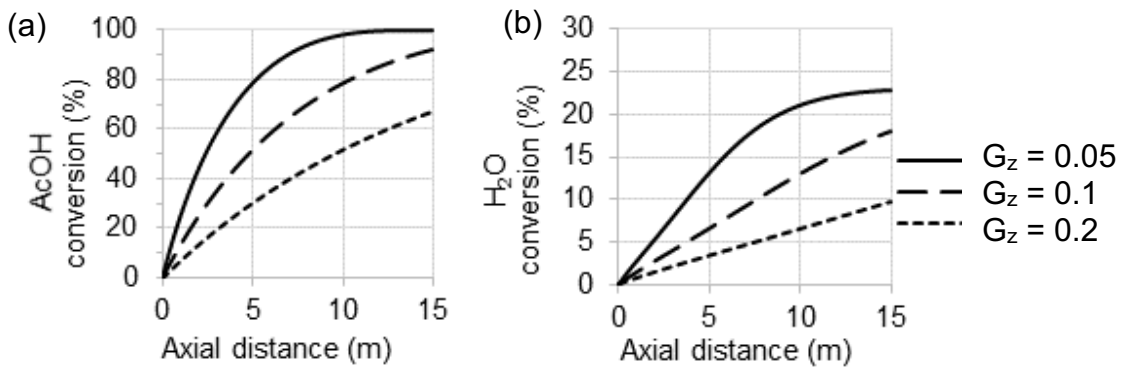
### 7.3.6 Reactor modelling

Having derived a kinetic model that provides reasonable accuracy, it is possible to create a dynamic packed bed reactor model. Steam reforming of acetic acid was modelled in an industrial scale reactor tube, and subjected to a series of sensitivity studies.

The previous section highlighted that the kinetic model is not suitable for extrapolation to higher pressure, so the reactor was modelled at low pressure. In addition, the kinetics are only for a single model compound rather than a whole bio-oil. Thus the model is not intended to represent a realistic example of a high-pressure industrial reactor. Instead, the model is

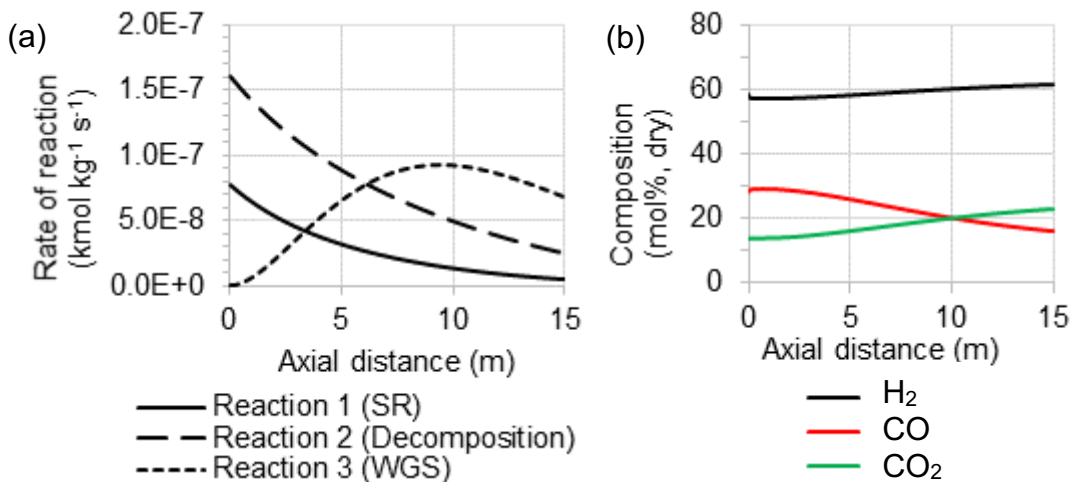
used to demonstrate how kinetics influence reactor design, and thus to link the kinetic study to the wider context.

**Figure 7.16** shows the impact of gas flux on reactor conversion and product composition. At low flux ( $0.05 \text{ kg m}^{-2} \text{ s}^{-1}$ ), 100% conversion is achieved around 10m into the tube. However, increasing the flux causes the conversion to drop. Due to slow reaction rates, a long residence time is required to reach high conversion. This would have to be achieved through a large reactor, including long tubes and low mass fluxes.



**Figure 7.16 – Reactant conversion vs axial distance for different values of mass flux in acetic acid steam reforming at 1.2 bar, 700°C with S/C = 3, effectiveness factor 0.3 (a) AcOH conversion (b) H<sub>2</sub>O conversion**

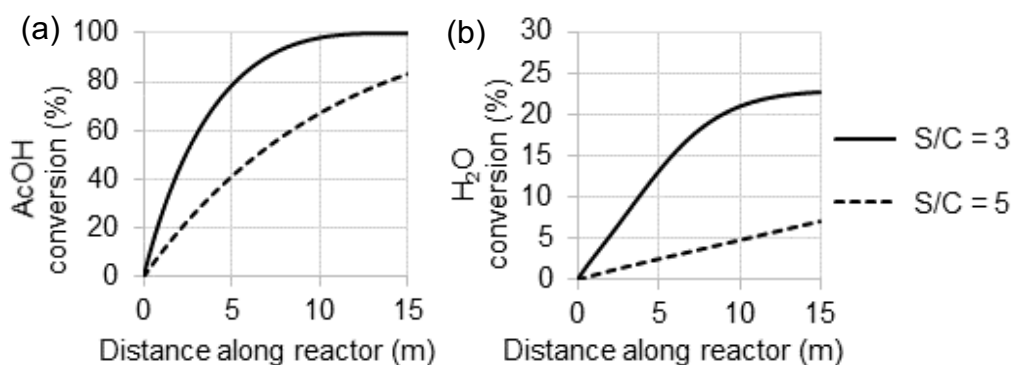
**Figure 7.17a** shows how the rates of reaction change throughout the length of the tube. Initially, the decomposition of AcOH (reaction 2) dominates, leading to large quantities of CO near the entrance to the tube (**Figure 7.17b**). This CO is gradually converted to CO<sub>2</sub> via the WGS reaction. Around 6 m into the tube, 60% of the AcOH is converted and WGS becomes the dominant reaction.



**Figure 7.17 – Model results from steam reforming of acetic acid at 1.2 bar, 700°C with S/C = 3,  $G_z = 0.1 \text{ kg m}^{-2} \text{ s}^{-1}$  (a) rates of reaction, (b) gas composition**

The techno-economic study in **Chapter 5** discussed the use of high S/C ratios to reduce carbon deposition, and the resulting effect on process economics. To better understand the effect of S/C ratio, a sensitivity was carried out in the dynamic reactor model. **Figure 7.18** shows the effect of increasing the S/C ratio from 3 to 5. When S/C ratio is increased, the conversion of AcOH is decreased. This may be partly explained by the reaction kinetics: according to the power law equation, as the partial pressure of AcOH is reduced by steam dilution, acetic acid SR (reaction 1) occurs more slowly. It is also explained by the increased mass flow through the reactor, or the reduced residence time, that results from increasing the amount of steam flow.

This highlights an additional effect of S/C ratio that was not previously discussed in the techno-economic study. Changing the S/C ratio would affect reaction kinetics and residence time and thus increase the quantity of catalyst required. However, as the literature review highlighted, existing reformer designs are often determined by heat transfer and mechanical constraints rather than catalyst activity [73]. Further work would be required to understand the impacts of S/C ratio on reformer design, taking into account a range of design considerations.

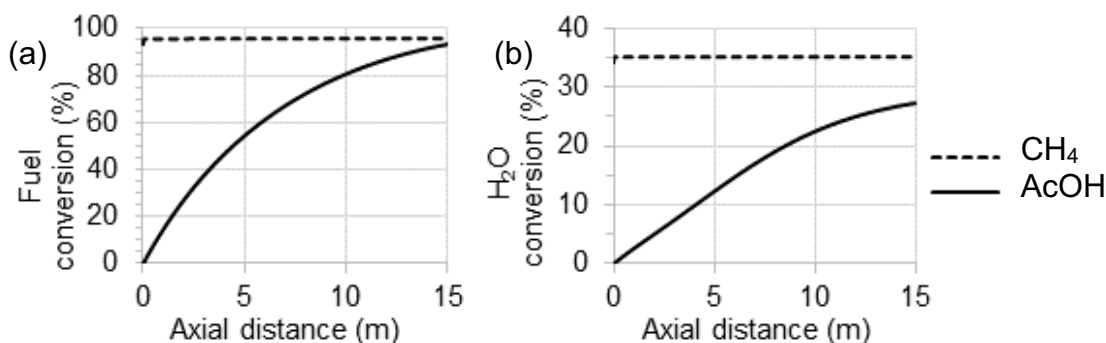


**Figure 7.18 – Reactant conversion profiles for different S/C ratios in AcOH steam reforming at 1.2 bar, 700°C. (a) AcOH conversion (b) H<sub>2</sub>O conversion**  
 $G_z$  of AcOH =  $0.0356 \text{ kg m}^{-2} \text{ s}^{-1}$  (total  $G_z$  is 0.1 for S/C = 3, 0.143 for S/C = 5).

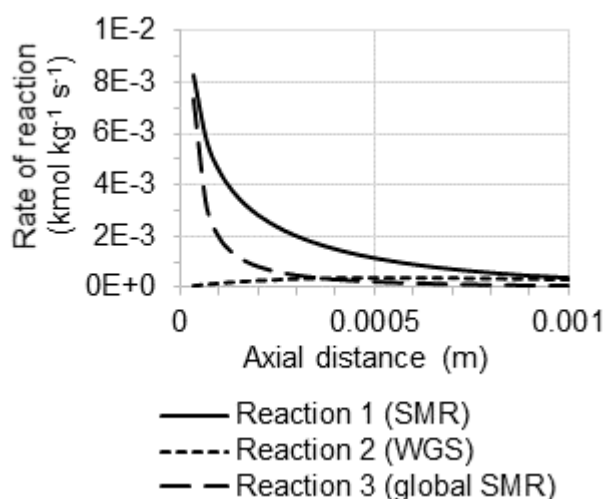
To better understand how a novel feedstock might affect reactor design, the acetic acid model was compared to an equivalent reactor tube for methane. To ensure an equivalent comparison, the S/C ratio was determined on the basis of stoichiometry, using the S/C ratio required for full steam reforming, plus a 100% excess. Thus the S/C ratio for AcOH was 2, while the S/C ratio for CH<sub>4</sub> was 4.

**Figure 7.19** compares reactant conversion for the two different feedstocks. In the case of methane, the reactor reaches equilibrium very close to the

inlet. This is because the reaction rate of methane at low pressure is extremely fast (**Figure 7.20**). In contrast, the rate of acetic acid SR is much slower (**Figure 7.17**), and so the conversion gradually increases along the length of the reactor. This suggests the slow reaction kinetics of bio-oil could be an important constraint in reactor design.



**Figure 7.19 – Reactant conversion vs axial distance for SR of methane and acetic acid at 1.2 bar, 700°C, mass flux 0.09 kg m<sup>-2</sup> s<sup>-1</sup>. 100% excess of H<sub>2</sub>O (S/C = 2 for AcOH, S/C = 4 for CH<sub>4</sub>). (a) fuel conversion, (b) H<sub>2</sub>O conversion.**



**Figure 7.20 – Reaction rates at entrance to reactor tube for SR of methane at 1.2 bar, 700°C, mass flux 0.09 kg m<sup>-2</sup> s<sup>-1</sup>, S/C = 4.**

To quantify the change in catalyst requirement, the model was used to estimate the number of tubes required to produce a given quantity of hydrogen. **Table 7.14** shows the comparison of acetic acid and methane. With a flux of 0.09 kg m<sup>-2</sup> s<sup>-1</sup>, both feedstocks achieve around 95% conversion in a 15 m tube. However, acetic acid produces a gas with lower H<sub>2</sub> purity, due to its high carbon content. As a consequence, a larger number of tubes would be required to achieve the same H<sub>2</sub> production capacity. A further consideration is the tube length. As seen in **Figure 7.19**, a large tube length of 15m is required to achieve high AcOH conversion, whereas CH<sub>4</sub> reacts rapidly at low pressure, so that the same tube length is not required.



**Table 7.14 – Comparison of reactor size for steam reforming of acetic acid and methane at 95% conversion**

	CH <sub>4</sub>	AcOH
Temperature (°C)	700	
Inlet pressure (bar)	1.2	
Gas mass flux (kg m <sup>-2</sup> s <sup>-1</sup> )	0.09	
Tube length (m)	15	
Tube diameter (mm)	125	
S/C ratio (100% excess)	4	2
Conversion of fuel (%)	95.5	93.5
Composition		
H <sub>2</sub> (mol%, wet)	48	38
CO (mol%, wet)	7	10
CO <sub>2</sub> (mol%, wet)	7	14
H <sub>2</sub> O (mol%, wet)	38	37
Capacity		
H <sub>2</sub> production per tube (kg h <sup>-1</sup> )	0.30	0.18
Tubes required for 100 kg h <sup>-1</sup> H <sub>2</sub>	334	561

This is a low pressure example, and therefore not directly transferable to an industrial process. Nonetheless, it demonstrates that slow bio-oil reaction kinetics may influence reactor design, and emphasises the importance of developing kinetic models for realistic operating conditions. This will be an important stage in process development, as it will allow researchers to assess catalytic requirements for bio-oil steam reforming, and ultimately process cost and feasibility. However, as discussed above, kinetic considerations are only aspect of design, and should be considered alongside mechanical and heat transfer constraints.

## 7.4 Conclusion

A kinetic study has been conducted for acetic acid steam reforming on an industrial nickel-based catalyst. After confirming the absence of mass transfer limitations, experimental data were used for parameter fitting in gPROMS. Four kinetic models were proposed, which described simplified reaction schemes. Power law rate equations were used for the primary reactions of acetic acid. Secondary reactions SMR and WGS were described by mass action rate equations from literature.

Of the models tested, Model 1A was found to be the most accurate. This was the simpler reaction scheme, which consisted of just acetic acid steam reforming, decomposition to CO, and WGS, and does not include reactions for the formation or consumption of methane. Model 1A gives around 6% error for the conversion of AcOH and H<sub>2</sub>O. Individual component compositions gave an absolute average deviation (AAD) of 11%. The mol% of H<sub>2</sub> was the most accurate, having only 4% AAD.

Testing against equilibrium results showed that Model 1A provided a good fit for low pressure conditions in the temperature region 600 - 700°C, with S/C ratios ranging from 3 to 8. However, extrapolation outside this region is not advisable, due to the empirical nature of the model, and the simplified reaction scheme that does not include methane formation.

A more complex kinetic model, including methane formation and reforming, could improve the prediction of acetic acid steam reforming, particularly in regions of low conversion where CH<sub>4</sub> is likely to form. However, a more detailed model (Model 2B), which included additional reactions for decomposition to CH<sub>4</sub> and steam methane reforming, did not provide suitably accurate fit on this occasion. To improve the accuracy of Model 2B, further work could be carried out on specific parts of the reaction scheme, for example by determining kinetics of SMR and WGS on this catalyst.

The results of the kinetic study were used in a full-scale reactor model, in order to evaluate the effect of reaction kinetics on reformer design. Modelling was carried out at low pressure, due to the limitations of the kinetic model. Nonetheless the results highlighted the importance of considering reaction kinetics in relation to process design and feasibility. The kinetics of acetic acid reforming are considerably slower than those of methane, suggesting that high conversion is achieved only through a long residence time. Future work should aim to achieve bio-oil kinetics that are valid at industrial conditions, and to use these to evaluate reactor design, cost and, ultimately, technical and economic feasibility.

## Chapter 8 – Conclusions and future work

### 8.1 Introduction

This work has provided a first assessment of the technical and economic feasibility of bio-oil reforming with carbon capture, as an alternative route to hydrogen production with negative emissions. In particular, it focused on an advanced reforming technique, sorption-enhanced chemical looping steam reforming (SE-CLSR), as a means to achieve this.

A thermodynamic assessment of different bio-oil reforming routes compared conventional steam reforming (C-SR) to advanced methods, sorption enhancement and chemical looping. This analysis highlighted several potential benefits of sorption-enhanced chemical looping steam reforming (SE-CLSR), including autothermal operation, reduced risk of carbon formation, and enhanced purity and yield of the hydrogen product at the reformer stage.

Having confirmed the thermodynamic feasibility of SE-CLSR, a techno-economic analysis was used to examine C-SR with CO<sub>2</sub> capture (C-SR-CCS) and SE-CLSR in more detail. The analysis identified that bio-oil C-SR-CCS or SE-CLSR may be feasible routes to hydrogen production, with potential to provide negative emissions.

High feed molar steam to carbon (S/C) ratios, used to reduce carbon deposition, could be economically feasible in C-SR only if excess heat can be used by neighbouring steam users. There could therefore be a useful parallel between bio-oil steam reforming and CO<sub>2</sub> capture, if high heat usage can be used to support heat integration with a CO<sub>2</sub> capture system.

SE-CLSR and C-SR-CCS have similar levelised cost of hydrogen, in the region of 3.8 to 4.6 \$ kg<sup>-1</sup>. However, SE-CLSR has a reduced level of fossil-based direct CO<sub>2</sub> emissions, because its autothermal nature eliminates the need for fuel gas. If a natural-gas based SMR process is used as the reference to calculate cost of carbon avoided (CCA), the cost of a carbon avoided is 90 to 160 \$ t<sub>CO2</sub><sup>-1</sup>, largely because methane is, at the time of this thesis publication, a considerably less expensive feedstock than bio-oil. However for larger-scale plants (100,000 Nm<sup>3</sup> h<sup>-1</sup>), the CCA of 95 to 105 \$ t<sub>CO2</sub><sup>-1</sup> is within the range of BECCS in other industries.

The techno-economic assessment in **Chapter 5** included a number of simplifying assumptions in order to obtain a heat and material balance for SE-CLSR. However, SE-CLSR in packed beds is a dynamic process, so it is

also important to consider dynamic aspects of each stage. This study made the first steps towards a dynamic model of the full bio-oil SE-CLSR process, by focussing on two key areas: carbon capture by simultaneous reduction-calcination, and the kinetics of steam reforming of bio-oil.

During the reduction-calcination stage in SE-CLSR, reduction of the nickel-based oxygen transfer material (OTM) occurs alongside CO<sub>2</sub> sorbent regeneration, bed cooling, and CO<sub>2</sub> capture. In **Chapter 6**, a rigorous packed bed model was validated and used to simulate the various complex and interacting phenomena in the reactor bed, to better understand the feasibility of this approach in Ni-based chemical looping systems.

The modelling confirmed that simultaneous reduction-calcination with the off-gas from pressure swing adsorption (PSA) is possible in a Ni-based chemical looping process, producing a stream of wet CO<sub>2</sub> with high purity. The evaluation showed that changing operating and design parameters, such as flux and feed gas composition, can help tune the bed and improve sequence timings. For example, by improving the synchronisation of the reduction and calcination fronts, it is possible to increase the proportion of time during which CO<sub>2</sub> product is on-specification, and therefore increase potential for CO<sub>2</sub> capture.

In **Chapter 7**, a simplified kinetic model was found for acetic acid (AcOH), which is commonly used as a model compound for bio-oil. Using parameter fitting in gPROMS, four kinetic models were tested. These featured simplified reaction schemes, in which power law rate equations were used for the primary reactions of acetic acid, and secondary reactions steam methane reforming (SMR) and water gas shift (WGS) were described by mass action rate equations from literature.

The simpler reaction scheme (Model 1A), consisting of acetic acid steam reforming, decomposition of CO, and WGS, was found to be the most accurate. This gave around 6% error for the conversion of AcOH and steam, and an absolute average deviation (AAD) of 10% for individual component compositions, including a 4% AAD for H<sub>2</sub>. When tested against equilibrium results, Model 1A provided a good fit for low pressure conditions in the temperature region 600 to 700°C, with S/C ratios ranging from 3 to 8. Extrapolation outside this region is not advisable, due to the empirical and simplified nature of the model, which does not include the formation or reactions of methane.

The kinetic model was used in a full-scale reactor model, in order to evaluate the effect of reaction kinetics on reactor design. The kinetics of acetic acid reforming are considerably slower than those of methane, suggesting that high conversion is achieved only through a long residence time. This highlights the importance of holistic analysis of bio-oil steam reforming, that considers how the kinetic nature of bio-oil reactions could influence process design, cost and, ultimately, its technical and economic feasibility.

## **8.2 Recommendations for future work**

This project has focussed on early-stage concept development and feasibility analysis for advanced reforming of bio-oils. As a result, it has identified a number of priority areas for future process development.

In the techno-economic analysis, SE-CLSR showed some promising characteristics, such as improving process thermal efficiency and reducing costs. However, at higher S/C ratios, these advantages are reduced, and heat integration of the autothermal process becomes more challenging. Thus it will be necessary to better understand the viability of operating at high temperatures ( $> 850^{\circ}\text{C}$ ) with a low S/C ratio, and whether the SE-CLSR cycle can sustain low carbon deposition levels over a long operating period.

In the techno-economic analysis, the role of desulphurisation was discussed. While previous studies on bio-oil reforming have assumed that desulphurisation is not required, due to low sulphur levels, closer examination has demonstrated that this area requires more scrutiny. This includes experimental research into catalyst deactivation in bio-oil reforming, considering the dual mechanisms of carbon deposition and sulphur poisoning. It also includes the design of cost-effective bulk sulphur removal, tailored to the unique chemistry of bio-oils. Ultimately, this could lead to a more in-depth techno-economic analysis, balancing the costs and benefits of strategies to improve catalyst performance and lifetime.

The techno-economic analysis also identified that major contributors to capital costs were the PSA system,  $\text{CO}_2$  capture (in the case of C-SR-CC) and three-way valves (in the case of SE-CLSR). To reduce uncertainty in the cost estimates, future work could prioritise these three aspects, taking into account to the specific chemistry of bio-oil reforming. Another area for future work could be to compare  $\text{CO}_2$  capture locations in bio-oil C-SR, in order to determine the optimal location. Other important aspects to consider are the

lifecycle emissions, feedstock cost reduction, and scalability of the bio-oil supply chain.

To further develop the reduction-calcination model in **Chapter 6**, future work could validate and refine the model using experimental results at a range of conditions. This work used an off-gas composition from bio-oil steam reforming (derived in **Chapter 5**), but the model could be used to model a range of scenarios for reduction and calcination in a mixed nickel catalyst/sorbent bed.

The kinetic study in **Chapter 7** focussed only on one model compound, acetic acid. For more complete reactor modelling, it will be necessary to develop kinetic models to represent a whole bio-oil. This may be a series of kinetic models of the major constituents, which can be combined to represent a mixture. Given the complex chemistry, an alternative may be to create lumped kinetic models of the type used for complex hydrocarbon fractions in oil refining. However, these models should be capable of representing different bio-oil feedstocks. A key advantage of the bio-oil reforming route is the diversity of possible bioenergy feedstocks, and the process modelling techniques ought to be similarly flexible in their application.

The proposed kinetic model is fairly limited in its applicability, due to its empirical nature and the simplification of the reaction scheme. Future kinetic studies should aim to achieve bio-oil kinetics that are valid at relevant industrial conditions, and to use these to evaluate reactor design, cost and, ultimately, technical and economic feasibility. This could include more detailed work on specific components of the reaction scheme, for example by determining the kinetics of SMR and WGS on this catalyst, as building blocks towards a more detailed and accurate model.

This work demonstrates one approach to process modelling, whereby whole process equilibrium modelling is linked to detailed kinetic modelling, using a mixture of qualitative analysis and the transferral of certain model inputs (such as PSA off-gas composition). While this approach can provide important findings for early-stage concept development, a longer term aim would be to have a fully integrated dynamic model for bio-oil SE-CLSR. This would be able to model all the sequence steps and their interactions at cyclic steady state, for a more thorough understanding of key constraints and opportunities for improvement.

## References

- [1] Grover VI. Introduction. In: Grover VI, editor. *Glob. Warm. Clim. Chang.* (2 Vols.), Enfield, NH, USA: Science Publishers; 2008, p. 3–42. <https://doi.org/10.1201/b11007-3>.
- [2] IPCC. *Managing the Risks of Extreme Events and Disasters to Advance Climate Change Adaptation. A Special Report of Working Groups I and II of the Intergovernmental Panel on Climate Change.* Cambridge, UK and New York, NY, USA: Cambridge University Press; 2012.
- [3] European Commission. *Paris Agreement 2016.* [http://ec.europa.eu/clima/policies/international/negotiations/paris/index\\_en.htm](http://ec.europa.eu/clima/policies/international/negotiations/paris/index_en.htm) (accessed June 30, 2016).
- [4] UNFCCC. *Paris Agreement 2015:3.* <https://doi.org/FCCC/CP/2015/L.9>.
- [5] IPCC. *Global Warming of 1.5°C. An IPCC Special Report on the impacts of global warming of 1.5°C above pre-industrial levels and related global greenhouse gas emission pathways, in the context of strengthening the global response to the threat of climate change.* 2018.
- [6] IPCC. *Summary for Policymakers.* In: Stocker TF, Qin D, Plattner G-K, Tignor M, Allen S., Boschung J, et al., editors. *Clim. Chang. 2013 Phys. Sci. Basis. Contrib. Work. Gr. I to Fifth Assess. Rep. Intergov. Panel Clim. Chang.*, Cambridge, UK and New York, NY, USA: Cambridge University Press; 2013, p. 3–29.
- [7] Ritchie H, Roser M. *CO2 and Greenhouse Gas Emissions. Our World Data 2019.* <https://ourworldindata.org/co2-and-other-greenhouse-gas-emissions> (accessed January 11, 2020).
- [8] Le Quéré C, Andrew RM, Friedlingstein P, Sitch S, Pongratz J, Manning AC, et al. *Annual territorial emissions of carbon dioxide (CO2) from fossil fuels and cement.* 2018.
- [9] The World Bank. *Population, total 2019.* <http://data.worldbank.org/indicator/SP.POP.TOTL> (accessed January 11, 2019).
- [10] IEA. *Global Energy & CO2 Status Report 2019.* 2019.
- [11] Nakicenovic N, Alcamo J, Davis G, de Vries B, Fenhann J, Gaffin S, et al. *Special Report on Emissions Scenarios. A Special Report of Working Group III of the Intergovernmental Panel on Climate Change.* Cambridge, UK and New York, NY, USA: Cambridge University Press; 2000.
- [12] IEA. *Energy and Climate Change. World Energy Outlook Spec Rep 2015.* <https://doi.org/10.1038/479267b>.
- [13] BP. *BP Energy Outlook 2016 Edition 2016.*
- [14] Milne TA, Elam CC, Evans RJ. *Hydrogen from biomass: state of the art and research challenges.* 2002. <https://doi.org/10.2172/792221>.
- [15] Marbán G, Valdés-Solís T. *Towards the hydrogen economy? Int J*

Hydrogen Energy 2007;32:1625–37.  
<https://doi.org/10.1016/j.ijhydene.2006.12.017>.

- [16] Soltani R, Rosen MA, Dincer I. Assessment of CO<sub>2</sub> capture options from various points in steam methane reforming for hydrogen production. *Int J Hydrogen Energy* 2014;39:20266–75.  
<https://doi.org/10.1016/j.ijhydene.2014.09.161>.
- [17] Barreto L, Makihira A, Riahi K. The hydrogen economy in the 21st century: A sustainable development scenario. *Int J Hydrogen Energy* 2003;28:267–84. [https://doi.org/10.1016/S0360-3199\(02\)00074-5](https://doi.org/10.1016/S0360-3199(02)00074-5).
- [18] Barton J, Gammon R. The production of hydrogen fuel from renewable sources and its role in grid operations. *J Power Sources* 2010;195:8222–35. <https://doi.org/10.1016/j.jpowsour.2009.12.100>.
- [19] IEA. Technology Roadmap - Hydrogen and Fuel Cells 2015.
- [20] Balat M. Potential importance of hydrogen as a future solution to environmental and transportation problems. *Int J Hydrogen Energy* 2008;33:4013–29. <https://doi.org/10.1016/j.ijhydene.2008.05.047>.
- [21] H21 Leeds City Gate. H21 Leeds City Gate Full Report. 2016.
- [22] ETI. Bioenergy - Delivering greenhouse gas savings through UK bioenergy value chains. 2015.
- [23] European Commission. Bioenergy Technical Background 2015. [http://ec.europa.eu/research/energy/eu/index\\_en.cfm?pg=research-bioenergy-background](http://ec.europa.eu/research/energy/eu/index_en.cfm?pg=research-bioenergy-background) (accessed July 7, 2016).
- [24] Committee on Climate Change. Bioenergy Review. 2011.
- [25] IPCC. Summary for Policymakers. In: Edenhofer O, Pichs-Madruga R, Sokona Y, Farahani E, Kadner S, Seyboth K, et al., editors. *Clim. Chang. 2014 Mitig. Clim. Chang. Contrib. Work. Gr. III to Fifth Assess. Rep. Intergov. Panel Clim. Chang.*, Cambridge, United Kingdom and New York, NY, USA: Cambridge University Press; 2014, p. 1–33.  
<https://doi.org/10.1017/CBO9781107415324>.
- [26] Adánez J, Abad A, García-Labiano F, Gayán P, De Diego LF. Progress in chemical-looping combustion and reforming technologies. *Prog Energy Combust Sci* 2012;38:215–82.  
<https://doi.org/10.1016/j.pecs.2011.09.001>.
- [27] Rydén M, Lyngfelt A, Mattisson T. Synthesis gas generation by chemical-looping reforming in a continuously operating laboratory reactor. *Fuel* 2006;85:1631–41.  
<https://doi.org/10.1016/j.fuel.2006.02.004>.
- [28] Gutiérrez Ortiz FJ, Ollero P, Serrera A, Sanz A. Thermodynamic study of the supercritical water reforming of glycerol. *Int J Hydrogen Energy* 2011;36:8994–9013. <https://doi.org/10.1016/j.ijhydene.2011.04.095>.
- [29] Rydén M, Lyngfelt A, Mattisson T. Two novel approaches for hydrogen production, chemical-looping reforming and steam reforming with carbon dioxide capture by chemical-looping combustion. *Fuel* 2006;85:1631–41.



- [30] Fathi M, Bjorgum E, Viig T, Rokstad OA. Partial oxidation of methane to synthesis gas: Elimination of gas phase oxygen. *Catal Today* 2000;63:489–97. [https://doi.org/10.1016/S0920-5861\(00\)00495-8](https://doi.org/10.1016/S0920-5861(00)00495-8).
- [31] Antzara A, Heracleous E, Silvester L, Bukur DB, Lemonidou AA. Activity study of NiO-based oxygen carriers in chemical looping steam methane reforming. *Catal Today* 2016;272:32–41. <https://doi.org/10.1016/j.cattod.2015.10.027>.
- [32] Neal L, Shafiefarhood A, Li F. Effect of core and shell compositions on MeOx@LaySr1-yFeO3 core-shell redox catalysts for chemical looping reforming of methane. *Appl Energy* 2015;157:391–8. <https://doi.org/10.1016/j.apenergy.2015.06.028>.
- [33] Ortiz M, De Diego LF, Abad A, García-Labiano F, Gayán P, Adánez J. Catalytic activity of ni-based oxygen-carriers for steam methane reforming in chemical-looping processes. *Energy and Fuels* 2012;26:791–800. <https://doi.org/10.1021/ef2013612>.
- [34] Silvester L, Antzara A, Boskovic G, Heracleous E, Lemonidou AA, Bukur DB. NiO supported on Al2O3 and ZrO2 oxygen carriers for chemical looping steam methane reforming. *Int J Hydrogen Energy* 2015;40:7490–501. <https://doi.org/10.1016/j.ijhydene.2014.12.130>.
- [35] Chen H, Zhang T, Dou B, Dupont V, Williams PT, Ghadiri M, et al. Thermodynamic analyses of adsorption-enhanced steam reforming of glycerol for hydrogen production. *Int J Hydrogen Energy* 2009;34:7208–22. <https://doi.org/10.1016/j.ijhydene.2009.06.070>.
- [36] Dou B, Rickett GL, Dupont V, Williams PT, Chen H, Ding Y, et al. Steam reforming of crude glycerol with in situ CO2 sorption. *Bioresour Technol* 2010;101:2436–42. <https://doi.org/10.1016/j.biortech.2009.10.092>.
- [37] Lea-Langton A, Giannakeas N, Rickett G, Dupont V, Twigg MV. Waste lubricating oil as a source of hydrogen fuel using chemical looping steam reforming. *SAE Int J Fuels Lubr* 2010;3:810–8.
- [38] Lea-Langton A, Zin RM, Dupont V, Twigg MV. Biomass pyrolysis oils for hydrogen production using chemical looping reforming. *Int J Hydrogen Energy* 2012;37:2037–43. <https://doi.org/http://dx.doi.org/10.1016/j.ijhydene.2011.05.083>.
- [39] Cormos C-C. Renewable hydrogen production concepts from bioethanol reforming with carbon capture. *Int J Hydrogen Energy* 2014;39:5597–606. <https://doi.org/10.1016/j.ijhydene.2014.01.114>.
- [40] Hufton JR, Mayorga S, Sircar S. Sorption-enhanced reaction process for hydrogen production. *AIChE J* 1999;45:248–56. <https://doi.org/10.1002/aic.690450205>.
- [41] Yahom A, Powell J, Pavarajarn V, Onbuddha P, Charojrochkul S, Assabumrungrat S. Simulation and thermodynamic analysis of chemical looping reforming and CO2 enhanced chemical looping reforming. *Chem Eng Res Des* 2014;92:2575–83. <https://doi.org/10.1016/j.cherd.2014.04.002>.
- [42] Lyon RK, Cole JA. Unmixed combustion: An alternative to fire.

Combust Flame 2000;121:249–61. [https://doi.org/10.1016/S0010-2180\(99\)00136-4](https://doi.org/10.1016/S0010-2180(99)00136-4).

- [43] Sherif SA, Yogi Goswami D, Lee Stefanakos EK, Steinfeld A. Handbook of Hydrogen Energy. CRC Press; 2014.
- [44] Levin DB, Chahine R. Challenges for renewable hydrogen production from biomass. Int J Hydrogen Energy 2010;35:4962–9. <https://doi.org/10.1016/j.ijhydene.2009.08.067>.
- [45] Nahar G, Dupont V. Recent advances in hydrogen production via autothermal reforming process (ATR): A review of patents and research articles. Recent Patents Chem Eng 2013;6:8–42. <https://doi.org/http://dx.doi.org/10.2174/2211334711306010003>.
- [46] Aasberg-Petersen K, Christensen TS, Nielsen CS, Dybkjær I. Recent developments in autothermal reforming and pre-reforming for synthesis gas production in GTL applications. Fuel Process Technol 2003;83:253–61. [https://doi.org/10.1016/S0378-3820\(03\)00073-0](https://doi.org/10.1016/S0378-3820(03)00073-0).
- [47] Hydrogen Council. Path to Hydrogen Competitiveness: A Cost Perspective - Hydrogen Council. n.d.
- [48] Turner J, Sverdrup G, Mann MK, Maness P-C, Kroposki B, Ghirardi M, et al. Renewable hydrogen production. Int J Energy Res 2008;32:379–407. <https://doi.org/10.1002/er.1372>.
- [49] Maton JP, Zhao L, Brouwer J. Dynamic modeling of compressed gas energy storage to complement renewable wind power intermittency. Int J Hydrogen Energy 2013;38:7867–80. <https://doi.org/10.1016/j.ijhydene.2013.04.030>.
- [50] Díaz-González F, Sumper A, Gomis-Bellmunt O, Villafáfila-Robles R. A review of energy storage technologies for wind power applications. Renew Sustain Energy Rev 2012;16:2154–71. <https://doi.org/10.1016/j.rser.2012.01.029>.
- [51] Hacatoglu K, Dincer I, Rosen MA. Sustainability of a wind-hydrogen energy system: Assessment using a novel index and comparison to a conventional gas-fired system. Int J Hydrogen Energy 2016;41:8376–85. <https://doi.org/10.1016/j.ijhydene.2016.01.135>.
- [52] Bhandari R, Trudewind CA, Zapp P. Life cycle assessment of hydrogen production via electrolysis - A review. J Clean Prod 2014;85:151–63. <https://doi.org/10.1016/j.jclepro.2013.07.048>.
- [53] Davis SJ, Lewis NS, Shaner M, Aggarwal S, Arent D, Azevedo IL, et al. Net-zero emissions energy systems 2018;9793. <https://doi.org/10.1126/science.aas9793>.
- [54] Twigg MV, Dupont V. Hydrogen production from fossil fuel and biomass feedstocks. In: Basile A, Iulianelli A, editors. Adv. Hydrog. Prod. Storage Distrib., Cambridge: Woodhead Publishing; 2014, p. 43–84.
- [55] Dufour J, Serrano DP, Gálvez JL, Moreno J, García C. Life cycle assessment of processes for hydrogen production. Environmental feasibility and reduction of greenhouse gases emissions. Int J

Hydrogen Energy 2009;34:1370–6.  
<https://doi.org/10.1016/j.ijhydene.2008.11.053>.

- [56] Muradov NZ. Chapter 2. Production of Hydrogen from Hydrocarbons. In: Gupta RB, editor. *Hydrog. Fuel*, CRC Press; 2008, p. 33–101.
- [57] Rostrup-Nielsen JR. Syngas in perspective. *Catal Today* 2002;71:243–7. [https://doi.org/10.1016/S0920-5861\(01\)00454-0](https://doi.org/10.1016/S0920-5861(01)00454-0).
- [58] Abbas HF, Wan Daud WM. Hydrogen production by methane decomposition: A review. *Int J Hydrogen Energy* 2010;35:1160–90. <https://doi.org/10.1016/j.ijhydene.2009.11.036>.
- [59] Fernández JR, Abanades JC, Murillo R. Modeling of sorption enhanced steam methane reforming in an adiabatic fixed bed reactor. *Chem Eng Sci* 2012;84:1–11. <https://doi.org/10.1016/j.ces.2012.07.039>.
- [60] Nahar G, Dupont V. Hydrogen via steam reforming of liquid biofeedstock. *Biofuels* 2012;3:167–91. <https://doi.org/10.4155/bfs.12.8>.
- [61] Speight J. *Handbook of Industrial Hydrocarbon Processes*. Elsevier; 2011.
- [62] Tarun CB, Croiset E, Douglas PL, Gupta M, Chowdhury MHM. Techno-economic study of CO<sub>2</sub> capture from natural gas based hydrogen plants. *Int J Greenh Gas Control* 2007;1:55–61. [https://doi.org/10.1016/S1750-5836\(07\)00036-9](https://doi.org/10.1016/S1750-5836(07)00036-9).
- [63] Shayegan J, Motamed Hashemi MMY, Vakhshouri K. Operation of an industrial steam reformer under severe condition: A simulation study. *Can J Chem Eng* 2008;86:747–55. <https://doi.org/10.1002/cjce.20082>.
- [64] Pena MA, Gómez JP, Fierro JLG. New catalytic routes for syngas and hydrogen production. *Appl Catal A Gen* 1996;144:7–57. [https://doi.org/10.1016/0926-860X\(96\)00108-1](https://doi.org/10.1016/0926-860X(96)00108-1).
- [65] Sehested J. Four challenges for nickel steam-reforming catalysts. *Catal Today* 2006;111:103–10. <https://doi.org/10.1016/j.cattod.2005.10.002>.
- [66] Fahim MA, Alsahhaf T., Elkilani A. *Fundamentals of Petroleum Refining*. Elsevier; 2010.
- [67] Chen WH, Lin MR, Jiang TL, Chen MH. Modeling and simulation of hydrogen generation from high-temperature and low-temperature water gas shift reactions. *Int J Hydrogen Energy* 2008;33:6644–56. <https://doi.org/10.1016/j.ijhydene.2008.08.039>.
- [68] Sarkar S, Kumar A. Large-scale biohydrogen production from bio-oil. *Bioresour Technol* 2010;101:7350–61. <https://doi.org/10.1016/j.biortech.2010.04.038>.
- [69] The Linde Group. CO shift conversion 2016. [http://www.linde-engineering.com/en/process\\_plants/hydrogen\\_and\\_synthesis\\_gas\\_plants/gas\\_generation/co\\_shift\\_conversion/index.html](http://www.linde-engineering.com/en/process_plants/hydrogen_and_synthesis_gas_plants/gas_generation/co_shift_conversion/index.html) (accessed December 16, 2016).
- [70] Rydén M, Lyngfelt A. Using steam reforming to produce hydrogen with

carbon dioxide capture by chemical-looping combustion. *Int J Hydrogen Energy* 2006;31:1271–83.  
<https://doi.org/10.1016/j.ijhydene.2005.12.003>.

- [71] Barelli L, Bidini G, Gallorini F, Servili S. Hydrogen production through sorption-enhanced steam methane reforming and membrane technology: A review. *Energy* 2008;33:554–70.  
<https://doi.org/10.1016/j.energy.2007.10.018>.
- [72] Franczyk E, Gołębiowski A, Borowiecki T, Kowalik P, Wróbel W. Influence of steam reforming catalyst geometry on the performance of tubular reformer-simulation calculations. *Chem Process Eng* 2015;36:239–50. <https://doi.org/10.1515/cpe-2015-0016>.
- [73] Rostrup-Nielsen JR, Hansen B. Steam Reforming for Fuel Cells. In: Shekhawat D, Spivey JJ, Berry DA, editors. *Fuel Cells - Technol. Fuel Process.*, Elsevier; 2011, p. 50–68.
- [74] Nakayama O, Ikenaga N, Miyake T, Yagasaki E, Suzuki T. Partial oxidation of CH<sub>4</sub> with air to produce pure hydrogen and syngas. *Catal Today* 2008;138:141–6. <https://doi.org/10.1016/j.cattod.2008.05.013>.
- [75] Tang M, Xu L, Fan M. Progress in oxygen carrier development of methane-based chemical-looping reforming: A review. *Appl Energy* 2015;151:143–56. <https://doi.org/10.1016/j.apenergy.2015.04.017>.
- [76] Mattos LV, Noronha FB. Hydrogen production for fuel cell applications by ethanol partial oxidation on Pt/CeO<sub>2</sub> catalysts: The effect of the reaction conditions and reaction mechanism. *J Catal* 2005;233:453–63. <https://doi.org/10.1016/j.jcat.2005.04.022>.
- [77] Holladay JD, Hu J, King DL, Wang Y. An overview of hydrogen production technologies. *Catal Today* 2009;139:244–60. <https://doi.org/10.1016/j.cattod.2008.08.039>.
- [78] Zhu J, Zhang D, King KD. Reforming of CH<sub>4</sub> by partial oxidation: thermodynamic and kinetic analyses 2001;80:899–905.
- [79] Cubeiro ML, Fierro JLG. Partial oxidation of methanol over supported palladium catalysts. *Appl Catal A Gen* 1998;168:307–22. [https://doi.org/http://dx.doi.org/10.1016/S0926-860X\(97\)00361-X](https://doi.org/http://dx.doi.org/10.1016/S0926-860X(97)00361-X).
- [80] Wang W. Thermodynamic analysis of glycerol partial oxidation for hydrogen production. *Fuel Process Technol* 2010;91:1401–8. <https://doi.org/10.1016/j.fuproc.2010.05.013>.
- [81] Kim DH, Kim SH, Byun JY. A microreactor with metallic catalyst support for hydrogen production by partial oxidation of dimethyl ether. *Chem Eng J* 2015;280:468–74. <https://doi.org/10.1016/j.cej.2015.06.038>.
- [82] Králeva E, Sokolov S, Nasillo G, Bentrup U, Ehrich H. Catalytic performance of CoAlZn and NiAlZn mixed oxides in hydrogen production by bio-ethanol partial oxidation. *Int J Hydrogen Energy* 2014;39:209–20. <https://doi.org/10.1016/j.ijhydene.2013.10.072>.
- [83] Mondal T, Pant KK, Dalai AK. Oxidative and non-oxidative steam reforming of crude bio-ethanol for hydrogen production over Rh

promoted Ni/CeO-ZrO<sub>2</sub> catalyst. *Appl Catal A Gen* 2015;499:19–31. <https://doi.org/10.1016/j.apcata.2015.04.004>.

- [84] Marda JR, DiBenedetto J, McKibben S, Evans RJ, Czernik S, French RJ, et al. Non-catalytic partial oxidation of bio-oil to synthesis gas for distributed hydrogen production. *Int J Hydrogen Energy* 2009;34:8519–34. <https://doi.org/10.1016/j.ijhydene.2009.07.099>.
- [85] Rennard D, French R, Czernik S, Josephson T, Schmidt L. Production of synthesis gas by partial oxidation and steam reforming of biomass pyrolysis oils. *Int J Hydrogen Energy* 2010;35:4048–59. <https://doi.org/10.1016/j.ijhydene.2010.01.143>.
- [86] Enger BC, Lødeng R, Holmen A. A review of catalytic partial oxidation of methane to synthesis gas with emphasis on reaction mechanisms over transition metal catalysts. *Appl Catal A Gen* 2008;346:1–27. <https://doi.org/10.1016/j.apcata.2008.05.018>.
- [87] Arku P, Regmi B, Dutta A. A review of catalytic partial oxidation of fossil fuels and biofuels: Recent advances in catalyst development and kinetic modelling. *Chem Eng Res Des* 2018;136:385–402. <https://doi.org/10.1016/j.cherd.2018.05.044>.
- [88] Halabi MH, de Croon MHJM, van der Schaaf J, Cobden PD, Schouten JC. Modeling and analysis of autothermal reforming of methane to hydrogen in a fixed bed reformer. *Chem Eng J* 2008;137:568–78. <https://doi.org/10.1016/j.cej.2007.05.019>.
- [89] Chaubey R, Sahu S, James OO, Maity S. A review on development of industrial processes and emerging techniques for production of hydrogen from renewable and sustainable sources. *Renew Sustain Energy Rev* 2013;23:443–62. <https://doi.org/10.1016/j.rser.2013.02.019>.
- [90] Czernik S, French R. Distributed production of hydrogen by autothermal reforming of fast pyrolysis bio-oil. *Int J Hydrogen Energy* 2014;39:744–50. <https://doi.org/10.1016/j.ijhydene.2013.10.134>.
- [91] Dybkjær I. Tubular reforming and autothermal reforming of natural gas - an overview of available processes. *Fuel Process Technol* 1995;42:85–107. [https://doi.org/10.1016/0378-3820\(94\)00099-F](https://doi.org/10.1016/0378-3820(94)00099-F).
- [92] Huber GW, Iborra S, Corma A. Synthesis of transportation fuels from biomass: Chemistry, catalysts, and engineering. *Chem Rev* 2006;106:4044–98. <https://doi.org/10.1021/cr068360d>.
- [93] Luberti M, Friedrich D, Brandani S, Ahn H. Design of a H<sub>2</sub> PSA for cogeneration of ultrapure hydrogen and power at an advanced integrated gasification combined cycle with pre-combustion capture. *Adsorption* 2014;20:511–24. <https://doi.org/10.1007/s10450-013-9598-0>.
- [94] Voldsund M, Jordal K, Anantharaman R. Hydrogen production with CO<sub>2</sub> capture. *Int J Hydrogen Energy* 2016;41:4969–92. <https://doi.org/10.1016/j.ijhydene.2016.01.009>.
- [95] Corradetti A, Desideri U. Should Biomass be Used for Power Generation or Hydrogen Production? *J Eng Gas Turbines Power*

2006;129:629–36. <https://doi.org/10.1115/1.2718226>.

- [96] Dincer I, Acar C. Review and evaluation of hydrogen production methods for better sustainability. *Int J Hydrogen Energy* 2014;40:11094–111. <https://doi.org/10.1016/j.ijhydene.2014.12.035>.
- [97] Sadegh-Vaziri R, Amovic M, Ljunggren R, Engvall K. A Medium-scale 50 MW fuel biomass gasification based Bio-SNG plant: A developed gas cleaning process. *Energies* 2015;8:5287–302. <https://doi.org/10.3390/en8065287>.
- [98] H2FC Supergen. Opportunities for hydrogen and fuel cell technologies to contribute to clean growth in the UK n.d. <http://www.h2fcsupergen.com/opportunities-for-hydrogen-fuel-cell-clean-growth-uk/> (accessed June 14, 2020).
- [99] Scarlat N, Dallemand JF. Recent developments of biofuels/bioenergy sustainability certification: A global overview. *Energy Policy* 2011;39:1630–46. <https://doi.org/10.1016/j.enpol.2010.12.039>.
- [100] Arregi A, Amutio M, Lopez G, Bilbao J, Olazar M. Evaluation of thermochemical routes for hydrogen production from biomass: A review. *Energy Convers Manag* 2018;165:696–719. <https://doi.org/10.1016/j.enconman.2018.03.089>.
- [101] Wang D, Czernik S, Montane D, Mann M, Chornet E. Biomass to Hydrogen via Fast Pyrolysis and Catalytic Steam Reforming of the Pyrolysis Oil or Its Fractions. *Abstr Pap Am Chem Soc* 1997;36:1507–18. <https://doi.org/10.1021/ie960396g>.
- [102] Pimenidou P, Rickett G, Dupont V, Twigg MV. Chemical looping reforming of waste cooking oil in packed bed reactor. *Bioresour Technol* 2010;101:6389–97. <https://doi.org/10.1016/j.biortech.2010.03.053>.
- [103] Dupont V, Ross AB, Hanley I, Twigg MV. Unmixed steam reforming of methane and sunflower oil: A single-reactor process for H<sub>2</sub>-rich gas. *Int J Hydrogen Energy* 2007;32:67–79. <https://doi.org/10.1016/j.ijhydene.2006.06.033>.
- [104] Markevich M, Farriol X, Medina F, Montane D. Hydrogen production by steam reforming of vegetable oils using nickel-based catalysts. *Ind Eng Chem Res* 2001;40:4757–66. <https://doi.org/10.1021/ie010135t>.
- [105] Dou B, Song Y, Wang C, Chen H, Xu Y. Hydrogen production from catalytic steam reforming of biodiesel byproduct glycerol: Issues and challenges. *Renew Sustain Energy Rev* 2014;30:950–60. <https://doi.org/10.1016/j.rser.2013.11.029>.
- [106] Silva JM, Soria MA, Madeira LM. Challenges and strategies for optimization of glycerol steam reforming process. *Renew Sustain Energy Rev* 2015;42:1187–213. <https://doi.org/10.1016/j.rser.2014.10.084>.
- [107] Wang H, Male J, Wang Y. Recent advances in hydrotreating of pyrolysis bio-oil and its oxygen-containing model compounds. *ACS Catal* 2013;3:1047–70. <https://doi.org/10.1021/cs400069z>.

- [108] Bridgwater A V. Review of fast pyrolysis of biomass and product upgrading. *Biomass and Bioenergy* 2012;38:68–94. <https://doi.org/10.1016/j.biombioe.2011.01.048>.
- [109] Liu C, Wang H, Karim AM, Sun J, Wang Y. Catalytic fast pyrolysis of lignocellulosic biomass. *Chem Soc Rev* 2014;43:7594–623. <https://doi.org/10.1039/C3CS60414D>.
- [110] Wang L, Cheng D. *Biomass Pyrolysis and Bio-Oil Utilization*. Sustain. Bioenergy Prod., CRC Press; 2014, p. 361–82. <https://doi.org/10.1201/b16764-22>.
- [111] Zhang Q, Chang J, Wang T, Xu Y. Review of biomass pyrolysis oil properties and upgrading research. *Energy Convers Manag* 2007;48:87–92. <https://doi.org/10.1016/j.enconman.2006.05.010>.
- [112] Bridgwater A V., Peacocke GV. Fast pyrolysis processes for biomass. *Renew Sustain Energy Rev* 2000;4:1–73.
- [113] Rogers JG, Brammer JG. Estimation of the production cost of fast pyrolysis bio-oil. *Biomass and Bioenergy* 2012;36:208–17. <https://doi.org/10.1016/j.biombioe.2011.10.028>.
- [114] Wang D, Montané D, Chornet E. Catalytic steam reforming of biomass-derived oxygenates: Acetic acid and hydroxyacetaldehyde. *Appl Catal A Gen* 1996;143:245–70. [https://doi.org/10.1016/0926-860X\(96\)00093-2](https://doi.org/10.1016/0926-860X(96)00093-2).
- [115] Yao D, Wu C, Yang H, Hu Q, Nahil MA, Chen H, et al. Hydrogen production from catalytic reforming of the aqueous fraction of pyrolysis bio-oil with modified Ni-Al catalysts. *Int J Hydrogen Energy* 2014;39:14642–52. <https://doi.org/10.1016/j.ijhydene.2014.07.077>.
- [116] Liu S, Chen M, Chu L, Yang Z, Zhu C, Wang J, et al. Catalytic steam reforming of bio-oil aqueous fraction for hydrogen production over Ni-Mo supported on modified sepiolite catalysts. *Int J Hydrogen Energy* 2013;38:3948–55. <https://doi.org/10.1016/j.ijhydene.2013.01.117>.
- [117] Zhang S, Li X, Li Q, Xu Q, Yan Y. Hydrogen production from the aqueous phase derived from fast pyrolysis of biomass. *J Anal Appl Pyrolysis* 2011;92:158–63. <https://doi.org/10.1016/j.jaap.2011.05.007>.
- [118] Medrano JA, Oliva M, Ruiz J, García L, Arauzo J. Hydrogen from aqueous fraction of biomass pyrolysis liquids by catalytic steam reforming in fluidized bed. *Energy* 2011;36:2215–24. <https://doi.org/10.1016/j.energy.2010.03.059>.
- [119] Trane R, Dahl S, Skjøth-Rasmussen MS, Jensen AD. Catalytic steam reforming of bio-oil. *Int J Hydrogen Energy* 2012;37:6447–72. <https://doi.org/10.1016/j.ijhydene.2012.01.023>.
- [120] Wu C, Liu R. Carbon deposition behavior in steam reforming of bio-oil model compound for hydrogen production. *Int J Hydrogen Energy* 2010;35:7386–98. <https://doi.org/10.1016/j.ijhydene.2010.04.166>.
- [121] Basagiannis AC, Verykios XE. Reforming reactions of acetic acid on nickel catalysts over a wide temperature range. *Appl Catal A Gen* 2006;308:182–93. <https://doi.org/10.1016/j.apcata.2006.04.024>.

- [122] Hu X, Lu G. Investigation of the steam reforming of a series of model compounds derived from bio-oil for hydrogen production. *Appl Catal B Environ* 2009;88:376–85. <https://doi.org/10.1016/j.apcatb.2008.10.021>.
- [123] Cheng F, Dupont V. Steam Reforming of Bio-Compounds with Auto-Reduced Nickel Catalyst. *Catalysts* 2017;7:114. <https://doi.org/10.3390/catal7040114>.
- [124] Vagia EC, Lemonidou AA. Thermodynamic analysis of hydrogen production via autothermal steam reforming of selected components of aqueous bio-oil fraction. *Int J Hydrogen Energy* 2008;33:2489–500. <https://doi.org/10.1016/j.ijhydene.2008.02.057>.
- [125] Bimbela F, Oliva M, Ruiz J, García L, Arauzo J. Hydrogen production by catalytic steam reforming of acetic acid, a model compound of biomass pyrolysis liquids. *J Anal Appl Pyrolysis* 2007;79:112–20. <https://doi.org/10.1016/j.jaap.2006.11.006>.
- [126] Galdámez JR, García L, Bilbao R. Hydrogen Production by Steam Reforming of Bio-Oil Using Coprecipitated Ni - Al Catalysts. Acetic Acid as a Model Compound. *Energy & Fuels* 2005;19:1133–42. <https://doi.org/10.1021/ef049718g>.
- [127] Vagia EC, Lemonidou AA. Hydrogen production via steam reforming of bio-oil components over calcium aluminate supported nickel and noble metal catalysts. *Appl Catal A Gen* 2008;351:111–21. <https://doi.org/10.1016/j.apcata.2008.09.007>.
- [128] Cheng F, Dupont V. Nickel catalyst auto-reduction during steam reforming of bio-oil model compound acetic acid. *Int J Hydrogen Energy* 2013;38:15160–72. <https://doi.org/10.1016/j.ijhydene.2013.09.111>.
- [129] Heracleous E. Well-to-Wheels analysis of hydrogen production from bio-oil reforming for use in internal combustion engines. *Int J Hydrogen Energy* 2011;36:11501–11. <https://doi.org/10.1016/j.ijhydene.2011.06.052>.
- [130] Collodi G, Azzaro G, Ferrari N, Santos S. Techno-economic Evaluation of Deploying CCS in SMR Based Merchant H<sub>2</sub> Production with NG as Feedstock and Fuel. *Energy Procedia*, vol. 114, Elsevier Ltd; 2017, p. 2690–712. <https://doi.org/10.1016/j.egypro.2017.03.1533>.
- [131] Ozbilen A, Dincer I, Rosen MA. Comparative environmental impact and efficiency assessment of selected hydrogen production methods. *Environ Impact Assess Rev* 2013;42:1–9. <https://doi.org/10.1016/j.eiar.2013.03.003>.
- [132] Acar C, Dincer I. Impact assessment and efficiency evaluation of hydrogen production methods. *Int J Chem React Eng* 2015;39:1757–68. <https://doi.org/10.1002/er.3302>.
- [133] Suleman F, Dincer I, Agelin-Chaab M. Comparative impact assessment study of various hydrogen production methods in terms of emissions. *Int J Hydrogen Energy* 2016;41:8364–75. <https://doi.org/10.1016/j.ijhydene.2015.12.225>.
- [134] Leung DYC, Caramanna G, Maroto-valer MM. An overview of current



status of carbon dioxide capture and storage technologies. *Renew Sustain Energy Rev* 2014;39:426–43.  
<https://doi.org/10.1016/j.rser.2014.07.093>.

- [135] Toftegaard MB, Brix J, Jensen PA, Glarborg P, Jensen AD. Oxy-fuel combustion of solid fuels. *Prog Energy Combust Sci* 2010;36:581–625. <https://doi.org/10.1016/j.pecs.2010.02.001>.
- [136] Meerman JC, Hamborg ES, van Keulen T, Ramírez A, Turkenburg WC, Faaij APC. Techno-economic assessment of CO<sub>2</sub> capture at steam methane reforming facilities using commercially available technology. *Int J Greenh Gas Control* 2012;9:160–71.  
<https://doi.org/10.1016/j.ijggc.2012.02.018>.
- [137] Alie C, Backham L, Croiset E, Douglas PL. Simulation of CO<sub>2</sub> capture using MEA scrubbing: A flowsheet decomposition method. *Energy Convers Manag* 2005;46:475–87.  
<https://doi.org/10.1016/j.enconman.2004.03.003>.
- [138] Khan FM, Krishnamoorthi V, Mahmud T. Modelling reactive absorption of CO<sub>2</sub> in packed columns for post-combustion carbon capture applications. *Chem Eng Res Des* 2011;89:1600–8.  
<https://doi.org/10.1016/j.cherd.2010.09.020>.
- [139] Webley PA. Adsorption technology for CO<sub>2</sub> separation and capture: A perspective. *Adsorption* 2014;20:225–31.  
<https://doi.org/10.1007/s10450-014-9603-2>.
- [140] Khalilpour R, Mumford K, Zhai H, Abbas A, Stevens G, Rubin ES. Membrane-based carbon capture from flue gas: A review. *J Clean Prod* 2015;103:286–300. <https://doi.org/10.1016/j.jclepro.2014.10.050>.
- [141] Olajire AA. CO<sub>2</sub> capture and separation technologies for end-of-pipe applications - A review. *Energy* 2010;35:2610–28.  
<https://doi.org/10.1016/j.energy.2010.02.030>.
- [142] Brunetti A, Scura F, Barbieri G, Drioli E. Membrane technologies for CO<sub>2</sub> separation. *J Memb Sci* 2010;359:115–25.  
<https://doi.org/10.1016/j.memsci.2009.11.040>.
- [143] Aaron D, Tsouris C. Separation of CO<sub>2</sub> from Flue Gas: A Review. *Sep Sci Technol* 2005;40:321–48. <https://doi.org/10.1081/SS-200042244>.
- [144] Reddy S, Vyas S. Recovery of Carbon Dioxide and Hydrogen from PSA Tail Gas. *Energy Procedia* 2009;1:149–54.  
<https://doi.org/10.1016/j.egypro.2009.01.022>.
- [145] Air Liquide. Cryocap™ CO<sub>2</sub> cold capture system 2015.  
<https://www.airliquide.com/connected-innovation/cryocap-co2-cold-capture-system-unlike-any-other-in-the-world> (accessed August 15, 2016).
- [146] Terrien P, Lockwood F, Granados L, Morel T. CO<sub>2</sub> capture from H<sub>2</sub> plants: Implementation for EOR. *Energy Procedia* 2014;63:7861–6.  
<https://doi.org/10.1016/j.egypro.2014.11.821>.
- [147] MIT. CCS Project Database. Carbon Capture Sequestration Technol MIT 2016. [https://sequestration.mit.edu/tools/projects/port\\_arthur.html](https://sequestration.mit.edu/tools/projects/port_arthur.html)

(accessed April 11, 2017).

- [148] Duarte P, Gottlund S. Capturing CO<sub>2</sub> with a Green Focus. *Chem Eng Prog* 2015;111:21.
- [149] Baade WF, Farnand S, Hutchison R, Welch K. CO<sub>2</sub> capture from SMRs: A demonstration project. *Hydrocarb Process* 2012;91.
- [150] National Energy Technology Laboratory. Recovery Act: Demonstration of CO<sub>2</sub> Capture and Sequestration for Steam Methane Reforming Process Gas Used for Large-Scale Hydrogen Production 2014. <http://netl.doe.gov/research/proj?k=FE0002381&show=ppp> (accessed April 11, 2017).
- [151] Global CCS Institute. Large-scale CCS facilities 2017. <https://www.globalccsinstitute.com/projects/large-scale-ccs-projects> (accessed June 13, 2017).
- [152] Shell Canada. Quest CCS Facility Captures and Stores Five Million Tonnes of CO<sub>2</sub> Ahead of Fifth Anniversary 2020. [https://www.shell.ca/en\\_ca/media/news-and-media-releases/news-releases-2020/quest-ccs-facility-captures-and-stores-five-million-tonnes.html](https://www.shell.ca/en_ca/media/news-and-media-releases/news-releases-2020/quest-ccs-facility-captures-and-stores-five-million-tonnes.html) (accessed July 26, 2020).
- [153] Tanaka Y, Abe M, Sawada Y, Tanase D, Ito T, Kasukawa T. Tomakomai CCS demonstration project in Japan, 2014 update. *Energy Procedia* 2014;63:6111–9. <https://doi.org/10.1016/j.egypro.2014.11.643>.
- [154] Japan CCS Co. Ltd. Regarding the report of Tomakomai CCS Demonstration Project at 300 thousand tonnes cumulative injection (Summary Report) 2020. <https://www.japanccs.com/en/news/en-20200529/> (accessed July 26, 2020).
- [155] Antzara A, Heracleous E, Bukur DB, Lemonidou AA. Thermodynamic analysis of hydrogen production via chemical looping steam methane reforming coupled with in situ CO<sub>2</sub> capture. *Energy Procedia* 2014;63:6576–89. <https://doi.org/10.1016/j.egypro.2014.11.694>.
- [156] Dou B, Wang C, Song Y, Chen H, Jiang B, Yang M, et al. Solid sorbents for in-situ CO<sub>2</sub> removal during sorption-enhanced steam reforming process: A review. *Renew Sustain Energy Rev* 2016;53:536–46. <https://doi.org/10.1016/j.rser.2015.08.068>.
- [157] Pimenidou P, Dupont V. Dolomite study for in situ CO<sub>2</sub> capture for chemical looping reforming. *Int J Ambient Energy* 2015;36:170–82. <https://doi.org/10.1080/01430750.2013.841590>.
- [158] Grasa GS, Abanades JC. CO<sub>2</sub> capture capacity of CaO in long series of carbonation/calcination cycles. *Ind Eng Chem Res* 2006;45:8846–51. <https://doi.org/10.1021/ie0606946>.
- [159] Martínez I, Grasa G, Murillo R, Arias B, Abanades JC. Kinetics of calcination of partially carbonated particles in a Ca-looping system for CO<sub>2</sub> capture. *Energy and Fuels* 2012;26:1432–40. <https://doi.org/10.1021/ef201525k>.
- [160] Dupont V, Ross AB, Knight E, Hanley I, Twigg MV. Production of

hydrogen by unmixed steam reforming of methane. *Chem Eng Sci* 2008;63:2966–79. <https://doi.org/10.1016/j.ces.2008.02.015>.

- [161] Francisco Morgado J, Cloete S, Morud J, Gurker T, Amini S. Modelling study of two chemical looping reforming reactor configurations: looping vs. switching. *Powder Technol* 2017;316:599–613. <https://doi.org/10.1016/j.powtec.2016.11.059>.
- [162] Nazir SM, Cloete S, Bolland O, Amini S. Techno-economic assessment of the novel gas switching reforming (GSR) concept for gas-fired power production with integrated CO<sub>2</sub> capture. *Int J Hydrogen Energy* 2018;43:8754–69. <https://doi.org/10.1016/j.ijhydene.2018.02.076>.
- [163] Noorman S, Annaland MVS, Kuipers H. Packed Bed Reactor Technology for Chemical-Looping Combustion. *Ind Eng Chem Res* 2007;46:4212–20. <https://doi.org/10.1021/ie061178i>.
- [164] Protasova L, Snijkers F. Recent developments in oxygen carrier materials for hydrogen production via chemical looping processes. *Fuel* 2016;181:75–93. <https://doi.org/10.1016/j.fuel.2016.04.110>.
- [165] Díez-Martín L, López JM, Fernández JR, Martínez I, Grasa G, Murillo R. Complete Ca/Cu cycle for H<sub>2</sub> production via CH<sub>4</sub> sorption enhanced reforming in a Lab-Scale fixed bed reactor. *Chem Eng J* 2018;350:1010–21. <https://doi.org/10.1016/j.cej.2018.06.049>.
- [166] Fernández JR, Abanades JC. Optimized design and operation strategy of a Ca-Cu chemical looping process for hydrogen production. *Chem Eng Sci* 2017;166:144–60. <https://doi.org/10.1016/j.ces.2017.03.039>.
- [167] Pröll T, Bolhàr-Nordenkamp J, Kolbitsch P, Hofbauer H. Syngas and a separate nitrogen/argon stream via chemical looping reforming - A 140 kW pilot plant study. *Fuel* 2010;89:1249–56. <https://doi.org/10.1016/j.fuel.2009.09.033>.
- [168] Rydén M, Ramos P. H<sub>2</sub> production with CO<sub>2</sub> capture by sorption enhanced chemical-looping reforming using NiO as oxygen carrier and CaO as CO<sub>2</sub> sorbent. *Fuel Process Technol* 2012;96:27–36. <https://doi.org/10.1016/j.fuproc.2011.12.009>.
- [169] Medrano JA, Oliva M, Ruiz J, García L, Arauzo J. Catalytic steam reforming of acetic acid in a fluidized bed reactor with oxygen addition. *Int J Hydrogen Energy* 2008;33:4387–96. <https://doi.org/10.1016/j.ijhydene.2008.05.023>.
- [170] Wang K, Dou B, Jiang B, Zhang Q, Li M, Chen H, et al. Effect of support on hydrogen production from chemical looping steam reforming of ethanol over Ni-based oxygen carriers. *Int J Hydrogen Energy* 2016;41:17334–47. <https://doi.org/10.1016/j.ijhydene.2016.07.261>.
- [171] Antzara A, Heracleous E, Lemonidou AA. Energy efficient sorption enhanced-chemical looping methane reforming process for high-purity H<sub>2</sub> production: Experimental proof-of-concept. *Appl Energy* 2016;180:457–71. <https://doi.org/10.1016/j.apenergy.2016.08.005>.

- [172] Cheng F, Dupont V, Twigg MV. Direct reduction of nickel catalyst with model bio-compounds. *Appl Catal B Environ* 2017;200:121–32. <https://doi.org/10.1016/j.apcatb.2016.06.044>.
- [173] González-Gil R, Chamorro-Burgos I, Herrera C, Larrubia MA, Laborde M, Mariño F, et al. Production of hydrogen by catalytic steam reforming of oxygenated model compounds on Ni-modified supported catalysts. Simulation and experimental study. *Int J Hydrogen Energy* 2015;40:11217–27. <https://doi.org/10.1016/j.ijhydene.2015.05.167>.
- [174] Matas Güell B, Babich I, Seshan K, Lefferts L. Steam reforming of biomass based oxygenates-Mechanism of acetic acid activation on supported platinum catalysts. *J Catal* 2008;257:229–31. <https://doi.org/10.1016/j.jcat.2008.04.019>.
- [175] Thaicharoensutcharittham S, Meeyoo V, Kitiyanan B, Rangsunvigit P, Rirksomboon T. Hydrogen production by steam reforming of acetic acid over Ni-based catalysts. *Catal Today* 2011;164:257–61. <https://doi.org/10.1016/j.cattod.2010.10.054>.
- [176] Basagiannis AC, Verykios XE. Catalytic steam reforming of acetic acid for hydrogen production. *Int J Hydrogen Energy* 2007;32:3343–55. <https://doi.org/10.1016/j.ijhydene.2007.04.039>.
- [177] An L, Dong C, Yang Y, Zhang J, He L. The influence of Ni loading on coke formation in steam reforming of acetic acid. *Renew Energy* 2011;36:930–5. <https://doi.org/10.1016/j.renene.2010.08.029>.
- [178] Hoang TMC, Geerdink B, Sturm JM, Lefferts L, Seshan K. Steam reforming of acetic acid - A major component in the volatiles formed during gasification of humin. *Appl Catal B Environ* 2015;163:74–82. <https://doi.org/10.1016/j.apcatb.2014.07.046>.
- [179] Hu X, Lu G. Comparative study of alumina-supported transition metal catalysts for hydrogen generation by steam reforming of acetic acid. *Appl Catal B Environ* 2010;99:289–97. <https://doi.org/10.1016/j.apcatb.2010.06.035>.
- [180] Iwasa N, Yamane T, Takei M, Ozaki J ichi, Arai M. Hydrogen production by steam reforming of acetic acid: Comparison of conventional supported metal catalysts and metal-incorporated mesoporous smectite-like catalysts. *Int J Hydrogen Energy* 2010;35:110–7. <https://doi.org/10.1016/j.ijhydene.2009.10.053>.
- [181] Takanabe K, Aika KI, Seshan K, Lefferts L. Sustainable hydrogen from bio-oil - Steam reforming of acetic acid as a model oxygenate. *J Catal* 2004;227:101–8. <https://doi.org/10.1016/j.jcat.2004.07.002>.
- [182] Takanabe K, Aika K, Seshan K, Lefferts L. Catalyst deactivation during steam reforming of acetic acid over Pt / ZrO<sub>2</sub> 2006;120:133–7. <https://doi.org/10.1016/j.cej.2006.04.001>.
- [183] Matas Güell B, Babich I, Nichols KP, Gardeniers JGE, Lefferts L, Seshan K. Design of a stable steam reforming catalyst-A promising route to sustainable hydrogen from biomass oxygenates. *Appl Catal B Environ* 2009;90:38–44. <https://doi.org/10.1016/j.apcatb.2009.02.008>.
- [184] Rioche C, Kulkarni S, Meunier FC, Breen JP, Burch R. Steam

reforming of model compounds and fast pyrolysis bio-oil on supported noble metal catalysts. *Appl Catal B Environ* 2005;61:130–9. <https://doi.org/10.1016/j.apcatb.2005.04.015>.

- [185] Davidian T, Guilhaume N, Daniel C, Mirodatos C. Continuous hydrogen production by sequential catalytic cracking of acetic acid. Part I. Investigation of reaction conditions and application to two parallel reactors operated cyclically. *Appl Catal A Gen* 2008;335:64–73. <https://doi.org/10.1016/j.apcata.2007.11.010>.
- [186] Ma Z, Xiao R, Zhang H. Catalytic steam reforming of bio-oil model compounds for hydrogen-rich gas production using bio-char as catalyst. *Int J Hydrogen Energy* 2017;42:3579–85. <https://doi.org/10.1016/j.ijhydene.2016.11.107>.
- [187] Hu RR, Yan CF, Zheng XX, Liu H, Zhou ZY. Carbon deposition on Ni/ZrO<sub>2</sub>-CeO<sub>2</sub> catalyst during steam reforming of acetic acid. *Int J Hydrogen Energy* 2013;38:6033–8. <https://doi.org/10.1016/j.ijhydene.2012.12.141>.
- [188] Lima Da Silva A, Müller IL. Hydrogen production by sorption enhanced steam reforming of oxygenated hydrocarbons (ethanol, glycerol, n-butanol and methanol): Thermodynamic modelling. *Int J Hydrogen Energy* 2011;36:2057–75. <https://doi.org/10.1016/j.ijhydene.2010.11.051>.
- [189] Goicoechea S, Kraveva E, Sokolov S, Schneider M, Pohl M-M, Kockmann N, et al. Support effect on structure and performance of Co and Ni catalysts for steam reforming of acetic acid. *Appl Catal A Gen* 2016;514:182–91. <https://doi.org/http://dx.doi.org/10.1016/j.apcata.2015.12.025>.
- [190] Gil M V., Feroso J, Pevida C, Chen D, Rubiera F. Production of fuel-cell grade H<sub>2</sub> by sorption enhanced steam reforming of acetic acid as a model compound of biomass-derived bio-oil. *Appl Catal B Environ* 2016;184:64–76. <https://doi.org/10.1016/j.apcatb.2015.11.028>.
- [191] Oladokun O, Ahmad A, Abdullah TAT, Nyakuma BB, Kamaruddin MFA, Nor SHM. Biohydrogen production from *Imperata cylindrica* bio-oil using non-stoichiometric and thermodynamic model. *Int J Hydrogen Energy* 2017;42:9011–23. <https://doi.org/10.1016/j.ijhydene.2016.05.200>.
- [192] Sahebdeifar S. Steam reforming of propionic acid: Thermodynamic analysis of a model compound for hydrogen production from bio-oil. *Int J Hydrogen Energy* 2017;42:16386–95. <https://doi.org/10.1016/j.ijhydene.2017.05.108>.
- [193] Vagia EC, Lemonidou AA. Thermodynamic analysis of hydrogen production via steam reforming of selected components of aqueous bio-oil fraction. *Int J Hydrogen Energy* 2007;32:212–23. <https://doi.org/10.1016/j.ijhydene.2006.08.021>.
- [194] Xie H, Yu Q, Wang K, Shi X, Li X. Thermodynamic Analysis of Hydrogen Production from Model Compounds of Bio-oil Through Steam Reforming. *Environ Sci Technol* 2014;33:1008–16. <https://doi.org/10.1002/ep.11846>.

- [195] Hajjaji N, Pons M-N. Hydrogen production via steam and autothermal reforming of beef tallow: A thermodynamic investigation. *Int J Hydrogen Energy* 2013;38:2199–211. <https://doi.org/10.1016/j.ijhydene.2012.11.120>.
- [196] Yenumala SR, Maity SK. Reforming of vegetable oil for production of hydrogen: A thermodynamic analysis. *Int J Hydrogen Energy* 2011;36:11666–75. <https://doi.org/10.1016/j.ijhydene.2011.06.055>.
- [197] Oakley JH, Hoadley AFA. Industrial scale steam reforming of bioethanol: A conceptual study. *Int J Hydrogen Energy* 2010;35:8472–85. <https://doi.org/10.1016/j.ijhydene.2010.05.003>.
- [198] Brown D, Rowe A, Wild P. Techno-economic comparisons of hydrogen and synthetic fuel production using forest residue feedstock. *Int J Hydrogen Energy* 2014;39:12551–62. <https://doi.org/10.1016/j.ijhydene.2014.06.100>.
- [199] Zhang Y, Brown TR, Hu G, Brown RC. Comparative techno-economic analysis of biohydrogen production via bio-oil gasification and bio-oil reforming. *Biomass and Bioenergy* 2013;51:99–108. <https://doi.org/10.1016/j.biombioe.2013.01.013>.
- [200] Martin S, Albrecht FG, Van Der Veer P, Lieftink D, Dietrich RU. Evaluation of on-site hydrogen generation via steam reforming of biodiesel: Process optimization and heat integration. *Int J Hydrogen Energy* 2016;41:6640–52. <https://doi.org/10.1016/j.ijhydene.2016.02.138>.
- [201] Hajjaji N. Thermodynamic investigation and environment impact assessment of hydrogen production from steam reforming of poultry tallow. *Energy Convers Manag* 2014;79:171–9. <https://doi.org/10.1016/j.enconman.2013.12.018>.
- [202] Song H, Ozkan US. Economic analysis of hydrogen production through a bio-ethanol steam reforming process: Sensitivity analyses and cost estimations. *Int J Hydrogen Energy* 2010;35:127–34. <https://doi.org/10.1016/j.ijhydene.2009.10.043>.
- [203] Tzanetis KF, Martavaltzi CS, Lemonidou AA. Comparative exergy analysis of sorption enhanced and conventional methane steam reforming. *Int J Hydrogen Energy* 2012;37:16308–20. <https://doi.org/10.1016/j.ijhydene.2012.02.191>.
- [204] Khan MN, Shamim T. Investigation of hydrogen generation in a three reactor chemical looping reforming process. *Appl Energy* 2016;162:1186–94. <https://doi.org/10.1016/j.apenergy.2015.08.033>.
- [205] Zhu L, Fan J. Thermodynamic analysis of H<sub>2</sub> production from CaO sorption-enhanced methane steam reforming thermally coupled with chemical looping combustion as a novel technology. *Int J Energy Res* 2015;39:356–69. <https://doi.org/10.1002/er.3248>.
- [206] Diglio G, Bareschino P, Mancusi E, Pepe F. Simulation of hydrogen production through chemical looping reforming process in a packed-bed reactor. *Chem Eng Res Des* 2016;105:137–51. <https://doi.org/10.1016/j.cherd.2015.11.013>.

- [207] Diglio G, Bareschino P, Solimene R, Mancusi E, Pepe F, Salatino P. Numerical simulation of hydrogen production by chemical looping reforming in a dual fluidized bed reactor. *Powder Technol* 2017;316:614–27. <https://doi.org/10.1016/j.powtec.2016.12.051>.
- [208] Wang S, Yan L, Zhao F, Lu H, Sun L, Zhang Q. Numerical Simulation of Hydrogen Production via Chemical Looping Reforming in Interconnected Fluidized Bed Reactor. *Ind Eng Chem Res* 2014;53:4182–91. <https://doi.org/10.1021/ie402787v>.
- [209] Spallina V, Marinello B, Gallucci F, Romano MC, Van Sint Annaland M. Chemical looping reforming in packed-bed reactors: Modelling, experimental validation and large-scale reactor design. *Fuel Process Technol* 2017;156:156–70. <https://doi.org/10.1016/j.fuproc.2016.10.014>.
- [210] Sánchez RA, Riboldi L, Jakobsen HA. Numerical modelling and simulation of hydrogen production via four different chemical reforming processes: Process performance and energy requirements. *Can J Chem Eng* 2017;95:880–901. <https://doi.org/10.1002/cjce.22758>.
- [211] Abbas SZ. Modelling of Sorption Enhanced Chemical Looping Steam Reforming (SE-CLSR) of methane in a packed bed reactor. University of Leeds, 2016.
- [212] Grasa G, Navarro M V., López JM, Díez-Martín L, Fernández JR, Murillo R. Validation of the H<sub>2</sub> production stage via SER under relevant conditions for the Ca/Cu reforming process practical application. *Chem Eng J* 2017;324:266–78. <https://doi.org/10.1016/j.cej.2017.04.134>.
- [213] Martínez I, Romano MC, Fernández JR, Chiesa P, Murillo R, Abanades JC. Process design of a hydrogen production plant from natural gas with CO<sub>2</sub> capture based on a novel Ca/Cu chemical loop. *Appl Energy* 2014;114:192–208. <https://doi.org/10.1016/j.apenergy.2013.09.026>.
- [214] Martini M, van den Berg A, Gallucci F, van Sint Annaland M. Investigation of the process operability windows for Ca-Cu looping for hydrogen production with CO<sub>2</sub> capture. *Chem Eng J* 2016;303:73–88. <https://doi.org/10.1016/j.cej.2016.05.135>.
- [215] Aspen Technology Inc. Aspen Plus v8.8 Help n.d.
- [216] Aspen Technology Inc. Aspen Plus V8.8 Property Methods Assistant n.d.
- [217] Chattanathan SA, Adhikari S, Abdoulmoumine N. A review on current status of hydrogen production from bio-oil. *Renew Sustain Energy Rev* 2012;16:2366–72. <https://doi.org/10.1016/j.rser.2012.01.051>.
- [218] Tian X, Wang S, Zhou J, Xiang Y, Zhang F, Lin B, et al. Simulation and exergetic evaluation of hydrogen production from sorption enhanced and conventional steam reforming of acetic acid. *Int J Hydrogen Energy* 2016;41:21099–108. <https://doi.org/10.1016/j.ijhydene.2016.09.184>.
- [219] Çengel YA, Boles MA. *Thermodynamics An Engineering Approach*.

7th Editio. New York: McGraw-Hill; 2011.

- [220] Fatih Demirbas M. Biorefineries for biofuel upgrading: A critical review. *Appl Energy* 2009;86:S151–61. <https://doi.org/10.1016/j.apenergy.2009.04.043>.
- [221] Resende KA, Ávila-Neto CN, Rabelo-Neto RC, Noronha FB, Hori CE. Thermodynamic analysis and reaction routes of steam reforming of bio-oil aqueous fraction. *Renew Energy* 2015;80:166–76. <https://doi.org/10.1016/j.renene.2015.01.057>.
- [222] Remón J, Broust F, Volle G, García L, Arauzo J. Hydrogen production from pine and poplar bio-oils by catalytic steam reforming. Influence of the bio-oil composition on the process. *Int J Hydrogen Energy* 2015;40:5593–608. <https://doi.org/10.1016/j.ijhydene.2015.02.117>.
- [223] Plou J, Lachén J, Durán P, Herguido J, Peña JA. Pure hydrogen from lighter fractions of bio-oil by steam-iron process: Effect of composition of bio-oil, temperature and number of cycles. *Fuel* 2017;203:452–9. <https://doi.org/10.1016/j.fuel.2017.04.127>.
- [224] Tande LN, Dupont V. Autothermal reforming of palm empty fruit bunch bio-oil: thermodynamic modelling. *AIMS Energy* 2016;4:68–92. <https://doi.org/10.3934/energy.2016.1.68>.
- [225] Dupont V, Abdul Halim Yun H, White R, Tande LN. High methane conversion efficiency by low temperature steam reforming of bio-feedstock. REGATEC 2017, Verona, Italy: 2017.
- [226] Garcia-Perez M, Chaala A, Pakdel H, Kretschmer D, Roy C. Characterization of bio-oils in chemical families. *Biomass and Bioenergy* 2007;31:222–42. <https://doi.org/10.1016/j.biombioe.2006.02.006>.
- [227] Pimenidou P, Dupont V. Characterisation of palm empty fruit bunch (PEFB) and pinewood bio-oils and kinetics of their thermal degradation. *Bioresour Technol* 2012;109:198–205. <https://doi.org/10.1016/j.biortech.2012.01.020>.
- [228] Abdul Halim Yun H, Dupont V. Thermodynamic analysis of methanation of palm empty fruit bunch (PEFB) pyrolysis oil with and without in situ CO<sub>2</sub> sorption. *AIMS Energy* 2015;3:774–97. <https://doi.org/10.3934/energy.2015.4.774>.
- [229] Teesside Collective. Teesside Collective 2015.
- [230] Ohta T. Energy Carriers And Conversion Systems With Emphasis On Hydrogen - Volume II. Oxford, UK: Eolss; 2009.
- [231] Health and Safety Executive. A guide to the Gas Safety (Management) Regulations 1996 1996.
- [232] Porter RTJ, Fairweather M, Pourkashanian M, Woolley RM. The range and level of impurities in CO<sub>2</sub> streams from different carbon capture sources. *Int J Greenh Gas Control* 2015;36:161–74. <https://doi.org/10.1016/j.ijggc.2015.02.016>.
- [233] CO<sub>2</sub> Europipe. Towards a transport infrastructure for large-scale CCS in Europe Development of large scale CCS in The North Sea. WP3.1



Report - Standards for CO<sub>2</sub>. 2009.

- [234] Eickhoff C, Brown A, Neele F. Techno-economic Issues and Trade-offs for CO<sub>2</sub> Purity in CCS Chains. *Energy Procedia* 2017;114:6698–707. <https://doi.org/10.1016/j.egypro.2017.03.1798>.
- [235] Harkin T, Filby I, Sick H, Manderson D, Ashton R. Development of a CO<sub>2</sub> Specification for a CCS Hub Network. *Energy Procedia* 2017;114:6708–20. <https://doi.org/10.1016/j.egypro.2017.03.1801>.
- [236] IEAGHG. Techno-Economic Evaluation of SMR Based Standalone (Merchant) Hydrogen Plant with CCS, 2017/02. 2017.
- [237] Kemper J, Sutherland L, Watt J, Santos S. Evaluation and analysis of the performance of dehydration units for CO<sub>2</sub> capture. *Energy Procedia* 2014;63:7568–84. <https://doi.org/10.1016/j.egypro.2014.11.792>.
- [238] Damen K, Troost M Van, Faaij A, Turkenburg W. A comparison of electricity and hydrogen production systems with CO<sub>2</sub> capture and storage. Part A: Review and selection of promising conversion and capture technologies. *Prog Energy Combust Sci* 2006;32:215–46. <https://doi.org/10.1016/j.pecs.2005.11.005>.
- [239] Porter RTJ, Fairweather M, Kolster C, Mac Dowell N, Shah N, Woolley RM. Cost and performance of some carbon capture technology options for producing different quality CO<sub>2</sub> product streams. *Int J Greenh Gas Control* 2017;57:185–95. <https://doi.org/10.1016/j.ijggc.2016.11.020>.
- [240] Spallina V, Shams A, Battistella A, Gallucci F, Annaland MVS. Chemical Looping Technologies for H<sub>2</sub> Production with CO<sub>2</sub> Capture: Thermodynamic Assessment and Economic Comparison. *Energy Procedia* 2017;114:419–28. <https://doi.org/10.1016/j.egypro.2017.03.1184>.
- [241] Lind F, Heyne S, Johnsson F. What is the efficiency of a biorefinery? In: Sanden B, Petterson K, editors. *Syst. Perspectives Biorefineries, Version 3.0*, Göteborg, Sweden: Chalmers University of Technology; 2014.
- [242] Spallina V, Motamedi G, Gallucci F, van Sint Annaland M. Techno-economic assessment of an integrated high pressure chemical-looping process with packed-bed reactors in large scale hydrogen and methanol production. *Int J Greenh Gas Control* 2019;88:71–84. <https://doi.org/10.1016/j.ijggc.2019.05.026>.
- [243] Turton R, Bailie RC, Whiting WB, Shaeiwitz JA. *Analysis, Synthesis and Design of Chemical Processes*. 3rd Editio. Prentice Hall; 2009.
- [244] Guthrie KM. Data and Techniques for Preliminary Capital Cost Estimating. *Chem Eng* 1969:114–42.
- [245] Guthrie KM. *Process Plant Estimating Evaluation and Control*. Solana Beach, CA: Craftsman Book Co.; 1974.
- [246] Ulrich GD. *A Guide to Chemical Engineering Process Design and Economics*. New York: Wiley; 1984.

- [247] Pootakham T, Kumar A. Bio-oil transport by pipeline: A techno-economic assessment. *Bioresour Technol* 2010;101:7137–43. <https://doi.org/10.1016/j.biortech.2010.03.136>.
- [248] Wright MM, Daugaard DE, Satrio JA, Brown RC. Techno-economic analysis of biomass fast pyrolysis to transportation fuels. *Fuel* 2010;89:S2–10. <https://doi.org/10.1016/j.fuel.2010.07.029>.
- [249] Peters MS, Timmerhaus KD, West RE. *Plant design and economics for chemical engineers*. 5th Ed. New York; London: McGraw-Hill; 2004.
- [250] US Department of Energy. *Levelized cost of energy (LCOE) 2015*.
- [251] Riva L, Martínez I, Martini M, Gallucci F, van Sint Annaland M, Romano MC. Techno-economic analysis of the Ca-Cu process integrated in hydrogen plants with CO<sub>2</sub> capture. *Int J Hydrogen Energy* 2018;43:15720–38. <https://doi.org/10.1016/j.ijhydene.2018.07.002>.
- [252] Fogler HS. *Elements of Chemical Reaction Engineering*. 4th Ed., New Jersey: Pearson Education, Inc.; 2006.
- [253] Froment GF. Fixed Bed Catalytic Reactors. *Technological and Fundamental Design Aspects*. *Chemie Ing Tech* 1974;46:374–86. <https://doi.org/10.1002/cite.330460903>.
- [254] Abbas SZ, Dupont V, Mahmud T. Kinetics study and modelling of steam methane reforming process over a NiO/Al<sub>2</sub>O<sub>3</sub> catalyst in an adiabatic packed bed reactor. *Int J Hydrogen Energy* 2017;42:2889–903. <https://doi.org/10.1016/j.ijhydene.2016.11.093>.
- [255] Akpan E, Akande A, Aboudheir A, Ibrahim H, Idem R. Experimental, kinetic and 2-D reactor modeling for simulation of the production of hydrogen by the catalytic reforming of concentrated crude ethanol (CRCCE) over a Ni-based commercial catalyst in a packed-bed tubular reactor. *Chem Eng Sci* 2007;62:3112–26. <https://doi.org/10.1016/j.ces.2007.03.006>.
- [256] Lee DK, Baek IH, Yoon WL. Modeling and simulation for the methane steam reforming enhanced by in situ CO<sub>2</sub> removal utilizing the CaO carbonation for H<sub>2</sub> production. *Chem Eng Sci* 2004;59:931–42. <https://doi.org/10.1016/j.ces.2003.12.011>.
- [257] Abbas SZ, Dupont V, Mahmud T. Modelling of high purity H<sub>2</sub> production via sorption enhanced chemical looping steam reforming of methane in a packed bed reactor. *Fuel* 2017;202:271–86. <https://doi.org/10.1016/j.fuel.2017.03.072>.
- [258] Alarcón JM, Fernández JR. CaCO<sub>3</sub> calcination by the simultaneous reduction of CuO in a Ca/Cu chemical looping process. *Chem Eng Sci* 2015;137:254–67. <https://doi.org/10.1016/j.ces.2015.06.030>.
- [259] Carberry JJ. *Chemical and Catalytic Reaction Engineering*. Dover Publications; 2001.
- [260] Ergun S. Fluid flow through packed columns. *Chem Eng Prog* 1952;48:89–94.

- [261] Edwards MF, Richardson JF. Gas dispersion in packed beds. *Chem Eng Sci* 1968;23:109–23. [https://doi.org/10.1016/0009-2509\(68\)87056-3](https://doi.org/10.1016/0009-2509(68)87056-3).
- [262] Yagi S, Kunii D, Wakao N. Studies on axial effective thermal conductivities in packed beds. *AIChE J* 1960;6:543–6.
- [263] Jarvis RB. *Robust Dynamic Simulation of Chemical Engineering* 1993.
- [264] Process Systems Enterprise. *gPROMS ModelBuilder Documentation Release 4.1.0* 2015.
- [265] Trane-Restrup R, Jensen AD. Steam reforming of cyclic model compounds of bio-oil over Ni-based catalysts: Product distribution and carbon formation. *Appl Catal B Environ* 2015;165:117–27. <https://doi.org/10.1016/j.apcatb.2014.09.026>.
- [266] Arregi A, Lopez G, Amutio M, Barbarias I, Santamaria L, Bilbao J, et al. Kinetic study of the catalytic reforming of biomass pyrolysis volatiles over a commercial Ni/Al<sub>2</sub>O<sub>3</sub> catalyst. *Int J Hydrogen Energy* 2018;43:12023–33. <https://doi.org/10.1016/j.ijhydene.2018.05.032>.
- [267] Bakhtiari M, Zahid MA, Ibrahim H, Khan A, Sengupta P, Idem R. Oxygenated hydrocarbons steam reforming over Ni/CeZrGdO<sub>2</sub> catalyst: Kinetics and reactor modeling. *Chem Eng Sci* 2015;138:363–74. <https://doi.org/10.1016/j.ces.2015.08.003>.
- [268] Gayubo AG, Valle B, Aramburu B, Montero C, Bilbao J. Kinetic model considering catalyst deactivation for the steam reforming of bio-oil over Ni/La<sub>2</sub>O<sub>3</sub>-Al<sub>2</sub>O<sub>3</sub>. *Chem Eng J* 2018;332:192–204. <https://doi.org/10.1016/j.cej.2017.09.063>.
- [269] Goicoechea S, Ehrich H, Arias PL, Kockmann N. Thermodynamic analysis of acetic acid steam reforming for hydrogen production. *J Power Sources* 2015;279:312–22. <https://doi.org/10.1016/j.jpowsour.2015.01.012>.
- [270] Omoniyi OA, Dupont V. Chemical looping steam reforming of acetic acid in a packed bed reactor. *Appl Catal B Environ* 2018;226:258–68. <https://doi.org/10.1016/j.apcatb.2017.12.027>.
- [271] Omoniyi OA. Sorption enhancement and chemical looping as process intensification measures for the steam reforming of acetic acid: A base-case for the enhanced steam reforming of pyrolysis oils. University of Leeds, 2017.
- [272] Omoniyi OA, Dupont V. Optimised cycling stability of sorption enhanced chemical looping steam reforming of acetic acid in a packed bed reactor. *Appl Catal B Environ* 2019;242:397–409. <https://doi.org/10.1016/j.apcatb.2018.09.083>.
- [273] Vogel AI, Mendham J. *Vogel's textbook of quantitative chemical analysis*. Prentice Hall; 2000.
- [274] Bloom R. *Development and Optimisation of Novel Fibrous Oxygen Carriers for Chemical Looping Reforming Processes*. University of Leeds, 2018.
- [275] Ranz WE, Marshall WR. Friction and transfer coefficients for single

particles in packed beds. *Chem Eng Prog* 1952;48:247–53.

- [276] Fuller EN, Schettler PD, Giddings JC. A new method for prediction of binary gas-phase diffusion coefficients. *Ind Eng Chem* 1966;58:18–27. <https://doi.org/10.1021/ie50677a007>.
- [277] Process Systems Enterprise. Model validation and model-based data analysis n.d. <https://www.psenderprise.com/products/gproms/technologies/model-validation> (accessed December 13, 2019).
- [278] S G Adiya ZI, Dupont V, Mahmud T. Chemical equilibrium analysis of hydrogen production from shale gas using sorption enhanced chemical looping steam reforming. *Fuel Process Technol* 2017;159:128–44. <https://doi.org/10.1016/j.fuproc.2017.01.026>.
- [279] Tippawan P, Thammasit T, Assabumrungrat S, Arpornwichanop A. Using glycerol for hydrogen production via sorption-enhanced chemical looping reforming: Thermodynamic analysis. *Energy Convers Manag* 2016;124:325–32. <https://doi.org/10.1016/j.enconman.2016.07.018>.
- [280] Cheng F. Bio-Compounds as Reducing Agents of Reforming Catalyst and their Subsequent Steam Reforming Performance. The University of Leeds, 2014.
- [281] Udomchoke T, Wongsakulphasatch S, Kiatkittipong W, Arpornwichanop A, Khaodee W, Powell J, et al. Performance evaluation of sorption enhanced chemical-looping reforming for hydrogen production from biomass with modification of catalyst and sorbent regeneration. *Chem Eng J* 2016;303:338–47. <https://doi.org/10.1016/j.cej.2016.05.115>.
- [282] García-Díez E, García-Labiano F, De Diego LF, Abad A, Gayán P, Adánez J. Autothermal chemical looping reforming process of different fossil liquid fuels. *Int J Hydrogen Energy* 2017;42:13633–40. <https://doi.org/10.1016/j.ijhydene.2016.12.109>.
- [283] Luo M, Yi Y, Wang S, Wang Z, Du M, Pan J, et al. Review of hydrogen production using chemical-looping technology. *Renew Sustain Energy Rev* 2018;81:3186–214. <https://doi.org/10.1016/j.rser.2017.07.007>.
- [284] Voitic G, Hacker V. Recent advancements in chemical looping water splitting for the production of hydrogen. *RSC Adv* 2016;6:98267–96. <https://doi.org/10.1039/c6ra21180a>.
- [285] Zeng D-W, Xiao R, Zhang S, Zhang H-Y. Bio-oil heavy fraction for hydrogen production by iron-based oxygen carrier redox cycle. *Fuel Process Technol* 2015;139:1–7. <https://doi.org/10.1016/j.fuproc.2015.08.007>.
- [286] Zeng D-W, Xiao R, Huang Z, Zeng J-M, Zhang H-Y. Continuous hydrogen production from non-aqueous phase bio-oil via chemical looping redox cycles. *Int J Hydrogen Energy* 2016;41:6676–84. <https://doi.org/10.1016/j.ijhydene.2016.03.052>.
- [287] Ridler DE, Twigg MV. Chapter 5 Steam reforming. In: Twigg M V., editor. *Catal. Handb.*, Wolfe Publishing Ltd; 1989, p. 225–80.

- [288] Yancheshmeh MS, Radfarnia HR, Iliuta MC. High temperature CO<sub>2</sub> sorbents and their application for hydrogen production by sorption enhanced steam reforming process. *Chem Eng J* 2016;283:420–44. <https://doi.org/10.1016/j.cej.2015.06.060>.
- [289] Lan P, Xu QL, Lan LH, Ren ZW, Zhang SP, Yan YJ. A Model for Carbon Deposition During Hydrogen Production by the Steam Reforming of Bio-oil. *Energy Sources, Part A Recover Util Environ Eff* 2013;36:250–8. <https://doi.org/10.1080/15567036.2012.754516>.
- [290] Zin RM, Lea-Langton A, Dupont V, Twigg M V. High hydrogen yield and purity from palm empty fruit bunch and pine pyrolysis oils. *Int J Hydrogen Energy* 2012;37:10627–38. <https://doi.org/10.1016/j.ijhydene.2012.04.064>.
- [291] Li M. Thermodynamic analysis of adsorption enhanced reforming of ethanol. *Int J Hydrogen Energy* 2009;34:9362–72. <https://doi.org/10.1016/j.ijhydene.2009.09.054>.
- [292] Chen J, Sun J, Wang Y. Catalysts for Steam Reforming of Bio-oil: A Review. *Ind Eng Chem Res* 2017;56:4627–37. <https://doi.org/10.1021/acs.iecr.7b00600>.
- [293] Li Z, Hu X, Zhang L, Lu G. Renewable hydrogen production by a mild-temperature steam reforming of the model compound acetic acid derived from bio-oil. *J Mol Catal A Chem* 2012;355:123–33. <https://doi.org/10.1016/j.molcata.2011.12.006>.
- [294] Li D, Li X, Gong J. Catalytic Reforming of Oxygenates: State of the Art and Future Prospects. *Chem Rev* 2016;116:11529–653. <https://doi.org/10.1021/acs.chemrev.6b00099>.
- [295] Seyedeyn-Azad F, Salehi E, Abedi J, Harding T. Biomass to hydrogen via catalytic steam reforming of bio-oil over Ni-supported alumina catalysts. *Fuel Process Technol* 2011;92:563–9. <https://doi.org/10.1016/j.fuproc.2010.11.012>.
- [296] Xie J, Su D, Yin X, Wu C, Zhu J. Thermodynamic analysis of aqueous phase reforming of three model compounds in bio-oil for hydrogen production. *Int J Hydrogen Energy* 2011;36:15561–72. <https://doi.org/10.1016/j.ijhydene.2011.08.103>.
- [297] Campanario FJ, Gutiérrez Ortiz FJ. Techno-economic assessment of bio-oil aqueous phase-to-liquids via Fischer-Tropsch synthesis and based on supercritical water reforming. *Energy Convers Manag* 2017;154:591–602. <https://doi.org/10.1016/j.enconman.2017.10.096>.
- [298] Do TX, Lim Y II. Techno-economic comparison of three energy conversion pathways from empty fruit bunches. *Renew Energy* 2016;90:307–18. <https://doi.org/10.1016/j.renene.2016.01.030>.
- [299] Zhang Y, Brown TR, Hu G, Brown RC. Techno-economic analysis of two bio-oil upgrading pathways. *Chem Eng J* 2013;225:895–904. <https://doi.org/10.1016/j.cej.2013.01.030>.
- [300] Lehto J, Oasmaa A, Solantausta Y, Kytö M, Chiaramonti D. Review of fuel oil quality and combustion of fast pyrolysis bio-oils from lignocellulosic biomass. *Appl Energy* 2014;116:178–90.

<https://doi.org/10.1016/j.apenergy.2013.11.040>.

- [301] Romano MC, Chiesa P, Lozza G. Pre-combustion CO<sub>2</sub> capture from natural gas power plants, with ATR and MDEA processes. *Int J Greenh Gas Control* 2010;4:785–97. <https://doi.org/10.1016/j.ijggc.2010.04.015>.
- [302] Dodds PE. Economics of hydrogen production. *Compend. Hydrog. Energy*, Elsevier; 2015, p. 63–79. <https://doi.org/10.1016/B978-1-78242-361-4.00003-0>.
- [303] Khan MN, Shamim T. Techno-economic assessment of a plant based on a three reactor chemical looping reforming system. *Int J Hydrogen Energy* 2016;41:22677–88. <https://doi.org/10.1016/j.ijhydene.2016.09.016>.
- [304] Khan MN, Shamim T. Exergoeconomic analysis of a chemical looping reforming plant for hydrogen production. *Int J Hydrogen Energy* 2017;42:4951–65. <https://doi.org/10.1016/j.ijhydene.2016.11.098>.
- [305] Khojasteh Salkuyeh Y, Saville BA, MacLean HL. Techno-economic analysis and life cycle assessment of hydrogen production from natural gas using current and emerging technologies. *Int J Hydrogen Energy* 2017;42:18894–909. <https://doi.org/10.1016/j.ijhydene.2017.05.219>.
- [306] Wassie SA, Cloete S, Spallina V, Gallucci F, Amini S, van Sint Annaland M. Techno-economic assessment of membrane-assisted gas switching reforming for pure H<sub>2</sub> production with CO<sub>2</sub> capture. *Int J Greenh Gas Control* 2018;72:163–74. <https://doi.org/10.1016/j.ijggc.2018.03.021>.
- [307] Cormos C-C. Biomass direct chemical looping for hydrogen and power co-production: Process configuration, simulation, thermal integration and techno-economic assessment. *Fuel Process Technol* 2015;137:16–23. <https://doi.org/10.1016/j.fuproc.2015.04.001>.
- [308] Darmstadt H, Garcia-Perez M, Adnot A, Chaala A, Kretschmer D, Roy C. Corrosion of metals by bio-oil obtained by vacuum pyrolysis of softwood bark residues. An X-ray photoelectron spectroscopy and Auger electron spectroscopy study. *Energy and Fuels* 2004;18:1291–301. <https://doi.org/10.1021/ef0340920>.
- [309] Agarwal P, Sharma DK. Comparative Studies on the Bio-desulfurization of Crude Oil with Other Desulfurization Techniques and Deep Desulfurization through Integrated Processes n.d. <https://doi.org/10.1021/ef900876j>.
- [310] Serefentse R, Ruwona W, Danha G, Muzenda E. A review of the desulphurization methods used for pyrolysis oil. *Procedia Manuf.*, vol. 35, 2019, p. 762–8. <https://doi.org/10.1016/j.promfg.2019.07.013>.
- [311] Maples RE. 16. Naphtha Desulfurization. *Pet. Refin. Econ.* 2nd ed., PenWell; 2000.
- [312] Srifa A, Chaiwat W, Pitakjakpipop P, Anutrasakda W, Faungnawakij K. Advances in bio-oil production and upgrading technologies. *Sustain. Bioenergy Adv. Impacts*, Elsevier; 2019, p. 167–98.

<https://doi.org/10.1016/B978-0-12-817654-2.00006-X>.

- [313] Parkash S. Refining Processes Handbook. Elsevier; 2003. <https://doi.org/10.1016/B978-0-7506-7721-9.X5000-2>.
- [314] Dorf Ketal. Sulphur Guard Catalysts 2020. <https://www.dorfketal.com/industry-solutions/catalysts-and-adsorbents/sulphur-guard-catalysts> (accessed July 5, 2020).
- [315] Eurecat. Sulfur Guard/Sulfur Trap n.d. <https://www.eurecat.com/nickel-sulfur-guard-catalyst.php> (accessed July 28, 2020).
- [316] Matheson. Nanochem GuardBed for Sulfur Removal 2020. <https://www.mathesongas.com/purification/sulfur-removal> (accessed July 5, 2020).
- [317] Unicat Catalyst Technologies Inc. Purification/Unipure - Sulfur Removal n.d. <https://www.unicatcatalyst.com/unipure/unipure-sulfur-removal/> (accessed July 5, 2020).
- [318] Dagle R, Li X, Spies K, Rainbolt J, Braunberger B, King D, et al. Coal-Derived Warm Syngas Purification and CO<sub>2</sub> Capture - Assisted Methane Production. Final Report. 2014.
- [319] Siriwardane R V., Cicero DC, Gupta RP, Turk BS. Durable Zinc Oxide-Based Regenerable Sorbents for Desulfurization of Syngas in a Fixed-Bed Reactor 2004.
- [320] Ritter JA, Ebner AD. State-of-the-Art Adsorption and Membrane Separation Processes for Hydrogen Production in the Chemical and Petrochemical Industries. *Sep Sci Technol* 2007;42:1123–93. <https://doi.org/10.1080/01496390701242194>.
- [321] Grande C a. Advances in Pressure Swing Adsorption for Gas Separation. *ISRN Chem Eng* 2012;2012:13 pages. <https://doi.org/10.5402/2012/982934>.
- [322] Sircar S, Golden TC. Purification of Hydrogen by Pressure Swing Adsorption. *Sep Sci Technol* 2000;35:667–87. <https://doi.org/10.1081/SS-100100183>.
- [323] Martínez I, Romano MC, Chiesa P, Grasa GS, Murillo R. Hydrogen production through sorption enhanced steam reforming of natural gas: Thermodynamic plant assessment. *Int J Hydrogen Energy* 2013;38:15180–99. <https://doi.org/10.1016/j.ijhydene.2013.09.062>.
- [324] Fernández JR, Alarcón JM, Abanades JC. Investigation of a Fixed-Bed Reactor for the Calcination of CaCO<sub>3</sub> by the Simultaneous Reduction of CuO with a Fuel Gas. *Ind Eng Chem Res* 2016;55:5128–32. <https://doi.org/10.1021/acs.iecr.5b04073>.
- [325] Baker EH. The Calcium Oxide-Carbon Dioxide System in the Pressure Range 1-300 Atmospheres. *J Chem Soc* 1962:464–70.
- [326] Saddiq HA, Perry S, Ndagana SF, Mohammed A. Modelling of Gas Turbine and Gas Turbine Exhaust and Its Utilisation As Combined Cycle in Utility System. *Int J Sci Eng Res* 2015;6:925–33.
- [327] Hamers HP, Romano MC, Spallina V, Chiesa P, Gallucci F, Annaland

- MVS. Comparison on process efficiency for CLC of syngas operated in packed bed and fluidized bed reactors. *Int J Greenh Gas Control* 2014;28:65–78. <https://doi.org/10.1016/j.ijggc.2014.06.007>.
- [328] Wright MM, Román-Leshkov Y, Green WH. Investigating the techno-economic trade-offs of hydrogen source using a response surface model of drop-in biofuel production via bio-oil upgrading. *Biofuels, Bioprod Biorefining* 2012;6:503–20. <https://doi.org/10.1002/bbb.1340>.
- [329] Zacher AH, Olarte M V., Santosa DM, Elliott DC, Jones SB. A review and perspective of recent bio-oil hydrotreating research. *Green Chem* 2014;16:491–515. <https://doi.org/10.1039/c3gc41382a>.
- [330] Seider WD, Seader J., Lewin DR. *Process design principles: synthesis, analysis and evaluation*. New York; Chichester: Wiley; 1999.
- [331] Schmidtsche Schack. Flue gas convection section in steam reformer plants for ammonia, methanol, hydrogen production n.d. <https://www.schmidtsche-schack.com/products/flue-gas-convection-section-in-steam-reformer-plants/> (accessed April 25, 2017).
- [332] Sadhukhan J, Ng KS, Martinez E. *Biorefineries and Chemical Processes: Design, Integration and Sustainability Analysis*. First edit. John Wiley & Sons; 2014. <https://doi.org/10.1002/9781118698129>.
- [333] Campanario FJ, Gutiérrez Ortiz FJ. Fischer-Tropsch biofuels production from syngas obtained by supercritical water reforming of the bio-oil aqueous phase. *Energy Convers Manag* 2017;150:599–613. <https://doi.org/10.1016/j.enconman.2017.08.053>.
- [334] Do TX, Lim Y II, Yeo H. Techno-economic analysis of biooil production process from palm empty fruit bunches. *Energy Convers Manag* 2014;80:525–34. <https://doi.org/10.1016/j.enconman.2014.01.024>.
- [335] Methanex. Methanex posts regional contract methanol prices for North America, Europe and Asia. n.d. <https://www.methanex.com/our-business/pricing> (accessed September 17, 2019).
- [336] Swanson RM, Platon A, Satrio JA, Brown RC. Techno-economic analysis of biomass-to-liquids production based on gasification. *Fuel* 2010;89:S11–9. <https://doi.org/10.1016/j.fuel.2010.07.027>.
- [337] Mendes D, Chibante V, Mendes A, Madeira LM. Determination of the Low-Temperature Water-Gas Shift Reaction Kinetics Using a Cu-Based Catalyst. *Ind Eng Chem Res* 2010;49:11269–79.
- [338] Okeke IJ, Mani S. Techno-economic assessment of biogas to liquid fuels conversion technology via Fischer-Tropsch synthesis. *Biofuels, Bioprod Biorefining* 2017;11:472–87. <https://doi.org/10.1002/bbb.1758>.
- [339] Spallina V, Pandolfo D, Battistella A, Romano MC, Van Sint Annaland M, Gallucci F. Techno-economic assessment of membrane assisted fluidized bed reactors for pure H<sub>2</sub> production with CO<sub>2</sub> capture. *Energy Convers Manag* 2016;120:257–73. <https://doi.org/10.1016/j.enconman.2016.04.073>.
- [340] European Commission. *Energy prices and costs in Europe*. 2019.



- [341] OFX. Yearly Average Rates 2017. <https://www.ofx.com/en-gb/forex-news/historical-exchange-rates/yearly-average-rates/> (accessed October 20, 2017).
- [342] Eurostat. Wages and labour costs n.d. <https://ec.europa.eu/eurostat/>.
- [343] Heng L, Xiao R, Zhang H. Life cycle assessment of hydrogen production via iron-based chemical-looping process using non-aqueous phase bio-oil as fuel. *Int J Greenh Gas Control* 2018;76:78–84. <https://doi.org/10.1016/j.ijggc.2018.06.020>.
- [344] Consuli C. Bioenergy and carbon capture and storage - 2019 perspective. 2019.
- [345] Jones S, Snowden-Swan L, Meyer P, Zacher A, Olarte M V., Wang H, et al. Fast Pyrolysis and Hydrotreating: 2015 State of Technology R&D and Projections to 2017. 2016.
- [346] Office of Science and Technical Information. Novel Sorbent to Clean Up Biogas for CHPs. 2015.
- [347] Frilund C, Simell P, Kaisalo N, Kurkela E, Koskinen-Soivi ML. Desulfurization of Biomass Syngas Using ZnO-Based Adsorbents: Long-Term Hydrogen Sulfide Breakthrough Experiments. *Energy and Fuels* 2020;34:3316. <https://doi.org/10.1021/acs.energyfuels.9b04276>.
- [348] Iliuta I, Tahoces R, Patience GS, Rifflart S, Luck F. Chemical-looping combustion process: Kinetics and mathematical modeling. *AIChE J* 2010;56:NA-NA. <https://doi.org/10.1002/aic.11967>.
- [349] Qin C, Feng B, Yin J, Ran J, Zhang L, Manovic V. Matching of kinetics of CaCO<sub>3</sub> decomposition and CuO reduction with CH<sub>4</sub> in Ca-Cu chemical looping. *Chem Eng J* 2015;262:665–75. <https://doi.org/10.1016/j.cej.2014.10.030>.
- [350] Fernández JR, Abanades JC, Murillo R, Grasa GS. Conceptual design of a hydrogen production process from natural gas with CO<sub>2</sub> capture using a Ca-Cu chemical loop. *Int J Greenh Gas Control* 2012;6:126–41. <https://doi.org/10.1016/j.ijggc.2011.11.014>.
- [351] Martini M, Martínez I, Romano MC, Chiesa P, Gallucci F, van Sint Annaland M. Increasing the carbon capture efficiency of the Ca/Cu looping process for power production with advanced process schemes. *Chem Eng J* 2017;328:304–19. <https://doi.org/10.1016/j.cej.2017.07.048>.
- [352] Dueso C, Ortiz M, Abad A, García-Labiano F, De Diego LF, Gayán P, et al. Reduction and oxidation kinetics of nickel-based oxygen-carriers for chemical-looping combustion and chemical-looping reforming. *Chem Eng J* 2012;188:142–54. <https://doi.org/10.1016/j.cej.2012.01.124>.
- [353] Abbas SZ, Dupont V, Mahmud T. Modelling of H<sub>2</sub> production via sorption enhanced steam methane reforming at reduced pressures for small scale applications. *Int J Hydrogen Energy* 2019;44:1505–13. <https://doi.org/10.1016/j.ijhydene.2018.11.169>.
- [354] Zhou Z, Han L, Bollas GM. Kinetics of NiO reduction by H<sub>2</sub> and Ni

oxidation at conditions relevant to chemical-looping combustion and reforming. *Int J Hydrogen Energy* 2014;39:8535–56.  
<https://doi.org/10.1016/j.ijhydene.2014.03.161>.

- [355] Young LC, Finlayson BA. Axial Dispersion in Nonisothermal Packed Bed Chemical Reactors. *Ind Eng Chem Fundam* 1973;12:412–22.  
<https://doi.org/10.1021/i160048a004>.
- [356] Diglio G, Hanak DP, Bareschino P, Pepe F, Montagnaro F, Manovic V. Modelling of sorption-enhanced steam methane reforming in a fixed bed reactor network integrated with fuel cell. *Appl Energy* 2018;210:1–15. <https://doi.org/10.1016/j.apenergy.2017.10.101>.
- [357] Froment GF, Bischoff KB. *Chemical Reactor Analysis and Design*. Second ed. New York: Wiley; 1990.
- [358] Rase H. *Chemical Reactor Design for Process Plants*. New York: Wiley; 1987.
- [359] Kim YJ, Nam YS, Kang YT. Study on a numerical model and PSA (pressure swing adsorption) process experiment for CH<sub>4</sub>/CO<sub>2</sub> separation from biogas. *Energy* 2015;91:732–41.  
<https://doi.org/10.1016/j.energy.2015.08.086>.
- [360] Yan H, Fu Q, Zhou Y, Li D, Zhang D. CO<sub>2</sub> capture from dry flue gas by pressure vacuum swing adsorption: A systematic simulation and optimization. *Int J Greenh Gas Control* 2016;51:1–10.  
<https://doi.org/10.1016/j.ijggc.2016.04.005>.
- [361] López E, Divins NJ, Anzola A, Schbib S, Borio D, Llorca J. Ethanol steam reforming for hydrogen generation over structured catalysts. *Int J Hydrogen Energy* 2013;38:4418–28.  
<https://doi.org/10.1016/j.ijhydene.2013.01.174>.
- [362] Joshi SS, Ranade V V. *Industrial Catalytic Processes for Fine and Specialty Chemicals*. Elsevier; 2016.
- [363] Levenspiel O. *Chemical Reaction Engineering*. 3rd Ed. New York: John Wiley & Sons; 1999.
- [364] Dubey VR, Vaidya PD. Kinetics of steam reforming of acetol over a Pt/C catalyst. *Chem Eng J* 2012;180:263–9.  
<https://doi.org/10.1016/j.cej.2011.11.034>.
- [365] Kaisalo N, Simell P, Lehtonen J. Benzene steam reforming kinetics in biomass gasification gas cleaning. *Fuel* 2016;182:696–703.  
<https://doi.org/10.1016/j.fuel.2016.06.042>.
- [366] Yadav AK, Vaidya PD. Kinetic investigation on butanol steam reforming over Ru/Al<sub>2</sub>O<sub>3</sub> catalyst. *Int J Hydrogen Energy* 2017;42:25203–12. <https://doi.org/10.1016/j.ijhydene.2017.08.021>.
- [367] Akande A, Aboudheir A, Idem R, Dalai A. Kinetic modeling of hydrogen production by the catalytic reforming of crude ethanol over a co-precipitated Ni - Al<sub>2</sub> O<sub>3</sub> catalyst in a packed bed tubular reactor. *Int J Hydrogen Energy* 2006;31:1707–15.  
<https://doi.org/10.1016/j.ijhydene.2006.01.001>.
- [368] Llera I, Mas V, Bergamini ML, Laborde M, Amadeo N. Bio-ethanol

steam reforming on Ni based catalyst. Kinetic study. *Chem Eng Sci* 2012;71:356–66. <https://doi.org/10.1016/j.ces.2011.12.018>.

- [369] Lopez E, Gepert V, Gritsch A, Nieken U, Eigenberger G. Ethanol steam reforming thermally coupled with fuel combustion in a parallel plate reactor. *Ind Eng Chem Res* 2012;51:4143–51. <https://doi.org/10.1021/ie202364y>.
- [370] Mas V, Bergamini ML, Baronetti G, Amadeo N, Laborde M. A kinetic study of ethanol steam reforming using a nickel based catalyst. *Top Catal* 2008;51:39–48. <https://doi.org/10.1007/s11244-008-9123-y>.
- [371] Örucü E, Gökalliler F, Aksoylu AE, Önsan ZI. Ethanol steam reforming for hydrogen production over bimetallic Pt-Ni/Al<sub>2</sub>O<sub>3</sub>. *Catal Letters* 2008;120:198–203. <https://doi.org/10.1007/s10562-007-9269-4>.
- [372] Soyal-Baltacioğlu F, Aksoylu AE, Önsan ZI. Steam reforming of ethanol over Pt-Ni Catalysts. *Catal Today* 2008;138:183–6. <https://doi.org/10.1016/j.cattod.2008.05.035>.
- [373] Wu YJ, Santos JC, Li P, Yu JG, Cunha AF, Rodrigues AE. Simplified kinetic model for steam reforming of ethanol on a Ni/Al<sub>2</sub>O<sub>3</sub> catalyst. *Can J Chem Eng* 2014;92:116–30. <https://doi.org/10.1002/cjce.21773>.
- [374] Cheng CK, Foo SY, Adesina AA. Steam reforming of glycerol over Ni/Al<sub>2</sub>O<sub>3</sub> catalyst. *Catal Today* 2011;178:25–33. <https://doi.org/10.1016/j.cattod.2011.07.011>.
- [375] Menezes JP da SQ, Manfro RL, Souza MMVM. Hydrogen production from glycerol steam reforming over nickel catalysts supported on alumina and niobia: Deactivation process, effect of reaction conditions and kinetic modeling. *Int J Hydrogen Energy* 2018;43:15064–82. <https://doi.org/10.1016/j.ijhydene.2018.06.048>.
- [376] Dave CD, Pant KK. Renewable hydrogen generation by steam reforming of glycerol over zirconia promoted ceria supported catalyst. *Renew Energy* 2011;36:3195–202. <https://doi.org/10.1016/j.renene.2011.03.013>.
- [377] Sutar PN, Vaidya PD, Rodrigues AE. Glycerol-reforming kinetics using a Pt/C catalyst. *Chem Eng Technol* 2010;33:1645–9. <https://doi.org/10.1002/ceat.201000055>.
- [378] Adhikari S, Fernando SD, Haryanto A. Kinetics and reactor modeling of hydrogen production from glycerol via steam reforming process over Ni/CeO<sub>2</sub> catalysts. *Chem Eng Technol* 2009;32:541–7. <https://doi.org/10.1002/ceat.200800462>.
- [379] Nabgan W, Mat R, Abdullah TAT, Nabgan B, Gambo Y, Zakaria ZY. Development of a kinetic model for hydrogen production from phenol over Ni-Co/ZrO<sub>2</sub> catalyst. *J Environ Chem Eng* 2016;4:4444–52. <https://doi.org/10.1016/j.jece.2016.10.013>.
- [380] Lemonidou AA, Vagia EC, Lercher J a. Acetic Acid Reforming over Rh Supported on La<sub>2</sub>O<sub>3</sub>/CeO<sub>2</sub>-ZrO<sub>2</sub>: Catalytic Performance and Reaction Pathway Analysis. *ACS Catal* 2013:1919–28. <https://doi.org/10.1021/cs4003063>.

- [381] Chen G, Tao J, Liu C, Yan B, Li W, Li X. Hydrogen production via acetic acid steam reforming: A critical review on catalysts. *Renew Sustain Energy Rev* 2017;79:1091–8. <https://doi.org/10.1016/j.rser.2017.05.107>.
- [382] Takanabe K, Aika K ichi, Inazu K, Baba T, Seshan K, Lefferts L. Steam reforming of acetic acid as a biomass derived oxygenate: Bifunctional pathway for hydrogen formation over Pt/ZrO<sub>2</sub> catalysts. *J Catal* 2006;243:263–9. <https://doi.org/10.1016/j.jcat.2006.07.020>.
- [383] Wang S, Li X, Guo L, Luo Z. Experimental research on acetic acid steam reforming over Co-Fe catalysts and subsequent density functional theory studies. *Int J Hydrogen Energy* 2012;37:11122–31. <https://doi.org/10.1016/j.ijhydene.2012.05.011>.
- [384] Barbarias I, Lopez G, Artetxe M, Arregi A, Bilbao J, Olazar M. Kinetic Modeling of the Catalytic Steam Reforming of High-Density Polyethylene Pyrolysis Volatiles. *Energy and Fuels* 2017;31:12645–53. <https://doi.org/10.1021/acs.energyfuels.7b01909>.
- [385] Xu JG, Froment GF. Methane Steam Reforming, Methanation and Water-Gas Shift .1. Intrinsic Kinetics. *Aiche J* 1989;35:88–96. <https://doi.org/10.1002/aic.690350109>.
- [386] Czernik S, Evans R, French R. Hydrogen from biomass-production by steam reforming of biomass pyrolysis oil. *Catal Today* 2007;129:265–8. <https://doi.org/10.1016/j.cattod.2006.08.071>.

## Appendix A – Plant capacity

Fast pyrolysis is still undergoing rapid development. In 2012, fast pyrolysis plant capacities ranged from 10 kg h<sup>-1</sup> up to several tonnes per hour. One plant undergoing commissioning at that time was designed to process up to 21,000 kg h<sup>-1</sup> [108,300].

The H<sub>2</sub> production rate is estimated using the following parameters:

- The total feed to a medium-sized pyrolysis plant is 5,000 kg h<sup>-1</sup>.
- Fast pyrolysis converts biomass to whole bio-oil (including water) with a mass yield of 70% [386].
- The hydrogen yield is 12.9g hydrogen per 100g whole bio-oil [386].

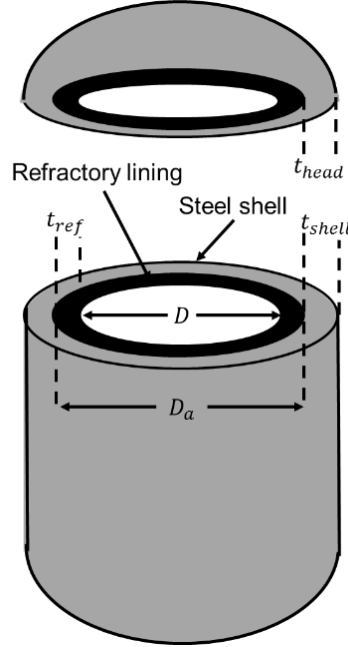
The H<sub>2</sub> production rate from each pyrolysis plant would therefore be:

$$\frac{\text{Biomass feed rate}}{h} \times \frac{\text{Bio - oil mass yield}}{kg_{biomass}} \times \frac{\text{H}_2 \text{ mass yield}}{kg_{bio-oil}} = 451.5 \frac{kg_{H_2}}{h}$$

On a volumetric basis, the hydrogen capacity from each pyrolysis plant would therefore be 5391 Nm<sup>3</sup> h<sup>-1</sup>.

## Appendix B – Reactor design

The reactor vessels consist of a steel shell with a refractory lining (**Figure B.1**).



**Figure B.1** Illustration of reactor vessel design

First, the volume of the reactors was estimated on the basis of the catalyst weight hourly space velocity (WHSV) and the sorbent quantity:

$$m_{cat} = \frac{WHSV}{\dot{m}_{bio-oil}} \quad \text{Eq. B.1}$$

$$m_{sorb} = m_{cat} X_{cat/sorb} \quad \text{Eq. B.2}$$

$$V = \left( \frac{m_{catalyst}}{\rho_{cat}} + \frac{m_{sorbent}}{\rho_{sorb}} \right) (1 - \varepsilon_{bed}) \quad \text{Eq. B.3}$$

where  $m_{cat}$  and  $m_{sorb}$  are the mass of catalyst and sorbent respectively, and  $\dot{m}_{bio-oil}$  is the mass flowrate of bio-oil in the reforming step.  $X_{cat/sorb}$  is the mass ratio of catalyst to sorbent, taken from the process simulation.  $\rho_{cat}$  and  $\rho_{sorb}$  are the densities of catalyst and sorbent respectively, and  $\varepsilon_{bed}$  is the bed void fraction. From this volume and the L/D ratio, the internal diameter  $D$  and the length  $L$  were calculated.

The thickness of refractory lining was calculated from an energy balance over the material [327]:

$$Q = \frac{2\pi\lambda L}{\ln(D_a/D)} (T_{max,cycle} - T_{steel}) \quad \text{Eq. B.4}$$

where  $Q$  is the heat loss from each reactor, and  $\lambda$  is the thermal conductivity of refractory material.  $L$  is the reactor length,  $D_a$  is the internal diameter of

refractory, and  $D$  is the internal diameter of the steel.  $T_{max,cycle}$  is the maximum operating temperature in the SE-CLSR cycle, and  $T_{steel}$  is the maximum temperature the steel is exposed to. It was assumed that total heat losses were equal to 0.25% of the total heat production, that  $T_{steel}$  was 300°C, and  $\lambda$  was 0.2 W (m K)<sup>-1</sup> [327].

The wall thickness of the steel vessel was calculated from equations in Peters et al. [249], based on the ASME Boiler and Pressure Vessel Code.

$$\text{For cylindrical shell:} \quad t_{shell} = \frac{Pr_i}{SE_j - 0.6P} + C_c \quad \text{Eq. B.5}$$

$$\text{For a hemi-spherical head:} \quad t_{head} = \frac{PL_a}{2SE_j - 0.2P} + C_c \quad \text{Eq. B.6}$$

The terms in the equations were defined as follows:

$t_{vessel}$	Minimum wall thickness	m
$P$	Maximum allowable internal pressure	kPa
$r_i$	Inside radius of the shell, before corrosion allowance is added	m
$S$	Maximum allowable working stress	kPa
$E_j$	Efficiency of joints, expressed as a fraction	-
$C_c$	Corrosion allowance	m
$L_a$	Inside radius of hemispherical head	m

The mass of a shell was calculated using the volume of a hollow cylinder:

$$m_{cylinder} = \rho_m \pi L (\pi r_o^2 - \pi r_i^2) \quad \text{Eq. B.7}$$

The mass of each hemi-spherical head was given by [249]:

$$m_{head} = \rho_m [2\pi L_a^2 t_{head}] \quad \text{Eq. B.8}$$

The total mass of steel and of refractory was given by:

$$m_{steel} = f(m_{cylinder,steel} + 2m_{head,steel}) \quad \text{Eq. B.9}$$

$$m_{ref} = m_{cylinder,ref} + 2m_{head,ref} \quad \text{Eq. B.10}$$

where the factor  $f$  was used to account for the extra mass of vessel hardware. For horizontal vessels,  $f$  was assumed to be 1.015, and for vertical vessels,  $f$  was assumed to be 1.2 [249]. SE-CLSR reactors were assumed to be vertical vessels.

The total cost of the reactor was then:

$$C_P^0 = C_{steel} + C_{ref} \quad \text{Eq. B.11}$$

where  $C_{steel}$  and  $C_{ref}$  are the cost of steel and refractory respectively. The cost of the steel vessel was calculated from Peters et al. [249], while the cost of refractory was calculated on a simple mass basis:

$$C_{steel} = (73m_{steel}^{-0.34})m_{steel} \quad \text{Eq. B.12}$$

$$C_{ref} = P_{ref}(m_{cylinder,ref} + m_{head,ref}) \quad \text{Eq. B.13}$$

where  $P_{ref}$  is the price of refractory material \$ kg<sup>-1</sup>.

According to Peters et al. [249], Eq B.12 is valid over a range of 400 to 50,000 kg. When the calculated mass of steel exceeded 50 tonnes, the total required volume was divided into smaller reactors. The total bare module cost was then found using the equation from Turton et al. [243],:

$$C_{BM} = C_p^0 F_M F_P \quad \text{Eq. B.14}$$

The pressure factor  $F_P$  was equal to 1, as the calculation had accounted for pressure. The material factor  $F_M$  for a stainless steel vessel was 3.2 [249].



## Appendix C – Kinetic parameters

### C.1 Kinetic parameters for model of reduction

**Table C1 Rate constants for model of reduction [348]**

Rate constant	Units
$k_{red,1} = 4.66 \exp\left(-\frac{77416}{RT}\right)$	$m s^{-1}$
$k_{red,2} = 1.31 \times 10^{-4} \exp\left(-\frac{24613}{RT}\right)$	$m s^{-1}$
$k_{red,3} = 1.097 \times 10^{-4} \exp\left(-\frac{26505}{RT}\right)$	$m s^{-1}$
$k_{red,4} = 4.18 \times 10^{-3} \exp\left(-\frac{23666}{RT}\right)$	$m s^{-1}$
$k_{rf,H_2O} = 6.237 \times 10^6 \exp\left(-\frac{209000}{RT}\right)$	$kmol (kg_{Ni} s bar^{0.25})^{-1}$
$k_{WGS} = 3.8 \times 10^{-2} \exp\left(-\frac{15400}{RT}\right)$	$kmol (kg_{Ni} s bar)^{-1}$
$k_m = 4.17 \times 10^6 \exp\left(-\frac{105000}{RT}\right)$	$kmol (kg_{Ni} s)^{-1}$
$k_{cd} = 43.4 \exp\left(-\frac{58900}{RT}\right)$	$kmol C (kg_{Ni} s)^{-1}$
$k_{rf,CO_2} = 0.207 \exp\left(-\frac{9920}{RT}\right)$	$kmol (kg_{Ni} s bar^2)^{-1}$
$k_{g,H_2O} = 3.08 \times 10^4 \exp\left(-\frac{166000}{RT}\right)$	$kmol C (kg_{Ni} s)^{-1}$
$k_{g,CO_2} = 8.37 \times 10^{10} \exp\left(-\frac{312000}{RT}\right)$	$kmol C (kg_{Ni} s)^{-1}$

**Table C2 Adsorption coefficients for model of reduction [348]**

Adsorption coefficient	Units
$K_{CO,rf,H_2O} = 5.18 \times 10^{-11} \exp\left(\frac{140000}{RT}\right)$	$bar^{-1}$
$K_{H_2,rf,H_2O} = 5.7 \times 10^{-9} \exp\left(\frac{93400}{RT}\right)$	$bar^{-0.5}$
$K_{H_2O,rf,H_2O} = 9.25 \exp\left(-\frac{15900}{RT}\right)$	$bar^{-0.5}$
$K_{CO,m} = 5.8 \times 10^{-4} \exp\left(\frac{42000}{RT}\right)$	$bar^{-0.5}$
$K_{H_2,m} = 1.6 \times 10^{-2} \exp\left(\frac{16000}{RT}\right)$	$bar^{-0.5}$
$K_{CH_4,cd} = 2.1 \times 10^{-6} \exp\left(\frac{78000}{RT}\right)$	$bar^{-1}$
$K_{r,cd} = 5.18 \times 10^7 \exp\left(-\frac{133000}{RT}\right)$	$bar^{1.5}$
$K_{CO_2,rf,CO_2} = 2.4 \times 10^{-3} \exp\left(\frac{77500}{RT}\right)$	$bar^{-1}$

Adsorption coefficient	Units
$K_{H_2O,g,H_2O} = 4.73 \times 10^{-6} \exp\left(\frac{97700}{RT}\right)$ $K_{CH_4,g,H_2O} = 3.49$	$bar^{-1}$
$K_{r,g,H_2O}'' = 1.83 \times 10^{13} \exp\left(-\frac{216000}{RT}\right)$ $K_{CO_2,rf,CO_2} = 2.4 \times 10^{-3} \exp\left(\frac{77500}{RT}\right)$	$bar^{-1}$

**Table C3 Equilibrium constants for model of reduction [348]**

Equilibrium constant	Units
$K_{eq,rf,H_2O} = 1.17 \times 10^{13} \exp\left(-\frac{26830}{T}\right)$	$bar^2$
$K_{eq,WGS} = 1.77 \times 10^{-2} \exp\left(\frac{4400}{T}\right)$	-
$K_{eq,cd} = \exp\left(\frac{104}{R}\right) \times \exp\left(-\frac{88400}{RT}\right)$	-
$K_{eq,g,H_2O} = \exp\left(\frac{137}{R}\right) \times \exp\left(-\frac{126000}{RT}\right)$	-
$K_{eq,g,CO_2} = \exp\left(\frac{178}{R}\right) \times \exp\left(-\frac{169000}{RT}\right)$	-

## C.2 Kinetic parameters for model of SE-SMR

**Table C4 Rate constants for model of SE-SMR [385]**

Rate constant	Units
$k_{SMR,1} = 1.17 \times 10^{12} \exp\left(\frac{-240100}{RT}\right)$	$kmol bar^{0.5} kg^{-1} s^{-1}$
$k_{WGS} = 5.43 \times 10^2 \exp\left(\frac{-67130}{RT}\right)$	$kmol bar^{0.5} kg^{-1} s^{-1}$
$k_{SMR,2} = 2.83 \times 10^{11} \exp\left(\frac{-243900}{RT}\right)$	$kmol bar^{0.5} kg^{-1} s^{-1}$
$k_{carb} = 0.6$	$s^{-1}$

**Table C5 Adsorption coefficients for model of SE-SMR [385]**

Adsorption coefficient	Units
$K_{CH_4} = 0.179 \exp\left[\frac{38280}{R} \left(\frac{1}{T} - \frac{1}{823}\right)\right]$	$bar^{-1}$
$K_{H_2O} = 0.4152 \exp\left[\frac{-88680}{R} \left(\frac{1}{T} - \frac{1}{823}\right)\right]$	$bar^{-1}$
$K_{H_2} = 0.0296 \exp\left[\frac{82900}{R} \left(\frac{1}{T} - \frac{1}{648}\right)\right]$	$bar^{-1}$
$K_{CO} = 40.91 \exp\left[\frac{70650}{R} \left(\frac{1}{T} - \frac{1}{648}\right)\right]$	$bar^{-1}$

**Table C6 Equilibrium constants for model of SE-SMR [385]**

Equilibrium constant	Units
$K_{SMR,1} = 4.707 \times 10^{12} \exp\left(-\frac{224000}{RT}\right)$	$bar^2$
$K_{WGS} = 1.142 \times 10^{-2} \exp\left(\frac{37300}{RT}\right)$	-
$K_{SMR,2} = K_{SMR,1}K_{WGS}$	$bar^2$

### C.3 Kinetic parameters for model of reduction-calcination

**Table C7 Rate constants for model of reduction-calcination [159,348]**

Rate constant	Units
$k_{red,1} = 4.66 \exp\left(-\frac{77416}{RT}\right)$	$m s^{-1}$
$k_{red,2} = 1.31 \times 10^{-4} \exp\left(-\frac{24613}{RT}\right)$	$m s^{-1}$
$k_{red,3} = 1.097 \times 10^{-4} \exp\left(-\frac{26505}{RT}\right)$	$m s^{-1}$
$k_{red,4} = 4.18 \times 10^{-3} \exp\left(-\frac{23666}{RT}\right)$	$m s^{-1}$
$k_{rf,H_2O} = 6.237 \times 10^6 \exp\left(-\frac{209000}{RT}\right)$	$kmol (kg_{Ni} s bar^{0.25})^{-1}$
$k_{WGS} = 3.8 \times 10^{-2} \exp\left(-\frac{15400}{RT}\right)$	$kmol (kg_{Ni} s bar)^{-1}$
$k_m = 4.17 \times 10^6 \exp\left(-\frac{105000}{RT}\right)$	$kmol (kg_{Ni} s)^{-1}$
$k_{rf,CO_2} = 0.207 \exp\left(-\frac{9920}{RT}\right)$	$kmol (kg_{Ni} s bar^2)^{-1}$
$k_{calc} = 0.35$	$s^{-1}$

**Table C8 Adsorption coefficients for model of reduction-calcination [348]**

Adsorption coefficient	Units
$K_{CO,rf,H_2O} = 5.18 \times 10^{-11} \exp\left(\frac{140000}{RT}\right)$	$bar^{-1}$
$K_{H_2,rf,H_2O} = 5.7 \times 10^{-9} \exp\left(\frac{93400}{RT}\right)$	$bar^{-0.5}$
$K_{H_2O,rf,H_2O} = 9.25 \exp\left(-\frac{15900}{RT}\right)$	-
$K_{CO,m} = 5.8 \times 10^{-4} \exp\left(\frac{42000}{RT}\right)$	$bar^{-0.5}$
$K_{H_2,m} = 1.6 \times 10^{-2} \exp\left(\frac{16000}{RT}\right)$	$bar^{-0.5}$

**Table C9 Equilibrium constants for model of reduction-calcination [348]**

<b>Equilibrium constant</b>	<b>Units</b>
$K_{eq,rf,H_2O} = 1.17$ $\times 10^{13} \exp\left(-\frac{26830}{T}\right)$	$bar^2$
$K_{eq,WGS} = 1.77 \times 10^{-2} \exp\left(\frac{4400}{T}\right)$	-

## Appendix D – Code for model of reduction-calcination

### Model file

#### PARAMETER

```

    components          AS          ORDERED_SET
    reactions           AS          INTEGER
    Reactor_Length     AS          REAL
    Cp_bed              AS          REAL # (J/(kg K))
    Hrxn                AS          ARRAY(reactions) OF REAL #(J/mol)
    nu_g                AS          REAL # (kg/(m s))
    dp                  AS          REAL # particle (m)
    Gs                  AS          REAL # (kg/(m2 s))
    k_o                 AS          ARRAY(reactions) OF REAL
    E                   AS          ARRAY(reactions) OF REAL
# (J/mol)
    Gas_constant       AS          REAL DEFAULT 8.314 # (J/mol K)
    K_large_o          AS          ARRAY(components) OF REAL
# reference adsorption constant
    H                   AS          ARRAY(components) OF REAL
# heat of adsorption (J/mol)
    Mol                 AS          ARRAY(components) OF REAL

# Reduction
    MNiO, MNi, MC      AS          REAL
    ao                  AS          REAL # (m2/g)

# Calcination
    Hcalc              AS          REAL # heat of calcination
    kcalc_o            AS          REAL

# Bed characteristics
    Z_bed              AS          notype # sorb/cat ratio
    Void_bed           AS          REAL # bed porosity
    Void_cat           AS          REAL # particle porosity
    Void_ad            AS          REAL # particle porosity
    Rho_cat            AS          REAL # cat pellet
density(kg/m3)
    Rho_ad             AS          REAL # sorbent density
(kg/m3)

```

```

DISTRIBUTION_DOMAIN
    Axial      AS      [0 : Reactor_Length ]
VARIABLE
    C          AS      DISTRIBUTION(components,Axial) OF
Concentration
    C_o        AS      ARRAY(components)   OF
Concentration
    u          AS      DISTRIBUTION(axial) OF notype
    T          AS      DISTRIBUTION(Axial) OF
Temperature # (K)
    T_o        AS      Temperature # initial (K)
    P          AS      DISTRIBUTION(Axial) OF notype
    Pin        AS      notype
    r_small    AS      DISTRIBUTION(components,Axial) OF Rate
# rate of consumption/formation (mol/(kgcat s))
    rcarb_small AS      DISTRIBUTION(components,Axial) OF Rate
# rate of formation, carbonation (mol/(kgcat s))
    R_large    AS      DISTRIBUTION(reactions,Axial) OF Rate
# (mol/(kgcat s))
    p_p        AS      DISTRIBUTION(components,axial) OF notype
# partial press (bar)
    K_eq       AS      DISTRIBUTION(reactions,Axial) OF notype
# equilibrium constant
    Omega      AS      DISTRIBUTION(Axial) Of notype
# dominator term in reaction
kinetics
    K_large    AS      DISTRIBUTION(components,Axial) OF notype
# adsorption constant

# dry reforming
    K_largeCO2 AS      DISTRIBUTION(Axial) OF notype

# methane decomposition
    K_largeCH4 AS      DISTRIBUTION(Axial) OF notype
    Kpd        AS      DISTRIBUTION(Axial) OF notype
    Krd        AS      DISTRIBUTION(Axial) OF notype

# carbon gasification with steam
    K_H2Og     AS      DISTRIBUTION(Axial) OF notype
    Kpg        AS      DISTRIBUTION(Axial) OF notype
    K_CH4g     AS      DISTRIBUTION(Axial) OF notype
    K_rg       AS      DISTRIBUTION(Axial) OF notype

# carbon gasification with CO2

```

K_CO2g	AS	DISTRIBUTION(Axial) OF notype
K_COg	AS	DISTRIBUTION(Axial) OF notype
Kpg_CO2	AS	DISTRIBUTION(Axial) OF notype
Rho_f	AS	DISTRIBUTION(Axial) OF notype
Cp_g	AS	notype # (J/(kg K))
Re	AS	notype
yi	AS	DISTRIBUTION(components,axial) OF notype
y	AS	DISTRIBUTION(components,axial) OF notype
Mav	AS	DISTRIBUTION(Axial) OF notype
# Reduction		
CNiO	AS	DISTRIBUTION(Axial) OF notype
CNi	AS	DISTRIBUTION(Axial) OF notype
Cc	AS	DISTRIBUTION(Axial) OF notype
Rred_1	AS	DISTRIBUTION(Axial) OF notype
Rred_2	AS	DISTRIBUTION(Axial) OF notype
Rred_3	AS	DISTRIBUTION(Axial) OF notype
Rred_4	AS	DISTRIBUTION(Axial) OF notype
k1,k2,k3,k4	AS	DISTRIBUTION(Axial) OF notype
X	AS	DISTRIBUTION(Axial) OF notype
CNiO_o,CNi_o,Cc_o	AS	Concentration
Carb	AS	DISTRIBUTION(Axial) OF notype
# Carbonation/calcination		
Rcarb	AS	DISTRIBUTION(Axial) OF notype
Rcalc	AS	DISTRIBUTION(Axial) OF notype
qi	AS	DISTRIBUTION(Axial) OF notype
kCO2	AS	notype
kcalc	AS	DISTRIBUTION(Axial) OF notype
yeq	AS	DISTRIBUTION(Axial) OF notype
peq	AS	DISTRIBUTION(Axial) OF notype
Ceq	AS	DISTRIBUTION(Axial) OF notype
Xmax	AS	DISTRIBUTION(Axial) OF notype
# Mixed bed characteristics		
v_cat	AS	notype # vol fraction catalyst
v_ad	AS	notype # vol fraction adsorbent
Rho_bed	AS	notype # density mixed bed

```

BOUNDARY
# At inlet, z = 0
    C(,0)          = C_o;
    T(0)           = T_o ;
    P(0)           = Pin;

# At outlet, z = Reactor_Length
    PARTIAL(C(,Reactor_Length),Axial) = 0 ;
    PARTIAL(T(Reactor_Length),Axial)  = 0 ;

EQUATION
# Mass balance
    FOR i IN components DO
        FOR z := 0|+ TO Reactor_Length|- DO
            Void_bed*(C(i,z) + PARTIAL(u(z)*C(i,z),Axial)
            - 0.3*v_cat*(1-Void_bed)*(1-Void_cat)
            *Rho_cat*r_small(i,z)*1000
            - v_ad*(1-Void_bed)*(1-
Void_ad)*Rho_ad*rcarb_small(i,z)
            = 0 ;
        END
    END

# Calcination
    FOR z := 0 TO Reactor_Length DO
        Rcarb(z) = 0;
        Rcalc(z) = -(1/100)*$qi(z)*1000;
        if qi(z) >= -1e-7 THEN
            $qi(z) = -
kcalc(z) * (abs(qi(z))/Xmax(z))^(2/3) * (Ceq(z) - C('CO2',z));
        ELSE
            $qi(z) = 0;
        END # IF loop

        kcalc(z) = kcalc_o*exp(-91700/Gas_constant/T(z));
        Xmax(z) = 0.08;
        yeq(z) = peq(z)/P(z);

```



```

# Equilibrium CO2
ceq(z) = 5.0451e11*exp(-20474/T(z))*(1/T(z)); #
mol/m3
peq(z) = ceq(z)*Gas_constant*T(z)*1e-5;
END

# Energy balance
FOR z := 0|+ TO Reactor_Length|- DO
Void_bed*Rho_f(z)*Cp_g*$T(z)
+ u(z)*Rho_f(z)*Cp_g*PARTIAL(T(z),Axial)
+(1-Void_bed)*Rho_bed*Cp_bed*$T(z)
= 0.3*v_cat*(1-Void_bed)*(1-Void_cat)*Rho_cat
*(-Hrxn(1)*R_large(1,z)*CNi(z)+(- Hrxn(2))
*R_large(2,z)*CNi(z)
+(-Hrxn(3))*R_large(3,z)*CNi(z)
+(-Hrxn(4))*R_large(4,z)+(-Hrxn(5))*R_large(5,z)+(-
Hrxn(6))*R_large(6,z)
+(-Hrxn(7))*R_large(7,z)+(-Hrxn(8))*R_large(8,z)*CNi(z)
+(-Hrxn(9))*R_large(9,z)*CNi(z)+(-
Hrxn(10))*R_large(10,z)*CNi(z)
+(-Hrxn(11))*R_large(11,z)*CNi(z))*1000
+v_ad*(1-Void_bed)*(1-Void_ad)*Rho_ad*Rcalc(z)*(-Hcalc);
END

# Pressure Dop
FOR z := 0|+ TO Reactor_Length DO
PARTIAL(P(z),axial) =
(-150*nu_g*((1-Void_bed)^2)*u(z)/((dp^2)*(void_bed^3))
-1.75*(1-
void_bed)*Rho_f(z)*(u(z)^2)/(dp*void_bed^3))*1E-5;
END

# Density
FOR z := 0 TO Reactor_Length DO
Rho_f(z) = (P(z)*Mav(z)/Gas_constant/T(z))*100;
END

# Reaction rate (not including Ni/NiO concentration) -
kmol/kg s
FOR z := 0 TO Reactor_Length DO

```

```

if p_p('H2',z)>1e-7
  THEN
    R_large(1,z)
      = k_o(1)*EXP(-E(1)/Gas_constant/T(z))
        *P_P('ch4',Z)*(abs(P_P('H2O',Z)))^0.5
          /((abs(p_p('H2',z)))^1.25)
            *(1 -
P_P('co',Z)*(abs(p_p('H2',z)))^3/(K_eq(1,z)*P_P('ch4',Z)*P_P(
'H2O',Z)))
              *(1/Omega(z)^2) ;

    R_large(2,z)
      = k_o(2)*EXP(-E(2)/Gas_constant/T(z))
        *p_p('CO',z)*(abs(p_p('H2O',z)))^0.5
          / (abs(p_p('H2',z)))^0.5
            *(1 - p_p('CO2',z)*(abs(p_p('H2',z))))
              / (K_eq(2,z)*p_p('CO',z)*p_p('H2O',z)))
                *(1/Omega(z)^2) ;

    Omega(z)
      = 1 + K_large('CO',z)*p_p('CO',z) +
K_large('H2',z)*(abs(p_p('H2',z)))^0.5 +
K_large('H2O',z)*p_p('H2O',z)/(p_p('H2',z));
  ELSE
    R_large(1,z)          = 0;
    R_large(2,z) = 0;
    R_large(3,z) = 0;
    Omega(z)          = 1;
  END # IF loop

  Rred_1(z) = R_large(4,z);
  Rred_2(z) = R_large(5,z);
  Rred_3(z) = R_large(6,z);
  Rred_4(z) = R_large(7,z);
END

# Reduction - kmol/kg s
FOR z:=0 TO Reactor_Length DO

```

```

Rred_1(z) = ao*k1(z)*C('CH4',z)*CNiO(z)*CNi(z)*(1-
X(z));
Rred_2(z) = ao*k2(z)*C('H2',z)*CNiO(z)*(1-X(z));
Rred_3(z) = ao*k3(z)*C('CO',z)*CNiO(z)*(1-X(z));
Rred_4(z) = ao*k4(z)*C('CH4',z)*CNiO(z)*CNi(z)*(1-
X(z));
END

FOR z:=0 TO Reactor_Length DO
# methanation of CO
R_large(3,z) = 0; # turned off for reduction-
calcination
# R_large(3,z) = k_o(3)*EXP(-E(3)/Gas_constant/T(z))
#
#K_COM(z)*K_H2m(z)^2*p_p('CO',z)^0.5*p_p('H2',z)/
#
(1+K_COM(z)*p_p('CO',z)^0.5+K_H2m(z)*p_p('H2',z)^0.5)^3

# CH4 decomposition & carbon formation
R_large(8,z) = 0; # turned off for reduction-
calcination
# R_large(8,z) = k_o(8)*EXP(-E(8)/Gas_constant/T(z))
#
#K_largeCH4(z)*(p_p('CH4',z)-
(p_p('H2',z)^2)/Kpd(z)) /
#
((1+1/Krd(z)*(p_p('H2',z)^1.5)+K_largeCH4(z)*p_p('CH4',z))^2)
;

# Dry methane reforming
R_large(9,z) = 0; # turned off for reduction-
calcination
# R_large(9,z) = k_o(9)*EXP(-E(9)/Gas_constant/T(z))
#
#p_p('CH4',z)*p_p('CO2',z)/(1+K_largeCO2(z)*p_p('CO2',z));

# Carbon gasification with steam
R_large(10,z) = 0; # tuned off for reduction-
calcination
# IF Cc(z) >= -1e-7 THEN
# R_large(10,z) = k_o(10)*EXP(-E(10)/Gas_constant/T(z))
#
# /K_H2Og(z)*(p_p('H2O',z)/p_p('H2',z)-
p_p('CO',z)/Kpg(z))

```

```

#
/((1+K_CH4g(z)*p_p('CH4',z)+1/K_H2Og(z)*p_p('H2O',z)/p_p('H2'
,z)
#
+1/K_rg(z)*(p_p('H2',z)^1.5))^2);
#
ELSE
#
R_large(10,z) = 0;
#
END # if

# Carbon gasificaiton with CO2
R_large(11,z) = 0;
#
IF Cc(z) >=-1e-8 THEN
#
R_large(11,z) # checked
#
= k_o(11)*EXP(-
E(11)/Gas_constant/T(z))/(K_CO2g(z)*K_COg(z))
#
*(p_p('CO2',z)/p_p('CO',z) -
p_p('CO2',z)/Kpg_CO2(z))
#
/((1+K_COg(z)*p_p('CO',z)
#
+1/(K_CO2g(z)*K_Cog(z))*p_p('CO2',z)/p_p('CO',z))^2);
#
ELSE
#
R_large(11,z) = 0;
#
END # if

END

# NiO conversion
FOR z:=0 TO Reactor_Length DO
$X(z) =
(2*Rred_1(z)+Rred_2(z)+Rred_3(z)+Rred_4(z))*MNiO/(CNiO_o);
END

# NiO and Ni
FOR z := 0 TO Reactor_Length DO
$CNiO(z) = -
(2*Rred_1(z)+Rred_2(z)+Rred_3(z)+Rred_4(z))*MNiO;
$CNi(z) =
(2*Rred_1(z)+Rred_2(z)+Rred_3(z)+Rred_4(z))*MNi;
$Cc(z) = (R_large(8,z)-R_large(10,z)-
R_large(11,z))*CNi(z)*MC;
END

# rate of formation - kmol/kgcat s

```

```

FOR z := 0 TO Reactor_Length DO
  r_small('CH4', z)
    = (-R_large(1, z)
      - R_large(3, z) - R_large(8, z) - R_large(9, z)) * CNi(z)
      - Rred_1(z) - Rred_4(z);

  r_small('CO2', z)
    = (R_large(2, z) + R_large(3, z) - R_large(9, z) -
      R_large(11, z)) * CNi(z) + Rred_1(z) + Rred_3(z);

  r_small('H2O', z)
    = (- R_large(1, z) - R_large(2, z) -
      2*R_large(3, z) - R_large(10, z)) * CNi(z) + Rred_2(z);

  r_small('H2', z)
    = (3*R_large(1, z) + R_large(2, z)
      + 4*R_large(3, z) + 2*R_large(8, z) + 2*R_large(9, z)
      + R_large(10, z)) * CNi(z)
      + 2*(Rred_1(z) + Rred_4(z)) - Rred_2(z);

  r_small('CO', z)
    = (R_large(1, z)
      - R_large(2, z) + 2*R_large(9, z) + R_large(10, z)
      + 2*R_large(11, z)) * CNi(z)
      + Rred_4(z) - Rred_3(z);

  r_small('N2', z) = 0;
  r_small('Ar', z) = 0;
  rcarb_small('CH4', z) = 0;
  rcarb_small('CO2', z) = Rcalc(z);
  rcarb_small('H2O', z) = 0;
  rcarb_small('H2', z) = 0;
  rcarb_small('CO', z) = 0;
  rcarb_small('N2', z) = 0;
  rcarb_small('Ar', z) = 0;
END

```

```
# Equilibrium constants
```

```
FOR z := 0 TO Reactor_Length DO
```

```

K_eq(1,z) = 1.17E13*exp(-26830/T(z));
K_eq(2,z) = 1.77e-2*exp(4400/T(z));
K_eq(3,z) = 1;
K_eq(4,z) = 1;
K_eq(5,z) = 1;
K_eq(6,z) = 1;
K_eq(7,z) = 1;
K_eq(8,z) = 1;
K_eq(9,z) = 1;
K_eq(10,z) = 1;
K_eq(11,z) = 1;

END

# adsorption constant
FOR i IN components DO
  FOR z := 0 TO Reactor_Length DO
    K_large(i,z) = K_large_o(i)*EXP(-H(i)
                                / (Gas_constant*T(z))) ;
  END # Length
END # Components

FOR z:=0 TO Reactor_Length DO
# Dry methane reforming
  K_largeCO2(z) = 2.4e-3*EXP(77500/(Gas_constant*T(z)));
# Methane decomposition
  K_largeCH4(z) = (2.1e-6)*EXP(78000/(Gas_constant*T(z)));
  Kpd(z) = exp(104/Gas_constant)*EXP(-
88400/(Gas_constant*T(z)));
  Krd(z) = (5.18e7)*exp(-133000/(Gas_constant*T(z)));
# Carbon gasification with steam
  K_H2Og(z) = (4.73e-6)*EXP(97700/(Gas_constant*T(z)));
  Kpg(z) = exp(137/Gas_constant)*EXP(-
126000/(Gas_constant*T(z)));
  K_CH4g(z) = 3.49;
  K_rg(z) = (1.83e13)*EXP(-216000/(Gas_constant*T(z)));
# Carbon gasification with CO2
  K_CO2g(z) = (8.17e7)*EXP(-
104000/(Gas_constant*T(z)));
  Kpg_CO2(z) = EXP(178/Gas_constant)*EXP(-
169000/(Gas_constant*T(z)));

```

```

        K_COg(z) = (37.8e-6)*EXP(100000/(Gas_constant*T(z)));
    END # length

    FOR i IN components DO
        FOR z:=0 TO Reactor_Length DO
            p_p(i,z) = abs(yi(i,z))*P(z)/100;
        END # length
    END # components

# velocity
    FOR z:=0 TO Reactor_Length DO
        u(z) = Gs/Rho_f(z) ;
    END

# Reynold's number
    Re = Gs * dp/nu_g ;

    FOR z:=0 TO Reactor_Length DO
        yi(,z) = abs(C(,z)/SIGMA(C(,z)))*100;

        Mav(z) =
        (yi('CH4',z)*Mol('CH4')+yi('CO',z)*Mol('CO')+yi('H2',z)*Mol('
H2')
+yi('H2O',z)*Mol('H2O')+yi('CO2',z)*Mol('CO2')+yi('N2',z)*Mol
('N2')
            +yi('Ar',z)*Mol('Ar'))/100;

        Carb(z) = (Cc(z)*0.1/MC)
            / (60*Gs*3.14159*(4e-
3)^2/4/Mav(z)*0.1)*100;
    END

# Dry mol%
    FOR z:=0 TO Reactor_Length DO
        y('H2',z) =
        C('H2',z)/(C('CH4',z)+C('H2',z)+C('CO',z)+C('CO2',z))*100;
        y('CH4',z) =
        C('CH4',z)/(C('CH4',z)+C('H2',z)+C('CO',z)+C('CO2',z))*100;
        y('CO',z) =
        C('CO',z)/(C('CH4',z)+C('H2',z)+C('CO',z)+C('CO2',z))*100;

```

```

        y('CO2',z) =
C('CO2',z)/(C('CH4',z)+C('H2',z)+C('CO',z)+C('CO2',z))*100;
        y('N2',z) = 0;
        y('H2O',z) = 0;
        y('Ar',z) = 0;

```

END

FOR z:=0 TO Reactor\_Length DO

```

        k1(z) = k_o(4)*EXP(-E(4)/(Gas_constant*T(z)));
        k2(z) = k_o(5)*EXP(-E(5)/(Gas_constant*T(z)));
        k3(z) = k_o(6)*EXP(-E(6)/(Gas_constant*T(z)));
        k4(z) = k_o(7)*EXP(-E(7)/(Gas_constant*T(z)));

```

END

### Process file

UNIT

flowsheet AS Reduction\_calcination

SET

WITHIN flowsheet DO

```

        components := ['CH4', 'CO', 'H2', 'H2O',
'CO2', 'N2', 'Ar'];
        reactions := 11;
        Void_bed := 0.4 ;
        Reactor_Length := 7.8 ; # m # shorter length
(pressure drop)
        Void_cat := 0.41;
        Void_ad := 0.48;
        Rho_cat := 3400 ; # kg/m3 # catalyst bulk
denisty # Grasa et al.
        Rho_ad := 2710; # kg/m3 # catalyst bulk
denisty # Grasa et al.
        Z_bed := 3; # sorbent to catalyst weight
ratio
        Cp_bed := 1220; # J/(kg K) Aspen (Z_bed = 3)
        dp := 0.01; # m # industrial (Abbas,
thesis)
        nu_g := 4.37e-4; # (kg/(m s))
        Gs := 0.3 ; # (kg/(m2 s))
        Hrxn := [227000,-33000,10000,

```



```

162000,-16000,-
49000,211000,91000,
259000,136000,169000]; # (J/mol)
k_o := [6.237e6,3.8E-2,1,4.66,1.31E-4,1.097E-4,4.18E-3,
43.4,0.207,3.08e4, 8.37e10] ;
E := [209000,15400,1,
77416,26413,26505,23666,58900, 9920,166000,312000] ; # J/mol
K_large_o := [0,5.18e-11,5.7e-9,9.25,0,0,0];
H := [0,-14e4,-93.4e3,15900,0,0,0]; # J/mol
Mol := [16,28,2,18,44,28,40];

# Reduction
MNi := 58.69; # kg/kmol
MNiO := 74.69; # kg/kmol
MC := 12; # kg/kmol
ao := 102; # m2/g

# calcination
Hcalc := 178800;
kcalc_o := 252.015; # rate constant

# Discretization Method
Axial := [BFDM, 1, 500];
END

ASSIGN
WITHIN flowsheet DO
C_o :=
[0.1467,0.2718,0.2325,7.0756,0.1412,0,0]; #
(mol/m3)
T_o := 1192; # K
Pin := 1.2; # bar
Cp_g := 2350; # off-gas with 90% H2O
CNiO_o := 0.16;
CNi_o := 0.001;
Cc_o := 0;
kCO2 := 0.35;
v_cat := 0.19;
v_ad := 0.81;
Rho_bed := 1558; # (kg/m3)

```

```

END

INITIAL
  WITHIN flowsheet DO
    FOR z := 0|+ TO Reactor_Length|- DO
      C(,z) = C_o() ; # (mol/m3)
      T(z) = 1192; # K # from Aspen Plus
    END

    FOR z := 0 TO Reactor_Length DO
      CNiO(z) = CNiO_o;
      CNi(z) = CNi_o;
      Cc(z) = Cc_o;
      X(z) = 0;
      qi(z) = 0.08; # eqn from Martinez et al.
    END
  END

END

SOLUTIONPARAMETERS
  DASolver := "DASOLV" [
    "OutputLevel" := 2,
    "VariablesWithLargestCorrectorSteps" := 2]
  PESolver := "MAXLKHD" [
    "MINLPSolver" := "SRQPD" [
      "OutputLevel" := 3,
      "Scaling" := 1 ],
    "OutputLevel" := 2]

SCHEDULE
  SEQUENCE
    Continue for 2400
  END

```